# Zn-based electrochemical energy storage devices

A thesis submitted to the University of Manchester for the degree of

Doctor of Philosophy

in the Faculty of Science and Engineering


JIE YANG

Department of Chemistry

2021

Blank Page

# *Table of Contents*

Word Count: 76820

## Abbreviations

| | |
|---|---|
| EES | electrochemical energy storage |
| SEI | solid electrolyte interphase |
| $MX_2$ | metal chalcogenides |
| PC | propylene carbonate |
| LFP | $LiFePO_4$ |
| GIC | graphite-intercalation-compounds |
| EC | ethylene carbonate |
| EV | electric vehicle |
| TR | thermal runaway |
| SOC | state of charge |
| PP | polypropylene |
| PE | polyethylene |
| EDLCs | electrical double layer capacitors |
| IHP | inner Helmholtz plane |
| OHP | outer Helmholtz plane |
| $C_t$ | total capacitance |
| $C_H$ | Helmholtz region capacitance |
| $C_d$ | diffusion region capacitance |
| $\varepsilon_r$ | relative permittivity |
| $\varepsilon_0$ | permittivity of vacuum |
| $d$ | effective thickness |
| EDCC | electrical double-cylinder capacitor |
| EWCC | electrical wire-in-cyclinder capacitor |
| AC | activated carbon |
| $TEA^+$ | tetraethylammonium |
| AN | acetonitrile |
| $BF_4^-$ | tetrafluoroborate |
| CNTs | carbon nanotubes |
| SWCNTs | sing-walled carbon nanotubes |

| | |
|---|---|
| MWCNTs | multi-walled carbon nanotubes |
| 0D | zero-dimensional |
| 1D | one-dimensional |
| 3D | three-dimensional |
| CVD | chemical vapor deposition |
| GO | graphene oxide |
| EGO | electrochemical graphene oxide |
| BOE | buffered oxide etchant |
| RGO | reduced graphene oxide |
| PPy | polypyrrole |
| PANI | polyaniline |
| PTh | polythiophene |
| PEDOT | poly(3,4-ethylenedioxythiophene) |
| HER | hydrogen evolution reaction |
| SHE | standard hydrogen electrode |
| GITT | galvanostatic intermittent titration technique |
| CuHCF | copper hexacyanoferrate |
| $TEABF_4$ | tetraethyl ammonium tetrafluoroborate |
| XRD | X-ray diffraction |
| AC | activated carbon |
| FWHM | full width at half maximum |
| SEM | scanning electron microscopy |
| EDS | energy-dispersive X-ray spectroscopy |
| kV | kilovolts |
| TEM | transmission electron microscopy |
| STEM | scanning transmission electron microscopy |
| SAED | selected area electron diffraction |
| XPS | X-ray photoelectron spectroscopy |
| IUPAC | International Union of Pure and Applied Chemistry |
| BET | Brunauer-Emmett-Teller |
| BJH | Barrett-Joyner-Halenda |

| | |
|---|---|
| NLDFT | non-local density functional theory |
| CV | cyclic voltammetry |
| $Fc^+$ | ferricenium |
| Fc | ferrocene |
| EIS | electrochemical impedance spectroscopy |
| $R_s$ | equivalent series resistance |
| $R_{ct}$ | charge transfer resistance |
| Å | angstrom |
| μm | micrometer |
| nm | nanometer |
| Hz | Hertz |
| V | volt |
| Wh | watt-hour |
| kg | kilogram |
| L | liter |
| mA | milliampere |
| A | ampere |
| g | gram |
| cm | centimeter |
| wt | weight |
| °C | Celsius |
| min | minute |
| s | second |
| F | Faraday's constant |
| mV | millivolt |
| S | siemens |
| K | Kelvin |

# List of Figures and Tables

## *Chapter 1*

## *Chapter 2*

***Chapter 3***

### *Chapter 4*

## *Chapter 5*

*Chapter 6*

## Abstract

As a new and promising type of energy storage device in terms of safety, cost and environmental compatibility, Zn-based electrochemical storage devices such as zinc-ion batteries and zinc ion hybrid supercapacitors are investigated in terms of the fundamental mechanism and electrochemical performance.

Firstly, $MnO_2$ prepared by a hydrothermal method was used to investigate reaction mechanism in aqueous Zn-$MnO_2$ batteries. Direct evidence was provided of the importance of $Mn^{2+}$ in this type of battery by using a bespoke cell. Without pre-addition of $Mn^{2+}$, the cell exhibited an abnormal discharge–charge profile, meaning it functioned as a primary battery. By adjusting the $Mn^{2+}$ content in the electrolyte, the cell recovered its charging ability through electrodeposition of $MnO_2$. Additionally, a dynamic pH variation was observed during the discharge–charge process, with a precipitation of $Zn_4(OH)_6(SO_4)\cdot 5H_2O$ buffering the pH of the electrolyte. Contrary to the conventional $Zn^{2+}$ intercalation mechanism, $MnO_2$ was first converted into MnOOH, which reverted to $MnO_2$ through disproportionation, resulting in the dissolution of $Mn^{2+}$. The charging process occurred by the electrodeposition of $MnO_2$, thus improving the reversibility through the availability of $Mn^{2+}$ ions in the solution.

Secondly, the voltage range and self-discharge phenomena have been systematically investigated in aqueous zinc ion hybrid supercapacitors by using cyclic voltammetry and galvanostatic charge-discharge method, which leads to better understanding of this hybrid device. The upper cut-off voltage is limited to 1.8 V (vs. $Zn^{2+}$/Zn) due to the oxidation of carbon surface functional groups or oxidation of the carbon bulk. The mechanism of the zinc ion hybrid supercapacitor involves the simultaneous adsorption/desorption of ions on the activated carbon cathode and zinc ion plating/stripping on the Zn anode. Constructed by the high capacity of the Zn metal negative electrode, neutral aqueous electrolyte and activated carbon positive electrode, this hybrid supercapacitor has demonstrated excellent electrochemical performance

including high specific capacitance (308 F $g^{-1}$ at 0.5 A $g^{-1}$ and 110 F $g^{-1}$ at 30 A $g^{-1}$), good cycling stability (10,000 cycles with 95.1% capacitance retention) and a high energy density 104.8 Wh $kg^{-1}$ at 383.5 W $kg^{-1}$ (30.8 Wh $kg^{-1}$ at 19.0 kW $kg^{-1}$) based on the active materials. Considering that the zinc foil can be simultaneously used as both current collector and active material, the unnecessary weight and volume of the devices can potentially be reduced to some extent. Additionally, the self-discharge was substantially suppressed in the hybrid supercapacitors compared with the symmetric supercapacitors, which is highly dependent on the initial voltage.

Thirdly, safe, low-cost and environmentally benign zinc-ion hybrid supercapacitors based on neutral aqueous electrolytes are promising for large scale and high power energy storage. A key challenge for Zn-ion hybrid supercapacitors is to increase their energy density without sacrificing the high power performance. A Zn-ion hybrid supercapacitor using a polypyrrole/electrochemical graphene oxide (PPy/EGO) composite cathode and aqueous zinc halide electrolyte (i.e., 1 M $ZnCl_2$ or $ZnBr_2$) was investigated. The EGO was used to prepare conducting polymer composite due to its low degree of oxidation and good integrity in conjugated structure, which are favoured for electron conduction. The water dispersible EGO allows one-step co-electrodeposition of PPy/EGO composite that has an interconnected porous structure for fast ion diffusion in pores. Moreover, the small-sized and monovalent anions in the optimized zinc halides electrolytes are highly mobile in bulk PPy for fast anion insertion/de-insertion. Hence, the PPy/EGO composite showed high specific capacitances > 440 F $g^{-1}$ and good rate capability in either 1 M $ZnCl_2$ or $ZnBr_2$. The as-fabricated Zn-PPy/EGO system that had an operation cell voltage from 0.5 to 1.5 V exhibited high energy and high power densities of 117.7 Wh $kg^{-1}$ and 72.1 Wh $kg^{-1}$ at 0.34 kW $kg^{-1}$ and 12.4 kW $kg^{-1}$, respectively, with 81% capacity retention over 5000 cycles. Electrochemical characterization and *ex-situ* X-ray photoelectron spectroscopy confirmed the anion dominated charge storage mechanism of PPy cathode in Zn-PPy system, rather than the reported insertion/de-insertion of divalent $Zn^{2+}$ cations.

Finally, we make full use of the principal greenhouse gas (i.e., $CO_2$), as an activating agent to prepare high-value hierarchically porous carbon derived from biomass using green chemistry principles in order to create a renewable resource-based sustainable society. The porous carbon was prepared by using starch as a precursor undergoing different processes including expansion, drying and carbonization as well as the final $CO_2$ activation. The reaction mechanism was investigated by *in-situ* thermogravimetric analysis (TGA) and real-time Fourier-transform infrared spectroscopy (FTIR). The as-prepared samples were characterized by $N_2$ physisorption, X-ray diffraction (XRD), Raman spectroscopy, scanning electron microscopy (SEM) and transmission electron microscopy (TEM). The as-prepared materials were further used in aqueous zinc-ion hybrid supercapacitors, exhibiting a high specific capacitance of 259 F $g^{-1}$ at a current density of 0.5 A $g^{-1}$, high rate capability (160 F $g^{-1}$ at 30 A $g^{-1}$) and excellent cycling stability with 97% capacity retention after 10000 cycles. A high energy density of 94.1 Wh $kg^{-1}$ was achieved at a power density of 399 W $kg^{-1}$ (58.5 Wh $kg^{-1}$ at 24.5 kW $kg^{-1}$) based on the mass of active materials. The excellent electrochemical performance can be attributed to the high specific surface area and well-combined micropores/mesopores within the texture, thus providing effective surface sites and facilitating high rate performance. The combination of sustainable electrode materials with a safe and environmentally friendly energy storage device is expected to provide alternative solutions to the growing environmental concerns and increasing energy demand.

## List of Publications

[1] **Jie Yang**, Mark A. Bissett, Robert A. W. Dryfe*. *Investigation of voltage range and self-discharge in aqueous zinc-ion hybrid supercapacitors.* ***ChemSusChem*** 2021, 14, 1700-1709.

[2] **Jie Yang**, Jianyun Cao, Yudong Peng, Wenji Yang, Suelen Barg, Zhu Liu, Ian A. Kinloch, Mark A. Bissett, Robert A. W. Dryfe*. *Unravelling the Mechanism of Rechargeable Aqueous Zn-$MnO_2$ Batteries: Implementation of Charging Process by Electrodeposition of $MnO_2$.* ***ChemSusChem***, 2020, 13, 4103-4110.

[3] **Jie Yang**, Jianyun Cao, Yudong Peng, Ian A. Kinloch, Mark A. Bissett, Robert A. W. Dryfe. *Unlocking the energy storage potential of polypyrrole via electrochemical graphene oxide for high performance zinc-ion hybrid supercapacitors.* ***Journal of Power Sources,*** **2021**, 516: 230663.

[4] **Jie Yang**, Han Li, Mark A. Bissett, Robert A. W. Dryfe*,Vitaliy L. Budarin,c James H. Clark, Michael North*. *Hierarchically porous carbon derived from starch via $CO_2$ activation for high performance zinc-ion hybrid supercapacitors.* To be submitted to ***Green chemistry***.

# Declaration

**The University of Manchester**

**Candidate Name:** Jie Yang

**Faculty:** Science and Engineering

**Thesis Title**: Zn-based electrochemical energy storage devices

**Declaration to be completed by the candidate:**

No portion of this work referred to in this thesis has been submitted in support of an application for another degree or qualification of this or any other university or other institute of learning.

## Copyright Statement

## Acknowledgements

From a scientific point of view, life is nothing but an electron looking for a place to rest, said by Nobel Prize-winning physiologist Albert Szent-Györgyi. As Steve Jobs said, stay hungry and stay foolish. This is specially true for a researcher. From a romantic perspective, life is like a long journey, with lessons to learn, problems to solve, people to love, but most of all, experiences to enjoy. The life in Manchester is a special experience to me, which will be a wonderful memory for my whole life.

Firstly, I gratefully appreciate all the help and guidance from my supervisor Prof. Robert Dryfe and Dr. Mark Bissett. They are always happy to support my idea and provide me constructive suggestions. Their passion for research and diligence as well as responsibility leave a deep impression on me. I would like to acknowledge all the people who have contributed to my project. My sincere thanks are expressed to everyone in the Electrochemistry Group. They are always friendly and obliging. I am particularly grateful to Dr. Lewis Le Fevre, Dr. Andinet Ejigu, Dr. Bin Wang, Dr. Pawin Iamprasertkun, Dr. Richard Fields and Dr. Edurne Redondo in the laboratory. Also, I want to thank my collaborators including Wenji Yang, Yudong Peng, Dr. Jianyun Cao, Prof. Suelen Barg, Dr. Zhu Liu, Prof. Ian A. Kinloch, Han Li and Prof. Michael North. I would like to extend my special thanks to all my friends and colleagues such as Dr. Zheling Li and Dr. Jincheng Tong, Yuling Zhuo and Jingwen Chu who have helped me a lot in my daily life. Then, I would like to acknowledge The University of Manchester to fund my research with the President Doctoral Scholarship Award. I really appreciate this precious and life-changing opportunity.

Additionally, I would like to acknowledge the support and love from my family, especially my great mother. They always support my decisions and their love is always my consistent motivation in the life journey.

Last but not least, I would like to thank myself. This thesis is a special tribute to my youthful days in the laboratory.

# Part I

# Introduction and Characterization

# Chapter 1 Introduction

The demand for energy is rapidly increasing with the development of the modern society. The traditional energy resources like fossil fuels are going to become exhausted in the future due to their non-renewable features. Additionally, the excessive consumption of these traditional energy resources leads to a large emission of carbon dioxide, accelerating the process of global warming. Therefore, to transform from a fossil fuel-based society to a renewable resource-based society, sustainable energy resources, such as solar and wind power, will need to be utilized. However, due to the unstable and intermittent features of these resources, electrochemical energy storage (EES) technology must be developed to store the electricity generated by them. Common EES devices such as lithium-ion batteries and supercapacitors play a critical role in a wide range of applications, such as various portable electronic devices (e.g., smartphones, laptops) and even a growing number of electric vehicles, in modern society. Considering that this thesis focuses on the novel energy storage technologies, the common EES technologies have been introduced, including the types, mechanisms, electrode materials and challenges.

## 1.1 Lithium-ion batteries

Among various batteries such as alkaline batteries, lead-acid batteries and nickel-cadmium batteries, lithium-ion batteries, as one of the revolutionary technologies in modern society, have reshaped our daily life since they were first commercialized by the Sony Corporation in 1991 [1]. The continuous advance in lithium-ion batteries will further reinforce the indispensable role in various fields including portable electronics, electric vehicles and the smart grid. Generally, lithium-ion batteries consist of cathode materials such as lithium transition metal oxides or phosphates, anode materials like graphite and a polymer separator soaked with a $Li^+$-containing organic electrolyte such as $LiPF_6$ dissolved in a mixture of carbonate-based solvents, as shown in Figure 1.1.

The common cathode materials include $LiCoO_2$ [2, 3], $LiMn_2O_4$ [4], $LiNi_{1/3}Co_{1/3}Mn_{1/3}O_2$ [5], $LiFePO_4$ [6], etc. Currently, graphite is the most common anode material used in commercial lithium-ion batteries [7]. However, new anode materials comprised of carbon and silicon materials are promising and are expected to be used as next generation anodes for high energy lithium-ion batteries. The working mechanism of lithium-ion batteries is rather straightforward. The most common cathode material $LiCoO_2$ is used as an example to explain the principle. During the charge process, in which external electrical current is applied, lithium ions are extracted from the cathode ($Li_{1-x}CoO_2$) and stored inside the interlayers of a graphite anode ($Li_xC_6$), thus converting electrical energy into chemical energy. During the discharge process, the stored lithium ions inside the anode go back to the cathode, thus releasing the chemical energy stored by generating an external electrical current. In the common commercial lithium-ion batteries using a $LiCoO_2$ cathode and graphite anode, the reaction mechanism can be briefly formulated as follows:

Cathode reaction: $LiCoO_2 \leftrightarrow Li_{1-x}CoO_2 + xLi^+ + xe^-$ (1.1)

Anode reaction: $C_6 + xLi^+ + xe^- \leftrightarrow Li_xC_6$ (1.2)

Overall reaction: $C_6 + LiCoO_2 \leftrightarrow Li_xC_6 + Li_{1-x}CoO_2$ (1.3)

The shuttling of lithium ions between the cathode and anode via the lithium-ion containing organic electrolyte enables the efficient conversion between electrical and chemical energy repeatedly. It is worth pointing out that passivation layers form at each electrode during the initial cycles of the battery. These layers, known as solid electrolyte interphases (SEI) on anode side and cathode electrolyte interphase (CEI) on cathode side, play a vital role in preventing the electrodes from further reactions with the electrolyte [8, 9].

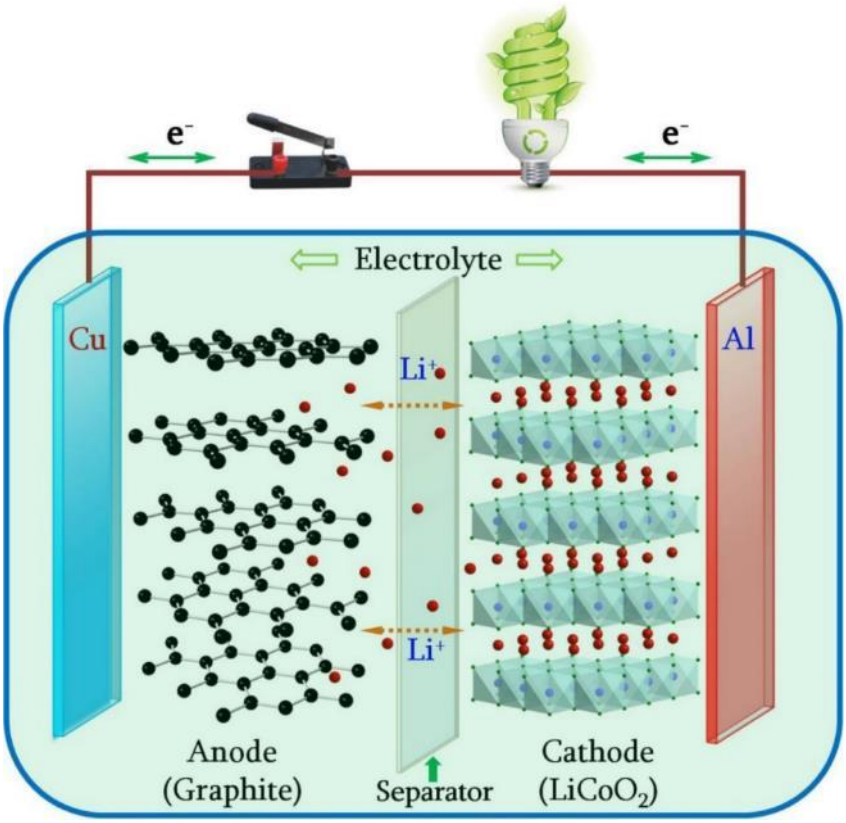


**Figure 1.1.** Schematic of rechargeable lithium-ion batteries. Reproduced from [10].

### 1.1.1 A brief history of lithium-ion batteries

A battery is known to be a complex system composed of multiple components. All the components inside the battery need to work synergistically to ensure the cell functions properly. Basically, a battery is composed of two electrodes physically separated by a separator containing electrolytes, as shown in Figure 1.1. Let us briefly look back at the history of modern lithium-ion batteries. Due to the concern of the oil crisis in the early 1970s, research activities regarding new alternative energy-related technologies began to receive more and more attention [11]. Among them, rechargeable batteries were considered as indispensable to power a variety of electronics and vehicles. Moreover, they can be used to harvest renewable energy from wind and solar sources to further reduce the dependence on fossil fuels. Among numerous researchers, Stanley Whittingham stood out due to the significant contribution in intercalation materials with layered structures [12-17]. In 1965, Rüdorff first proved chemical intercalation by treating titanium disulfide ($TiS_2$) with lithium dissolved in liquid ammonia, leading to

the formation of $Li_{0.6}TiS_2$ [18, 19]. Such an intercalation effect was further proved by Stanley Whittingham and co-workers [13]. They showed that lithium can be chemically intercalated into the $LixTiS_2$ layered materials in a large stoichiometric range ($0 < x \leq 1$) without significant volume expansion. Whittingham was further inspired by these appealing results to investigate electrochemical intercalation in these layered materials and proposed using such materials as battery electrodes in 1974 [20].

A rechargeable battery using $TiS_2$ as cathode, lithium metal as anode and $LiPF_6$ as electrolyte in propylene carbonate (PC) was subsequently demonstrated in 1976 [21], which indicated the beginning of the development of commercial rechargeable lithium-ion batteries. In 1977, aluminum metal was used as an anode to form an alloy with Li and $TiS_2$ was used as the cathode, thus giving rise to a true lithium-ion battery by definition without pure Li metal being used [11, 22]. Due to the significant volume change of the Al host during the charge-discharge process, the cycle life of this type of battery was found to be unsatisfactory. This common issue associated with alloy-type electrodes is still puzzling researchers.

Despite the relatively low $Li^+$ intercalation potential of chalcogenides (~2.0 V vs. $Li^+/Li$) compared with the final cathode materials used in modern lithium-ion batteries, various sulfide-based cathode materials were widely explored [11]. Meanwhile, $MoS_2$ was regarded as a superior electrode to replace the $TiS_2$ in view of the natural abundance of $MoS_2$ and the complicated synthesis of $TiS_2$ [23-25]. Despite the potential hazards related to the highly reactive Li metal anode, Moli Energy, as a leader in the molybdenum mining industry, managed to commercialize this type of high-energy battery using $MoS_2$ as the cathode and Li metal as the anode in 1985, although it finally proved to be a failure because of fire incidents caused by lithium dendrites in this battery when used in cell phones [11].

The cathode materials widely adopted in modern lithium-ion batteries were successfully developed by Goodenough and co-workers [26-28]. Unlike sulfides which are easily oxidized at high potentials, transition metal oxides are stable at higher potentials (> 4.0 V vs. $Li^+/Li$), thus providing higher operating voltages and energy densities. Therefore, a variety of layered structure materials with a formula of $LiMO_2$

(M= Co, Ni, Cr, V) were prepared and investigated. Among them, $LiCoO_2$ was a successful candidate, in which 0.927 of the content of Li could be extracted when the cell was charged to 4.7 V [26]. Unfortunately, $LiCoO_2$ exhibited a significant capacity degradation after a limited number of cycles in the $LiBF_4$/PC electrolyte at that time. The results achieved by Goodenough et al. inspired more researchers to investigate and optimize the $LiCoO_2$ performance and further explore more cathode materials. The common cathode materials subsequently explored include spinel structures ($LiMnO_2$), olivine ($LiFePO_4$) and various solid solutions of Ni, Mn, and Co oxides. These various types of cathode materials will be discussed later. Today some of them have been widely used in commercial lithium-ion batteries. Due to a good trade-off between electrochemical reversibility and energy density, $LiCoO_2$ is still the dominant cathode material in the electronics market of lithium-ion batteries.

Although successful cathode materials had been discovered, the anode materials were still a big obstacle preventing the birth of modern lithium-ion batteries. To make an optimal full battery, an ideal anode was also critical, which seemed to be more challenging than the cathode counterpart. Although use of lithium metal as an anode has a series of advantages such as low electrode potential and a high gravimetric capacity, the safety issue associated with lithium metal excludes the possibility of directly using it as anode for commercial batteries. The recall of batteries from Moli Energy strangled the hope of developing Li metal rechargeable batteries and the incidents drove the development of safer batteries. Meanwhile, companies like Sony and Sanyo were searching for anode materials to fabricate better batteries with higher safety and energy density to meet the development demand of portable electronics [11].

Among various anode candidates, carbon-based materials were chosen as anodes due to the better safety, relatively low Li-intercalation potential, a moderate capacity (~372 mAh $g^{-1}$), and low cost as well as the ease of processing. Before graphite was investigated as an anode in lithium-ion batteries, it was known to host various guest species such as cations ($Li^+$, $K^+$, $Cs^+$, etc.) and anions (halide-based complexes, etc.), or neutral ($NH_3$) species [11, 29]. It was found that alkali metal cations could intercalate into graphite under conditions such as molten metal or vapor via chemical methods. It

was believed that these intercalated alkali species existed in the interlayer of graphite in ionic states to varying degrees and the electrons from alkali metals were transferred to the conduction band of the $sp^2$-hybridized carbon [30]. In fact, most guest species existed in the form of an atom. In 1938, Rüdorff and co-workers demonstrated that $HSO_4^-$ anions could electrochemically shuttle between symmetrical graphite electrodes [11, 31]. This process is quite similar to the operating mechanism in modern lithium-ion batteries. However, electrochemical intercalation of $Li^+$ into graphite was not highly reversible due to the exfoliation and destruction of graphite by solvent co-intercalation with $Li^+$. Initially, graphite was not used as an anode in lithium-ion batteries. The search for better anode materials never stopped. In 1985, Akira Yoshino et al. achieved a significant breakthrough when they found that petroleum coke could be effectively used for electrochemical intercalation of $Li^+$ with a low potential of 0.5 V (vs. $Li^+$/Li) [32]. They constructed a battery based on petroleum coke as anode, $Li_xCoO_2$ as cathode and $LiClO_4$ in PC as electrolyte, which successfully passed the safety test without causing fires or explosions. Later, $LiClO_4$ was replaced by $LiPF_6$ in commercial batteries because of its strong oxidation.

Due to a series of discoveries and advances mentioned above, the first-generation lithium-ion batteries were successfully commercialized by Sony Corporation in 1991. This type of battery was able to deliver a high energy density of ~80 Wh $kg^{-1}$ or ~200 Wh $L^{-1}$. Owing to the high energy density of lithium-ion batteries, they were highly competitive in comparison with other batteries like lead-acid batteries and Ni-Cd batteries. Finally, they have come to dominate in portable electronics from cell phones to laptops and even electric vehicles. Considering the significant contributions of John B. Goodenough, M. Stanley Whittingham, and Akira Yoshino in lithium-ion batteries, they were awarded the Nobel Prize in Chemistry in 2019. The important role of lithium-ion batteries in our modern society is obvious. They have not only powered a mobile world, but also will accelerate a switch from fossil fuels-based society to a clean society driven by renewable energy sources.

### 1.1.2 Cathode materials

Among the multiple components inside lithium-ion batteries, the cathode materials are critical in determining the energy density of the battery and dominate the overall cost of the battery. Initially, sulfide-based materials such as $TiS_2$ and $MoS_2$ were used as cathodes in lithium-ion batteries with a relatively low cell voltage of 2.5 V [26, 33]. In order to increase the cell voltage and maximize the energy output, Goodenough and co-workers started to explore oxide cathodes in 1980 [26].

The cell voltage is mainly dependent on the potential difference between the cathode and the anode. In principle, the potential of the cathode should be as high as possible and the potential of the anode should be as low as possible if the stability window of the electrolyte is not considered. From the viewpoint of energy bands, the anode would possess a higher energy band while the cathode would have a lower energy band. As shown in Figure 1.2, the 3p band of $S^{2-}$ is higher than that of the 2p band of $O^{2-}$, which means the $S^{2-}$ ions are prone to be oxidized at high potentials [33]. Therefore, the utilization of redox reactions such as $Co^{3+}/Co^{4+}$ and $Ni^{2+}/Ni^{3+}$ located at lower energy bands would be restricted by the relatively high energy band of $S^{2-}$. As a result, the sulfide-based materials are excluded as an ideal cathode due to the limited cell voltage. Compared with sulfide-based materials, the redox energy bands in oxides can be much lower, thus providing a high cell voltage of up to 4 V in $LiCoO_2$. The energy bands of materials are becoming one of the main criteria to design and select electrode materials.

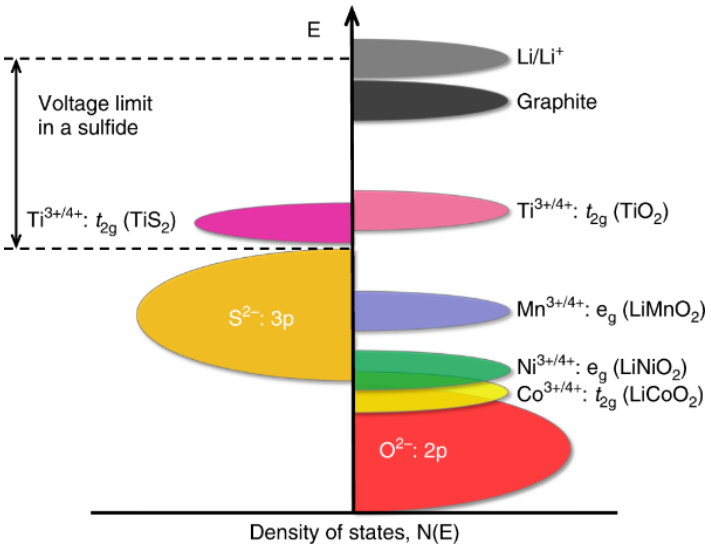


**Figure 1.2.** Energy positions of various redox species relative to the top of the anion p band. Reproduced from [33].

The common cathode materials for lithium-ion batteries can be divided into three types: layered lithium transition metal oxides $LiMO_2$ (M = Ni, Mn, Co, or $Ni_xMn_yCo_z$, x + y + z = 1), spinel $LiM_2O_4$ (M = Mn, Ti, Co, or V) and olivine-type $LiMPO_4$ (M = Fe, Mn, Co, and Ni) [34]. The typical crystal structure is show in Figure 1.3.

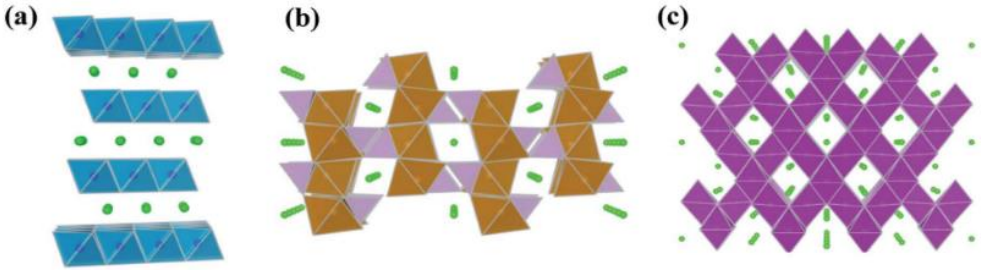


**Figure 1.3.** Schematic of crystal structures of the common cathode materials. **(a)** $LiMO_2$ (layered structure observed along (111) plane, blue: $MO_6$ octahedron, M: transition metal), **(b)** $LiFePO_4$ (olivine structure observed along [010] direction, light purple: $PO_4$ tetrahedron, brown: $FeO_6$ octahedron) and **(c)** $LiMn_2O_4$ (spinel structure observed along [110] direction, purple: $MnO_6$ octahedron). The small green balls

represent $Li^+$. Reproduced from [34].

The electrochemical features of the most common cathode materials are compared in the Table 1.1.

**Table 1.1.** Electrochemical characteristics of cathode materials. Reproduced from [36].

| | $LiCoO_2$ | $LiNi_{0.80}Mn_{0.10}Co_{0.1}O_2$ | $LiNi_{0.80}Co_{0.15}Al_{0.05}O_2$ | $LiNi_{1/3}Mn_{1/3}Co_{1/3}O_2$ | $LiMn_2O_4$ | $LiFePO_4$ |
|---|---|---|---|---|---|---|
| Structure | Layered | Layered | Layered | Layered | Spinel | Olivine |
| Theoretical capacity (mAh $g^{-1}$) | 274 | 275 | 279 | 275 | 148 | 170 |
| Available capacity (mAh $g^{-1}$) | 190@ 4.45 V 215@ 4.55V | 210 | 200@ 4.3V 210@ 4.4V | 160@ 4.3V 185@ 4.5V | 110 | 160 |
| Electrode density (g $cm^{-3}$) | 3.9 | 3.2 | 3.4 | 3.4 | 3.2 | 2.3 |
| Gravimetric energy density (Wh $kg^{-1}$) | 740@ 4.45 V 840@ 4.55 V | 800@ 4.4 V | 760@ 4.3 V 800@ 4.4 V | 610@ 4.3 V 730@ 4.5 V | 410 | 540 |
| Volumetric energy density (Wh $L^{-1}$) | 2900@ 4.45 V 3300@ 4.55 V | 2600@ 4.4 V | 2600@ 4.3 V 2700@ 4.4 V | 2080@ 4.3 V 2480@ 4.5 V | 1300 | 1240 |
| Operating voltage (V) | 3.9 | 3.8 | 3.8 | 3.8 | 4.0 | 3.4 |
| Application | Mobile IT devices, Power tools | Power tools, EVs, Energy storage systems (EESs) | Power tools, EVs, EESs | Power tools, EVs, EESs | Power tools, EVs, EESs | EVs, EESs |

### 1.1.2.1 Layered lithium transition metal oxides

As a typical representative of layered lithium transition metal oxide, $Li_xCoO_2$ was first discovered and investigated by John B. Goodenough and co-workers in 1980. It showed

a high voltage range from 3.9 V to 4.7 V for $0.07 < x \leq 1$ in the electrolyte of $LiBF_4$/PC [26]. Although it was possible to electrochemically extract all the lithium inside $LiCoO_2$, the reversibility was maintained only with less than half of the lithium removed from $LiCoO_2$. Similar layered structures can also be found in other lithium transition metal oxides which possess a general formula $LiMO_2$ (M represents V, Cr, Ni and Fe).

Later, the electrochemical properties of $LiCoO_2$ were comprehensively studied. $LiCoO_2$ exhibits a semiconducting property, but its electronic behavior would change from semiconductor to conductor with the extraction of $Li^+$, which can be regarded as a benefit for fast charge transfer [37]. Furthermore, the ion diffusion in the layered structure of $Li_xCoO_2$ is very fast, rendering it ideal for lithium-ion batteries [38]. Due to its high electrical and $Li^+$ conductivity as well as good reversibility, $LiCoO_2$ remains the flagship cathode material widely used in the portable electronics market. Compared with the sulfide cathode materials, the use of the $LiCoO_2$ cathode not only provided a high operating voltage of ~ 4 V, but also eliminated the need to assemble cells using a lithium metal anode. However, as shown in Figure 1.2, owing to the overlapping of $Co^{3+/4+}$ band with the top of 2p band of $O^{2-}$, $O^{2-}$ would be oxidized into oxygen released from the crystal lattice when more than half of the lithium ions are extracted from $LiCoO_2$. Additionally, cobalt dissolution was found to correlate with structural changes when the cell was operated over 4.2 V, which led to capacity loss with repeated cycles [39]. Therefore, the practical capacity of $LiCoO_2$ is restricted to about 140 mAh $g^{-1}$ at the upper cut-off voltage of 4.2 V although it possesses a high theoretical capacity of 274 mAh $g^{-1}$.

Driven by the ever-increasing demand for high energy density lithium-ion batteries in the portable electronics market, both the industrial community and academia have designed various strategies including surface coatings and element doping to solve the above issues and further improve the capacity of $LiCoO_2$ [40, 41]. Currently, the upper cut-off voltage of $LiCoO_2$ used in commercial lithium-ion batteries has been increased to 4.5 V to deliver a reversible capacity of about 185 mAh $g^{-1}$ [36]. However, there is

still an urgent need to break the cut-off voltage limit of 4.5 V to further enhance the energy density of lithium-ion batteries using $LiCoO_2$ as a cathode. For example, Qian and co-workers [40] modified the bare $LiCoO_2$ with a class of ternary lithium, aluminum, fluorine-containing layers by employing a hydrothermal method and annealing treatment. The protective layer could effectively prevent the direct contact of $LiCoO_2$ particles and electrolytes, thus reducing the dissolution of cobalt. Additionally, it retarded the phase transition of $LiCoO_2$ over 4.55 V with a capacity retention of 81.8% after 200 cycles. Furthermore, Li and co-workers [42] reported that trace amounts of Ti-Mg-Al co-doping (each dopant with ~0.1 wt%) enabled good cyclability of $LiCoO_2$ at an upper voltage of 4.6 V. After 100 cycles, a high reversible discharge capacity of 174 mAh $g^{-1}$ was obtained with a capacity retention of 86% much higher than that obtained in the bare $LiCoO_2$, as shown in Figure 1.4. The good battery performance of this modified $LiCoO_2$ was explained by benefiting from the microstructural changes and electronic structure reconfiguration induced by the ternary elements co-doping. Although some promising progress in $LiCoO_2$-based lithium-ion batteries with high voltage above 4.5 V has been achieved in the laboratory, the long-term cyclability and practical safety issue are still needed to be considered for full cells under various practical conditions.

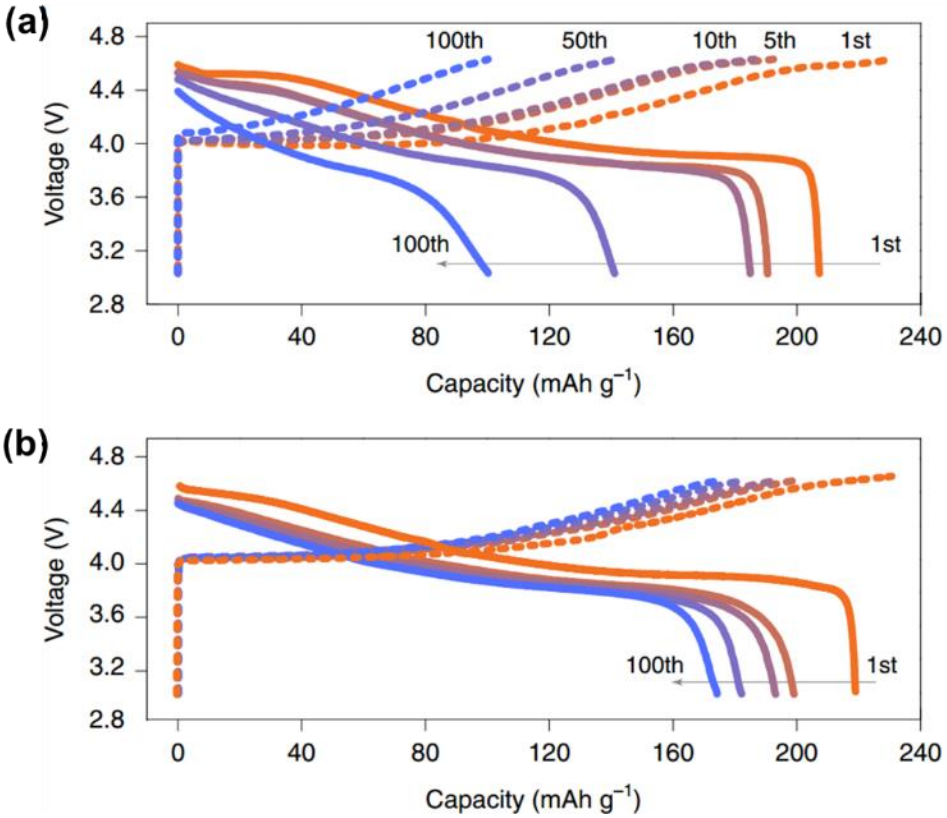


**Figure 1.4.** Charge-discharge curves of **(a)** bare $LiCoO_2$ and **(b)** Ti-Mg-Al co-doping $LiCoO_2$ half cells for the 1st, 5th, 10th, 50th and 100th cycles. The charge and discharge tests were conducted at 0.1 C for the first cycle and 0.5 C for the subsequent cycles. Reproduced from [42].

The success of $LiCoO_2$ as cathode has driven the further development of numerous layered lithium transition metal oxides with a general formula of $LiMO_2$ in which M can represent Mn, Fe, Co, Ni, Ti, etc [33]. Among them, $LiNi_{1-y-z}Mn_yCo_zO_2$ is considered as a promising alternative to substitute part of cobalt with other transition metals in the view of the high cost and limited capacity of $LiCoO_2$. In $LiNi_{1-y-z}Mn_yCo_zO_2$, $Mn^{3+}$ has tendency to be oxidized into $Mn^{4+}$ via the reduction of $Ni^{3+}$ into $Ni^{2+}$ during the synthetic process. Consequently, $Mn^{4+}$ aids the incorporation of $Ni^{2+}$ into the host structure and does not participate in the charge storage. However, the structural stability of Mn is not as good as Co due to a lower octahedral-site stabilization energy, leading to the migration of Mn from the transition-metal plane to the lithium plane through a neighboring tetrahedral site [33]. This can give rise to the transition

from a layered structure to a spinel structure accompanied by the voltage decay during repeated cycles. Another important issue is the cation mixing between the lithium ions and nickel ions due to their close ionic radius, which is detrimental to the electrochemical performance [43]. Currently, a few types of this cathode material have already been commercialized in lithium-ion batteries such as $LiNi_{1/3}Mn_{1/3}Co_{1/3}O_2$, $LiNi_{0.5}Mn_{0.3}Co_{0.2}O_2$ and $LiNi_{0.6}Mn_{0.2}Co_{0.2}O_2$ [44]. In view of the higher specific capacity and low cost, this type of cathode material with even higher nickel content such as $LiNi_{0.8}Mn_{0.1}Co_{0.1}O_2$ are still attracting extensive research interest.

#### 1.1.2.2 Spinel cathode materials

Considering that cobalt resources are scarce and toxic, there is a trend in developing cobalt-free cathode materials such as $LiMn_2O_4$. Among various candidates, spinel $LiMn_2O_4$ is regarded as one of the potential cathode materials to be used in electric vehicles because of its abundance, low cost, environmental friendliness and high safety [45]. The spinel $LiMn_2O_4$ has a theoretical capacity of 148 mAh $g^{-1}$ and delivers a practical capacity of 120 mAh $g^{-1}$. Despite the advantages presented by $LiMn_2O_4$, its cyclability and high-rate capability are not very satisfactory, especially at elevated temperatures, which hinder its wider applications. The inferior electrochemical performance can be interpreted by manganese ions that undergo the Jahn Teller effect. The manganese ions in the crystal structure exist in the form of $Mn^{3+}$ and $Mn^{4+}$. During the discharge process, the $Mn^{3+}$ concentration will increase accordingly and a disproportionation reaction (i.e., $2Mn^{3+} \rightarrow Mn^{4+} + Mn^{2+}$) will occur on the material surface, leading to the dissolution of $Mn^{2+}$ into the electrolyte and the loss of Mn [46].

Although $LiMn_2O_4$ cathode materials began to be commercialized very early, they do not occupy a large market share owing to their poor cyclability and fast capacity degradation at elevated temperatures. The common strategies used to solve the above issues include doping and surface modification. The introduction of small amounts of other elements into the lattice of $LiMn_2O_4$ has been demonstrated to improve its

electrochemical performance. For example, Liu and co-workers investigated the doping effects of $Fe^{3+}$, $Co^{3+}$, and $Al^{3+}$ on the structure, particle morphology and electrochemical performance of $LiMn_2O_4$ [47]. Compared with $Fe^{3+}$ and $Al^{3+}$, $LiMn_2O_4$ doped with $Co^{3+}$ (i.e., $LiCo_{0.05}Mn_{1.95}O_4$) exhibited an initial capacity of 111.7 mAh $g^{-1}$ and a capacity retention of 87.2% after 200 cycles. Prakash and co-workers synthesized a series of Sc-doped $LiSc_xMn_{2-x}O_4$ (x= 0.04, 0.06, 0.08 and 0.1) using a solid-state reaction, as shown in Figure 1.5 [48]. Among them, $LiSc_{0.06}Mn_{1.94}O_4$ exhibited a discharge capacity of 114 mAh $g^{-1}$ at 1 C (1 C = 148 mA $g^{-1}$) with a capacity retention of 89% after 500 cycles due to the improved structural stability derived from Sc-doping.

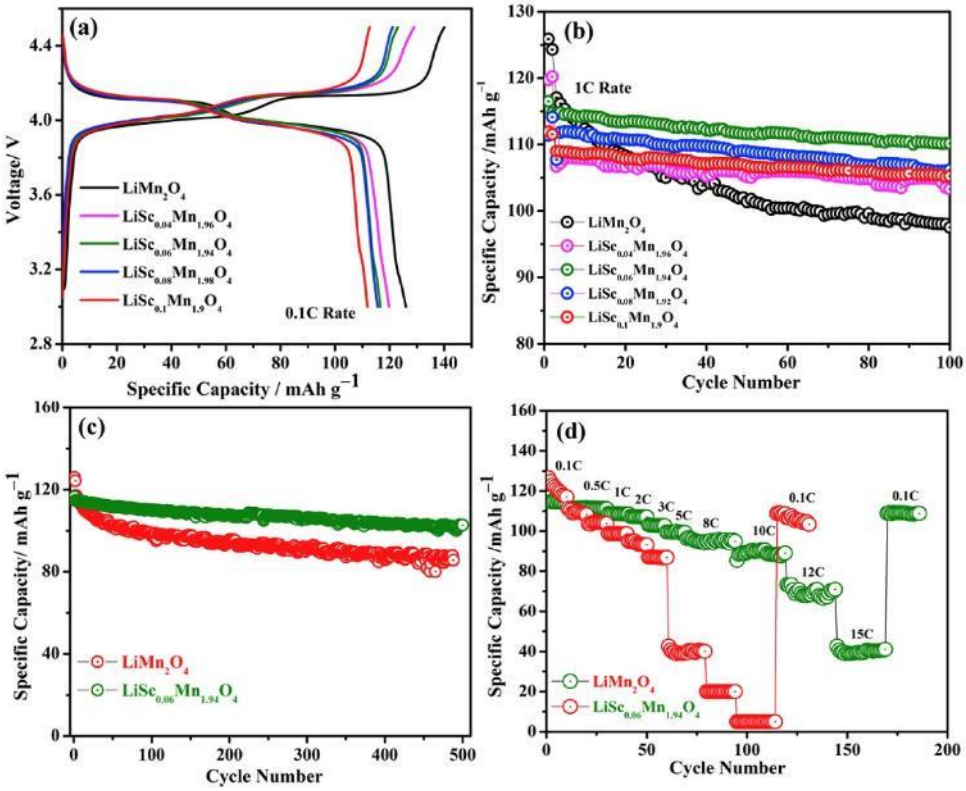


**Figure 1.5. (a)** Comparison of 1st charge/discharge profiles of $LiSc_xMn_{2-x}O_4$ (x=0, 0.04, 0.06, 0.08 and 0.1) in the voltage range between 3.0 V and 4.5 V (vs. $Li^+/Li$) at 0.1 C (1 C = 148 mA $g^{-1}$), **(b)** Cycling stability of samples (100 cycles at 1 C rate), **(c)** Discharge capacity vs. cycle number of $LiMn_2O_4$ and $LiSc_{0.06}Mn_{1.94}O_4$ for 500 cycles **(d)** Rate capability profile of $LiMn_2O_4$ and $LiSc_{0.06}Mn_{1.94}O_4$. Reproduced from [48].

Additionally, surface modification is another common strategy used to improve the electrochemical performance of $LiMn_2O_4$. Surface coatings such as $Al_2O_3$, $ZrO_2$ and $AlF_3$ can effectively prevent the direct contact between the active materials with the electrolyte, thus mitigating the undesired side reactions [45]. For instance, Liu et al. synthesized the $LiMn_2O_4$ coated by $AlF_3$, which delivered a capacity of 108.5 mAh $g^{-1}$ and a capacity retention of 91.7 % after 100 cycles, higher than that (86.3 %) of the pristine $LiMn_2O_4$ [49].

#### 1.1.2.3 Polyanion oxides

In addition to the development of cathode materials with high energy densities, safety is also another critical issue required in the battery system. Due to the outstanding safety characteristics, $LiFePO_4$, as a typical olivine cathode, has received a lot of attention in both academia and industry since it was first developed by Goodenough and co-workers in 1997 [50]. $LiFePO_4$ exhibits a theoretical specific capacity of 170 mAh $g^{-1}$ and a moderate operating voltage of 3.4 V (vs. $Li^+/Li$). Furthermore, its safety, abundance, low cost and environmental compatibility render it an attractive cathode material for large-scale applications such as hybrid electric vehicles and grid storage of electricity generated from various renewable sources [33, 51]. Nevertheless, its low electrical conductivity, low $Li^+$ diffusion coefficient and relatively low volumetric energy density are the main drawbacks for the wider applications [52]. To effectively resolve these issues, various strategies have been designed to optimize the electrochemical performance of $LiFePO_4$, including introduction of conductive coatings, element doping and particle nanosizing [53-55]. Carbon coating is the most common approach employed to improve the electrical conductivity of $LiFePO_4$. Although carbon coating is effective in ensuring the electron transport between the $LiFePO_4$ particles, its thickness and structure should be considered to allow the effective transportation of $Li^+$. For example, Wan et al. [56] used the in-situ polymerization of dopamine followed by heat treatment under $Ar/H_2$ atmosphere to form a continuous and uniform carbon

coating on the surface of $LiFePO_4$, as shown in Figure 1.6. The carbon thickness can be readily controlled by tunning the concentration of dopamine or polymerization time. The $LiFePO_4$ coated with a 5 nm carbon layer exhibited a discharge capacity of 147.9 mAh $g^{-1}$ at 0.1 C (1 C= 170 mA $g^{-1}$) and optimal rate capability among the investigated samples. It also should be noted that the introduction of carbon will significantly lower the volumetric energy density of the electrode materials. Therefore, the amount of carbon coating should be optimized to further improve the energy densities of $LiFePO_4$ in practical applications.

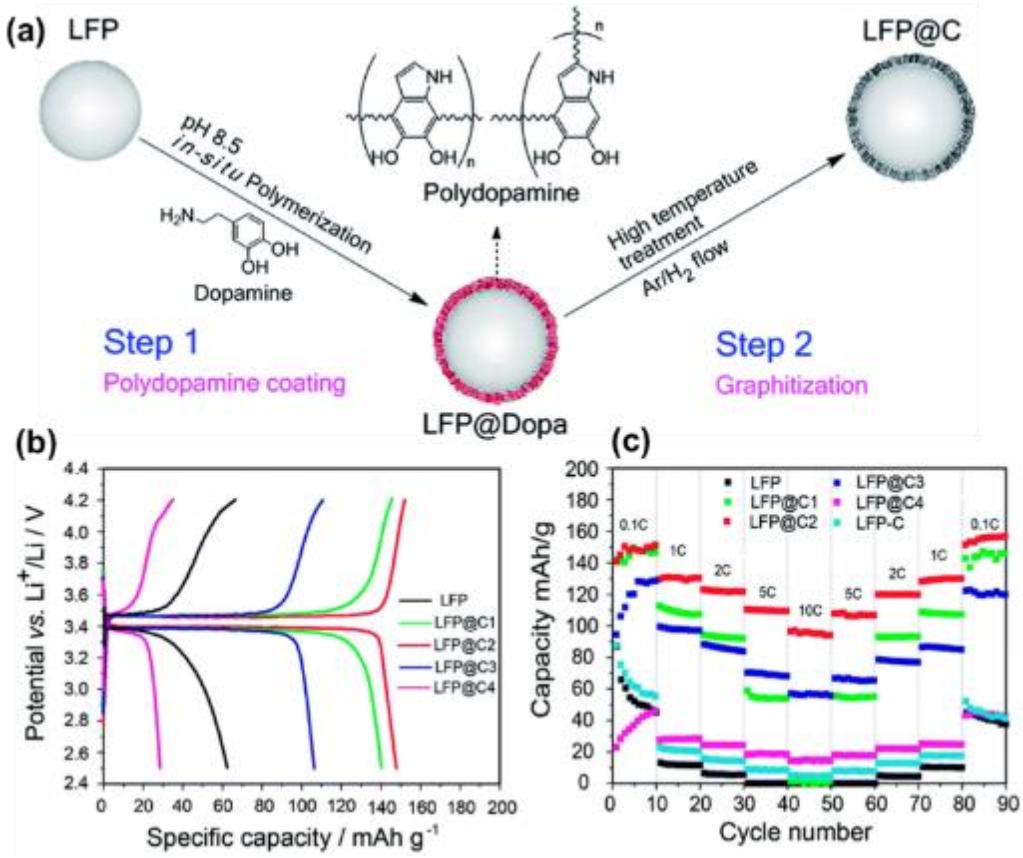


**Figure 1.6. (a)** Schematic illustration of the synthesis of $LiFePO_4$@ carbon (denoted as LFP@C) composites and the coating mechanism of dopamine, **(b)** Comparison of the first charge/discharge curves of LFP, LFP@C1–4, **(c)** Comparison of the rate-capability among LFP, LFP@C1–4 and LFP-C. LFP@C1–4 correspond to the coating thickness of 2 nm, 5 nm, 8 nm and 15 nm, respectively. Reproduced from [56].

Considering that the relatively low discharge plateau of $LiFePO_4$ limits the output

energy density, replacing Fe with other transition metals such as Mn and Ni has also been performed to further enhance its energy density [51]. Polyanion oxide materials like $LiMnPO_4$, $LiNiPO_4$ and $LiCoPO_4$ have also been explored. Compared with the voltage of 3.4 V (vs. $Li^+/Li$) in $LiFePO_4$, $LiMnPO_4$ exhibits a higher voltage of 4.1 V (vs. $Li^+/Li$), which is a great advantage in improving the energy density [57]. However, $LiMnPO_4$ suffers from the same problems as $LiFePO_4$, such as low electrical and ionic conductivity. Moreover, $LiMnPO_4$ presents additional problems such as the Jahn-Teller effect caused by $Mn^{3+}$ and large interface strain due to the mismatched interface of $LiMnPO_4$ and $MnPO_4$ [58]. Although higher operating voltages can be delivered by $LiCoPO_4$ (4.8 V vs. $Li^+/Li$) and $LiNiPO_4$ (5.1 V vs. $Li^+/Li$) to potentially improve the energy densities, they still suffer from poor electrical conductivity and electrochemical instability. It should be noted that common electrolytes suffer from severe degradation under the high operating voltages. Therefore, high voltage electrolytes should be developed to pave the way for the commercialization of high voltage cathode materials.

### 1.1.3 Anode materials

Generally, an ideal anode for lithium-ion batteries should possess the following features: (1) high safety, (2) a low reaction potential to maximize the output voltage, (3) a high reversible capacity, (4) good structural stability to achieve long cycle life, (5) abundance and low cost for large-scale applications, (6) high-rate capability for fast charge-discharge [59-61]. Various anode materials have been extensively explored, including graphite, carbon nanotubes, graphene, porous carbon, silicon, transition metal oxides and so on. According to the reaction mechanism, the anode materials can be divided into three categories [61]: (1) intercalation anodes, such as carbon-based materials and $Li_4Ti_5O_{12}$, (2) alloy anodes, such as Si, Sn and Al, and (3) conversion anodes, such as transition metal oxides and transition metal sulfides. The corresponding capacities and redox potentials of these materials are displayed in Figure 1.7.

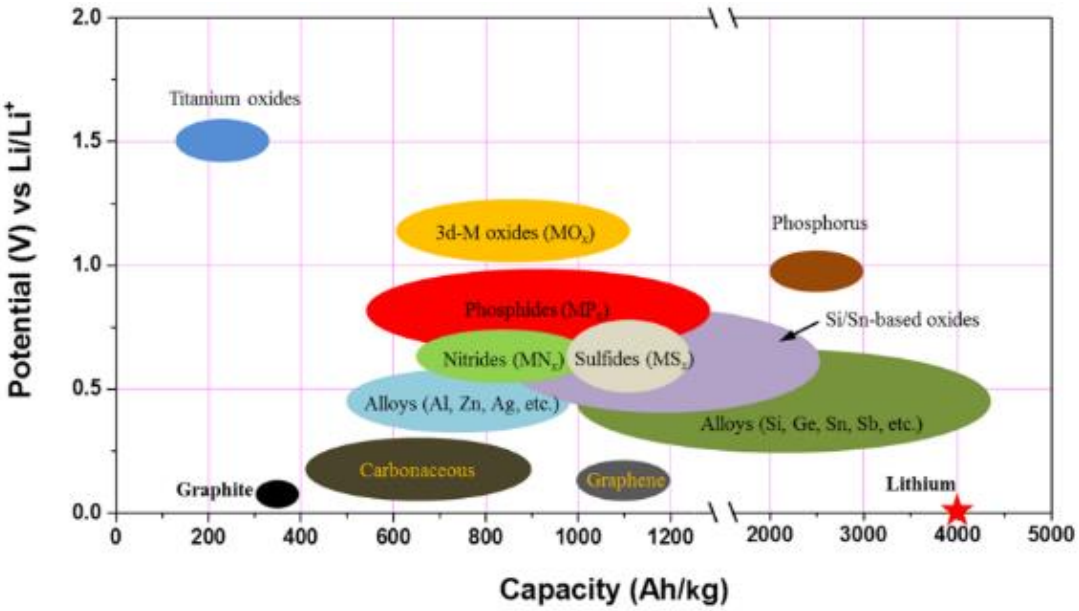


**Figure 1.7.** Schematic illustration of various anode materials investigated in lithium-ion batteries. Reproduced from [61].

### 1.1.3.1 Intercalation anode materials

Since petroleum coke was first used as an anode in the commercial lithium-ion batteries in 1991, carbon-based materials have been widely investigated as anodes in further optimizing the performance of lithium-ion batteries [62]. As a typical representative of carbon-based materials, graphite has now replaced the petroleum coke widely used in high-performance lithium-ion batteries. The early attempt of electrochemical $Li^+$ intercalation into graphite was shown to be unsuccessful due to the side reactions which were triggered by the co-intercalation of solvent with $Li^+$ [63, 64]. Such a co-intercalation resulted in the release of gas and exfoliation of graphite by solvent molecules, thus failing to form an effective SEI [11, 65]. It was found that the interlayer space inside graphite was easily invaded by guest species [66, 67]. When graphite was cathodically polarized in various electrolytes, graphite-intercalation-compounds (GIC, i.e., graphite, $Li^+$, and solvent) were formed via co-intercalation before the reduction of the solvent [11]. The property of a GIC is highly dependent on the electrochemical stability of the solvent, thus leading to three different scenarios occurring on the

graphite, as shown in Figure 1.8.

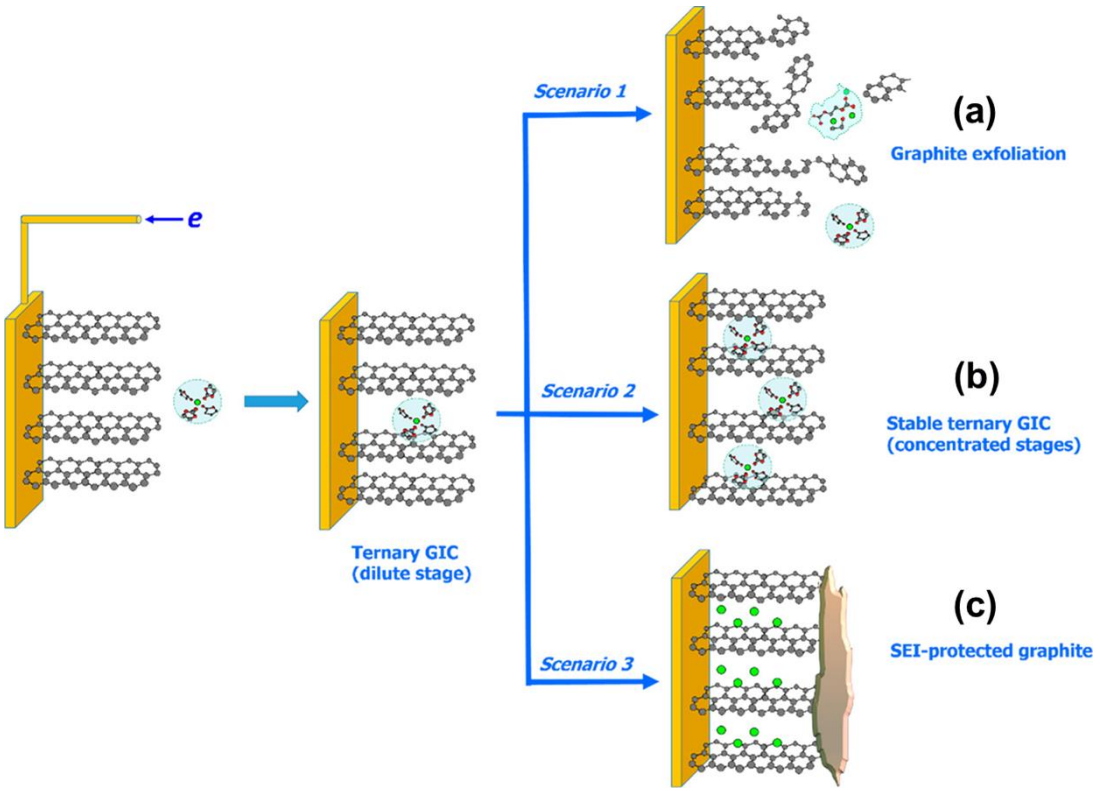


**Figure 1.8.** Three different scenarios on graphite: **(a)** Extensive graphite exfoliation caused by the reductive decomposition of unstable solvent molecules within the graphitic structure, **(b)** Formation of graphite-intercalation-compound (GIC) due to the high stability of solvent molecules toward reduction, **(c)** Reductive decomposition of electrolyte components resulting in the formation of a protective SEI which ensures the reversible intercalation of $Li^+$ into graphite. Reproduced from [11].

If the solvent is unstable against reduction, the decomposition of the solvent will cause the exfoliation of graphite. For example, propylene carbonate (PC) molecules can be decomposed to exfoliate graphite [68, 69]. If the solvent is stable against reduction, it is possible to form a stable and even reversible ternary GIC. This is the case when dimethoxyethane or dimethyl sulfoxide is chosen as the solvent. These two cases are not helpful in building efficient lithium-ion batteries. If the solvent is unstable against reduction and the resulting decomposition products are coated on the graphite surface, a passivation layer will be formed to suppress the further decomposition of electrolytes, thus enabling the use of graphite as an anode in lithium-ion batteries. At the initial

development of lithium-ion batteries, PC or ethers were mainly employed as electrolyte solvents due to their low melting point and the absence of a deep understanding of the interphase. The exfoliation of graphite caused by co-intercalation of electrolyte solvent could not be effectively avoided. Therefore, numerous efforts were devoted to seeking less-graphitic carbon materials which could mitigate solvent co-intercalation.

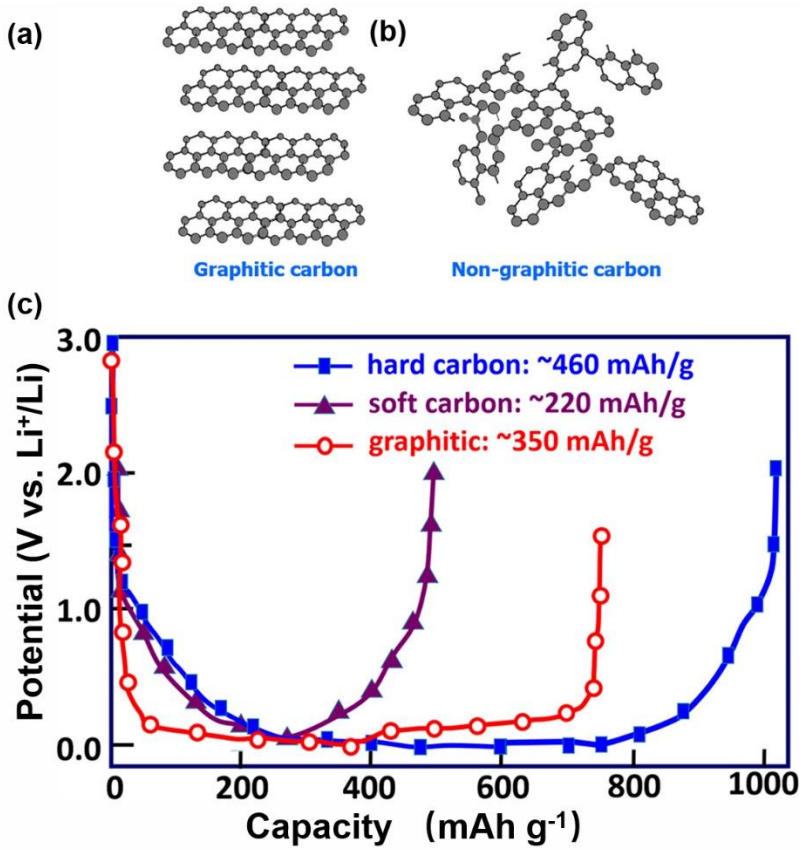


**Figure 1.9.** Schematics of **(a)** graphitic carbon lattice and **(b)** non-graphitic (both soft and hard) carbon composed of randomly oriented graphitic islands combined by amorphous carbon regions. **(c)** Typical potential profiles for the electrochemical lithiation and de-lithiation of soft, hard, and typical graphitic carbons in 1$^{st}$ cycle. Reproduced from [11].

Carbonaceous materials with less-graphitic structures can be mainly divided into hard carbon and soft carbon [70]. Hard carbon, also known as non-graphitizable carbon, is a kind of carbon which cannot be crystallized into graphitic structure, while soft carbon can be converted into graphitizable carbon by heat-treatment at 3000 °C [71, 72]. These two types of carbons show good compatibility with the PC electrolyte solvent, thus

avoiding the exfoliation. They exhibit a sloping profile in the potential range from 0 to 1.0 V (vs. $Li^+/Li$) in comparison to a well-defined plateau at ~0.1 V (vs. $Li^+/Li$) observed in graphite, shown in Figure 1.9. Hard carbon can deliver a higher capacity of 460 mAh $g^{-1}$, while a lower capacity of 220 mAh $g^{-1}$ can be obtained for soft carbon, compared with a theoretical capacity of 372 mAh $g^{-1}$ in graphite. Due to significant capacity loss in the first cycle and sloping potential profile of hard carbon and soft carbon, they are not ideal anode materials used in lithium-ion batteries although they exhibit good compatibility with the PC solvent.

It was not possible to use graphite as an anode in lithium-ion batteries until PC was replaced by using the mixed solvents composed of a short-chain linear alkyl carbonates and ethylene carbonate (EC) [11]. Although these solvents are thermodynamically unstable at low potentials, the decomposition of EC in the initial cycle leads to a protective layer forming on the graphite surface, thus preventing the further co-intercalation of solvent molecules. To date, graphite is still the dominant anode material used in commercial lithium-ion batteries. As the practical capacity obtained almost approaches the theoretical capacity of graphite, current efforts on graphite are made to minimize the irreversible capacity loss in the first cycle and improve the rate capability and cyclability [73].

It is worth mentioning another promising intercalation anode material, i.e., $Li_4Ti_5O_{12}$, which was first investigated as electrode materials in 1994 [74]. This material exhibited a voltage plateau of about 1.55 V (vs. $Li^+/Li$) during the operation, which indicated it was not suitable for use as a cathode material, as shown in Figure 1.10. Additionally, a relatively low theoretical capacity of 175 mAh $g^{-1}$ was delivered by this material. Although a lower energy density is delivered by a lithium-ion battery using $Li_4Ti_5O_{12}$ as anode in comparison with that of graphite anode, $Li_4Ti_5O_{12}$ is still promising as a potential alternative anode to graphite in terms of safety and long stability. Considering that the electrolytes used in lithium-ion batteries are thermodynamically stable at 1.55 V (vs. $Li^+/Li$), the decomposition of electrolytes can be effectively avoided, thus circumventing the formation of a SEI on the anode surface. Moreover, the working

potential of $Li_4Ti_5O_{12}$ is far from the potential range in which metallic lithium can electroplate on the anode surface, thereby avoiding the formation of lithium dendrites [75]. Additionally, the volume change associated with the lithiation/de-lithiation process is almost negligible (~ 0.2 %), ensuring excellent cycling stability due to good structural stability [61].

The electrochemical lithiation/de-lithiation process in $Li_4Ti_5O_{12}$ involves a two-phase mechanism from spinel phase to rock-salt phase, which can be described as follows [76]:

$$Li_4Ti_5O_{12} + x\,Li^+ + x\,e^- \leftrightarrow Li_{4+x}Ti_5O_{12} \quad (0 < x \leq 3) \qquad (1.4)$$

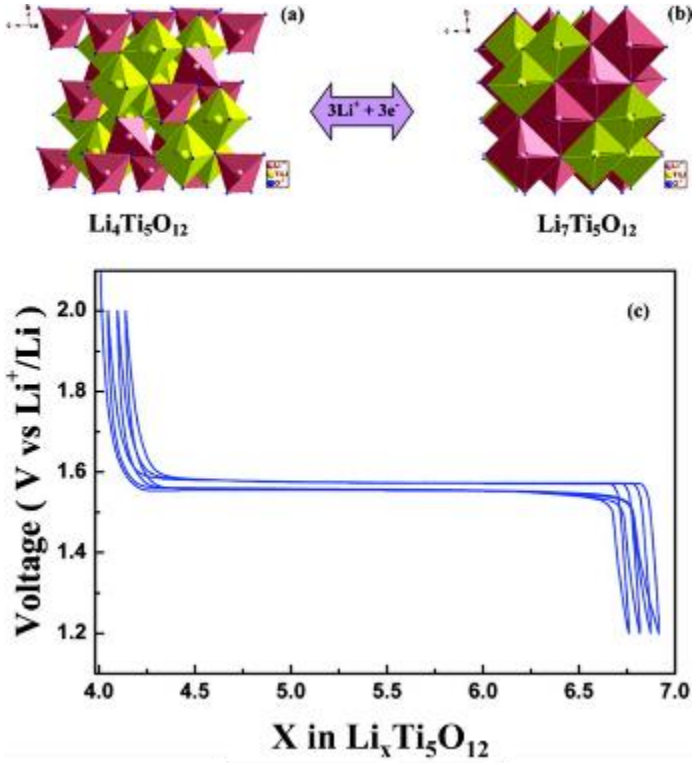


**Figure 1.10.** Schematic structure of **(a)** spinel $Li_4Ti_5O_{12}$ and **(b)** ordered rock salt-phase $Li_7Ti_5O_{12}$, and **(c)** voltage-composition profiles exhibiting the electrochemical transformation between $Li_4Ti_5O_{12}$ and $Li_7Ti_5O_{12}$ at 0.5 C rate. Reproduced from [77].

Although $Li_4Ti_5O_{12}$ is considered as a promising alternative anode for lithium-ion batteries, its low electrical conductivity and poor lithium-ion diffusion coefficient are major barriers for the efficient applications in energy storage [78]. Therefore, various

strategies have been proposed to optimize the electrochemical performance of $Li_4Ti_5O_{12}$, including reducing the particle size, constructing composites, surface coating and so on. Nano-structuring is the most commonly used means to effectively shorten the diffusion length for $Li^+$ ions and increase the contact area of electrode with electrolyte, thus boosting the electrochemical performance [79, 80]. For example, Shukla et al. synthesized nanocrystalline $Li_4Ti_5O_{12}$ with varying sizes from 20 nm to 50 nm by a single-step solution combustion approach, which exhibited a high capacity of 170 mAh $g^{-1}$ at 0.5 C and 70 mAh $g^{-1}$ at 100 C [77]. Wei and coworkers synthesized nanostructured $Li_4Ti_5O_{12}$/carbon nanotube composite particles to achieve superior rate performance up to 100 C with a capacity of 108 mAh $g^{-1}$ and high capacity retention of 89% over 8000 cycles [81]. However, nanostructured materials inevitably result in a low packing density, which is not beneficial for improving the volumetric energy density of the batteries in practical applications.

Another issue about $Li_4Ti_5O_{12}$ is the gassing behavior which is mainly caused by the interfacial reactions between the lithiated $Li_4Ti_5O_{12}$ and surrounding electrolytes, especially at high temperatures [82]. Generally, the components of the generated gas include $H_2$, CO, $CO_2$ and other hydrocarbons like $CH_4$, $C_2H_4$, $C_2H_8$, etc. Chen and coworkers reported that a spontaneous charge transfer reaction (i.e., $Ti^{3+} \leftrightarrow e^- + Ti^{4+}$) took place on the surface of lithiated $Li_4Ti_5O_{12}$, which was considered as an essential step to trigger the gassing reaction [83]. In view of the gassing caused by the interfacial reaction between $Li_4Ti_5O_{12}$ and electrolytes, it is necessary to avoid their direct contact to prevent the gassing reaction. Surface modification like carbon coating and constructing a robust SEI layer is the common strategy used to control interfacial reaction, thus suppressing the evolution of gas. For example, Qu et al. modified the commercial $Li_4Ti_5O_{12}$ by adding an $AlF_3$ coating which effectively suppressed the gas releasing reaction and no obvious swelling of soft-packed batteries was observed after 300 cycles [84]. Although some issues facing the $Li_4Ti_5O_{12}$ anode are urgent to be resolved, $Li_4Ti_5O_{12}$ is still considered as a promising candidate in constructing safer and high-power lithium-ion batteries for large-scale applications.

### 1.1.3.2 Alloying anode materials

Graphite is still the dominant anode for commercial lithium-ion batteries due to its low cost and good stability. However, the drawbacks of graphite in terms of a low theoretical capacity of 372 mAh $g^{-1}$ and safety issues caused by lithium deposition drives the development of alternative anode materials with enhanced safety, high capacity, long stability as well as low cost [85, 86]. Different from the intercalation anode materials with relatively low capacities, alloying anode materials are characterized by high capacity, thus attracting widespread research attention. The typical representative is the Si anode, which exhibits an ultrahigh theoretical specific capacity of 4200 mAh $g^{-1}$ [87]. The general reaction in alloying anode materials can be described as follows:

$$x\,Li^{+} + x\,e^{-} + M \leftrightarrow Li_xM \qquad (1.5)$$

Where M can be Si, Ge and Sn.

The alloy mechanism brings high capacity in storing lithium and meanwhile gives rise to some challenging issues. The most common issue associated with alloying anode materials is the volume expansion. Since a large amount of lithium is stored in the anode materials, it is inevitable that a volume expansion occurs during the lithiation process. For instance, the volume expansions in Si, Ge and Sn are 4 times, 3.7 times and 2.6 times, respectively [61]. Such a large volume expansion leads to the pulverization of the anode materials, thus destroying the contact between the electrode materials and current collector [88]. As a result, electrode materials can be detached from the current collector and the battery capacity degrades rapidly. Another issue associated with volume expansion is the instability of the SEI layer formed on the anode surface [89]. The integrity of the SEI layer is the key to determine the reversibility and cyclability of the battery. The SEI layer formed on the anode surface will break as the volume of anode changes and the newly exposed surface will continue to form a new SEI layer during the subsequent charge-discharge process. The continuous growth of the SEI layer will continue to consume the electrolyte, eventually leading to an increase in the

internal resistance of the battery and a rapid decline in capacity.

Over the past few years, a variety of strategies have been designed to address the issues of alloying anode materials [90, 91]. Among them, Si is believed to be one of the most promising candidates due to its extremely high specific capacity and low cost. However, some critical issues associated with Si anode still need to be addressed, as shown in Figure 1.11.

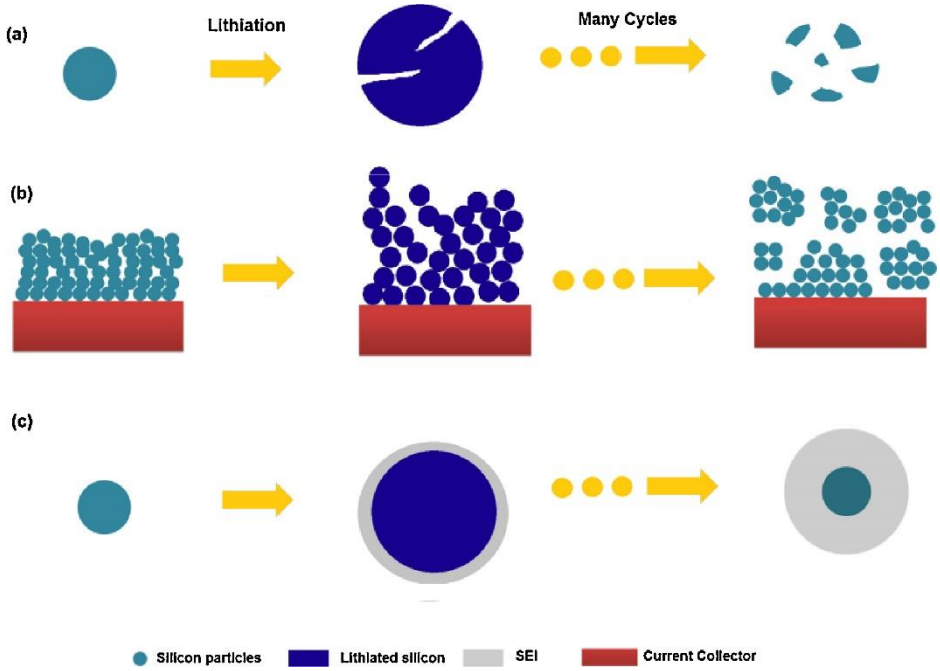


**Figure 1.11.** Failure mechanisms of Si electrode: **(a)** Material pulverization, **(b)** Morphology and volume change of the entire Si electrode, **(c)** Continuous SEI growth. Reproduced from [92].

It was found that the particle size of the silicon is of importance in determining its electrochemical performance. Compared with micro-sized silicon, nano-sized silicon particles with nano-size are more likely to reduce the mechanical stress caused by the volume expansion during the lithiation process [15]. It was demonstrated that the pulverization of silicon can be effectively mitigated by controlling the particle size below 150 nm [93, 94]. Modification of morphology is also a common strategy adopted to improve the electrochemical performance of silicon anode. For example, 1D silicon nanowires and nanotubes were fabricated to accommodate the volume expansion due to their strong ability in strain relaxation without cracks [95, 96]. Cui et al. designed

double-walled silicon nanotubes in which silicon oxides (SiOx) acted as a confining layer coated on the outer wall. This type of Si anode exhibited excellent stability with a high retention of 88% after 6000 cycles due to the mechanically rigid confining layer of SiOx, as shown in Figure 1.12 [96].

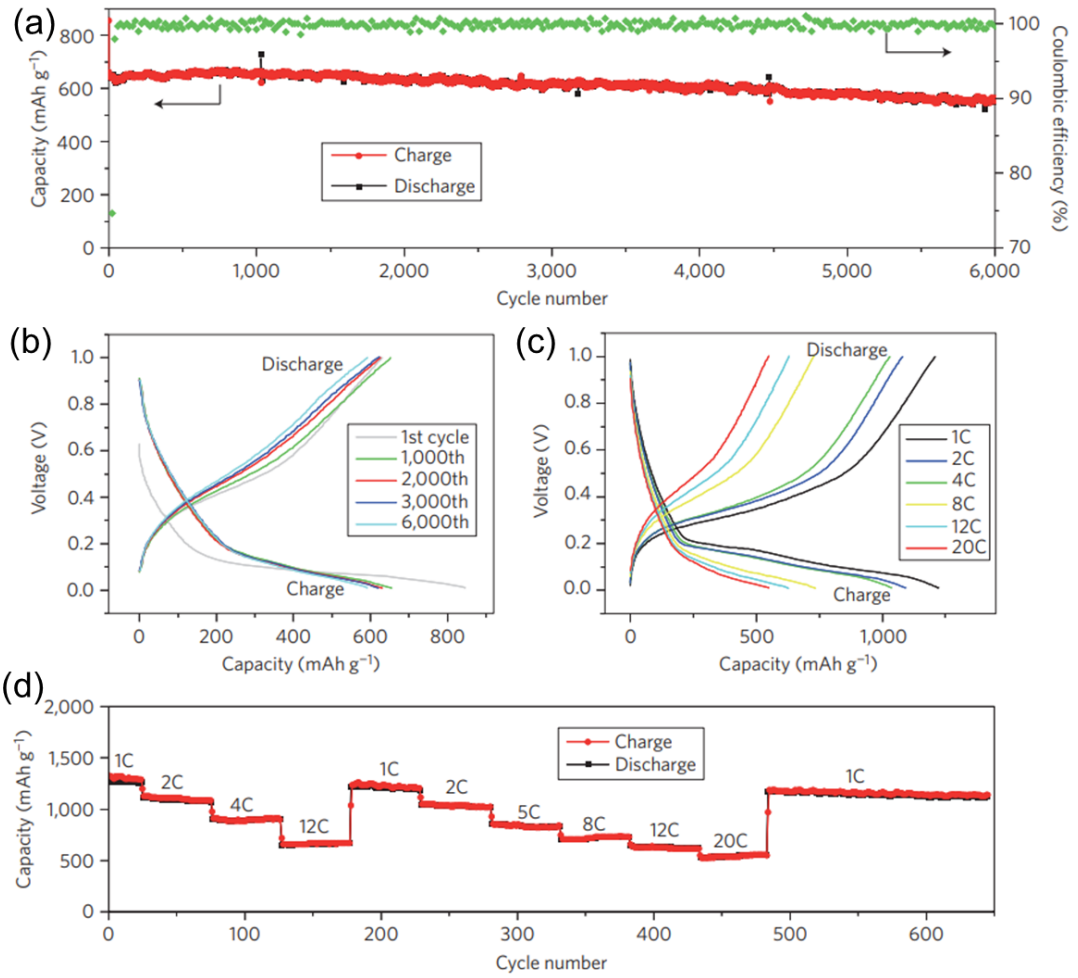


**Figure 1.12. (a)** Lithiation/de-lithiation capacity and coulombic efficiency cycled at 12 C for 6000 cycles, **(b)** Potential profiles plotted for the 1st, 1000th, 2000th, 3000th, and 6000th cycles, **(c-d)** Galvanostatic charge-discharge profiles and capacities at various rates from 1 C to 20 C. Reproduced from [96].

### 1.1.3.3 Conversion anode materials

As the name suggests, the conversion reaction occurring in this type of anode generally

means a redox reaction between the transition metal compounds and $Li^+$ ions. The general reaction can be described as follows [97-99]:

$$M_aX_b + (\mathrm{b}\cdot\mathrm{n})Li^+ + (\mathrm{b}\cdot\mathrm{n})\,e^- \leftrightarrow aM + bLi_nX \qquad (1.6)$$

Where M is transition metal like Mn, Fe, Co, Ni and Cu; X represents O, S, F, N and P; n is the oxidation state of X.

Generally, the potential of the conversion reaction is located at the range from 0.5 to 1.0 V (vs. $Li^+/Li$), which depends on the bond energy of M-X. It is thermodynamically feasible for the forward reaction to proceed to form $Li_nX$, while the reverse reaction can be quite difficult due to the low electrochemical activity of $Li_nX$ [100]. As shown in Figure 1.13, the reversibility of the conversion reaction is highly dependent on the electroactivity of M particles to decompose $Li_nX$ matrix surrounded by a SEI layer [101]. The nanosized M particles are believed to facilitate the formation/decomposition of $Li_nX$ due to their high electrochemical activity, thus favoring the reversibility. Moreover, the large voltage hysteresis between the charge/discharge profiles is a challenging issue for the energy efficiency due to substantial structural rearrangement during the lithiation/de-lithiation process [102]. Basically, the sequence of voltage hysteresis is: phosphides < nitrides < sulfides < oxides < fluorides, which is determined by the character of the anionic species in the conversion anodes due to different binding energies with the transition metal [101]. Furthermore, rapid capacity loss and inferior rate performance are the common issues observed in this type of material due to the poor intrinsic electrical conductivity and the pulverization of particles over cycling [103].


**Figure 1.13.** Schematic of the local chemistry transformation of transition-metal compounds during the conversion reaction. Reproduced from [101].

In order to resolve the issues mentioned above, nanoscale engineering is the common strategy employed to improve their electrochemical performance [79, 103, 104]. It is believed that nanostructured materials can effectively reduce the strain caused by solid transformation and shorten the ion diffusion. For example, a pioneering work from Tarascon's group revealed the correlation of reversible capacity and particle sizes of transition metal oxide [100]. When the micro-sized starting particles were transformed into metal nanoparticles with 1-5 nm over cycles, the stability was improved. In order to improve their conductivity, nanoparticles of transition metal compounds such as $Co_3O_4$, $MnO_2$ and $VO_2$ are usually used to combine with graphene [105], carbon nanotubes [106] or reduced graphene oxide [107]. Although a high capacity of 700–1200 mAh $g^{-1}$ can be achieved by transition metal compounds, the cycling stability is not very satisfactory [61, 108]. Therefore, the commercialization of the conversion anode materials is still a long way off.

### 1.1.4 Safety issues in lithium-ion batteries

Although lithium-ion batteries have been widely used in electronics and even electric vehicles, safety issues related to them are still one of main concerns in their practical applications. Generally, the safety issues are caused by thermal runaway (TR) in the cells and the TR refers to a self-heating rate of 10 °C $min^{-1}$ or higher [109]. The occurrence of TR in a single cell can trigger a chain reaction in the whole battery pack, potentially resulting in an explosion or fire in electronics or electric vehicles [110]. The main causes of TR include mechanical abuse, thermal abuse and electrical abuse, which would give rise to a short circuit in the cell [109, 111]. Basically, the TR process includes three different stages based on the internal heat generation rate, as shown in Figure 1.14 [109, 112].

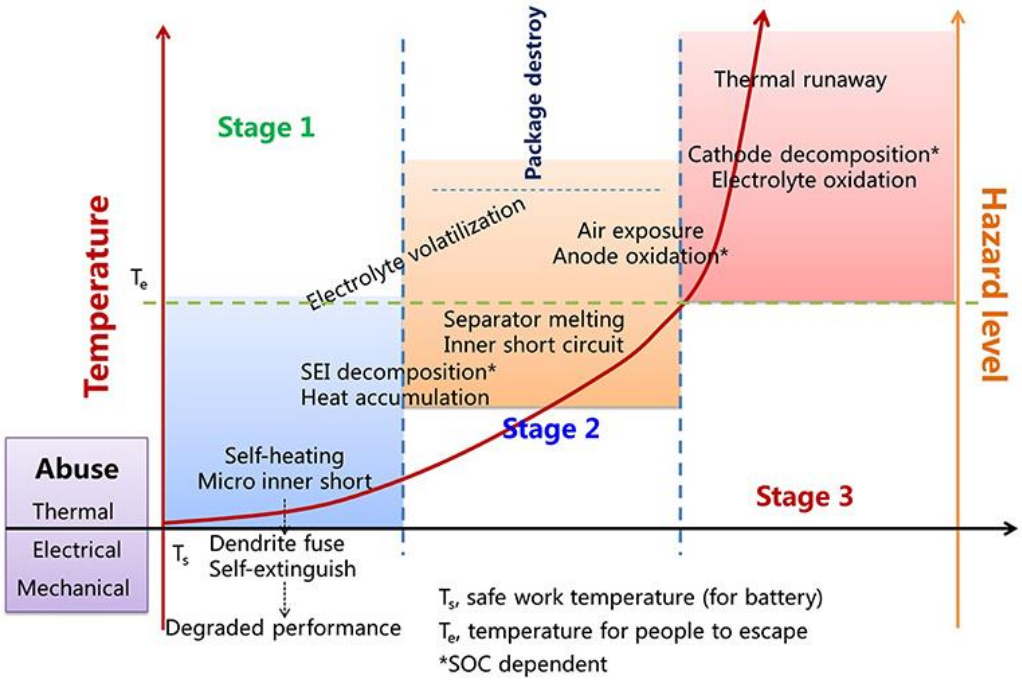


**Figure 1.14.** Three stages in battery TR. $T_s$ represents safe working temperature for battery); $T_e$ represents temperature for people to escape; * state of charge (SOC). Reproduced from [110].

The first stage usually starts from the battery overheating which is caused by the micro-shorts derived from the dendrites formed. It is possible for the battery to self-extinguish since the dendrite can be fused by the heat generated during the initial process. If the self-extinguishing does not occur, the heat would increase causing the decomposition of the SEI layer on the anode, which indicates the start of the second stage. With the heat continuing to accumulate, more side reactions between the electrolyte and electrode materials would be triggered. The side reactions would significantly increase the heat generation. The heat generated during the second stage can melt the separators. With the breakdown of the separators, large-scale short circuiting would occur, eventually resulting in uncontrollable overheating. During this stage, the battery may explode due to a release of gas and the electrode materials begin to burn. It should also be noted that the SEI layer is a fragile part inside the battery and has a tendency to decompose upon heating in the temperature range from 60 °C to 130 °C [110]. Additionally, the polymer separator can easily fail due to melting or shrinkage caused by the continuous accumulation of heat. The multilayer separator composed of

polypropylene (PP)-polyethylene (PE)-PP is designed to serve in a shutdown role as the temperature increases to the melting point of PE. To some degree, the melted PE (melting point, ca. 115 °C) would stop ions from passing and PP (melting point, ca. 160 °C) could still prevent the short circuit. Although the graphite anode has excellent thermal and chemical stability exposed to oxygen, the lithiated graphite is very reactive due to the lithium atoms stored in the spacing. Once the packaging materials are broken due to the over-pressure, the exposed anode would react with $O_2$ or $H_2O$ in the air to further generate heat. In this stage, it is possible for the temperature to increase to 200 °C or higher, leading to other components inside the battery to burn. Finally, the TR is completely triggered.

In order to solve the TR, various strategies have been proposed, such as optimization of the electrolyte and separator as well as battery redesign [110]. Generally, the electrolytes and separators mainly contain organic compounds, such as alkyl carbonates and polyolefin, which are vulnerable under high temperatures. The common organic electrolytes used in the commercial lithium-ion batteries can only safely function below 80 °C due to their volatility and flammability [113]. The development of solid-state electrolytes is considered as one of the promising solutions for the safety concerns of lithium-ion batteries [114, 115]. As for the separator, it plays a critical role in preventing the short circuit. Thus, it is of vital importance to comprehensively consider its properties such as mechanical strength, thermal stability and electrolyte permeability [116]. A high-quality separator must achieve a good trade-off between safety and electrochemical performance in batteries. Various strategies including ceramic coating and polymer matrix optimization have been proposed to explore new separators with high safety [117, 118]. For example, Shi et al. used $Al_2O_3$ powder and a polyimide binder coated on the PE membrane surface to fabricate a ceramic-coated separator which showed no thermal shrinkage up to 160 °C in a dry state and kept stable when packed in the cells up to 165 °C [117]. Beyond lithium-ion batteries, various other types of aqueous energy devices such as aqueous zinc-ion batteries have also been developed to fundamentally resolve the safety concerns related to the flammable organic

electrolytes, as will be discussed in this thesis [119]. Safety concerns and the high cost of lithium-ion batteries are the main driving force to develop novel energy storage devices, especially aqueous Zn-based electrochemical energy storage devices.

## 1.2 Supercapacitors

Compared with batteries, supercapacitors, also called electrochemical capacitors or ultracapacitors, are an important type of energy storage device, which are characterized by fast charge-discharge rates within the timescale of seconds or minutes. In terms of the charge storage mechanism, supercapacitors can generally be classified into two main categories: electrical double layer capacitors (EDLCs) and pseudocapacitors. For EDLCs, charge is stored at the interface between the electrode and electrolyte by electrostatic interaction and there is no charge transfer across the interface. However, the charge storage mechanism of pseudocapacitors involves fast, reversible redox reaction at the surface or near surface of the active materials, leading to a Faradaic charge transfer process.

### 1.2.1 Electrical double layer capacitors (EDLCs)

When an electronic conductor is immersed in an electrolyte solution, a boundary between the two phases forms, thus leading to the spontaneous formation of an electrical double layer because of the reorganization of charges at the interface. The history of the oldest capacitor, also called "Leyden jar", can date back to the $18^{th}$ century [120, 121]. It was independently invented by a German cleric called Ewald Georg von Kleist in 1745 and by a Dutch scientist named Pieter van Musschenbroek of Leyden in 1745-1746 [122]. This invention was named after the city, i.e., "Leyden jar". Typically, it is composed of a water-filled glass jar with metal foil coated to the inside and outside surfaces of the jar, and a metal terminal connecting the inner metal through the jar lid. This design has promoted the idea of storing charge or electricity at the electrode/electrolyte interface. Furthermore, it has led to the critical concept of an

electrical double layer in electrochemistry.

The electrical double layer model was first proposed by Hermann von Helmholtz in 1853 when he was studying colloidal suspensions [121, 123]. It was found that a charged electrode immersed in electrolyte would attract counter-ions to the electrode surface while repelling co-ions of the same charge. The stored charge linearly depended on the applied voltages which were below the decomposition voltage of the electrolyte. The electrical double layer was formed at the interface between electrode and electrolyte with one layer of electronic charge at the electrode surface and the other layer of counter-ions in the electrolyte. This model assumed that a monolayer of counter-ions was formed near the electrode surface, as illustrated in Figure 1.15a. This structure is analogous to a conventional dielectric capacitor composed of two planar electrodes separated by an atomic distance. A constant differential capacitance was predicted based on this simple model.

Since the observed capacitance was not a constant and varied with the applied potential and ion concentration, the Helmholtz model was further modified by Louis Georges Gouy [124] and David Leonard Chapman [125]. Considering a continuous distribution of electrolyte ions in the solution driven by thermal motion, the Gouy-Chapman model was further proposed by introducing a diffuse layer in which the ions' diffusion as a function of distance from the electrode surface obeys Boltzmann statistics, as shown in Figure 1.15b. This indicates that the electrical potential exponentially decreases from the interface to the bulk electrolyte. However, this model results in an overestimation of the electrical double layer capacitance since an extremely high capacitance value would be obtained in the case of point-charge ions close to the electrode surface.

Later, the Helmholtz model and Gouy-Chapman model were well combined by Stern [125] who proposed two distinct regions in the double layer: the inner region also named as the Stern layer or compact layer and the outer region called the diffuse layer, shown in Figure 1.15c. The ions are mobile in the diffuse layer due to the joint influence of thermal and electrostatic forces, which is analogous to the Gouy-Chapman model. Additionally, the Stern layer is further divided into the inner Helmholtz plane (IHP,

specifically adsorbed ions) and outer Helmholtz plane (OHP, non-specifically adsorbed counterions) by Grahame [126].

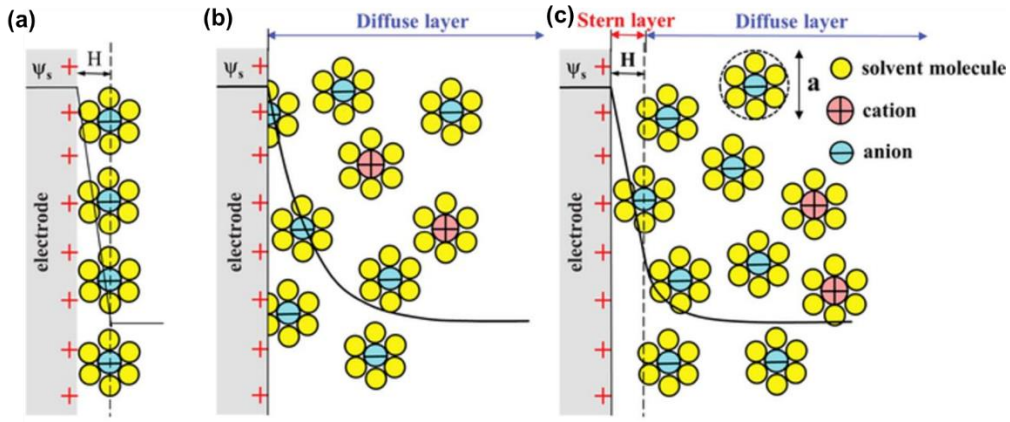


**Figure 1.15.** Schematic illustration of electrical double layer at a positively charged surface: **(a)** Helmholtz model, **(b)** Gouy-Chapman model, and **(c)** Gouy-Chapman-Stern model. *H* represents the double layer distance described by the Helmholtz model and $\Psi_s$ represents the potentials at the electrode surface. Reproduced from [127].

The total capacitance ($C_t$) in the electrical double layer is contributed by the Helmholtz region capacitance ($C_H$) and diffuse region capacitance ($C_d$) at the interfacial region. Therefore, the total capacitance can be described as follows [128]:

$$\frac{1}{C_t} = \frac{1}{C_H} + \frac{1}{C_d} \qquad (1.7)$$

The electrical double layer behaviour at a planar electrode can be influenced by a variety of factors such as the properties of solvents and electrolyte ions, the potential applied to the electrode as well as the chemical affinity between electrode surface and adsorbed ions. Compared with a planar electrode, the electrical double layer behaviour within a porous electrode would be much more complicated, considering that the ion transport under confined conditions is more likely to be impacted by factors like pore volume, wetting properties of the pore surface and tortuosity of mass transport [128]. In general, the corresponding capacitance of an EDLC can be evaluated by using a parallel-plate capacitor equation:

$$C = \frac{\varepsilon_r \varepsilon_0 A}{d} \qquad (1.8)$$

where is $\varepsilon_r$ the electrolyte relative permittivity, $\varepsilon_0$ is the permittivity of vacuum ($\sim$8.854 × $10^{-12}$ F $m^{-1}$), $A$ is the accessible surface area of electrode materials for electrolyte ions, and $d$ is the effective thickness of the electrical double layer.

Generally, the effective thickness of the electrical double layer varies from 5 Å to10 Å, depending on the size and concentration of the electrolyte ions as well as the corresponding solvation shell [121, 129]. As an intrinsic property of solvents, the relative permittivity of common solvents at 25 ℃ is 78.3 (water), 64 (propylene carbonate) and 36 (acetonitrile), respectively [130]. It is worth noting that the values are based on the bulk properties of the solvents and the values would vary when the solvents are confined within the small pores or near the electrode surfaces [131]. The formation and relaxation process of the electrical double layer at the electrode surface can be implemented quickly with a time constant of $\sim 10^{-8}$ s, so the electrical double layer is able to respond quickly to potential changes [132]. This process solely involves a charge rearrangement at the interface and no Faradic reaction occurs.

According to equation (1.8), the specific capacitance should exhibit a linear correlation with specific surface area. However, this ideal relationship was not always supported by some experimental data [133, 134]. It was traditionally considered that the narrow micropores in the electrode materials do not contribute to the capacitance of the electric double layer as they are difficult to be accessed by the solvated ions. However, F. Béguin et al. [135] observed the important capacitance contribution from ultramicropores when they studied a series of microporous activated carbons in different electrolytes. Also, Simon and co-workers [136] observed an abnormal increase of capacitance in porous carbon electrodes with pore sizes smaller than 1 nm when the electrode pore size matched the electrolyte ion size due to the partial deformation or removal of the solvation shell of ions, as shown in Figure 1.16. It was observed that the normalized capacitance decreased as the pore size decreased until it reached a critical value. This was different from the traditional view that the capacitance would continue to decrease. The results further supported the important capacitance contributions from pores possessing sizes less than the size of the solvated ions.

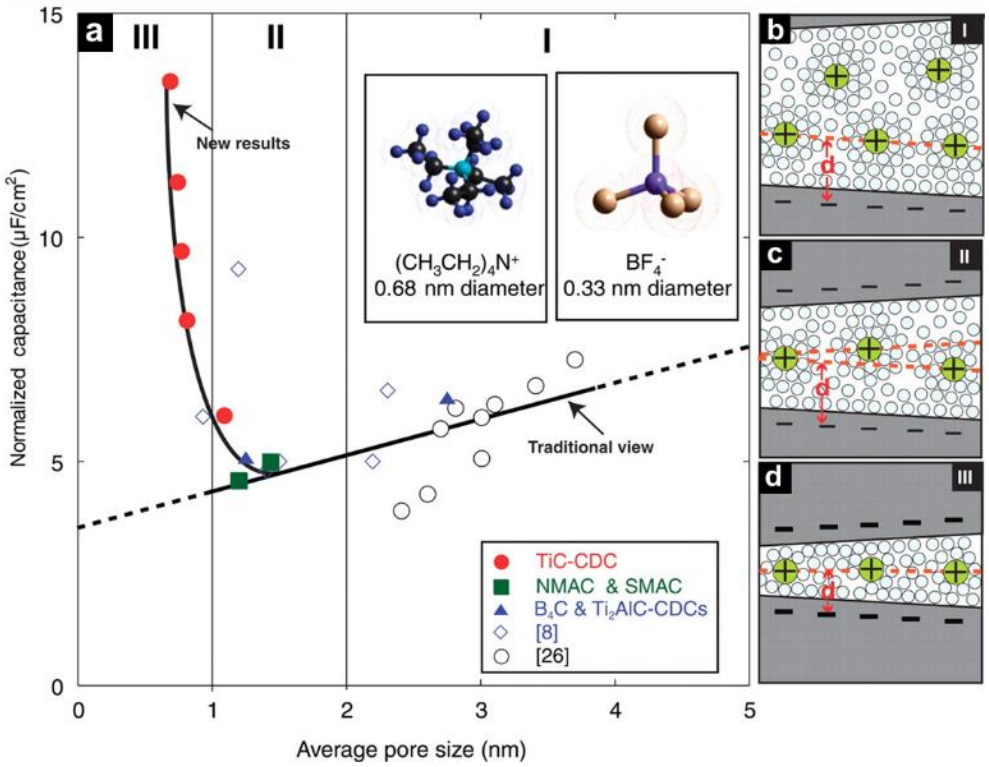


**Figure 1.16. (a)** Plot of specific capacitance normalized by Brunauer-Emmett-Teller (BET) specific surface area for the carbons investigated with identical electrolytes. **(b** to **c)** Drawings of solvated ions residing in pores with distance between adjacent pore walls: **(b)** larger than 2 nm, **(c)** between 1 and 2 nm, and **(d)** smaller than 1 nm. Reproduced from [136].

There is a challenge to explain the new experimental results under confined conditions through the conventional electrical double layer model since both the diffuse layer and compact layer cannot be simultaneously accommodated in the limited space of micropores. Huang et al. [137] proposed a universal model for nanoporous carbon supercapacitors in which the pore curvature is considered and the capacitive behaviour varies with the size of the pore. As shown in Figure 1.16, an electrical double-cylinder capacitor (EDCC) is proposed to describe mesoporous carbon materials (pore size, 2-50 nm) while counterions enter mesoporous carbon electrodes and approach the pore wall. In the case of micropores (< 2 nm), an electrical wire-in-cyclinder capacitor (EWCC) is formed by solvated/de-solvated counterions aligning along the pore axis.

When the pore size (macropores > 50 nm) is large enough, the pore curvature is not important anymore so the EDCC model can be evolved naturally to the EDLC model. The estimation of capacitance base on the two new models is expressed as following:

$$C = \frac{\varepsilon_r \varepsilon_0 A}{b \ln\left(\frac{b}{b-d}\right)} \quad \text{(EDCC model)} \qquad (1.9)$$

$$C = \frac{\varepsilon_r \varepsilon_0 A}{b \ln\left(\frac{b}{a_0}\right)} \quad \text{(EWCC model)} \qquad (1.10)$$

where $b$ is the pore radius, $d$ is the distance of approaching ions to the surface of the carbon electrode, and $a_0$ is the effective size of the counterions.

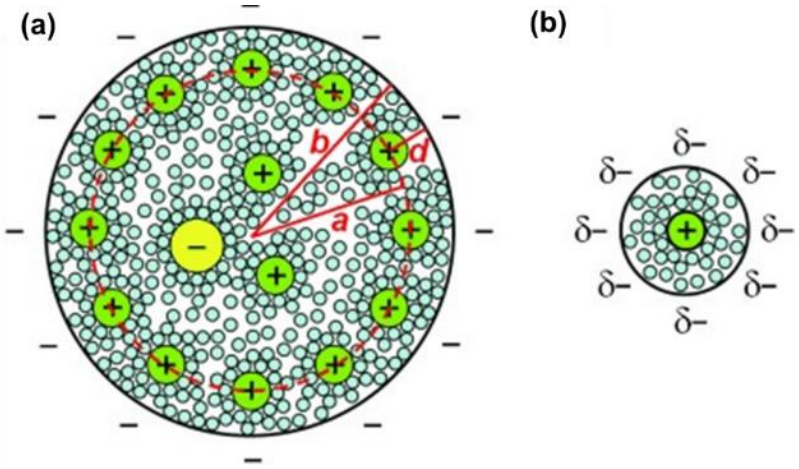


**Figure 1.17.** Schematic illustrations (top views) of **(a)** a negatively charged mesopore with solvated cations approaching the pore wall to form an electrical double-cylinder capacitor (EDCC) with radii b (outer cylinder) and a (inner cylinder), respectively, separated by a distance d, and **(b)** a negatively charged micropore of radius b with solvated cations of radius $a_0$ lining up to form an electrical wire-in-cylinder capacitor (EWCC). Reproduced from [137].

The proposed EDCC/EWCC model can be applied to various carbon materials, such as activated carbon, template carbon and carbide-derived carbon, in different electrolytes. The EDCC/EWCC model provides a good theoretical guidance in the correlation of capacitance properties with specific surface area, pore size, Debye length, and relative permittivity as well as the electrolyte ion size.

Although some advances have been achieved experimentally and theoretically, the

electrical double layer charge storage mechanism under confined conditions is far from being fully understood. More fundamental research regarding detailed charge storage processes within the nanopores are required for the further development of EDLCs. For instance, since the relative permittivity we usually obtain is a property of the bulk electrolyte, it should be quite interesting to investigate how the dielectric constant changes in the nanopores during the charge/discharge process. Additionally, ions in the different sized pores may have a solvation shell with different thicknesses, thus leading to different double layer thicknesses. Furthermore, the visualization of the ion transportation inside the nanopores would be interesting and challenging.

### 1.2.2 Electrode materials for EDLCs

Compared with a conventional parallel-plate capacitor, EDLCs can store more electrical energy due to the larger interfacial area and nanoscale charge separation distance. Various carbon-based materials are widely explored and employed in EDLCs due to their high specific surface area, high electrical conductivity, good thermal and chemical stability as well as environmental benignity. The most common carbon-based materials include activated carbon [135, 138-141], carbon aerogels [142-144], carbon nanotubes [145-147], graphene [147, 148], etc. Generally, the measured specific capacitance of carbon-based materials is in the range of 10−40 μF $cm^{-2}$ [132, 149, 150]. To obtain a high capacitance, a high specific surface area (1000−3000 $m^2g^{-1}$) of carbon-based materials is in principle required.

#### 1.2.2.1 Activated carbons (ACs)

ACs are widely employed as electrode materials in supercapacitors for energy storage owing to their high specific surface area, good chemical stability, environmental friendliness and low cost [151, 152]. Generally, ACs are prepared by physical and/or chemical activation methods by using various types of carbonaceous materials such as wood, nutshell, etc. The physical activation process is usually implemented at high temperatures (700−1200 °C) under an atmosphere of $CO_2$, steam or air, while chemical

activation is generally performed at lower temperatures (400−800 ℃) by using activating agents such as KOH, NaOH, $ZnCl_2$ and $H_3PO_4$ [153]. The properties of the obtained ACs are highly dependent on the carbon precursors and the activation method. Generally, ACs prepared by activation methods have a wide and random pore size distribution comprised of micropores (< 2 nm), mesopores (2−50 nm) and macropores (> 50 nm).

Although AC could be prepared with a high surface area up to 3000 $m^2\ g^{-1}$, it is still difficult to achieve the theoretical electric double layer capacitance (10−40 μF $cm^{-2}$). The practical specific capacitance was in the range of 7−11 μF $cm^{-2}$, which indicated the unavailability of all the surface sites, especially in the extremely porous materials [154]. Therefore, specific surface area is undoubtedly a critical factor in determining the performance of EDLCs, but other factors of the carbon materials like pore size distributions, pore structure, surface functionalities and electrical conductivity should also be taken into account in terms of the electrochemical performance [128].

Significant effort has been devoted to understanding the relationship between the pore size of carbon materials and their specific capacitance in various electrolytes. For example, Gogotsi and co-workers have investigated the desolvation of ions in sub-nanometer pores and its effect on the capacitance [155]. Various porous-carbon materials with pores smaller than the size of the solvated ions were studied as samples in double-layer capacitors. As shown in Figure 1.18, the results showed that a decrease in the pore size caused an increase in the number of solvent molecules removed, along with a similar increase in the capacitance, indicating at least a partial removal of the solvent shell. Additionally, the surface of carbon materials may contain rich functional groups which could undergo a redox reaction during the charge-discharge process, thus leading to a pseudocapacitive effect. The common functional groups such as carboxyl, hydroxide and quinone can be introduced into the surface of carbon materials through electrochemical oxidation, plasma oxidation and chemical oxidation. For example, Ling and co-workers [156] have used petroleum coke-based activated carbons (ACs) treated by $H_2$ reduction and $HNO_3$ oxidation to investigate the effect of surface

chemistry of ACs on their electrochemical properties. The treatment of $HNO_3$ oxidation generated a lot of oxygen groups on the surface, especially the carbonyl groups, contributing to capacitance through faradic process and improving the wettability to aqueous electrolytes. Meanwhile, the increased amount of surface oxygen groups resulted in the increase of internal resistance and self-discharge.

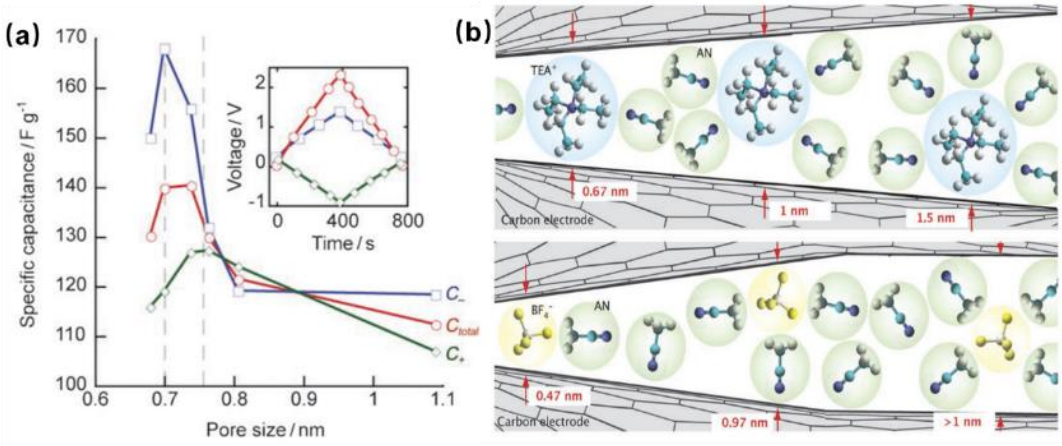


**Figure 1.18. (a)** Dependence of the specific capacitance on the pore size, **(b)** Geometric confinement of ions in extremely small pores. Both anions and cations enter the pores with no solvent-molecule screening charge at pore sizes below 1.5 and 1 nm, respectively. The ions enter the pores either bare or with partial solvent shells ($TEA^+$ represents tetraethylammonium, $BF_4^-$ represents tetrafluoroborate and AN is acetonitrile). Reproduced from [155].

To accelerate the transformation from a fossil fuel-based society to a renewable resource-based sustainable society, it is urgent and vital to utilize renewable materials for harnessing clean energy to alleviate the energy crisis and reduce carbon dioxide emissions. In recent years, biomass-derived carbons are considered as a promising candidate for electrode materials in energy storage due to the abundant and sustainable features of biomass resources [151]. The low cost and environmental benignity of carbons derived from biomass make them extremely attractive materials for practical application in supercapacitors. To effectively convert biomass into value-added carbon materials, different carbonization methods (e.g., pyrolysis and hydrothermal

carbonization) and activation methods (e.g., physical and chemical activations) are usually employed. As shown in Figure 1.19, the common methods to prepare biomass-derived carbons are summarized [153]. The properties of carbon materials such as surface area, surface functionalities, porosities, morphologies and cost can be varied by controlling the experimental parameters such as activating reagents, reaction temperature, reaction time and atmosphere. For example, Hou and co-workers [157] used raw rice brans activated by KOH to prepare three-dimensional carbon with a micro/mesopores interconnected structure. The highest specific surface area of 2475 $m^2$ $g^{-1}$ with optimized pore volume of 1.21 $cm^3$ $g^{-1}$ was obtained with the mass ratio of 4 (KOH/rice brans). The electrode exhibited high specific capacitance at high current densities in 6 M KOH electrolyte (i.e., 265 F $g^{-1}$ at 10 A $g^{-1}$ and 182 F $g^{-1}$ at 100 A $g^{-1}$). Furthermore, a high energy density of 70 Wh $kg^{-1}$ and a power density of 1223 W $kg^{-1}$ were obtained based on the mass of the active materials in an ionic liquid.

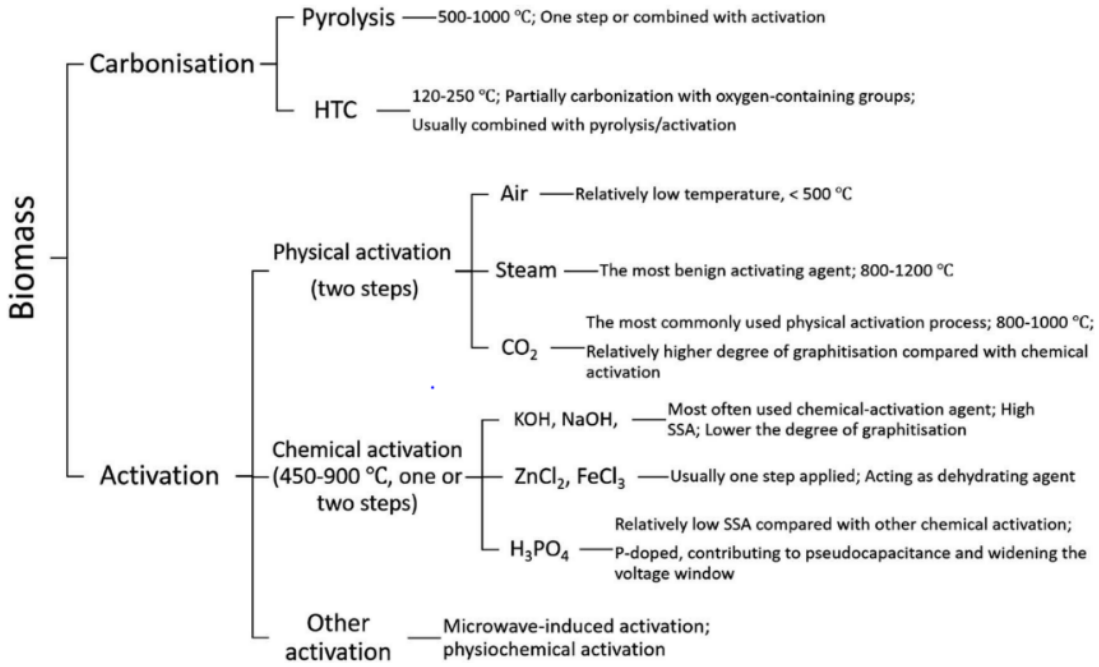


**Figure 1.19.** Common methods for converting biomass to carbon materials. Reproduced from [153].

### 1.2.2.2 Carbon nanotubes

A new class of carbon materials, carbon nanotubes (CNTs) were first discovered by a Japanese scientist called Sumio Iijima in 1991 [158]. The discovery of CNTs has triggered intensive research interest in both fundamental research and various potential applications. As one type of carbon allotropes, CNTs are tubes composed of carbon atoms with nanometer diameter and micrometer length [159]. Since CNTs usually possess a high aspect ratio (> 1000), they can be regarded as an approximately one-dimensional structure. To some degree, the structure of CNTs can be considered as a hollow cylinder with a diameter in nanometers by scrolling single or multilayered graphitic sheets (graphene), as shown in Figure 1.20 [159].

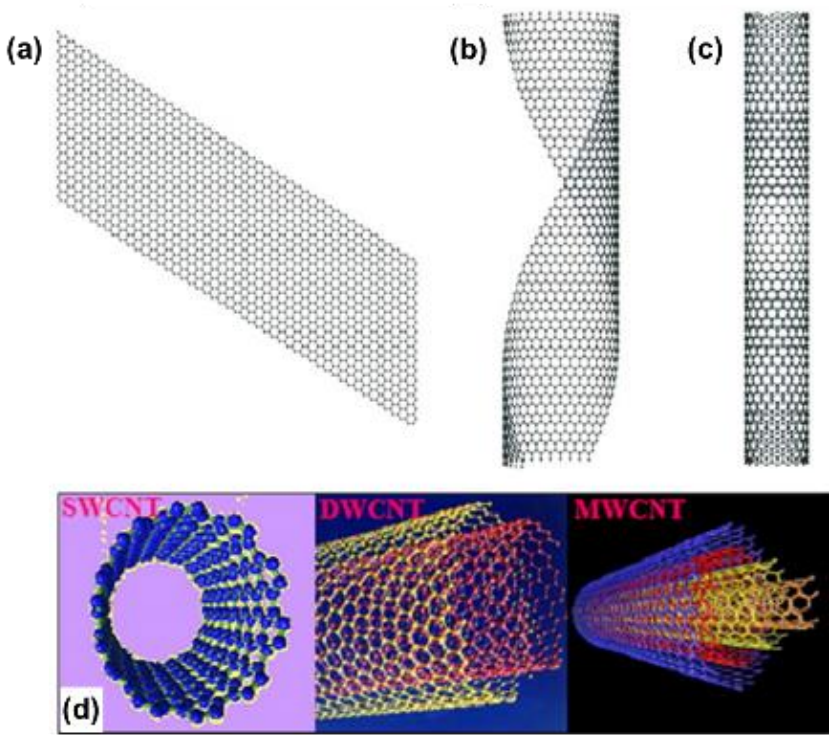


**Figure 1.20.** Schematic diagrams exhibiting different types of CNTs and other carbon structures: **(a)** Flat sheet of graphene, **(b)** Partially rolled sheet of graphene, **(c)** SWCNT, **(d)** Structures of the three CNT types; SWCNT, DWCNT, and MWCNT, respectively. Reproduced from [159].

There are two main types of CNTs, i.e., single-walled carbon nanotubes (SWCNTs) and multi-walled carbon nanotubes (MWCNTs). The SWCNTs can be regarded as a single layer of graphene rolled into a seamless cylinder. The diameter of most SWCNTs is in the range of 1 nm [160]. MWCNTs can be viewed as a collection of concentric SWCNTs with varying diameters. The diameter and length of MWCNTs are greatly different from those of SWCNTs, thus leading to different properties compared with those of SWCNTs.

CNTs can be synthesized by various methods such as arc discharge [161, 162], laser ablation [163, 164], chemical vapor deposition (CVD) [165], pyrolysis [166] and catalytic combustion [167]. The laser ablation and arc discharge of graphite are common approaches employed to prepare CNTs from carbon vapor at elevated temperatures. As an attractive technique owing to the lower temperature range (500–1200 °C) compared with laser ablation and arc discharge of graphite, the CVD method is widely adopted to prepare various CNT structures by using hydrocarbons, methanol, and ethanol as common carbon sources [168-172]. Additionally, the properties of the CNTs such as diameter, length and wall number can be well controlled by varying the CVD parameters such as temperature, time, and catalyst [173, 174]. Although various CNTs can be prepared via various techniques, cheaper synthesis techniques for mass production of CNTs are still under development.

The unique structures of CNTs endow their excellent mechanical, thermal and electrical properties. For example, the Young's modulus values of SWCNTs range from 320 to 1470 GPa measured through atomic force microscopy [175]. Dai and co-workers reported that the thermal conductivity of a SWCNT of diameter 1.7 nm and length 2.6 μm was determined to be about 3500 W $m^{-1}$ $K^{-1}$ at room temperature and proposed a simple analytical model dependent on the length and temperature for estimating the thermal conductivity of SWCNTs [176]. The electrical conductivity of CNTs reaches values as high as $10^7$ S $m^{-1}$ [177, 178].

There have been numerous studies on supercapacitor applications using CNTs as electrode materials. Lee and co-workers [179] used SWNTs as electrodes and a

maximum specific capacitance of 180 F $g^{-1}$ and an energy density of 7 Wh $kg^{-1}$ at a power density of 20 kW $kg^{-1}$were achieved in 7.5 M KOH solution. Considering that high specific surface areas are a key factor in electrical double-layer capacitors to provide high specific capacitance, much effort has been devoted to improving the specific surface area of CNTs. Pan and co-workers [180] prepared tubes-in-tube multiwalled CNTs based on the anodic aluminum oxide template method. A high specific capacitance of 203 F $g^{-1}$ was obtained in 0.5 M $H_2SO_4$ due to the larger surface area, better pore-size distribution, and high conductivity. Najafabadi and co-workers [181] used vertically aligned SWNTs prepared by water-assisted chemical vapor deposition to achieve negligible amounts of impurities and a near-ideal specific surface area of 1300 $m^2$ $g^{-1}$. A high energy density (94 Wh $kg^{-1}$, 47 Wh $L^{-1}$) and a power density (210 kW $kg^{-1}$, 105 kW $L^{-1}$) were obtained at a high voltage of 4 V operated in 1 M $Et_4NBF_4$/propylene carbonate electrolyte.

Besides increasing the specific surface area of CNTs, activation and functionalization of the CNTs are also considered as effective strategies to enhance their specific capacitances by introducing more defects and pseudocapacitance. For instance, a mixed acid $H_2SO_4$/$HNO_3$ was employed to oxidize MWCNTs to introduce carboxyl groups to their surface, thus leading to the improved capacitance in 1 M $H_2SO_4$ electrolyte due to a good trade-off between hydrophilicity and conductivity [182]. But the excessive oxidation led to a significant decrease in the electrical conductivity of the MWNT electrode, which was detrimental to the EDLC performance. Therefore, the balance between hydrophilicity and conductivity is an important factor in designing electrode materials for EDLCs. Li and co-workers [183] synthesized nitrogen-doped carbon nanotubes by carbonization of polyaniline coated CNTs. The amount of nitrogen doping was tuned by controlling the aniline amount. Supercapacitors using nitrogen-doped CNTs achieved a maximum capacitance of 205 F $g^{-1}$ in 6 M KOH solution, which was much higher than that (10 F $g^{-1}$) of the pristine CNTs. The enhanced capacitance could be explained by the additional pseudocapacitance and improved

hydrophilicity contributed by the nitrogen functional groups. Moon and co-workers [184] synthesized nitrogen-doped CNT spherical particles by the evaporation of emulsion droplets of CNTs and subsequent heat-treatment of melamine to introduce nitrogen doping. The nitrogen-doped CNT spherical particles exhibited a high specific capacitance of 215 F $g^{-1}$, which was three times higher than that of the bare CNT spherical particles.

The capacitances of CNTs reported by most researchers are still lower or comparable to those of AC materials. Considering the high production cost of CNTs, they are not a promising candidate for high energy density electrode materials. Nevertheless, CNTs can be employed as a conductive agent to boost the energy storage capability of other electrode materials like metal oxides and conducting polymers [185-189].

#### 1.2.2.3 Graphene-based materials

Graphene is a single layer (monolayer) of carbon atoms bonded in a two-dimensional hexagonal honeycomb lattice, which was isolated by Novoselov et al. through a micromechanical exfoliation method with “Scotch tape” in 2004 [190]. It has attracted worldwide research interest since its isolation [191-195]. Andre Geim and Konstantin Novoselov were rewarded the Nobel Prize in Physics in 2010. Graphene can be considered as a building block to construct other carbon allotropes like fullerenes, carbon nanotubes and graphite. As displayed in Figure 1.21, graphene can be employed to construct zero-dimensional (0D) fullerenes, one-dimensional (1D) carbon nanotubes and three-dimensional (3D) graphite [195].

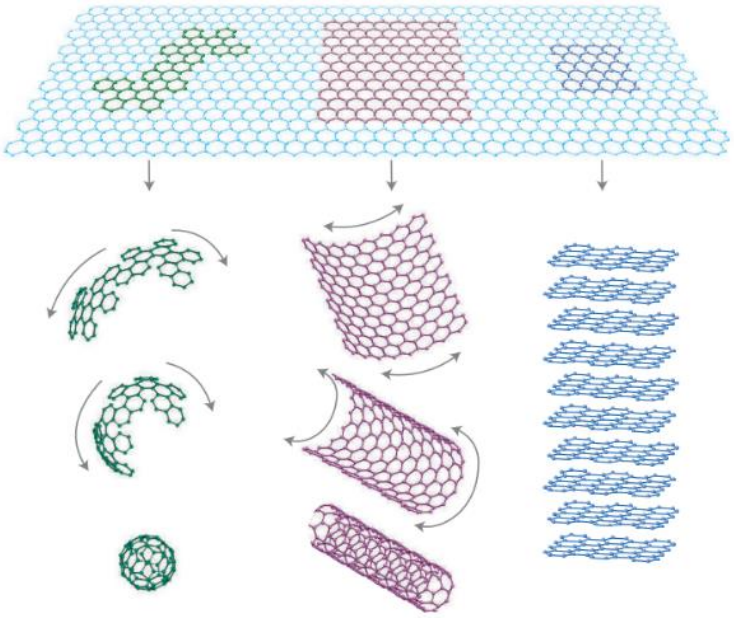

**Figure 1.21.** Graphene is the mother of all graphitic forms including 0D fullerene, 1D SWCNT, and 3D graphite. Reproduced from [195].

Graphene can be synthesized by a variety of methods. As mentioned above, graphene sheets were isolated by using adhesive tape to repeatedly peel highly oriented pyrolytic graphite until atomically thin sheets was obtained, which was also known as the mechanical exfoliation method [190]. This method allows the production of high-quality graphene which provides a good platform to investigate the physical properties of graphene and other unexpected physical phenomena [190, 195]. The mechanical exfoliation method is a good way to obtain high-quality graphene sheets and is still the main method for producing single-layer high-quality graphene. However, its controllability is rather poor and the efficiency is quite low so it is not suitable for large-scale production.

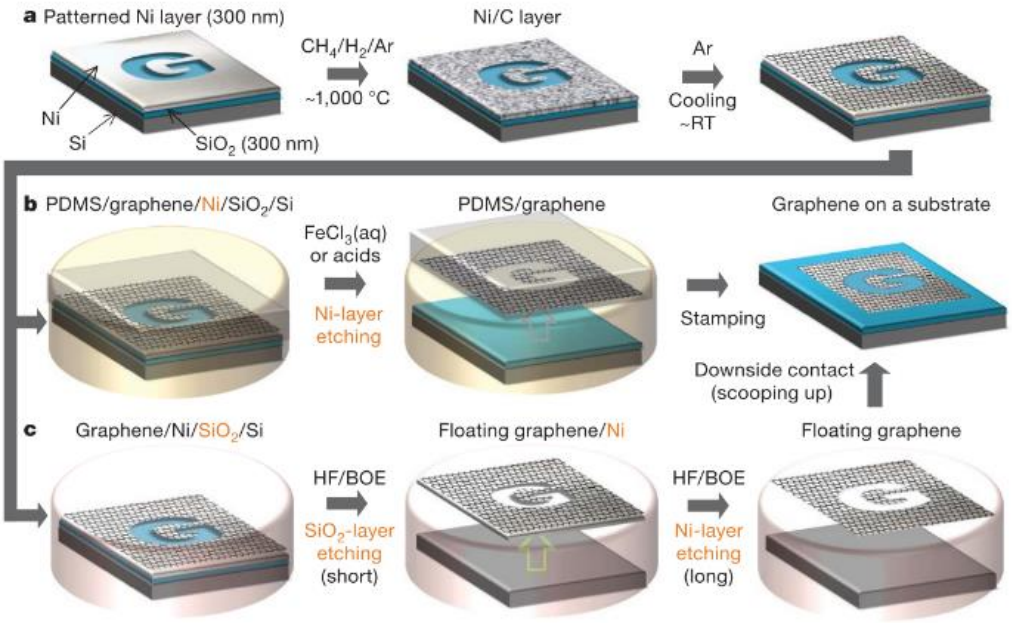


**Figure 1.22.** Synthesis, etching and transfer processes for the largescale and patterned graphene films. **(a)** Synthesis of patterned graphene films on thin nickel layers, **(b)** Etching and transfer of graphene films using a polydimethylsiloxane (PDMS) stamp, **(c)** Etching using buffered oxide etchant (BOE) or hydrogen fluoride (HF) solution and transfer of graphene films. Reproduced from [200].

Besides the mechanical exfoliation method, Emtsev and co-workers demonstrated a method of preparing graphene on silicon carbide (SiC), i.e., SiC epitaxial growth method, in which a SiC single crystal was heated at high temperatures (1500 to 2000 °C) to remove the Si atoms, leading to the formation of graphene via the reconstruction of C atoms on the SiC substrate [196, 197]. Another common way to prepare graphene is using chemical vapour deposition (CVD), which is a powerful method widely adopted to prepare thin films or coatings on solid substrates. In the CVD process, volatile precursors can react or decompose on the surface of the substrate at elevated temperatures and under vacuum in a reaction chamber [198]. For example, large area and few-layer graphene films were prepared by CVD on thin Ni substrate [199, 200] while single-layer graphene films were synthesized by CVD on Cu foil [201, 202]. Large scale production of graphene can be achieved by the reduction of graphene oxide

(GO) via chemical reduction like hydrazine [203, 204] or sodium borohydride [205] or thermal reduction such as annealing in vacuum or argon or hydrogen atmosphere [206, 207]. Generally, GO sheets can be prepared by chemical routes such as the Hummers method [208, 209] and electrochemical routes [210] (shown in Figure 1.23). Since more structural disruption is likely to be generated by solution chemical reactions, the quality of graphene obtained by reduction of GO is much lower than that produced by mechanical exfoliation, epitaxial growth on SiC substrate and CVD methods.

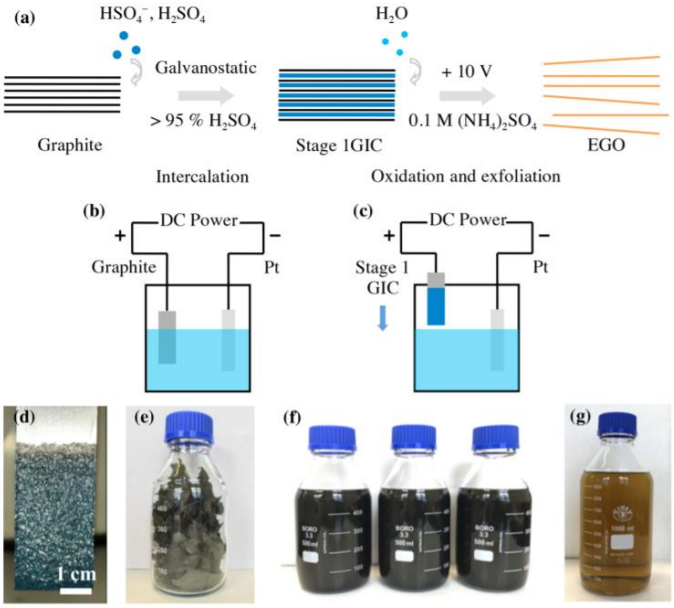


**Figure 1.23.** Production of electrochemical graphene oxide (EGO): **(a)** Schematic of two-step electrochemical intercalation and oxidation process, **(b)** Cell setup for intercalation of graphite, **(c)** Cell setup for oxidation of stage 1 GIC, **(d)** Photographs of intercalated graphite foil, **(e)** Freeze-dried EGO powder, **(f)** Aqueous dispersion of EGO, and **(g)** Dilute EGO aqueous dispersion. Reproduced from [210].

Due to graphene's outstanding properties such as high theoretical specific surface area, excellent electrical and thermal conductivity, as well as good mechanical properties [211-213], graphene can be potentially used in various applications such as sensors [214], photovoltaic devices [215], environmental applications (e.g., contaminant adsorption and water decontamination) [216], and electrochemical energy storage

devices [217]. Particularly, a lot of efforts have been devoted to exploiting graphene-based electrode materials for advanced energy storage devices, attempting to enhance the corresponding energy and power capabilities [212, 218]. Here the relevant research in supercapacitors is briefly introduced.

The combination of the very high theoretical specific surface area (2630 $m^2$ $g^{-1}$) and excellent electrical conductivity of graphene renders it appealing in energy storage, especially in EDLCs. In principle, an ultrahigh specific capacitance of 550 F $g^{-1}$ can be obtained with a graphene electrode [150, 219]. Ruoff and co-workers [220] have pioneered research on graphene-based supercapacitors. They used chemically modified graphene as electrodes which were prepared by reducing graphene oxide sheets using hydrazine hydrate. Due to the formation of agglomerates, a specific surface area of 705 $m^2$ $g^{-1}$ was achieved by the chemically modified graphene, much lower than the theoretical value of 2630 $m^2$ $g^{-1}$. The specific capacitances of 135 F $g^{-1}$ and 99 F $g^{-1}$ were obtained at a discharge current of 10 mA, in KOH and $TEABF_4$/AN, respectively. Chen and co-workers [221] fabricated partially reduced graphene oxide (RGO) by using a weak reductant (hydrobromic acid) so that part of oxygen functional groups remained on the RGO, boosting the penetration of aqueous electrolytes and introducing a pseudocapacitive contribution. The maximum specific capacitances of 348 F $g^{-1}$ and 158 F $g^{-1}$ were achieved at 0.2 A $g^{-1}$ in 1 M $H_2SO_4$ and $BMIPF_6$, respectively.

Graphene can be also obtained by direct thermal treatment of GO at elevated temperatures without using hazardous reductive agents. Ruoff and co-workers used thermal treatment at 150 and 200 °C to reduce the GO suspensions in propylene carbonate and a specific capacitance of 122 F $g^{-1}$ was obtained at a current density of 1 A $g^{-1}$ in $TEABF_4$/PC [222]. They also reported a rapid microwave irradiation method to simultaneously exfoliate and reduce the graphite oxide [223]. The supercapacitor based on this material achieved a specific capacitance of 191 F $g^{-1}$ at 150 mA $g^{-1}$ in KOH electrolyte. Lv and co-workers [224] reported a relatively low temperature (~200 °C) method to exfoliate graphite oxide in a high vacuum environment. The obtained graphene had a specific surface area of ~ 400 $m^2$ $g^{-1}$ and exhibited a specific

capacitance of 264 F $g^{-1}$ at 0.1 A $g^{-1}$ in a 5.5 M KOH solution. The graphene obtained from the reduction of GO suffers from significant particle agglomeration, thus leading to a relatively low specific surface area of the resultant graphene [225]. Therefore, massive efforts have been made to prevent the agglomeration of graphene.

For example, Shi and co-workers [226] reported a self-assembled graphene hydrogel by using a one-step hydrothermal method. The obtained hydrogel used as an electrode material exhibited a specific capacitance of 175 F $g^{-1}$ at a scan rate of 10 mV $s^{-1}$ in a 5 M KOH solution. Lin and co-workers [227] prepared pristine graphene aerogels by room-temperature freeze gelation, which exhibited a specific capacitance of 123 F $g^{-1}$ at 1 A $g^{-1}$ in 1M $TEABF_4$/PC. Another common means to effectively prevent the restacking of graphene is to introduce spacers or stabilizers [228-234]. The spacer is expected to enhance the specific surface area and expand the interlayer of the graphene sheets, thus facilitating the effective utilization of the active sites of the graphene materials. For example, Zhang and co-workers [235] prepared different surfactant-stabilized graphene materials by intercalating GO with various surfactants and then subsequently reducing the GO with hydrazine. It was found that the presence of the surfactants was able to stabilize the morphology of graphene sheets and improve the wettability of the graphene surface, thus leading to a performance improvement in the energy storage. Among all the modified graphene materials, the graphene-stabilized by tetrabutylammonium hydroxide showed the highest specific capacitance of 194 F $g^{-1}$ at 1 A $g^{-1}$ in a 2 M $H_2SO_4$ solution. Wang and co-workers [236] prepared high surface area nano-structured graphene composites (1256 $m^2$ $g^{-1}$) by using 1wt. % hydrophilic carbons as a spacer. The electrode materials based on the graphene composites exhibited a high specific capacitance of 324.6 F $g^{-1}$ at 0.3 A $g^{-1}$ in 1 M $H_2SO_4$ electrolyte. Chemical activation was also employed to further increase the specific surface area of graphene-based materials. Ruoff and co-workers [237] synthesized a porous carbon with an ultrahigh surface area of 3100 $m^2$ $g^{-1}$ by KOH activation of microwave exfoliated GO. A specific capacitance of 200 F $g^{-1}$ at 0.7 A $g^{-1}$ was achieved in the ethyl-methyl- imidazolium bis(trifluormethylsulfonyl)imide ionic liquid with an

operating voltage of 3.5 V.

Doping is another effective strategy widely used to tune the properties of graphene. For instance, nitrogen-doped graphene sheets were obtained by using a facile treatment of nitrogen plasma, demonstrating a high specific capacitance of ~280 F $g^{-1}$ at 1 A $g^{-1}$ in 6 M KOH electrolyte, which was about fourfold larger than that using pristine graphene counterpart [238]. The enhanced capacitance was attributed to the N-doped sites on the basal planes. Guo and co-workers [239] produced a nitrogen-doped graphene hydrogel via a one-pot hydrothermal method using GO as the precursor and urea as the reducing-doping reagent. A high specific capacitance of 308 F $g^{-1}$ was obtained at 3 A $g^{-1}$ in 6 M KOH solution. Zhao and co-workers [240] prepared a N-doped three-dimensional graphene framework by hydrothermally treating the mixture of a GO suspension with pyrrole, followed by freeze drying and annealing at 1050 °C in argon atmosphere. The N-doped graphene framework showed an ultrahigh specific capacitance of 484 F $g^{-1}$ at 1 A $g^{-1}$ in a 1 M $LiClO_4$ solution. The improved capacitance was attributed to the combination of the highly open porous structure with minimum stacking of graphene and the possible pseudocapacitance from the heteroatoms. Similar to N-doping in graphene, Han and co-workers [241] prepared B-doped graphene nanoplatelets through the reduction of GO using a borane-tetrahydrofuran adduct under reflux conditions. A specific capacitance of 200 F $g^{-1}$ was obtained at 0.1 A $g^{-1}$ in a 6 M KOH solution by using the as-prepared materials in supercapacitors. Additionally, multi-element doping is a common strategy adopted to tune the properties of graphene. For instance, N/P co-doped thermally reduced GO with abundant surface groups was prepared via thermal annealing of GO in the presence of $(NH_4)_3PO_4$ [242].

Although various methods have been used to prepare graphene and improve the electrochemical performance of graphene in supercapacitors, the energy storage performance is far from being satisfactory when graphene is merely employed as the active materials in electrode. Considering its excellent electrical conductivity and good

mechanical properties, graphene has been widely used to construct composites with metal oxides, metal hydroxides and conducting polymers [222, 243-246]. Although in principle graphene possesses a variety of ideal properties such as high specific surface area, excellent electrical conductivity and superb thermal conductivity, the large-scale production of high-quality graphene, and prevention of re-aggregation of graphene sheets, are still major obstacles for the widespread use of graphene or graphene-based materials. When the graphene "gold rush" is slowing down, we may need to rethink the practical value of graphene in energy storage. We still have a long way to go to bridge the gap between the ideal properties and practical properties of graphene.

### 1.2.3 Pseudocapacitors

The mechanism of EDLCs is based on electrostatic adsorption/desorption of ions at the electrode/electrolyte surface without charge transfer across the interface. The electrochemical performance of EDLCs is highly dependent on the specific surface area, pore size and surface functional groups as well as the electrical conductivity of carbon-based materials. By contrast to EDLCs, the mechanism of pseudocapacitors involves fast and reversible redox reactions (i.e., Faradaic processes) at the surface or near-surface of the pseudocapacitive materials, which is accompanied by a change in the valence state of the active materials. The term "pseudocapacitance" is formally employed to describe the electrochemical behavior of electrode materials which exhibit a typical feature of a capacitive electrode (i.e., a linear correlation between the stored charge and the width of operating window) but actually involve fast and reversible charge-transfer reactions across the interface [247].

Generally, the specific faradaic processes in electrochemical supercapacitors can be divided into three different mechanisms: (1) underpotential deposition, (2) redox pseudocapacitance and (3) intercalation pseudocapacitance, shown in Figure 1.24. Underpotential deposition refers to ions that can deposit at the metal surface at a potential less negative than the equilibrium potential for the reduction of ions. This

phenomenon is quite common on the catalytic noble metal surface. For example, $H^+$ is adsorbed as hydrogen atoms on the surface of Pt and $Pb^{2+}$ is deposited on Au surface [248, 249]. Redox pseudocapacitance means a surface charge transfer process which is fulfilled by electrochemical adsorption of ions on the electrode surface and subsequent redox reaction of the active materials. The general reaction can be described as follows,

$$O_X + nC^+ + ne^- \leftrightarrow RedC_n \quad (1.11)$$

Where C is the surface-absorbed electrolyte cation $C^+$ (e.g., $H^+$, $Li^+$, $K^+$, and $Na^+$) and n is the number of transferred electrons. The representative redox pseudocapacitive materials include $RuO_2$ [250] and $MnO_2$ [251], conducting polymers like polypyrrole [252] and polyaniline [253].

Intercalation pseudocapacitance involves the fast intercalation of ions into the bulk of layered materials without phase transitions. The reaction can be described as follows,

$$M + nC^+ + ne^- \leftrightarrow C_nM \quad (1.12)$$

Where $M$ is the layered host material and n is the number of the electrons transferred. The common intercalation pseudocapacitive materials include $V_2O_5$ [254], $Nb_2O_5$ [255, 256] and MXenes [257-259]. The electrical neutrality of the host materials is balanced by a change of metal valence.

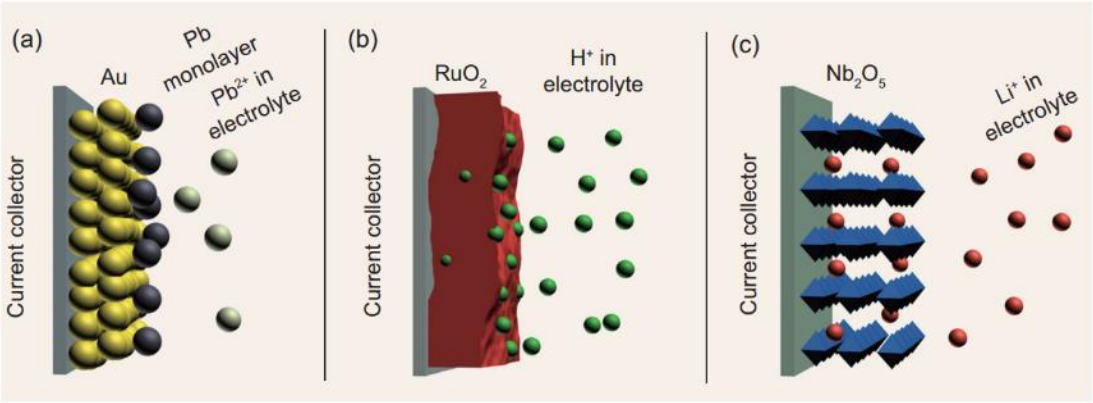


**Figure 1.24.** Different types of reversible redox mechanisms that give rise to pseudocapacitance: **(a)** underpotential deposition, **(b)** redox pseudocapacitance and **(c)** intercalation pseudocapacitance. Reproduced from [260].

The main difference between redox pseudocapacitance and intercalation

pseudocapacitance lies in the reaction region of the electrode materials. The former occurs mainly on the electrode surface or within a shallow surface region, while the latter involves the bulk of the electrode materials. Considering that both intercalation pseudocapacitive behavior and battery behavior involve a Faradaic charge transfer process, their distinctions can be reflected by several typical electrochemical signatures. The former is characterized by fast ion transport and high-rate performance, exhibiting a sloping charge-discharge profile similar to that in EDLCs. By contrast, the latter displays a plateau in the charge-discharge profile and is often limited by solid-state diffusion. The detailed cyclic voltammetry responses and galvanostatic discharge profiles based on different charge storage mechanisms are compared, as shown in Figure 1.25.

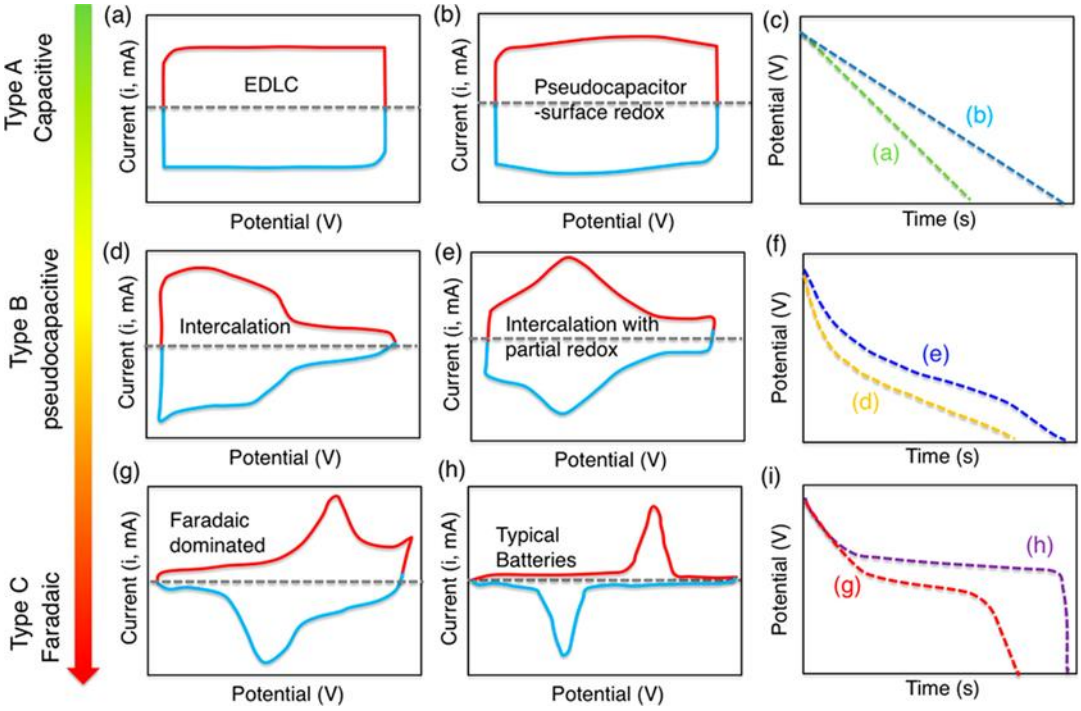


**Figure 1.25.** Comparison of the electrochemical behaviors for various energy-storage materials: **(a, b, d, e, g, h)** schematic cyclic voltammograms and **(c, f, i)** corresponding galvanostatic discharge profiles. Reproduced from [261].

### 1.2.4 Pseudocapacitive materials

The most widely studied pseudocapacitive materials include transition metal oxides, metal sulfides, conducting polymers, MXenes and so on. Here, the most common pseudocapacitive materials are briefly introduced.

#### 1.2.4.1 Transition metal oxides

Among various transition metal oxides, $RuO_2$ has been widely investigated due to its high conductivity, high theoretical specific capacitance and superior stability over the past few decades [262, 263]. The charge storage mechanism of $RuO_2$ involves a fast reversible electron transfer in an acidic solution which is accompanied by proton adsorption/desorption on its surface. The corresponding reaction can be described as follows:

$$RuO_2 + x\,H^+ + x\,e^- \leftrightarrow RuO_{2-x}(OH)_x \qquad (1.13)$$

Where x ranges from 0 to 2, i.e., from $Ru^{4+}$ to $Ru^{2+}$.

This reaction mechanism is expected to deliver a high specific capacitance (1400-2000 F $g^{-1}$) in $RuO_2$ [264]. However, the experimentally obtained value is much lower the theoretical specific capacitance due to the low utilization of the active materials and poor conductivity between the particles. In order to fully use the capacitance of $RuO_2$, reducing particle sizes and constructing composites with conductive materials such as metal, carbon nanotubes and graphene are the extensively employed strategies to improve its electrochemical performance. For example, when $RuO_2$ was electrodeposited on a porous film composed by carbon nanotubes, it displayed a high specific capacitance of 1084 F $g^{-1}$ at 50 mV $s^{-1}$ in a 1 M $H_2SO_4$ solution [265]. Chen et al. synthesized the three-dimensional composite composed of $RuO_2$ and nanoporous gold, which exhibited a high specific capacitance of 1450 F $g^{-1}$ and 1150 F $g^{-1}$ at 20 A $g^{-1}$ and 170 A $g^{-1}$, respectively, in 0.5 M $H_2SO_4$ [264]. The electron-proton transport within the $RuO_2$ was considerably improved by introducing the conductive and

nanoporous gold particles. Although $RuO_2$ exhibits superior electrochemical performance, its toxicity and high cost are still the major obstacles for large-scale applications in energy storage.

Among various other transition metal oxides, $MnO_2$ is considered as one of the promising candidates to replace $RuO_2$ due to its low cost, high abundance, high theoretical capacitance (ca. 1370 F $g^{-1}$) as well as environmental friendliness [266]. The charge storage mechanism of $MnO_2$ involves the oxidation state conversion between $Mn^{4+}$ and $Mn^{3+}$ at or near the $MnO_2$ electrode surface. The corresponding reaction can be described as follows [251]:

$$MnO_2 + C^+ + e^- \leftrightarrow MnOOC \qquad (1.14)$$

Where C can be cations such as $H^+$, $Li^+$, $Na^+$ and $K^+$.

In terms of the surface pseudocapacitive behaviour, the related faradaic reaction is implemented by adsorption/desorption of electrolyte cations on the surface of $MnO_2$ accompanied by the valance change of Mn. As for the bulk pseudocapacitive behavior, it is highly dependent on the embedding/de-embedding of cations into/from the bulk of $MnO_2$. However, the bulk pseudocapacitive behavior is only restricted to a thin subsurface layer of $MnO_2$ (ca. 420 nm thickness) because of the poor electrical conductivity ($10^{-5} - 10^{-6}$ S $cm^{-1}$) of $MnO_2$ and sluggish cation diffusion within the bulk $MnO_2$ [251, 267].

Despite the high theoretical capacitance of $MnO_2$, the practical specific capacitance is just about 200 F $g^{-1}$ due to the low utilization of the active material caused by its low electrical conductivity and dense morphology and texture [266, 268]. Additionally, the cycling performance of $MnO_2$ electrode is not very satisfactory due to the unstable structural stability caused by the dissolution of active materials. Therefore, extensive efforts have been made to increase the capacitance via the design of various nanostructured materials with enhanced electrical conductivity and favourable morphology as well as good stability. For example, Sadak and co-workers [269] demonstrated a facile approach to electrochemically deposit $MnO_2$ on graphene paper. The $MnO_2$ “nano-flower” formed on the graphene paper exhibited a high specific

capacitance of 385.2 F $g^{-1}$ at 1 mV $s^{-1}$ in a 0.1 M $Na_2SO_4$ electrolyte and a capacitance retention of 85.4% after 5000 cycles at 4 A $g^{-1}$ due to the fast transport of electrolyte ions and good electrical conductivity. Wang and co-workers [270] prepared interconnected $MnO_2$ nanosheets by using in-situ redox reaction between $KMnO_4$ solution and a sacrificial carbon template, which exhibited a high capacitance of 516.7 F $g^{-1}$ at 0.2 A $g^{-1}$ and excellent stability with a capacitance retention of 129% after 10000 cycles in a 1 M $Na_2SO_4$ solution.

Although the electrochemical performance associated with $MnO_2$-based electrode materials still needs to be further improved, they are still one of the promising candidates for large-scale applications in pseudocapacitors in view of their low cost, high abundance and easy accessibility. Incorporation of nanostructured $MnO_2$ with highly porous and conductive network (i.e., carbon-based materials) is one of the future directions to effectively employ both the pseudocapacitive effect and electrical double layer effect in the designed electrodes.

### 1.2.4.2 Conducting polymers

As another kind of electrode material, conducting polymers such as polypyrrole (PPy), polyaniline (PANI), polythiophene (PTh) and poly(3,4-ethylenedioxythiophene) (PEDOT) are considered as promising pseudocapacitive materials used in supercapacitors due to their high theoretical capacitance, good conductivity, flexibility, low cost and ease of production, as shown in Figure 1.26 [271, 272].

Generally, conducting polymers can be synthesized by two routes: (1) chemical polymerization with common oxidants such as ammonium persulfate and $Fe^{3+}$; (2) electrochemical polymerization. They can exist in various forms such as powders, films and hydrogels. Furthermore, different morphologies such as nanofibers, nanoarrays and nanotubes can be achieved by using different synthetic and processing methods [273-275]. The easy accessibility of conducting polymers in various forms and morphologies makes them attractive in flexible supercapacitors for wearable electronic devices.

The major problem of conducting polymers used for supercapacitors is the poor cycling stability due to the volume change (i.e., swelling and shrinking) during the charge-discharge process [272, 276]. Constructing composites with carbon-based materials such as carbon nanotubes and graphene is the common strategy to mitigate this issue. For example, Zhang et al. fabricated a ternary composite film composed of polyaniline, carbon nanotubes and graphene, which exhibited a high specific capacitance of 569 F $g^{-1}$ at 0.1 A $g^{-1}$ and a high capacitance retention of 96% over 5000 cycles due to the hierarchical structure and high electrical conductivity of the as-prepared composite [277]. Li and co-workers used glucose as the carbon precursor to deposit a thin carbonaceous shell on the surface of the PANI and PPy nanowire, which showed excellent cycling stability with a capacitance retention of 95% and 85%, respectively, over 10000 cycles [278].

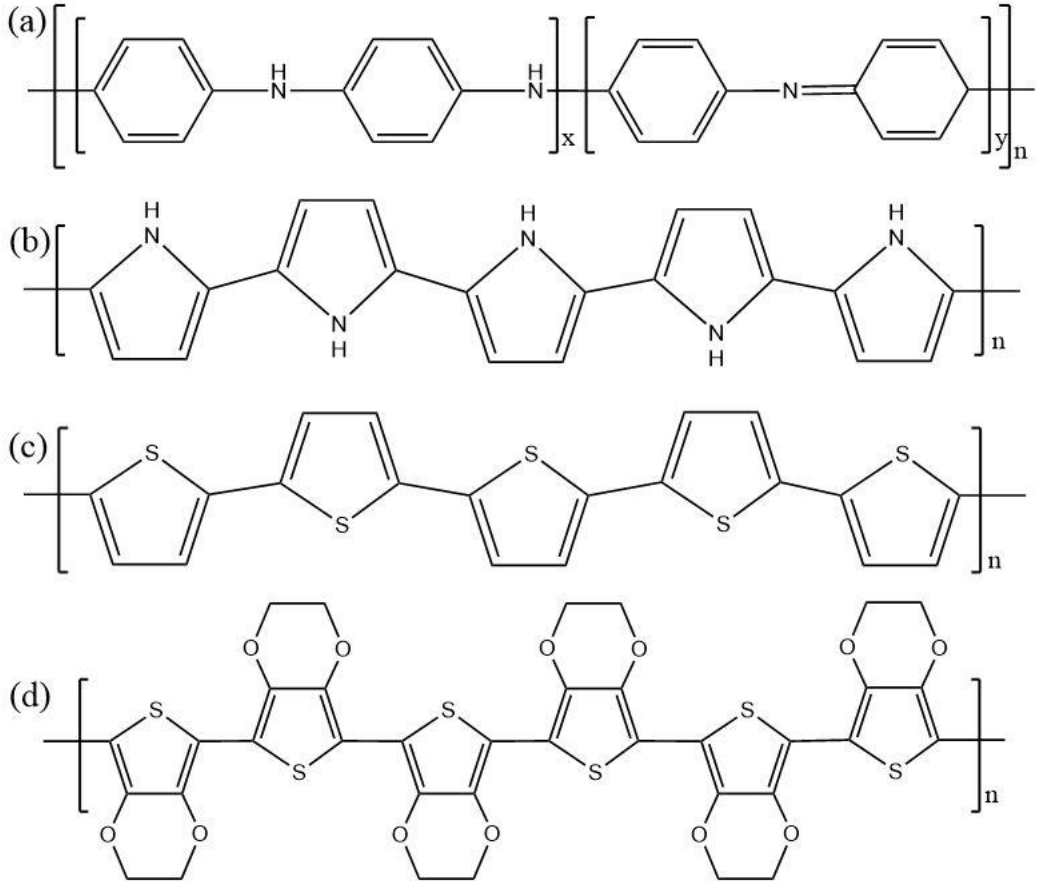


**Figure 1.26.** Representative chemical structure of **(a)** PANI (x + y = 1), **(b)** PPy, **(c)** PTh, and **(d)** PEDOT. Reproduced from [272].

### 1.2.4.3 MXenes

MXenes are a family of 2D early transition metal carbides and carbonitrides, which were first prepared by the selective etching of the A elements (mainly groups 13 and 14) from MAX phases in 2011 [279]. Generally, MXenes are defined as $M_{n+1}X_nT_x$, where M represents an early transition metal, X is carbon or nitrogen, T represents surface termination groups such as =O, –OH, –Cl and –F, *n* can be equal to 1, 2, 3 or 4, and *x* is the number of terminating groups per formula unit [259]. Their good metallic conductivity, high density, redox active surface and hydrophilic nature give them huge potential in the energy storage field, especially in supercapacitors [280]. Among them, the $Ti_3C_2T_x$ MXene has been widely investigated as electrode materials in supercapacitors due to the ease of synthesis and superior charge storage capability [259, 280-282]. The typical synthesis process of $Ti_3C_2T_x$ is shown below in Figure 1.27.

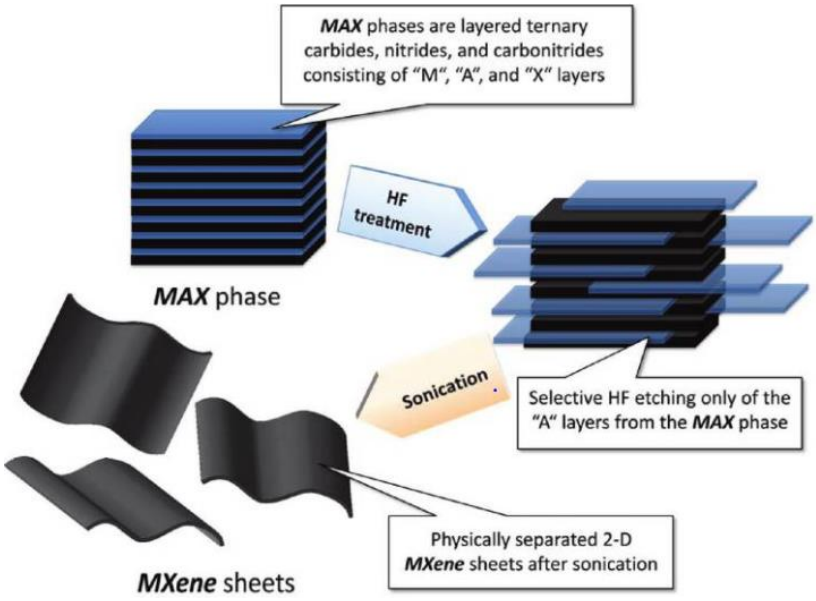


**Figure 1.27.** Schematic for the exfoliation process of MAX phases and formation of MXenes. Reproduced from [283].

For Al-containing MAX phases, the reaction mechanism of production is presumed to be described as follows:

$$M_{n+1}AlX_n + 3HF = AlF_3 + M_{n+1}X_n + 1.5\,H_2 \qquad (1.15)$$

$$M_{n+1}X_n + 2H_2O = M_{n+1}X_n(OH)_2 + H_2 \quad (1.16)$$

$$M_{n+1}X_n + 2HF = M_{n+1}X_nF_2 + H_2 \quad (1.17)$$

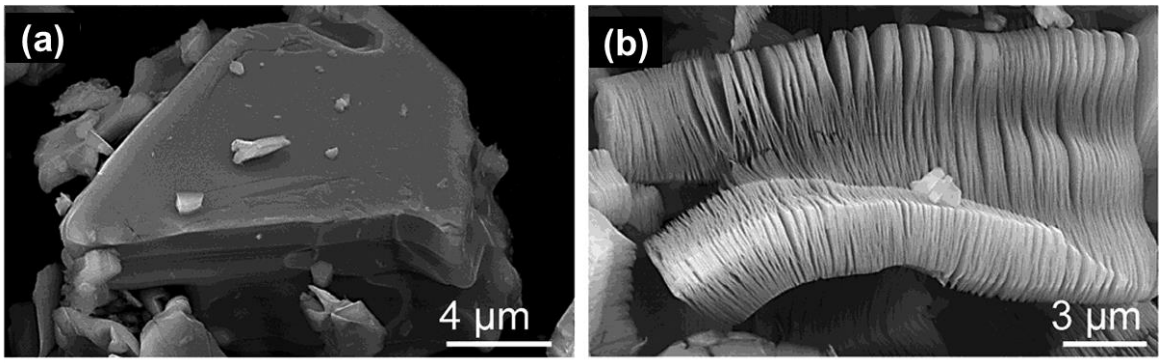


**Figure 1.28.** Scanning electron microscopy images for **(a)** $Ti_3AlC_2$ particle before treatment, **(b)** $Ti_3AlC_2$ after HF treatment. Reproduced from [283].

When $Ti_3C_2T_x$ was used as an electrode material in supercapacitors, the aqueous sulfuric acid electrolyte was often employed to exhibit the pseudocapacitive behavior, as shown in Figure 1.29.

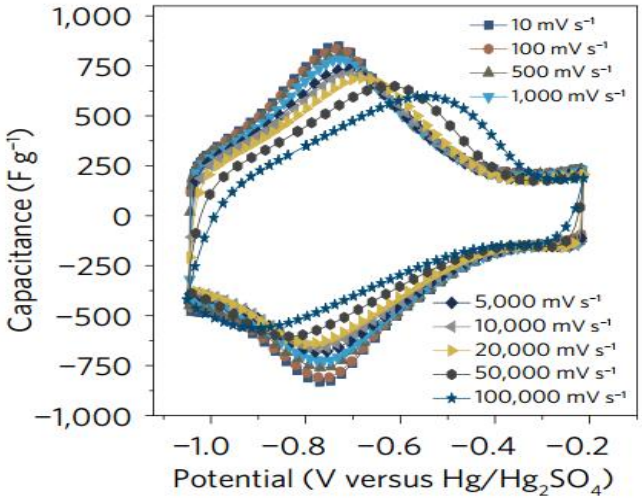


**Figure 1.29.** Cyclic voltammetry curves at scan rates from 10 to 100,000 mV $s^{-1}$ for a 90-nm-thick $Ti_3C_2T_x$ MXene in 3 M $H_2SO_4$. Reproduced from [284].

The charge storage mechanism in $Ti_3C_2T_x$ involves the change of the valence state of Ti atoms ($Ti^{2+}/Ti^{3+}$), which is balanced by the reversible intercalation reaction of protons [285, 286]. The electrochemical reaction can be described as following [284]:

$$Ti_3C_2O_x(OH)_yF_z + \delta e^- + \delta H^+ \rightarrow Ti_3C_2O_{x-\delta}(OH)_{y+\delta}F_z \quad (1.18)$$

A high gravimetric capacitance up to 450 F $g^{-1}$ and volumetric capacitance up to 1,500 F $cm^{-3}$ as well as a high areal capacitance of up to 4 F $cm^{-2}$ were achieved in a three-electrode cell using 3 M $H_2SO_4$ [284].

Since the common synthesis of MXenes involves hazardous chemicals such as HF, tremendous efforts have been devoted to exploiting new methods to produce MXenes and their derivatives. Besides HF etching, fluorine-containing salts like LiF/HCl [287] and NaF/HCl [288] were considered as alternative milder etchants to form HF for further etching. Although longer reaction times are required for this method, the safety of operation has been improved. Considering that F-containing surface groups on MXenes are detrimental to their electrochemical performance [289, 290], new fluorine-free methods have also been developed to optimize the electrochemical performance. For example, Zhang et. al reported an alkali-assisted hydrothermal approach to synthesize a typical MXene-$Ti_3C_2T_x$ (T= -OH, -O) using 27.5 M NaOH at 270 °C [291]. As shown in Figure 1.30, the etching process of Al layers in $Ti_3AlC_2$ by $OH^-$ involves two steps:(1) oxidation of Al into Al (oxide) hydroxides and (2) dissolution of the resulting Al-based products in the alkali solution. It is easy to oxidize the outer Al atoms located on the surface and they would be dissolved in NaOH. If such a process continues, the inner Al atoms would be successfully further oxidized. However, at low temperatures, the Al oxides such as $Al(OH)_3$ and AlO(OH) would be confined in the Ti layers, preventing them from forming dissolvable $Al(OH)_4^-$. As a result, the so called "jamming effect" hinders the formation of the MXene. In contrast, at higher temperatures and higher alkali concentrations, the Al (oxide) hydroxides are able to dissolve due to the endothermic characteristic of the reaction of Al (oxide) hydroxides with $OH^-$, thus promoting the entire selective etching process to continue smoothly.

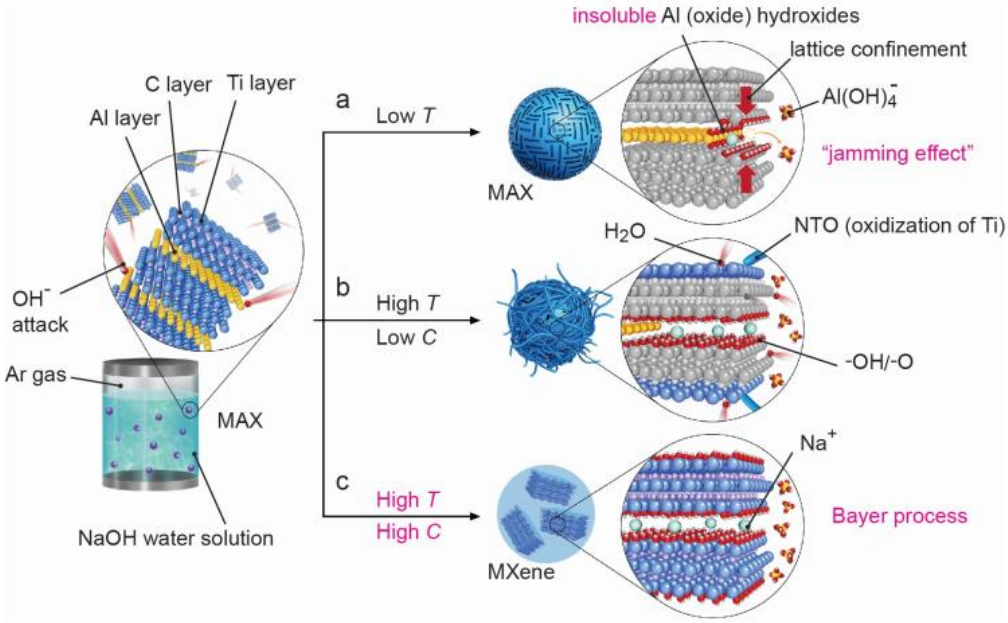


**Figure 1.30.** Schematic of the reaction between $Ti_3AlC_2$ and NaOH solution under various conditions. **(a)** Al (oxide) hydroxides block the Al extraction process under low temperatures, **(b)** Some Al (oxide) hydroxides dissolve in low-concentration NaOH under high temperatures. **(c)** High temperatures and high NaOH concentrations will help dissolve the Al (oxide) hydroxides in NaOH. Reproduced from [291].

Although great progress has been made in the applications of MXenes in supercapacitors over the past few years, some concerns still need to be resolved. The most effective and popular synthesis route of MXenes involves using HF or HCl/LiF etching, which is hazardous in lab preparation and large-scale production. Although the preparation of MXenes with fluorine-free methods, such as electrochemical method, has been explored [292, 293], the complexity and low yield of these methods have limited their wide implementation. Furthermore, most research on MXenes in supercapacitors is mainly associated with the aqueous electrolyte (i.e., $H_2SO_4$), which is also hazardous and limits the potential window. Therefore, more efforts should be devoted into the organic or ionic liquid systems.

## 1.3 Zn-based electrochemical energy storage devices

Although lithium-ion batteries and electric double-layer capacitors are widely employed in modern energy storage technologies, the search for alternative electrochemical energy storage systems is still ongoing to better meet the various market requirements. Recently, aqueous Zn-based electrochemical energy storage devices such as zinc ion batteries and zinc ion hybrid supercapacitors have attracted extensive attention due to their relatively low cost and good operational safety.

Zn metal used as an anode is appealing since Zn is a highly abundant and easily accessible resource, which can potentially reduce the manufacturing cost of the final devices [294]. Moreover, Zn is a non-toxic metal and is chemically stable in aqueous solutions in comparison to the common alkali metals [295]. Furthermore, a high over-potential is required to trigger hydrogen evolution reaction (HER) on the surface of Zn metal and Zn can be easily oxidized into $Zn^{2+}$ without the generation of intermediates in the case of mildly acidic solutions (i.e., pH about 4-6) [296]. Additionally, Zn exhibits a relatively high theoretical capacity of 820 mAh $g^{-1}$ via a two-electron reaction. Due to the advantages mentioned above, Zn has been widely employed as an anode material for various Zn-based electrochemical energy devices.

### 1.3.1 Zinc chemistry

The behaviour of Zn metal can vary with the pH value of solution environments, as shown in Figure 1.31. Generally, Zn metal is electrochemically oxidized into $Zn^{2+}$ by losing electrons during the discharge process. The following reactions of $Zn^{2+}$ are influenced by the pH value of the solution. In alkaline solution, the $Zn^{2+}$ ions cannot exist in the form of $Zn^{2+}$ but rather $Zn(OH)_4^{2-}$ due to abundant $OH^-$ species near the anode. These zincate ions will form the precipitate (i.e., ZnO) when zincate reaches the local saturation limit. Such a precipitation leads to the passivation of Zn metal and thus impedes the re-chargeability of the alkaline batteries. The corresponding reactions in alkaline solutions can be described as follows [296, 297]:

$$Zn\,(s) \rightarrow Zn^{2+}(aq) + 2e^{-} \qquad (1.19)$$

$$Zn^{2+}(aq) + 4\,OH^{-}\,(aq) \rightarrow Zn(OH)_4{}^{2-}(aq) \qquad (1.20)$$

$$Zn(OH)_4{}^{2-}(aq) \rightarrow ZnO\,(s) + H_2O\,(l) + 2\,OH^{-}\,(aq) \qquad (1.21)$$

Compared with the complex reactions occurring in alkaline solutions, the reactions can be simpler in mildly acidic solutions such as $ZnSO_4$. The $Zn^{2+}$ species present in the form of ions guarantee good reversibility of stripping and plating of Zn, thus enabling the re-chargeability of batteries. The corresponding reactions in mildly acidic electrolyte can be described as follows [296]:

$$Discharge:\ Zn\,(s) \rightarrow Zn^{2+}(aq) + 2\,e^{-} \qquad (1.22)$$

$$Charge:\ Zn^{2+}(aq) + 2\,e^{-} \rightarrow Zn\,(s) \qquad (1.23)$$

When Zn is used as an anode, the pH value of the media is critical. Although it allows the existence of $Zn^{2+}$ in acidic environment, a lower pH value will accelerate the HER both chemically and electrochemically during the operation of the battery. For instance, when the pH value of the utilized solution is 4, the potential for HER is calculated to be -0.236 V (vs. standard hydrogen electrode (SHE)). Considering that the standard reduction potential of Zn is -0.763 V (vs. SHE), it means that the HER is thermodynamically more favourable than the plating of Zn. However, from a kinetics perspective, HER can be effectively suppressed in mildly acidic solution due to the high overpotential on the surface of Zn metal, thus ensuring the reversible stripping/plating of Zn. It is worth pointing out that the overpotential is highly dependent on the current density applied. If the pH value is lower than 3, Zn metal can directly react with the solution to generate $H_2$ bubbles on the surface of Zn metal, leading to the continuous consumption of Zn and electrolyte solvent. Therefore, the use of Zn metal in strongly acidic electrolytes is not feasible.

Another issue associated with Zn metal is the potential formation of dendrites during the long-term cycling process. In alkaline electrolytes with high pH values, Zn dendrite is associated with the instability of $Zn(OH)_4{}^{2-}$, which would decompose into the passivation layer of ZnO on the surface of Zn anode, thus affecting the plating/striping

of Zn. In acidic electrolytes with low pH values, the metallic Zn anode can directly react with the solution to generate $H_2$ gas, which leads to the severe corrosion and consumption of Zn. Therefore, the acidic solutions will be not employed in the Zn-based electrochemical energy storage devices. In neutral/mildly acidic electrolytes, the growth of Zn dendrites is highly dependent on the applied current densities and mass loading of the cathode materials over repeated cycle [298]. Various strategies like optimization of electrolyte formulations and modification of Zn anodes have been developed to address the issues associated with the Zn dendrite formation [296, 299]. Despite the challenges associated with the Zn anode, the key issue in Zn-based energy devices is to develop cost-effective and environmentally friendly cathode materials with high capacity and good stability. In this thesis, the focus is given to the cathode materials used in the Zn-based energy devices.

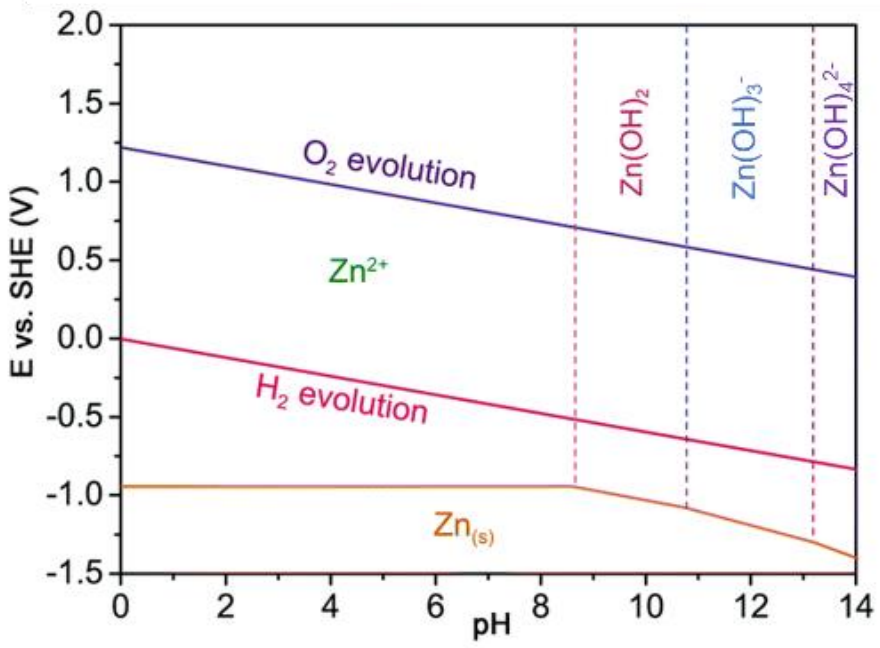


**Figure 1.31.** A Pourbaix diagram of Zn in aqueous solution. Reproduced from [300].

### 1.3.2 Aqueous zinc-ion batteries

Compared with organic lithium-ion batteries, aqueous batteries are rather promising in terms of safety, cost and environmental compatibility, as shown in Figure 1.32a. The

short circuit in organic batteries can generate a large amount of heat and the organic electrolytes can serve as a fuel to cause a fire. By replacing the organic electrolytes with aqueous counterparts to construct aqueous batteries, the risk of a fire can be effectively mitigated. Additionally, aqueous batteries are more likely to achieve high-rate capabilities benefiting from the higher ionic conductivity of aqueous electrolytes compared with that of organic electrolytes.

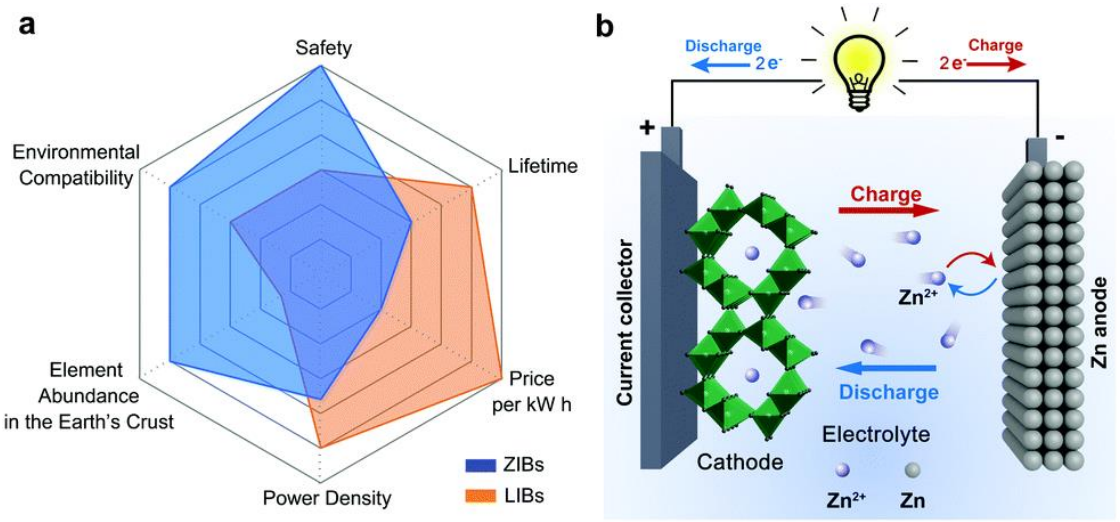


**Figure 1.32. (a)** Multi-facet comparison of zinc-ion and lithium-ion batteries, **(b)** Schematic illustration of the operating principle of aqueous rechargeable zinc-ion batteries. Reproduced from [300].

Among various emerging aqueous batteries, aqueous zinc ion batteries are considered as a very promising candidate for large-scale energy storage. A typical aqueous zinc-ion battery is composed of $Zn^{2+}$ host materials as cathodes, Zn metal as the anode and aqueous $Zn^{2+}$-containing electrolytes, as shown in Figure 1.32b. Generally, the electrochemical performance is determined by the cathode materials. Therefore, numerous efforts have been devoted to the development of cathode materials. In general, the common cathode materials for aqueous zinc ion batteries can be divided into three categories: (1) Manganese-based oxides, (2) Prussian blue analogues, and (3) Vanadium-based compounds [295].

### 1.3.2.1 Manganese-based oxides

Manganese oxides have been widely employed as electrode materials in primary and rechargeable batteries because of their high theoretical capacity, moderate discharge potential, high abundance, low cost and environmental benignity [301].

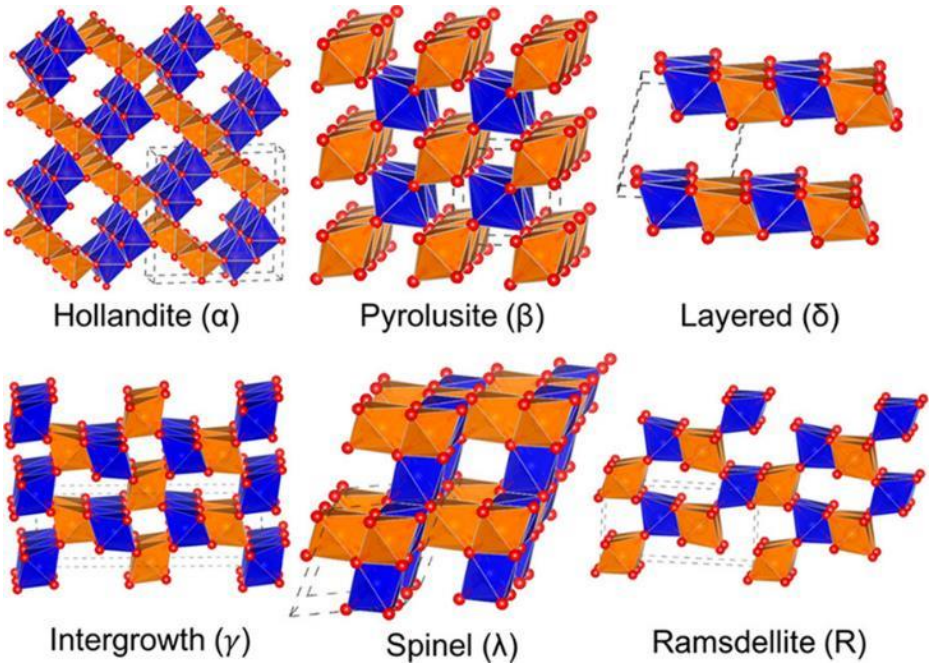


**Figure 1.33.** $MnO_2$ polymorphs. The orange and blue octahedra surround spin up and down Mn atoms, respectively. The red atoms represent O. Pictured are the lowest energy configurations. Reproduced from [304].

Manganese oxides can exist in various chemical formulas such as $MnO_2$ and $Mn_2O_3$ and $Mn_3O_4$ [301-303]. Among them, $MnO_2$ is the most common manganese oxide with various polymorphs such as α-, β-, γ-, δ-, λ-, R-, and ε-type. The various polymorph structures are constructed by $MnO_6$ octahedral units via the linking of edges or corners. As shown in Figure 1.33, the $MnO_2$ polymorphs can be classified into three types [295]: (a) tunnel structures, such as α-$MnO_2$ (2 × 2, 4.6 × 4.6 $Å^2$), β- $MnO_2$ (1 × 1, 2.3 × 2.3 $Å^2$), γ-$MnO_2$, R-$MnO_2$ (randomly arranged 1 × 2 and 1 × 1 $Å^2$) and todorokite-$MnO_2$ (3 × 3 $Å^2$); (b) layered-like structure, such as δ-$MnO_2$ with a interlayer distance of ~7 Å; (c) spinel structures such as λ-$MnO_2$. Most of these $MnO_2$ polymorphs have been

explored as cathode materials for aqueous zinc ion batteries. The crystallographic information of the common $MnO_2$ polymorphs is shown in Table 1.2.

**Table 1.2.** Crystallographic information of the common $MnO_2$ polymorphs [305]

| $MnO_2$ Polymorphs | Unit Cell Parameter | | | | Space Group |
|---|---|---|---|---|---|
| α | a | 9.785 Å | α | 90° | $I_4/m$ |
| | b | 9.785 Å | β | 90° | |
| | c | 2.863 Å | γ | 90° | |
| β | a | 4.404 Å | α | 90° | $P4_2/mnm$ |
| | b | 4.404 Å | β | 90° | |
| | c | 2.877 Å | γ | 90° | |
| γ- | a | 9.305 Å | α | 90° | C2/m |
| | b | 2.85 Å | β | 90° | |
| | c | 4.45 Å | γ | 90° | |
| δ | a | 2.85 Å | α | 90° | $P6_3/mmc$ |
| | b | - | β | 90° | |
| | c | 4.48 Å | γ | 120° | |
| λ | a | 5.828 Å | α | 60° | $Fd\bar{3}m$ |
| | b | 5.822 Å | β | 60° | |
| | c | 5.831 Å | γ | 60° | |
| R | a | 2.916 Å | α | 90° | Pnma |
| | b | 4.581 Å | β | 90° | |
| | c | 9.434 Å | γ | 90° | |
| ε | a | 2.786 Å | α | 90° | $P6_3/mmc$ |
| | b | 2.786 Å | β | 90° | |
| | c | 4.412 Å | γ | 120° | |

The concept of a rechargeable zinc-ion battery was first introduced in 1986 [306]. The batteries composed of $MnO_2$ cathode, Zn anode and $ZnSO_4$ electrolyte exhibited an

average discharge voltage of 1.3 V and no significant degradation after 30 cycles. In 2012, this type of battery was revived by Kang and co-workers [307]. The rechargeable zinc ion batteries composed of α-$MnO_2$ cathode, zinc anode, and mild $ZnSO_4$ or $Zn(NO_3)_2$ aqueous electrolyte delivered a high capacity of 210 mAh $g^{-1}$ at 0.5 C. Even at 126 C, a relatively high capacity of 68 mAh $g^{-1}$ was still obtained within 27 s, indicating excellent rate capability, as shown in Figure 1.34.

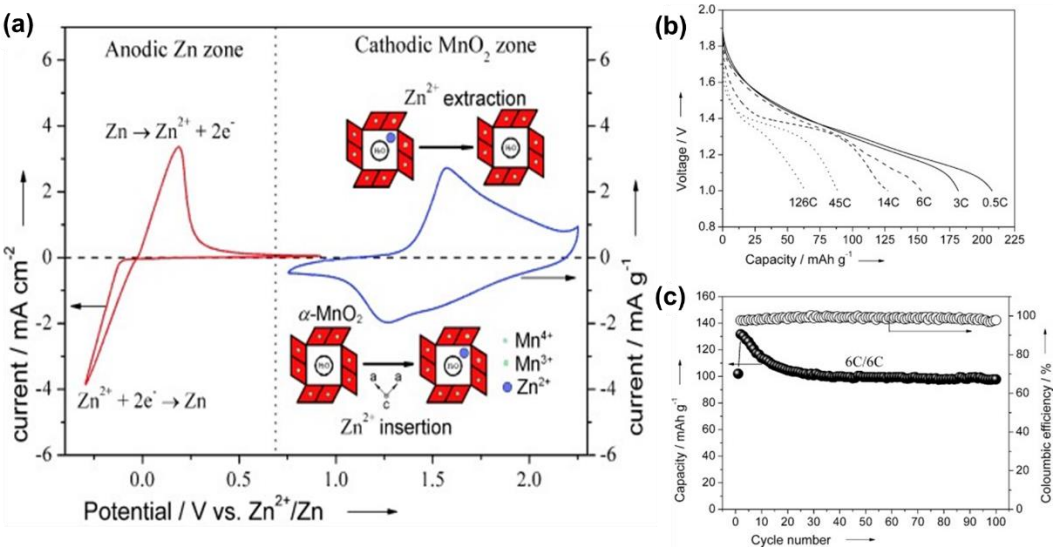


**Figure 1.34. (a)** Cyclic voltammogram of the Zn anode (red line) and the α-$MnO_2$ cathode (blue line) in the $Zn(NO_3)_2$ aqueous electrolyte, **(b)** Discharge curves at various rates, **(c)** Cycling stability at 6 C. Reproduced from [307].

This promising electrochemical performance has inspired more researchers to set foot in this field since then. It was further proposed that $Zn^{2+}$ can reversibly intercalate/extract into/from the tunnel of α-$MnO_2$ during the discharge/charge process and accordingly, the Zn anode undergoes a stripping and plating process, as shown in Figure 1.34. The corresponding mechanism can be described by one-step reaction as follows [307]:

$$Zn^{2+} + 2\,e^{-} + 2\,MnO_2 \leftrightarrow\ ZnMn_2O_4 \qquad (1.24)$$

A similar work was also carried out by Kim and co-workers [308]. They synthesized α-$MnO_2$ nanorods via a facile hydrothermal reaction, which delivered an initial discharge

capacity of 233 mAh $g^{-1}$ at 83 mA $g^{-1}$ and exhibited a capacity retention of 63% after 50 cycles. The structural changes of α-$MnO_2$ during the Zn ion insertion/extraction process was investigated by the synchrotron X-ray diffraction (XRD) method, which indicated the formation of $ZnMn_2O_4$ during the discharge process, as shown in Figure 1.35. According to the XRD data obtained from the $MnO_2$ electrode at different states, the spacing values for the (110) plane were calculated to be 7.036 Å (Zn-inserted state) and 6.915 Å (Zn-extracted state) respectively, implying the volume expansion of ca.3.12% in a unit cell during Zn-insertion. Considering the two distinct peaks observed at around 1.3 and 1.2 V in the cyclic voltammogram, a two-step Zn-insertion mechanism was further proposed as follows [308]:

$$0.5\ Zn^{2+} + e^{-} + 2\ MnO_2 \leftrightarrow Zn_{0.5}Mn_2O_4 \qquad (1.25)$$

$$0.5\ Zn^{2+} + e^{-} + Zn_{0.5}Mn_2O_4 \leftrightarrow ZnMn_2O_4 \qquad (1.26)$$

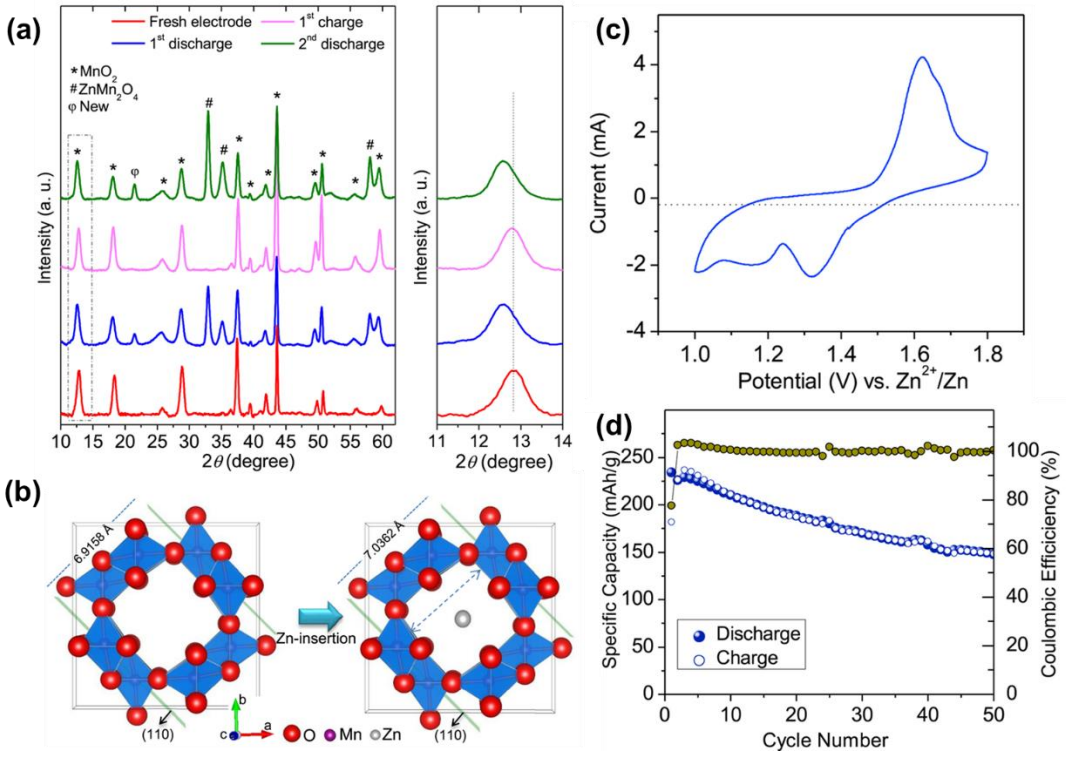


**Figure 1.35. (a)** Ex-situ synchrotron XRD and magnification of (110) peak of the α-$MnO_2$ nanorods electrode after discharging/charging, **(b)** Schematic illustration for the zinc insertion into tunnel structure α-$MnO_2$ causing the expansion of tunnel, **(c)** Cyclic

voltammograms at a scan rate of 0.5 mV $s^{-1}$, **(d)** Cycling stability between 1.0 and 1.8 V vs. $Zn^{2+}$/Zn at 83 mA $g^{-1}$. Reproduced from [308].

Later, Liu et al. [309] proposed a new mechanism based on a conversion reaction between $MnO_2$ and $H^+$ without zinc ion intercalation and de-intercalation since MnOOH was detected as discharge product. The reaction can be outlined as follows:

Cathode: $H_2O \leftrightarrow H^+ + OH^-$ (1.27)

$$MnO_2 + H^+ + e^- \leftrightarrow MnOOH \quad (1.28)$$

$$1/2\ Zn^{2+} + OH^- + 1/6\ ZnSO_4 + x/6\ H_2O \leftrightarrow 1/6\ ZnSO_4[Zn(OH)_2]_3 \cdot x\ H_2O \quad (1.29)$$

Anode: $1/2\ Zn \leftrightarrow 1/2\ Zn^{2+} + e^-$ (1.30)

Similarly, Oh et al. observed precipitation of zinc hydroxide sulfate ($Zn_4(OH)_6(SO_4)\cdot 5H_2O$) on the surface of α-$MnO_2$ without zinc intercalation into the tunnels of $MnO_2$ [310]. This precipitation was caused by the pH value change of the electrolyte owing to the disproportionation of the unstable $Mn^{3+}$. The corresponding cathode reaction was described as follows [310]:

$$MnO_2 + 2\ H_2O + 2e^- \rightarrow Mn^{2+} + OH^- \quad (1.31)$$

$$3MnO_2 + 8Zn^{2+} + 2ZnSO_4 + 16\ H_2O + 6e^- \rightarrow 3Mn^{2+} + 2Zn_4(OH)_6SO_4(5H_2O) \quad (1.32)$$

Wang and co-workers [311] subsequently proposed a $H^+$ and $Zn^{2+}$ co-insertion mechanism since the successive discharge products of MnOOH and $ZnMn_2O_4$ were detected at 1.3 V and 1.0 V respectively, as shown in Figure 1.36a. The reaction mechanism of $MnO_2$ cathode was further investigated using galvanostatic intermittent titration technique (GITT), as show in Figure 1.36b. They concluded that the region I corresponded to the $H^+$ insertion, while the region II was mainly ascribed to the $Zn^{2+}$ insertion. However, only the co-insertion concept was proposed based on the experimental results and no detailed reactions were provided. It is worth mentioning that a high capacity of 290 mAh $g^{-1}$ at 0.3 C with an average discharge voltage of 1.3

V and a stable capacity of 50–70 mAh $g^{-1}$ was achieved at 6.5 C for 10000 cycles. This co-insertion mechanism of $H^+$ and $Zn^{2+}$ was also reported by Huang and co-workers in polyaniline (PANI)-intercalated layered $MnO_2$ [312]. During the discharge process, the $H^+$ insertion resulted in the local concentration increase of $OH^-$, thus forming the flake-like product zinc hydroxide sulfate hydrate surface ($Zn_4(OH)_6(SO_4)\cdot 5H_2O$) on the surface of $MnO_2$. The cell exhibited a reversible discharge capacity of 280 mA h $g^{-1}$ at 200 mA $g^{-1}$ and a capacity of 110 mAh $g^{-1}$ at 3 A $g^{-1}$ as well as long-term stability of 5000 cycles.

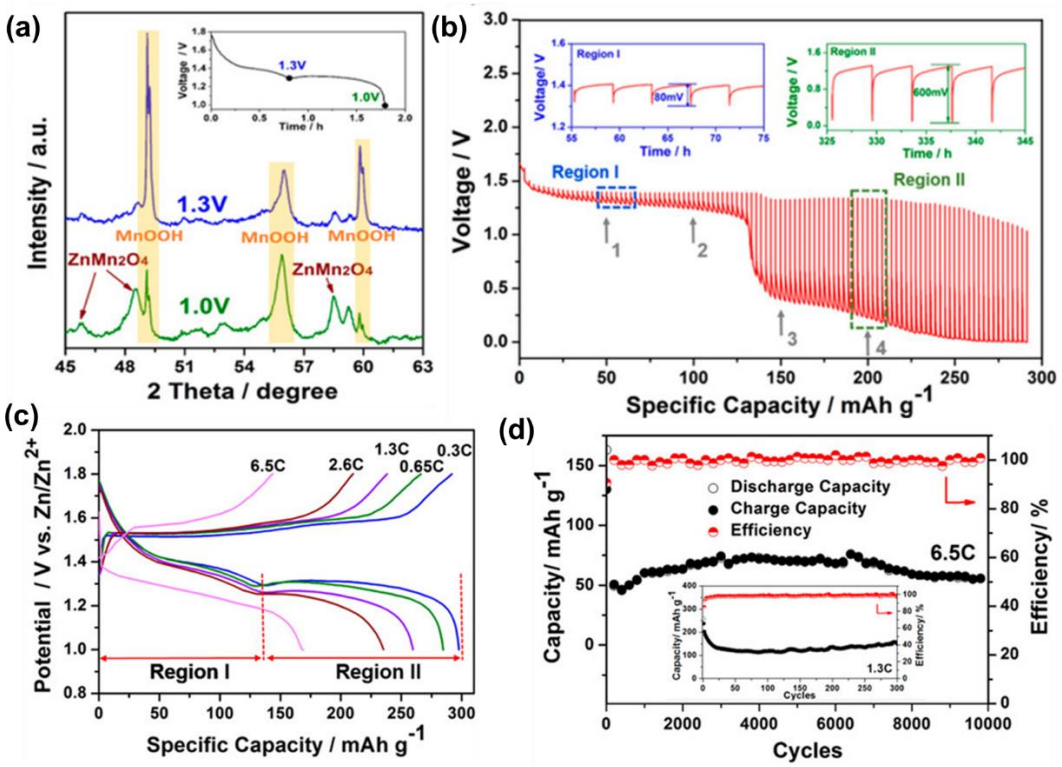


**Figure 1.36. (a)** Ex situ XRD patterns of the $MnO_2$ cathode at depth of discharge at 1.3 and 1.0 V, respectively, **(b)** Discharge profiles of the Zn-$MnO_2$ cell (50 mA $g^{-1}$ for 120 s followed by a 4 h rest) based on GITT, **(c)** Electrochemical performance of the cell in 2 M $ZnSO_4$ + 0.2 M $MnSO_4$ electrolyte, **(d)** cycling stability at rates of 6.5 C (1 C = 290 mA $g^{-1}$, and 1.3 C (inset). Reproduced from [311].

According to the above discussions, three different energy storage mechanisms in manganese oxides have been proposed in different cases: (1) $Zn^{2+}$ intercalation, (2)

conversion reaction based on $H^+$, and (3) $H^+$ and $Zn^{2+}$ co-insertion. It is evident that the reaction mechanism associated with $MnO_2$ is complex and under debate. More precise and comprehensive experiments are required to reveal the complex mechanism. If similar phenomena and experimental results can be independently reported by more researchers, it would facilitate the clarification of the reaction mechanism, especially those that prove to be more controversial.

#### 1.3.2.2 Prussian blue analogues

As shown in Figure 1.37, Prussian blue analogues with a three-dimensional open framework are considered as one of the promising electrode materials for batteries. The Prussian blue analogues belong to hexacyanometallates with a general formula as follows [313]:

$$A_x M[M'(CN)_6]_{1-y}\,\gamma_y \cdot wH_2O$$

where $A$ denotes the alkaline cations, $M$ and $M'$ represent the transition metal ions coordinated octahedrally to the cyanide groups, and $\gamma$ represents vacancies in the crystallographic structure. The water can be either zeolitic water in the octahedral centre of the sub-cells or water coordinated with the transition metals. The unit cell in the crystal structure is composed of eight large interstitial sites which enable the accommodation of various monovalent ions (e.g., $Li^+$, $Na^+$ and $K^+$), divalent ions (e.g., $Mg^{2+}$ and $Zn^{2+}$) and even trivalent ions like $Al^{3+}$ [314].

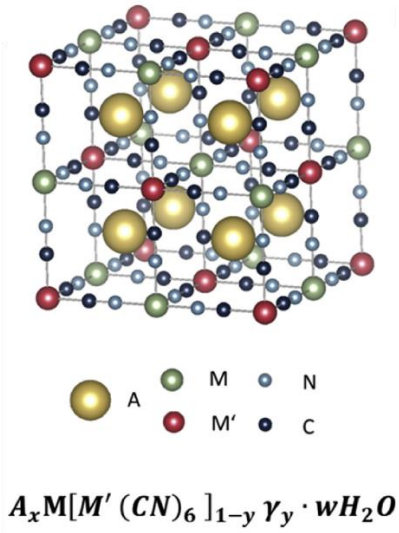


**Figure 1.37.** Schematic diagram of the crystal structure of Prussian blue analogues. Reproduced from [313].

Zhen and co-workers [315] prepared Iron(III) hexacyanoferrate(III) ($FeFe(CN)_6$) nano-cubic nanoparticles with an averaged 150 nm diameter by using a solution precipitation method. The electrochemical property of $FeFe(CN)_6$ cathode was characterized in a flooded cell containing 1 M zinc acetate/(choline acetate + 30 wt % water) electrolyte with Zn wire/sheet as counter and reference electrodes. A reversible discharge capacity of 120 mAh $g^{-1}$ was obtained at a current density of 10 mA $g^{-1}$. Following up on this work, they also demonstrated bio-degradable zinc ion batteries using Prussian blue analogue as cathode, Zn powder as anode and a bio-degradable ionic liquid-water mixture as electrolyte, which exhibited a specific capacity of 54 mAh $g^{-1}$ and nearly no capacity fading after 50 cycles [316].

Jia and co-workers [317] demonstrated the feasibility of prepared copper hexacyanoferrate (CuHCF, $KCuFe^{III}(CN)_6$) nano-cubes for zinc ion batteries in 1 M $ZnSO_4$. A pair of redox peaks was observed in the cyclic voltammetry, which was ascribed to the insertion/extraction of $Zn^{2+}$ into/from the host accompanied by the state change between $Fe^{3+}$ and $Fe^{2+}$. It delivered a capacity of 56 mA h $g^{-1}$ at a current density of 20 mA $g^{-1}$ and 77% of the initial discharging capacity was maintained after 20 cycles. The cycling stability of CuHCF was further improved by using a 20 mM $ZnSO_4$

aqueous solution, in which a capacity retention of 96.3% was obtained after 100 cycles [318]. The corresponding reactions can be described as follows:

$$KCuFe^{III}(CN)_6 + x\ Zn^{2+} + 2x\ e^- \leftrightarrow Zn_xKCu[Fe^{III}(CN)_6]_{1-2x}[Fe^{II}(CN)_6]_{2x} \quad (1.33)$$

$$x\ Zn \leftrightarrow x\ Zn^{2+} + 2x\ e^- \ (\ 0 \le x \le 0.5\ ) \quad (1.34)$$

Further, Liu and co-workers [319] synthesised $Zn_3[Fe(CN)_6]_2$ (ZnHCF) for aqueous zinc ion batteries. It was found that ZnHCF experienced rapid dissolution in 0.5 M $Na_2SO_4$ and 0.5 M $K_2SO_4$ solutions, while it remained stable in 1 M $ZnSO_4$ solution. Constructed by a ZnHCF cathode, zinc anode and 1 M $ZnSO_4$ electrolyte, the aqueous zinc ion battery exhibited a discharge capacity of 65.4 mAh $g^{-1}$ at 60 mA $g^{-1}$ and a high operating voltage of about 1.7 V, as shown in Figure 1.38. Moreover, it demonstrated a capacity retention of 76% after 100 cycles. The reaction mechanism can be described as follows:

$$x\ Zn^{2+} + 2x\ e^- + Zn_3[Fe(CN)_6]_2 \leftrightarrow Zn_{3+x}[Fe(CN)_6]_2 \quad (1.35)$$

$$x\ Zn \leftrightarrow x\ Zn^{2+} + 2x\ e^- \quad (1.36)$$

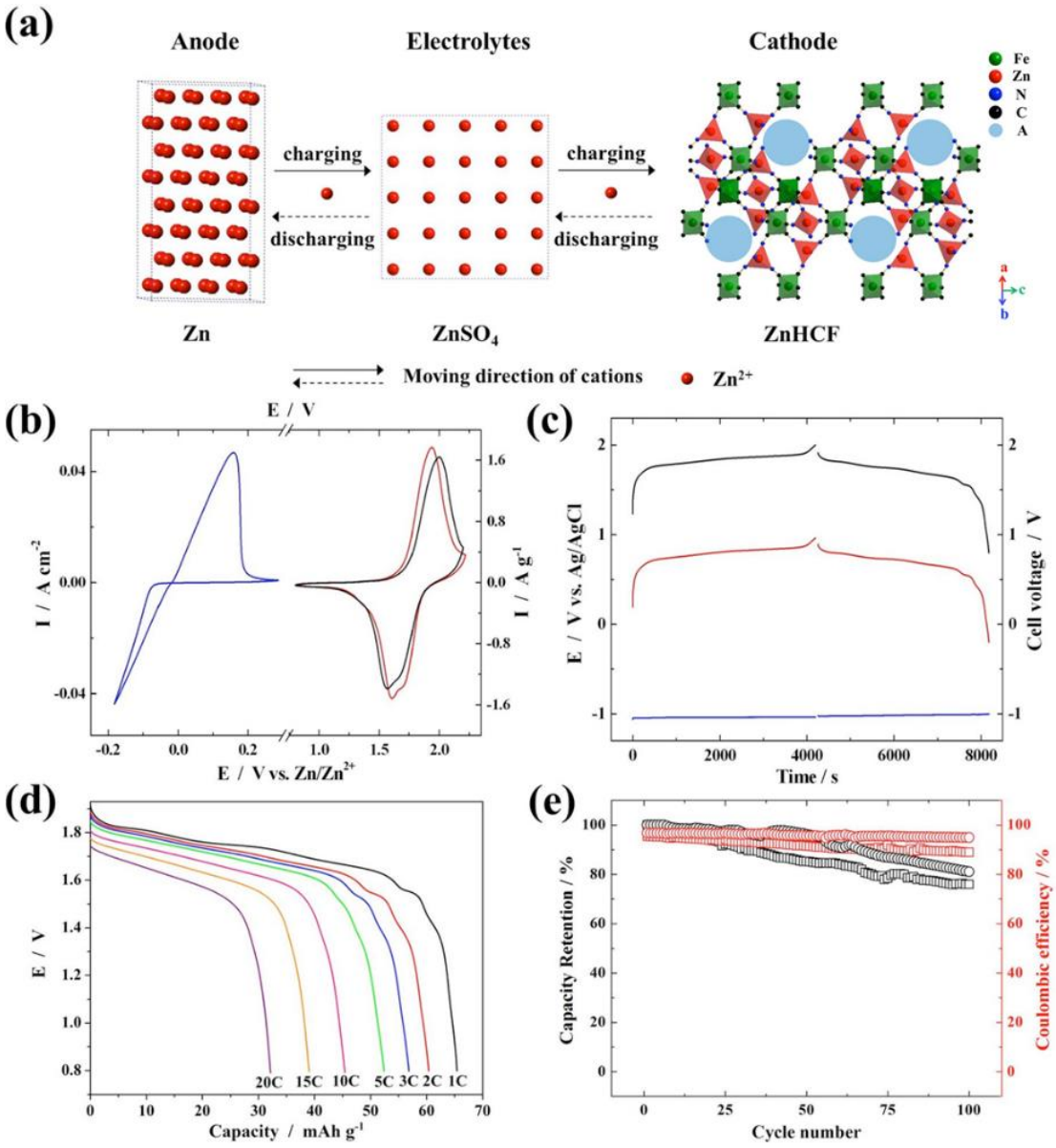


**Figure 1.37. (a)** A schematic of the battery, **(b)** CVs at a scan rate of 2 mV $s^{-1}$ and **(c)** GCD profiles at 1 C for anode (blue), cathode (red) and full cell (black) in 1 M $ZnSO_4$, **(d)** Rate capability of the battery, **(e)** Cycle life tests at 1 C (black) and 5 C (red). 1 C = 60 mA $g^{-1}$, 5 C = 300 mA $g^{-1}$. Reproduced from [319].

Although Prussian blue analogues show a high operating voltage and excellent rate performance, their discharge capacity is still relatively low compared with other types of cathode materials. Constructing composites or introducing more vacancy sites in the host can be promising strategies employed to enhance the capacity.

### 1.3.2.3 Vanadium-based compounds

Vanadium-based materials, such as $V_2O_5$, $VO_2$, $Zn_XV_2O_5{\cdot}nH_2O$ and $Na_XV_2O_5{\cdot}nH_2O$, are considered as an important type of cathodes for zinc ion batteries due to their multiple oxidation states, high specific capacity and long stability.

Hu and co-workers [320] synthesized porous $V_2O_5$ for aqueous zinc ion batteries using the "water-in-salt" electrolyte composed of 21 m LiTFSI and 1 m $Zn(CF_3SO_3)_2$, which demonstrated a high capacity of 238 mAh $g^{-1}$ at 50 mA $g^{-1}$ and a capacity of 156 mAh $g^{-1}$ at 1 A $g^{-1}$ as well as a capacity retention of 80% after 2000 cycles at 1 A $g^{-1}$. It was noted that the "water-in-salt" electrolyte enabled a higher discharge platform of 1.0 V, which is much higher than that (0.6 V) seen in 1 m $Zn(CF_3SO_3)_2$ electrolyte, shown in Figure 1.39. Furthermore, Zhou and co-workers [321] studied the effects of different types of electrolytes (i.e., $ZnSO_4$, $ZnCl_2$, $Zn(CH_3COO)_2$, and $Zn(NO_3)_2$) and concentrations of $ZnSO_4$ electrolyte on the electrochemical performance of aqueous Zn-$V_2O_5$ batteries. The Zn-$V_2O_5$ cells based on 3 M $ZnSO_4$ aqueous electrolyte exhibited better electrochemical performance with a capacity of 224 mAh $g^{-1}$ at 100 mA $g^{-1}$ and good stability up to 400 cycles. Chen and co-workers [322] prepared $VO_2$ hollow nanospheres for zinc ion batteries using 3 M $ZnSO_4$ electrolyte, which exhibited a high discharge capacity of 408 mA h $g^{-1}$ at 0.1 A $g^{-1}$, and good rate capability (200 mA h $g^{-1}$ at 20 A $g^{-1}$). Moreover, when the cell was measured at a high current density of 10 A $g^{-1}$, the as-prepared $VO_2$ delivered a high initial capacity of 292 mA h $g^{-1}$ and retained a capacity of 89 mA h $g^{-1}$ after 30000 cycles with a low degradation rate of 0.0023% per cycle.

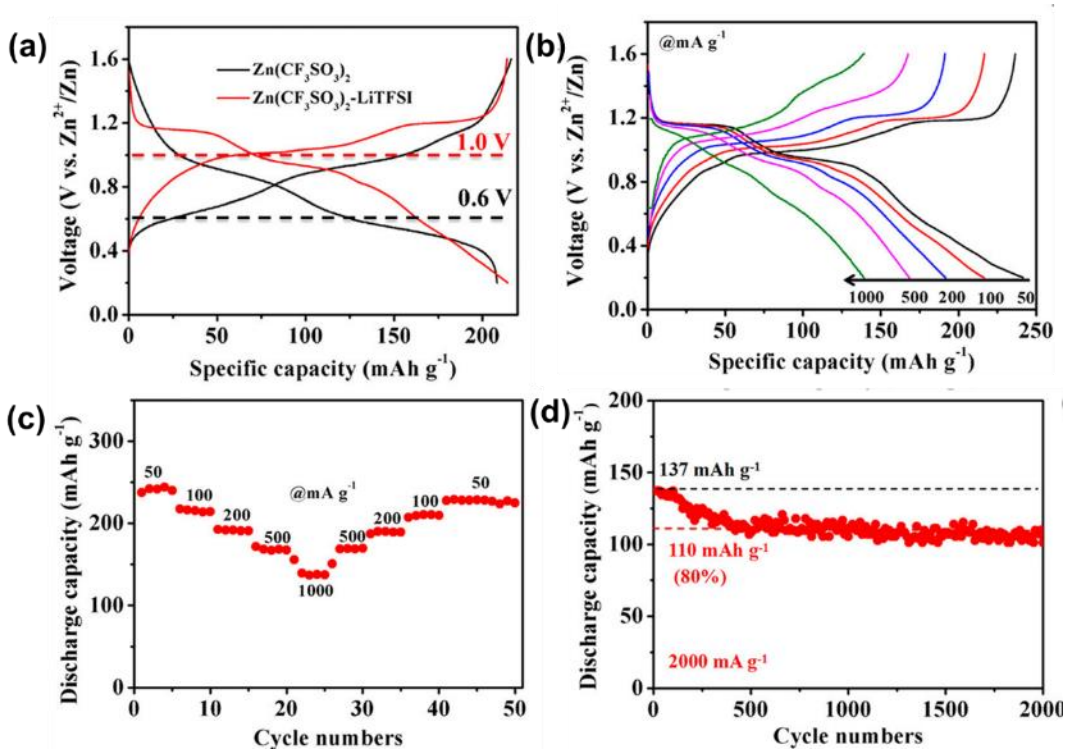


**Figure 1.38. (a)** Charge/discharge curves of Zn-$V_2O_5$ batteries at 100 mA $g^{-1}$ using different electrolytes, **(b)** Charge/discharge curves and **(c)** Rate performance of the $V_2O_5$ at various current densities ranging from 50 to 1000 mA $g^{-1}$, respectively, in "water-in-salt" electrolyte (1 m $Zn(CF_3SO_3)_2$-21 m LiTFSI), **(d)** Cyclability of the $V_2O_5$ at 2 A $g^{-1}$ in "water-in-salt" electrolyte. Reproduced from [320].

Nazar and co-workers [323] reported a vanadium oxide pillared by $Zn^{2+}$ ions and water ($Zn_{0.25}V_2O_5{\cdot}nH_2O$) for zinc ion batteries. It delivered a high capacity of 282 mAh $g^{-1}$ at 300 mA $g^{-1}$ and a high discharge capacity of 183 mAh $g^{-1}$ was maintained even at a high current density of 6 A $g^{-1}$, indicating superior rate capability. Additionally, excellent cyclability was obtained with a capacity retention of 81% after 1000 cycles at 2.4 A $g^{-1}$, as shown in Figure 1.40. The operando XRD results indicated that the water molecules facilitated the insertion/extraction of $Zn^{2+}$ in the layered galleries of $Zn_{0.25}V_2O_5$, resulting in high-rate capability. The indigenous Zn ions in the crystal structure helped stabilize the layered structure, thus guaranteeing excellent cyclability. The corresponding reaction of the $Zn_{0.25}V_2O_5{\cdot}nH_2O$ can be described as follows:

$$Zn_{0.25}V_2O_5 \cdot nH_2O \; + \; 1.1\, Zn^{2+} + 2.2\, e^- \leftrightarrow \; Zn_{1.35}V_2O_5 \cdot nH_2O \quad (1.37)$$

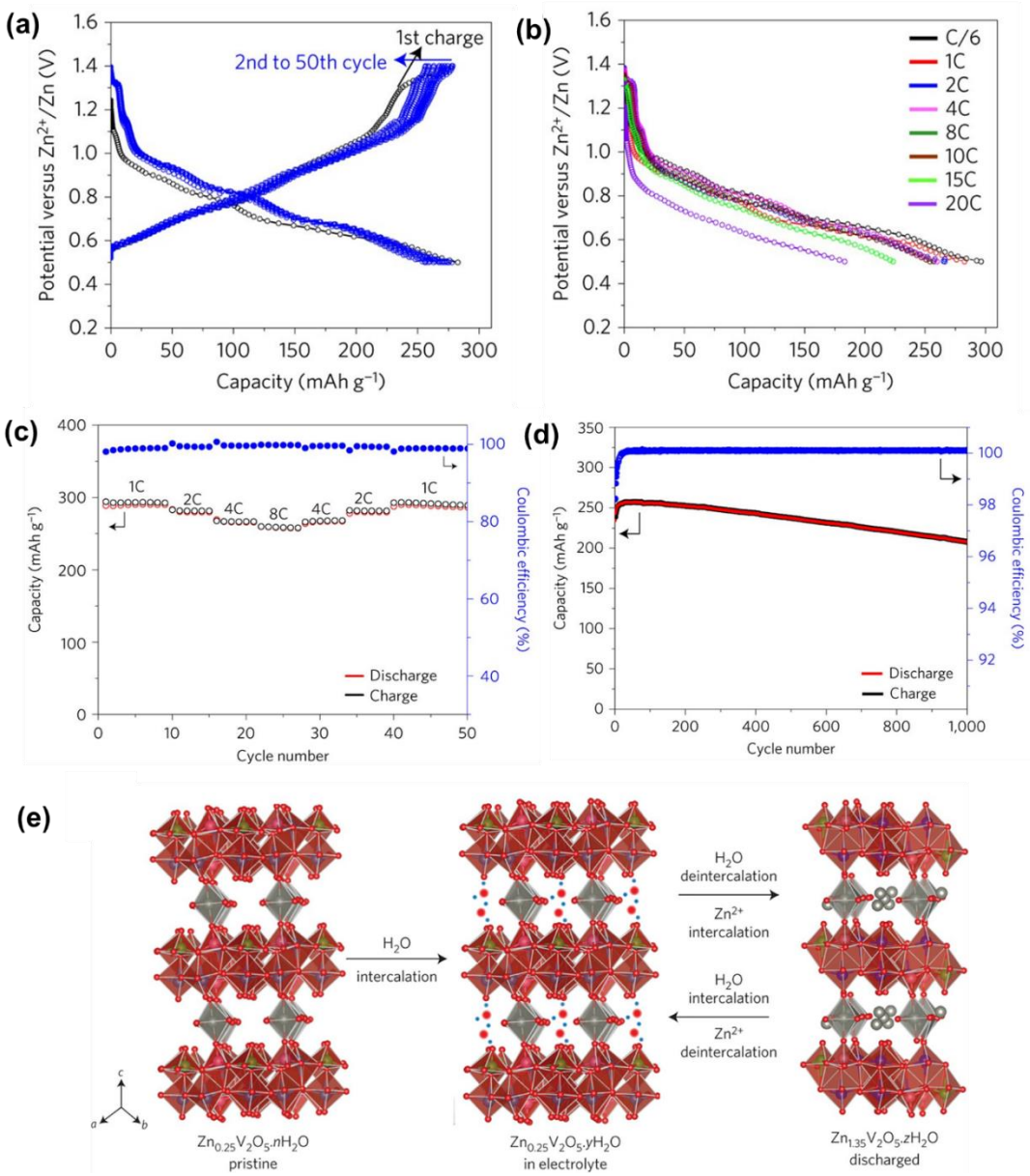


**Figure 1.39. (a)** Galvanostatic discharge-charge profiles of the $Zn_{0.25}V_2O_5 \cdot nH_2O$ cathode at a 1 C rate, **(b)** Galvanostatic discharge profiles at different C rates (1 C = 300 mA $g^{-1}$), **(c)** Rate capability at various C rates, **(d)** Cycling stability and the corresponding coulombic efficiency at an 8 C rate (i.e., 2.4 A $g^{-1}$), **(e)** Scheme exhibiting reversible water intercalation into $Zn_{0.25}V_2O_5 \cdot nH_2O$ immersed in electrolyte/$H_2O$, and the water de-intercalation accompanying $Zn^{2+}$ intercalation upon electrochemical discharge. Reproduced from [323].

By replacing Zn ions with Ca ions, this work was further extended to a new cathode material (i.e., $Ca_{0.25}V_2O_5 \cdot nH_2O$) [324]. Owing to the larger ionic radius of $Ca^{2+}$ (1.00

Å) than $Zn^{2+}$ (0.74 Å), the expanded interlayer spacing in the crystal structure enhanced the ionic conductivity. Additionally, $Ca_{0.25}V_2O_5{\cdot}nH_2O$ exhibited higher electrical conductivity than that of $Zn_{0.25}V_2O_5{\cdot}nH_2O$. It delivered a high capacity of 340 mAh $g^{-1}$, 289 mAh $g^{-1}$ and 72 mAh $g^{-1}$ at 0.2 C, 1 C and 80 C, respectively. Also, it showed excellent stability with 96% capacity retention after 3000 cycles at 80 C. Furthermore, He and co-workers [325] replaced $Zn^{2+}$ ions in the layered galleries of $Zn_{0.25}V_2O_5$ with $Na^+$ ions to prepare sodium-ion-stabilized vanadium oxide ($Na_{0.33}V_2O_5$) nanowires, which delivered a high capacity of 367.1 mA h $g^{-1}$ at 0.1 A $g^{-1}$ and exhibited cycling stability with a capacity retention of 93% after 1000 cycles.

Yan and co-workers [326] reported a detailed investigation of the role of $H_2O$ in bilayer $V_2O_5{\cdot}nH_2O$ ($n \geq 1$) as a prototype cathode material for zinc ion batteries. It was discovered that the solvating $H_2O$ with charge shielding reduced the effective charges of $Zn^{2+}$ ions, thus lowering the electrostatic interactions between $Zn^{2+}$ and the $V_2O_5$ host structure and facilitating ion transport. A high capacity of 372 mAh $g^{-1}$ was obtained at 0.3 A $g^{-1}$ and a capacity of 248 mAh $g^{-1}$ was still achievable at 30 A $g^{-1}$. The battery based on $V_2O_5{\cdot}nH_2O$ cathode exhibited a capacity retention of 71% after 900 cycles at 6 A $g^{-1}$, while the counterpart $V_2O_5$ without structural water exhibited a low initial capacity of 157 mAh $g^{-1}$ and rapidly decreased to 78 mAh $g^{-1}$ after 50 cycles at 6 A $g^{-1}$.

Although great advances in vanadium-based cathode materials have been achieved in terms of capacity, rate performance and cycling stability, a relatively low operating voltage of the batteries can be one of the primary drawbacks. This can inevitably give rise to low energy density of the final device. It also should be further noted that vanadium-based materials are toxic and have low environmental compatibility.

### 1.3.3 Aqueous zinc-ion hybrid supercapacitors

In recent years, hybrid supercapacitors have attracted extensive research interest due to their enhanced performance in terms of energy densities without significantly lowering

their power densities [121, 327, 328]. They are expected to bridge the energy gap between batteries and supercapacitors, as shown in Figure 1.41. There is no unambiguous definition about a hybrid supercapacitor. Generally, a hybrid supercapacitor is considered as a device in which two electrodes operate under different charge-storage mechanisms. One is capacitor-type electrode, while the other one is battery-type electrode. The terms such as “asymmetric supercapacitors” and “hybrid supercapacitors” have been comparably employed in some cases. In fact, the term of “asymmetric supercapacitors” is proposed to differentiate from the standard “symmetric supercapacitors” based on congruent electrode materials in both electrodes. Generally, “asymmetric supercapacitors” should cover a wider range of devices in comparison to “hybrid supercapacitors”.

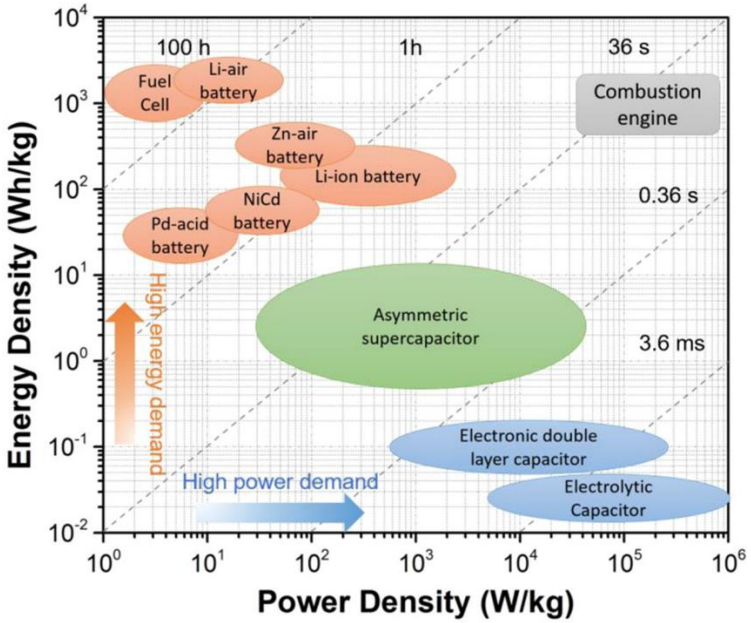


**Figure 1.40.** Ragone plot illustrating the performances of specific power vs. specific energy for various electrical energy-storage technologies. Reproduced from [121].

The comparison of different metal anodes is shown in Table 1.3. Compared with other metal anodes such as Li, Na, K, Mg and Ca, Zn anode shows great advantages in terms of volumetric capacity and cost. More importantly, the Zn anode is stable in aqueous electrolytes, while other metals cannot be directly employed as anode materials in

aqueous electrolytes, leading to a complicated fabrication process. Although Al anode is cheaper and has a higher volumetric capacity than Zn anode, its application in aqueous electrolytes is hindered by anode corrosion and hydrogen evolution reaction associated with the aqueous electrolytes.

**Table 1.3.** A compasiron of different metal anodes in various aspects [329]

| | **Li** | **Na** | **K** | **Mg** | **Ca** | **Zn** | **Al** |
|---|---|---|---|---|---|---|---|
| Valence | +1 | +1 | +1 | +2 | +2 | +2 | +3 |
| Atomic weight | 6.94 | 22.99 | 39.10 | 24.30 | 40.30 | 65.41 | 26.98 |
| Cation radius (Å) | 0.76 | 1.02 | 1.38 | 0.72 | 0.99 | 0.74 | 0.535 |
| Standard potential (V) | -3.05 | -2.71 | -2.93 | -2.35 | -2.84 | -0.76 | -1.67 |
| Gravimetric Capacity (mAh $g^{-1}$) | 3862 | 1166 | 685 | 2205 | 1340 | 820 | 2980 |
| Volumetric Capacity (mAh $mL^{-1}$) | 2062 | 1128 | 591 | 3832 | 2060 | 5857 | 8046 |
| Abundance (ppm) | 18 | 22700 | 18400 | 23000 | 41000 | 75 | 82000 |
| Cost (USD $kg^{-1}$) | 19.2 | 3.1 | 13.1 | 2.2 | 2.4 | 2.2 | 1.9 |

Among various hybrid supercapacitors such as Li-ion supercapacitors [330] and Na-ion batteries [331], aqueous zinc ion hybrid supercapacitors are considered as a type of promising energy storage device due to relatively high energy densities, high safety, low cost and environmental friendliness [332, 333]. Generally, a typical aqueous zinc ion hybrid supercapacitor is composed of a capacitor-type carbon-based cathode (e.g., activated carbon (AC), carbon nanotube and graphene), a battery-type Zn anode and a $Zn^{2+}$-containing electrolyte (e.g., $ZnSO_4$, $Zn(CF_3SO_3)_2$ and $ZnCl_2$), as shown in Figure 1.42.

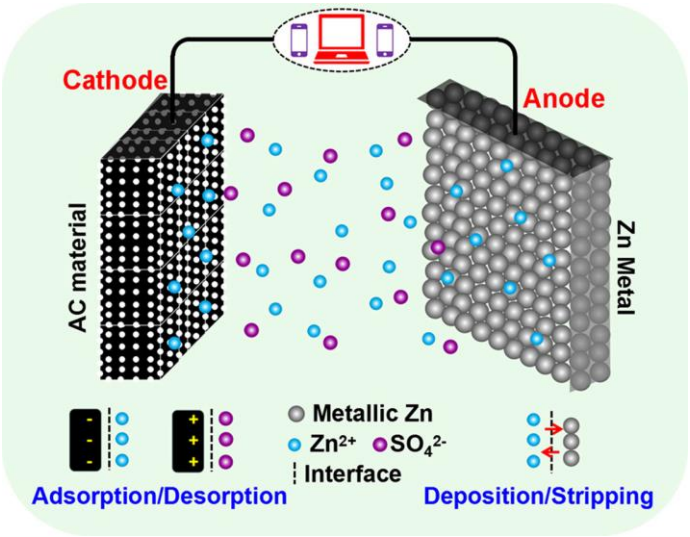


**Figure 1.41.** Schematic of AC//$ZnSO_4$ (aq)//Zn energy storage system. AC is used as cathode, Zn foil severs as anode and 2 M $ZnSO_4$ aqueous solution is employed as electrolyte. Reproduced from [334].

In 2016, Wang and co-workers reported the first zinc ion hybrid supercapacitor comprised of oxidized carbon nanotubes cathode, Zn anode and $ZnSO_4$ electrolyte, which exhibited a low specific capacitance of 53 F $g^{-1}$ at 10 mV $s^{-1}$ operating in the range of 0 V to 1.8 V [335]. Then, in 2018 the electrochemical performance of this device was further improved by Kang et al. using activated carbon (AC) as a cathode material [334]. The device (AC//$ZnSO_4$ (aq)//Zn) delivered a capacity of 121 mAh $g^{-1}$ in the voltage range of 0.2 V to 1.8 V and exhibited good cyclability with a capacity retention of 91% after 10000 cycles as well as an energy density of 84 Wh $kg^{-1}$ at a power density of 69 W $kg^{-1}$. The overall capacitance is determined by the carbon-based cathode, which mainly involves the physical adsorption and desorption of electrolyte ions. Therefore, one of the key issues associated with zinc ion hybrid supercapacitors is to rationally design the microstructure of carbon-based materials and develop novel cathode materials with low cost and high performance.

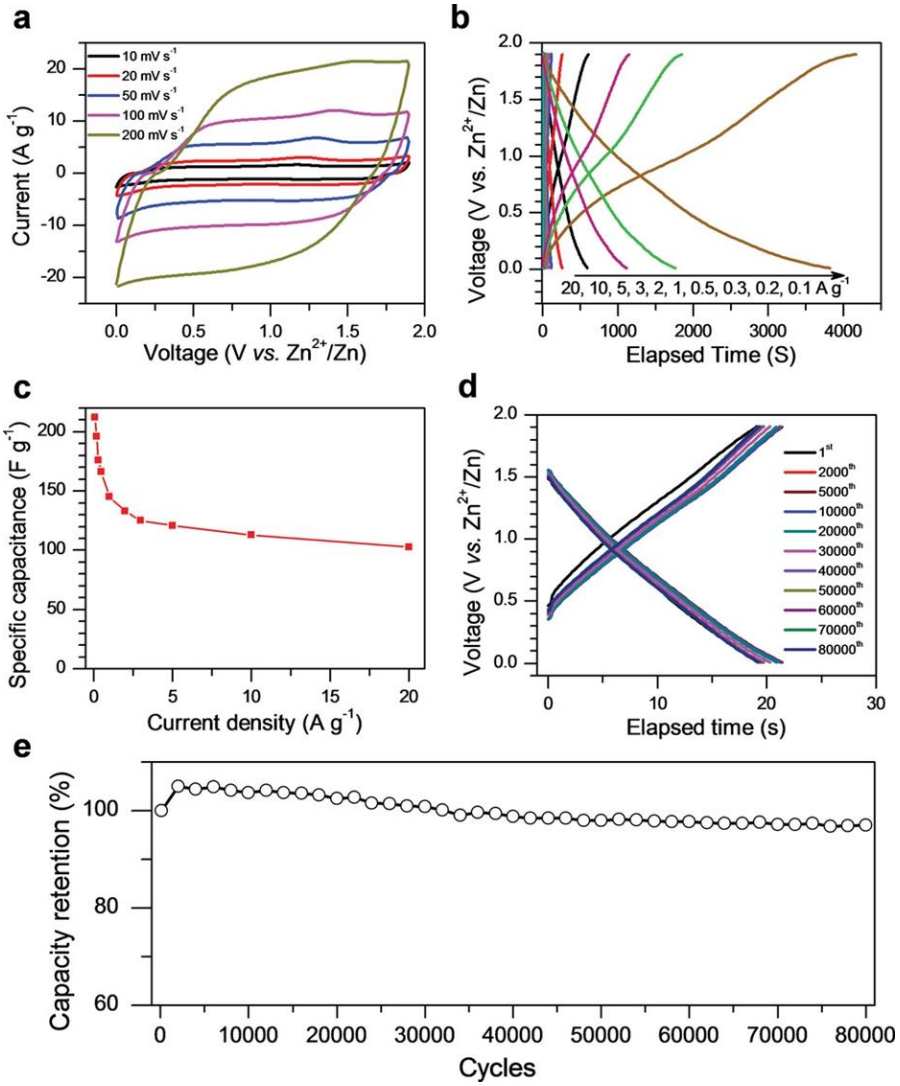


**Figure 1.42.** Electrochemical performance of the Zn-CAG hybrid supercapacitor in 3 M $Zn(CF_3SO_3)_2$ electrolyte. **(a)** Cyclic voltammetry as a function of scan rate, **(b)** Galvanostatic charge-discharge curves at various current densities, **(c)** Rate capability, **(d)** Galvanostatic charge-discharge curves recorded after specific cycles at 8 A $g^{-1}$, **(e)** Cycling stability cycled at 8 A $g^{-1}$. Reproduced from [336].

For example, Zhang and co-workers [336] prepared porous carbon derived from chemically-activated graphene (CAG) to construct a zinc ion hybrid supercapacitor. The cell using 3 M $Zn(CF_3SO_3)_2$ electrolyte demonstrated a wide operating voltage ranging from 0 to 1.9 V, an energy density of 106.3 Wh $kg^{-1}$ and a power density of 31.4 kW $kg^{-1}$. Additionally, ultralong stability was achieved with a capacity retention of 93% after 80000 cycles, as shown in Figure 1.43. Lu and co-workers [337]

synthesized a novel N-doped hierarchically porous carbon (denoted as HNPC) by employing furfuryl alcohol as carbon precursor and zeolite NaY as template via a modified isostatic pressure-assisted impregnation process and subsequent thermal treatment under an atmosphere of $NH_3$, as shown in Figure 1.44. The zinc ion hybrid supercapacitors based on HNPC demonstrated a high capacity of 177.8 mAh $g^{-1}$ at 4.2 A $g^{-1}$, much higher than that (67.8 mAh $g^{-1}$) of the counterpart porous carbon (PC) due to the good conductivity, improved surface wettability and enhanced electrochemically active sites. Moreover, long-term cyclability was obtained with a capacity retention of 99.7% after 20000 cycles (≈73.6% capacity retention after 100000 cycles).

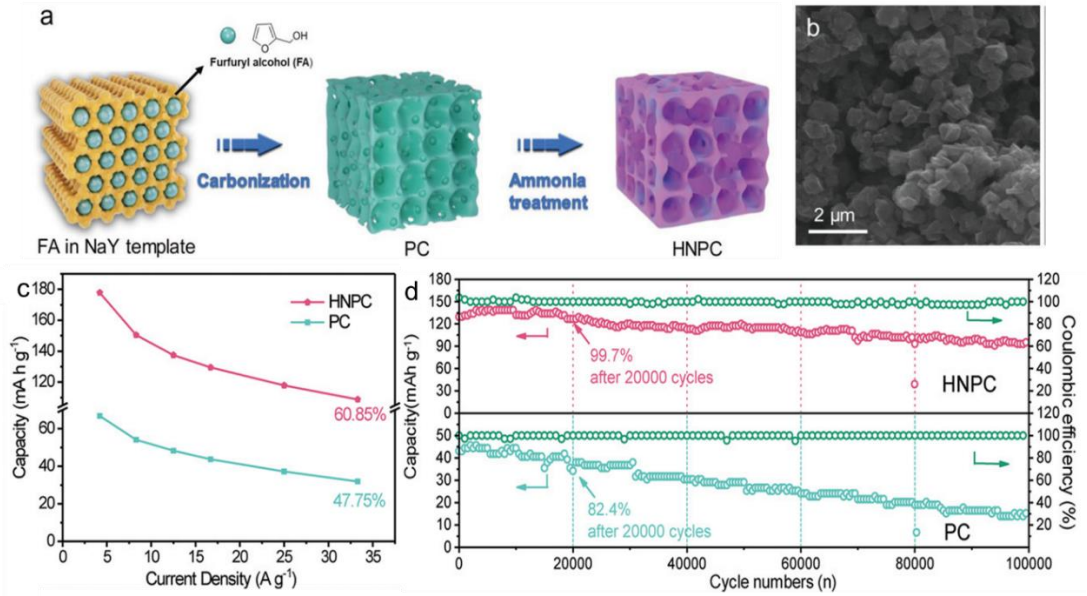


**Figure 1.43. (a)** Schematic illustration of the synthesis route of the HNPC, **(b)** SEM image of HNPC, **(c)** Specific capacitances and rate performance at different current densities, **(d)** Cycling stability at 16.7 A $g^{-1}$. Reproduced from [337].

**Table 1.4.** Performance comparison of recently reported zinc-ion hybrid supercapacitors with various cathode materials. Reproduced from [332].

| Positive electrode materials | Electrolyte | Potential (V) | Specific capacitance ($F\ g^{-1}$) | Cyclability | Energy density ($Wh\ kg^{-1}$) | Power density ($kW\ kg^{-1}$) | Reference |
|---|---|---|---|---|---|---|---|
| oCNT | $ZnSO_4$/PVA hydrogel | 0-1.8 | 53 (10 $mV\ s^{-1}$) | 100% (5000 cycles) | - | - | [335] |
| AC | $ZnSO_4$ | 0.2-1.8 | 272 (0.1 $A\ g^{-1}$) | 91% (10000 cycles) | 84 | 14.9 | [334] |
| CAG | $Zn(CF_3SO_3)_2$ | 0-1.9 | 210 (0.1 $A\ g^{-1}$) | 93% (80000 cycles) | 106 | 31.4 | [336] |
| HNPC | $ZnSO_4$ | 0-1.8 | 356 (4.2 $A\ g^{-1}$) | 99.7% (20000 cycles) | 107 | 24.9 | [337] |
| AC | $Zn(CF_3SO_3)_2$ in acetonitrile | 0-1.8 | 170 (0.1 $A\ g^{-1}$) | 91% (20000 cycles) | 53 | 1.7 | [338] |
| AC | $ZnSO_4$/PVA hydrogel | 0.2-1.8 | 468 (0.5 $A\ g^{-1}$) | 99% (10000 cycles) | 208 | 0.50 | [339] |
| HPC | $ZnSO_4$/$NaSO_4$ | 0.01-1.8 | 613 (0.1 $A\ g^{-1}$) | 94.9% (20000 cycles) | 118 | 3.2 | [340] |
| MCHSs | $ZnSO_4$ | 0.2-1.8 | 393 (0.1 $A\ g^{-1}$) | 96% (10000 cycles) | 129 | 13.7 | [341] |
| HCSs | $ZnSO_4$/polyacrylamide hydrogel | 0.15-1.95 | 174 (0.5 $A\ g^{-1}$) | 98% (15000 cycles) | 60 | 0.45 | [342] |
| LDC | $ZnSO_4$/gelatin hydrogel | 0.2-1.8 | 287 (0.5 $A\ g^{-1}$) | 81.3% (6500 cycles) | 98 | 12.2 | [343] |
| OPC | $ZnSO_4$/gelatin hydrogel | 0.2-1.8 | 299 (0.2 $A\ g^{-1}$) | 87.6% (10000 cycles) | 82 | 3.8 | [344] |
| N-HPC | $ZnSO_4$ | 0.2-1.8 | 308 (0.1 $A\ g^{-1}$) | 90.9% (5000 cycles) | 191 | 3.6 | [345] |
| MDC | $ZnSO_4$ | 0.1-1.7 | 123 (0.2 $A\ g^{-1}$) | 99% (20000 cycles) | 36 | 85.5 | [346] |
| PCNF | $ZnSO_4$ | 0.1-1.7 | 243 (0.5 $A\ g^{-1}$) | 90% (10000 cycles) | 142 | 15.4 | [347] |
| AC | $ZnSO_4$ | 0.5-1.5 | 259 (0.05 $A\ g^{-1}$) | 100% (10000 cycles) | 23 | 0.78 | [348] |
| AC | $ZnSO_4$ hydrogel | 1.4-2.4 | 1010 (0.25 $A\ g^{-1}$) | 85.9% (10000 cycles) | 287 | 1.9 | [349] |
| RG-R | $ZnSO_4$ | 0.2-1.6 | 371 (0.1 $A\ g^{-1}$) | 94.5% (10000 cycles) | 101 | 0.07 | [350] |
| MXene-rGO aerogel | $ZnSO_4$ | 0.2-1.6 | 129 (0.4 $A\ g^{-1}$) | 95% (75000 cycles) | 35 | 4.0 | [351] |

Abbreviation: oCNT, oxidized carbon nanotube; AC, activated carbon; CAG, chemically activated graphene; HPC, hierarchical porous carbon; MCHS, mesoporous carbon hollow sphere; HCS, hollow carbon spheres; HNPC, N-doped hierarchically porous carbon; LDC, layered B/N co-doped porous carbon; OPC, oxygen-enriched porous carbon; RG-R, reduced graphene oxide foam; rGO, reduced graphene oxides; N-HPC, N-doped hierarchical porous carbon; MDC, metal–organic framework derived carbon; PCNF, porous carbon nanoflakes.

More electrochemical performance of carbon-based materials for zinc ion hybrid supercapacitors is compared and summarized in Table 1.4. Considering that their electrochemical performance is mainly determined by the cathode materials and this research area is still in its infancy, this type of devices can be further developed by the design and synthesis of more novel cathode materials, such as biomass-derived carbon materials and composites constructed by two-dimensional materials with three-dimensional materials. Additionally, novel electrolytes like “water-in-salt” can be explored to further expand the operation window, thus effectively enhancing the output energy density.

## 1.4 Motivation and Objectives

Electrochemical energy storage devices, such as batteries and supercapacitors, play a critical role in exploiting the electricity generated from renewable but intermittent energy sources such as wind and solar energy. Lithium-ion batteries have gained a dominant role in the rechargeable battery market due to their high energy density and good cycling stability. However, their high cost, safety concerns and environmental issues significantly hamper their wider penetration in large-scale applications, thus driving the development of alternative battery chemistries such as Na-ion batteries, K-ion batteries, Al-ion batteries and Zn-ion batteries. Among them, aqueous zinc ion batteries such as Zn-$MnO_2$ batteries are attracting significant attention as novel energy storage devices due to their high safety, low cost and environmental friendliness. However, the reaction mechanism of Zn-$MnO_2$ batteries is controversial. Therefore, it is important and interesting to reveal the underlying mechanism. Unlike batteries, supercapacitors (especially EDLCs) store charges at or near the surface of the active materials and can deliver energy in a short time, thus providing high power densities and low energy densities. However, their wider applications have been limited by the low energy densities (ca.10 Wh $kg^{-1}$). Additionally, current commercial supercapacitors use organic electrolytes which also have concerns in terms of environmental and safety as well as cost. Therefore, it is also of great importance to

develop high energy density, low-cost and environmentally friendly supercapacitors without sacrificing the merits in terms of power densities and cycle life. Constructing better energy storage devices not only relies on the properties of the electrode materials and electrolytes but also depends significantly on the configuration of the devices. Zinc ion hybrid supercapacitors, as novel energy storage devices, are emerging in recent years. The corresponding mechanism and electrode materials used in this type of hybrid supercapacitor have been investigated and explored.

In summary, the aim of this thesis is to investigate zinc-based electrochemical energy storage devices in terms of reaction mechanism and improvement of their electrochemical performance by exploring advanced cathode materials used in this type of device. It is expected to facilitate better understanding of the underlying science and accelerate the industrial development of zinc-based electrochemical energy devices based on various cathode materials. The detailed objectives are outlined as follows:

In Chapter 3, the reaction mechanism of rechargeable aqueous Zn-$MnO_2$ batteries have been investigated. Primary alkaline batteries have been commercialized for many years. To make this type of battery rechargeable, the alkaline electrolyte has been replaced by a mild neutral electrolyte, i.e., $ZnSO_4$, to construct rechargeable aqueous Zn-$MnO_2$ batteries. Although remarkable developments have been achieved in Zn-$MnO_2$ batteries using mild aqueous electrolytes, the mechanism of the Zn-$MnO_2$ battery is not fully understood and remains controversial. In-depth understanding of the mechanism in Zn-$MnO_2$ batteries is of importance in optimizing the battery chemistry in terms of performance and lifetime and thus promoting the large-scale application of this type of battery.

In Chapter 4, the voltage range and self-discharge of zinc ion hybrid supercapacitors have been systematically investigated. Despite great advances in zinc ion hybrid supercapacitors by developing various carbon-based materials, to the best of our knowledge, the potential window and self-discharge of this hybrid device has not been investigated in detail. Considering that the potential window is crucial to the energy output and lifespan of supercapacitors, and high self-discharge rates compromise their

practical value, it is necessary to perform a comprehensive and systematic investigation of the potential window and self-discharge in the zinc ion hybrid supercapacitors.

In Chapter 5, polypyrrole (PPy), as an important type of electrode material, has not been explored significantly in the context of zinc ion hybrid supercapacitors. To date, only a few papers reported using PPy in zinc-based supercapacitors. Nevertheless, the electrochemical performance based on PPy is not satisfactory and the reaction mechanism of this hybrid supercapacitors based on PPy materials is not well understood. Therefore, the highly interconnected three-dimensional composite electrodes composed of PPy and electrochemical graphene oxide (EGO) were produced by using a facile one-step electrochemical polymerization to further improve the electrochemical performance and reveal the reaction mechanism of the zinc-ion hybrid supercapacitors based on PPy/EGO composite electrode.

In Chapter 6, considering the transformation from a fossil fuel-based society to a renewable resource-based sustainable society, it is urgent and important to develop electrode materials via a facile and green way to alleviate the energy crisis and reduce carbon dioxide emissions. Herein, to make the full use of greenhouse gas, $CO_2$ was selected as an activating agent to prepare hierarchically porous carbon derived from biomass. The as-prepared materials with different pore structures and specific surface areas were further used for aqueous zinc-ion hybrid supercapacitors. The excellent combination of the sustainable electrode materials with safe and environmentally friendly energy storage device is expected to provide promising solutions on the growing environmental concerns and increasing energy demand.

## References

[1] Y. Nishi, J. Power Sources, 100 (2001) 101-106.

[2] Z. Yang, R. Li, Z. Deng, Sci. Rep., 8 (2018) 1-8.

[3] M. Okubo, E. Hosono, J. Kim, M. Enomoto, N. Kojima, T. Kudo, H. Zhou, I. Honma, J. Am. Chem. Soc., 129 (2007) 7444-7452.

[4] A.R. Armstrong, P.G. Bruce, Nature 381 (1996) 499-500.

[5] N. Yabuuchi, T. Ohzuku, J. Power Sources, 119-121 (2003) 171-174.

[6] Y. Zhang, Q.-y. Huo, P.-p. Du, L.-z. Wang, A.-q. Zhang, Y.-h. Song, Y. Lv, G.-y. Li, Synth. Met., 162 (2012) 1315-1326.

[7] C. Mao, M. Wood, L. David, S.J. An, Y. Sheng, Z. Du, H.M. Meyer, R.E. Ruther, D.L. Wood, J. Electrochem. Soc., 165 (2018) A1837-A1845.

[8] S.K. Heiskanen, J. Kim, B.L. Lucht, Joule, 3 (2019) 2322-2333.

[9] H. Wang, X. Li, F. Li, X. Liu, S. Yang, J. Ma, Electrochem. commun., 122 (2021) 106870.

[10] C. Liu, Z.G. Neale, G. Cao, Mater. Today, 19 (2016) 109-123.

[11] M. Winter, B. Barnett, K. Xu, Chem. Rev., 118 (2018) 11433-11456.

[12] M.S. Whittingham, J. Chem. Soc., Chem. Commun., (1974) 328-329.

[13] M.S. Whittingham, F.R.G. Jr, Mater. Res. Bull., 10 (1975) 363-371.

[14] M.S. Whittingham, J. Electrochem. Soc., 122 (1975) 713-714.

[15] M.S. Whittingham, J. Electrochem. Soc., 123 (1976) 315-319.

[16] J. Besenhard, R. Schöllhorn, J. Electrochem. Soc., 124 (1977) 968-971.

[17] M.S. Whittingham, Prog. Solid State Chem., 12 (1978) 41-99.

[18] M.S. Whittingham, A. Yoshino, (2019).

[19] W. RUDORFF, Chimia, 19 (1965) 489-499.

[20] M.S. Whittingham, J. Chem. Soc., Chem. Commun., 9 (1974 ) 328-329.

[21] M.S. Whittingham, Science, 192 (1976) 1126-1127.

[22] B.M.I. Rao, R.W. Francis, H.A. Christopher, J. Electrochem. Soc., 124 (1977) 1490-1492.

[23] J. Dahn, R.R. Haering, Mater. Res. Bull., 14 (1979) 1259-1262.

[24] M. Py, R. Haering, Can. J. Phys., 61 (1983) 76-84.

[25] K. Brandt, F. Laman, J. Power Sources, 25 (1989) 265-276.

[26] K. Mizushima, P.C. Jones, P.J. Wiseman, J.B. Goodenough, Mater. Res. Bull., 15 (1980) 783-789.

[27] K. MIZUSHIMA, P.C. JONES, P.J. WISEMAN, J.B. GOODENOUGH, Solid

State Ion., 3 (1981) 171-174.

[28] J.B. Goodenough, K. Mizuchima, U.S. Patent No. 4,302,518. , (1981).

[29] Y. Li, Y. Lu, P. Adelhelm, M.M. Titirici, Y.S. Hu, Chem. Soc. Rev., 48 (2019) 4655-4687.

[30] J.O. Besenhard, H.P. Fritz, Angew. Chem. Int. Ed., 22 (1983) 950-975.

[31] W. Rüdorff, U. Hofmann, Allg. Chem. , 238 (1938) 1-50.

[32] J. Xie, Y.C. Lu, Nat. Commun., 11 (2020) 2499.

[33] A. Manthiram, Nat. Commun., 11 (2020) 1550.

[34] L. Yang, K. Yang, J. Zheng, K. Xu, K. Amine, F. Pan, Chem. Soc. Rev., 49 (2020) 4667-4680.

[35] P. He, H. Yu, D. Li, H. Zhou, J. Mater. Chem., 22 (2012) 3680-3695.

[36] Y. Lyu, X. Wu, K. Wang, Z. Feng, T. Cheng, Y. Liu, M. Wang, R. Chen, L. Xu, J. Zhou, Y. Lu, B. Guo, Adv. Energy Mater., 11 (2020) 2000982.

[37] J. Molenda, A. Stokłosa, T. Bąk, Solid State Ionics, 36 (1989) 53-58.

[38] A. Honders, J.M.d. Kinderen, A.H.v. Heeren, J.H.W.d. Wit, G.H.J. Broers, Solid State Ion., 15 (1985) 265-276.

[39] G.G. Amatucci, J.M. Tarascon, L.C. Klein, Solid State Ion., 83 (1996) 167-173.

[40] J. Qian, L. Liu, J. Yang, S. Li, X. Wang, H.L. Zhuang, Y. Lu, Nat. Commun., 9 (2018) 4918.

[41] L. Wang, J. Ma, C. Wang, X. Yu, R. Liu, F. Jiang, X. Sun, A. Du, X. Zhou, G. Cui, Adv. Sci., 6 (2019) 1900355.

[42] J.-N. Zhang, Q. Li, C. Ouyang, X. Yu, M. Ge, X. Huang, E. Hu, C. Ma, S. Li, R. Xiao, W. Yang, Y. Chu, Y. Liu, H. Yu, X.-Q. Yang, X. Huang, L. Chen, H. Li, Nat. Energy, 4 (2019) 594-603.

[43] C.M. Julien, A. Mauger, K. Zaghib, H. Groult, Inorganics, 2 (2014) 132-154.

[44] K. Märker, P.J. Reeves, C. Xu, K.J. Griffith, C.P. Grey, Chem. Mater., 31 (2019) 2545-2554.

[45] M.J. Lee, S. Lee, P. Oh, Y. Kim, J. Cho, Nano Lett., 14 (2014) 993-999.

[46] K.Y. Chung, H.S. Lee, W.-S. Yoon, J. McBreen, X.-Q. Yang, J. Electrochem. Soc.,

153 (2006) A774-A780.

[47] L. Xuewu, W. Xiaojuan, C. Shuhua, T. Jie, Mater. Today: Proc., 3 (2016) 672-680.

[48] S. Bhuvaneswari, U.V. Varadaraju, R. Gopalan, R. Prakash, Electrochim. Acta, 301 (2019) 342-351.

[49] Y. Liu, J. Lv, Y. Fei, X. Huo, Y. Zhu, Ionics, 19 (2013) 1241-1246.

[50] A.K. Padhi, K.S. Nanjundaswamy, J.B. Goodenough, J. Electrochem. Soc., 144 (1997) 1188.

[51] J. Hu, W. Huang, L. Yang, F. Pan, Nanoscale, 12 (2020) 15036-15044.

[52] S.Y. Chung, J.T. Bloking, Y.M. Chiang, Nat. Mater., 1 (2002) 123-128.

[53] R. Malik, D. Burch, M. Bazant, G. Ceder, Nano Lett., 10 (2010) 4123-4127.

[54] T.-F. Yi, X.-Y. Li, H. Liu, J. Shu, Y.-R. Zhu, R.-S. Zhu, Ionics, 18 (2012) 529-539.

[55] J. Wang, X. Sun, Energy Environ. Sci., 5 (2012) 5163-5185.

[56] Z.-X. Chi, W. Zhang, F.-Q. Cheng, J.-T. Chen, A.-M. Cao, L.-J. Wan, RSC Adv., 4 (2014) 7795-7798.

[57] J.-N. Zhu, W.-C. Li, F. Cheng, A.-H. Lu, J. Mater. Chem. A, 3 (2015) 13920-13925.

[58] V. Aravindan, J. Gnanaraj, Y.-S. Lee, S. Madhavi, J. Mater. Chem. A, 1 (2013) 3518-3539.

[59] D. Deng, Energy Sci. Eng., 3 (2015) 385-418.

[60] B.N. Loeffler, D. Bresser, S. Passerini, M. Copley, Johnson Matthey Technol. Rev. , 59 (2015) 34-44.

[61] J. Lu, Z. Chen, F. Pan, Y. Cui, K. Amine, Electrochem. Energ. Rev., 1 (2018) 35-53.

[62] Y.P. Wu, E. Rahm, R. Holze, J. Power Sources, 114 (2003) 228-236.

[63] Y. Nishi, J. Power Sources, 100 (2001) 101-106.

[64] Y. Nishi, Chem. Rec., 1 (2001) 406-413.

[65] A. Dey, B. Sullivan, J. Electrochem. Soc., 117 (1970) 222.

[66] J.O. Besenhard, H.P. Fritz, J. Electroanal. Chem. Interf. Electrochem., 53 (1974) 329-333.

[67] J.O. BESENHARD, Carbon 14 (1976) 111-115.

[68] A.N. Dey, B.P. Sullivan, J. Electrochem. Soc., 117 (1970) 222.

[69] J. Wang, K.K. Manga, Q. Bao, K.P. Loh, J. Am. Chem. Soc., 133 (2011) 8888-8891.

[70] M. Endo, C. Kim, K. Nishimura, T. Fujino, K. Miyashita, Carbon, 38 (2000) 183-197.

[71] H. Zheng, Q. Qu, L. Zhang, G. Liu, V.S. Battaglia, RSC Adv., 2 (2012) 4904-4912.

[72] X. Dou, I. Hasa, D. Saurel, C. Vaalma, L. Wu, D. Buchholz, D. Bresser, S. Komaba, S. Passerini, Mater. Today, 23 (2019) 87-104.

[73] J. Asenbauer, T. Eisenmann, M. Kuenzel, A. Kazzazi, Z. Chen, D. Bresser, Sustain. Energy Fuels, 4 (2020) 5387-5416.

[74] E. Ferg, R.J. Gummow, A.d. Kock, J. Electrochem. Soc., 141 (1994) L147-L150.

[75] I. Belharouak, G.M. Koenig, K. Amine, J. Power Sources, 196 (2011) 10344-10350.

[76] L. Cheng, J. Yan, G.-N. Zhu, J.-Y. Luo, C.-X. Wang, Y.-Y. Xia, J. Mater. Chem., 20 (2010) 595-602.

[77] A.S. Prakash, P. Manikandan, K. Ramesha, M. Sathiya, J.M. Tarascon, A.K. Shukla, Chem. Mater., 22 (2010) 2857-2863.

[78] T.-F. Yi, S.-Y. Yang, Y. Xie, J. Mater. Chem. A 3 (2015) 5750-5777.

[79] A.S. Aricò, P. Bruce, B. Scrosati, J.-M. Tarascon, W.v. Schalkwijk, Nat. Mater., 4 (2005) 366-377.

[80] E. Kang, Y.S. Jung, G.-H. Kim, J. Chun, U. Wiesner, A.C. Dillon, J.K. Kim, J. Lee, Adv. Funct. Mater., 21 (2011) 4349-4357.

[81] X. Jia, Y. Kan, X. Zhu, G. Ning, Y. Lu, F. Wei, Nano Energy, 10 (2014) 344-352.

[82] C. Han, Y.-B. He, M. Liu, B. Li, Q.-H. Yang, C.-P. Wong, F. Kang, J. Mater. Chem. A 5 (2017) 6368-6381.

[83] X. Lu, L. Gu, Y.S. Hu, H.C. Chiu, H. Li, G.P. Demopoulos, L. Chen, J. Am. Chem. Soc., 137 (2015) 1581-1586.

[84] W. Li, X. Li, M. Chen, Z. Xie, J. Zhang, S. Dong, M. Qu, Electrochim. Acta, 139 (2014) 104-110.

[85] A.K. Shukla, T.P. Kumar, Curr. Sci., 94 (2008) 314-331.

[86] W.-J. Zhang, J. Power Sources, 196 (2011) 13-24.

[87] J. Liu, P. Kopold, P.A. van Aken, J. Maier, Y. Yu, Angew. Chem. Int. Ed., 127 (2015) 9768-9772.

[88] U. Kasavajjula, C. Wang, A.J. Appleby, J. Power Sources, 163 (2007) 1003-1039.

[89] C.K. Chan, R. Ruffo, S.S. Hong, Y. Cui, J. Power Sources, 189 (2009) 1132-1140.

[90] W. Qi, J.G. Shapter, Q. Wu, T. Yin, G. Gao, D. Cui, J. Mater. Chem. A 5 (2017) 19521-19540.

[91] M.T. McDowell, S.W. Lee, W.D. Nix, Y. Cui, Adv. Mater., 25 (2013) 4966-4985.

[92] H. Wu, Y. Cui, Nano Today, 7 (2012) 414-429.

[93] M.T. McDowell, I. Ryu, S.W. Lee, C. Wang, W.D. Nix, Y. Cui, Adv. Mater., 24 (2012) 6034-6041.

[94] M. Gu, Y. Li, X. Li, S. Hu, X. Zhang, W. Xu, S. Thevuthasan, D.R. Baer, J.-G. Zhang, J. Liu, C. Wang, ACS Nano, 6 (2012) 8439-8447.

[95] C.K. Chan, H. Peng, G. Liu, K. McIlwrath, X.F. Zhang, R.A. Huggins, Y. Cui, Nat. Nanotechnol., 3 (2008) 31-35.

[96] H. Wu, G. Chan, J.W. Choi, I. Ryu, Y. Yao, M.T. McDowell, S.W. Lee, A. Jackson, Y. Yang, L. Hu, Y. Cui, Nat. Nanotechnol., 7 (2012) 310-315.

[97] J. Cabana, L. Monconduit, D. Larcher, M.R. Palacin, Adv. Mater., 22 (2010) E170-E192.

[98] X. Xu, W. Liu, Y. Kim, J. Cho, Nano Today, 9 (2014) 604-630.

[99] X.-Y. Yu, L. Yu, X.W.D. Lou, Adv. Energy Mater., 6 (2016) 1601177.

[100] P. Poizot, S. Laruelle, S. Grugeo, L. Dupont, J.-M. Tarascon, Nature, 407 (2000) 496-499.

[101] Y. Lu, L. Yu, X.W. Lou, Chem, 4 (2018) 972-996.

[102] D. Bresser, S. Passerini, B. Scrosati, Energy Environ. Sci., 9 (2016) 3348-3367.

[103] G. Chen, L. Yan, H. Luo, S. Guo, Adv. Mater., 28 (2016) 7580-7602.

[104] P.G. Bruce, B. Scrosati, J.M. Tarascon, Angew. Chem. Int. Ed., 47 (2008) 2930-2946.

[105] A. Jana, E. Scheer, S. Polarz, Beilstein J Nanotechnol, 8 (2017) 688-714.

[106] H. Zhou, L. Zhang, D. Zhang, S. Chen, P.R. Coxon, X. He, M. Coto, H.K. Kim, K. Xi, S. Ding, Sci. Rep., 6 (2016) 1-11.

[107] H. Wang, L.-F. Cui, Y. Yang, H.S. Casalongue, J.T. Robinson, Y. Liang, Y. Cui, H. Dai, J. Am. Chem. Soc., 132 (2010) 13978-13980.

[108] M.V. Reddy, G.V. Subba Rao, B.V. Chowdari, Chem. Rev., 113 (2013) 5364-5457.

[109] D. Doughty, E.P. Roth, Electrochem Soc Interface, 21 (2012) 37.

[110] X. Wu, K. Song, X. Zhang, N. Hu, L. Li, W. Li, L. Zhang, H. Zhang, Front. Energy Res. , 7 (2019) 65.

[111] X. Feng, M. Ouyang, X. Liu, L. Lu, Y. Xia, X. He, Energy Storage Mater., 10 (2018) 246-267.

[112] X. Feng, S. Zheng, D. Ren, X. He, L. Wang, H. Cui, X. Liu, C. Jin, F. Zhang, C. Xu, H. Hsu, S. Gao, T. Chen, Y. Li, T. Wang, H. Wang, M. Li, M. Ouyang, Appl. Energy, 246 (2019) 53-64.

[113] A. Hammami, N. Raymond, M. Armand, Nature, 301 (2003) 635-636.

[114] Y. Zheng, Y. Yao, J. Ou, M. Li, D. Luo, H. Dou, Z. Li, K. Amine, A. Yu, Z. Chen, Chem. Soc. Rev., 49 (2020) 8790-8839.

[115] W.D. Richards, L.J. Miara, Y. Wang, J.C. Kim, G. Ceder, Chem. Mater., 28 (2015) 266-273.

[116] H. Lee, M. Yanilmaz, O. Toprakci, K. Fu, X. Zhang, Energy Environ. Sci., 7 (2014) 3857-3886.

[117] C. Shi, J. Dai, X. Shen, L. Peng, C. Li, X. Wang, P. Zhang, J. Zhao, J. Membr. Sci., 517 (2016) 91-99.

[118] H. Li, B. Zhang, W. Liu, B. Lin, Q. Ou, H. Wang, M. Fang, D. Liu, S. Neelakandan, L. Wang, Electrochim. Acta, 290 (2018) 150-164.

[119] G. Fang, J. Zhou, A. Pan, S. Liang, ACS Energy Lett., 3 (2018) 2480-2501.

[120] M. Lu, Supercapacitors: materials, systems, and applications, John Wiley & Sons, 2013.

[121] Y. Shao, M.F. El-Kady, J. Sun, Y. Li, Q. Zhang, M. Zhu, H. Wang, B. Dunn, R.B.

Kaner, Chem. Rev., 118 (2018) 9233-9280.
[122] J.L. Heilbron, Electricity in the 17th and 18th centuries: A study of early modern physics, Univ of California Press, 1979.
[123] H.v. Helmholtz, of Scientific Memoirs, 1 (1862) 114.
[124] M. Gouy, (1910).
[125] D.L. Chapman, The London, Edinburgh, and Dublin philosophical magazine and journal of science, 25 (1913) 475-481.
[126] D.C. Grahame, Chem. Rev., 41 (1947) 441-501.
[127] L. Pilon, H. Wang, A. d'Entremont, J. Electrochem. Soc., 162 (2015) A5158-A5178.
[128] L.L. Zhang, X.S. Zhao, Chem. Soc. Rev., 38 (2009) 2520-2531.
[129] R. Ko¨tz, M. Carlen, Electrochim. Acta, 45 (2000) 2483-2498.
[130] C. Hamann, A. Hamnett, W. Vielstich, VCH: New York, 17 (1998) 121.
[131] L. Fumagalli, A. Esfandiar, R. Fabregas, e. al., Science, 360 (2018) 1339-1342.
[132] M.B. Winter, R., Chem. Rev., 104 (2004) 4245-4270.
[133] M. Endo, T. Maeda, T. Takeda, Y.J. Kim, K. Koshiba, H. Hara, M.S. Dresselhaus, J. Electrochem. Soc., 148 (2001) A910-A914.
[134] D. Qu, H. Shi, J. Power Sources, 74 (1998) 99-107.
[135] E. Raymundo-Piñero, K. Kierzek, J. Machnikowski, F. Béguin, Carbon, 44 (2006) 2498-2507.
[136] J. Chmiola, G. Yushin, Y. Gogotsi, C. Portet, P. Simon, P.L. Taberna, Science 313 (2006) 1760-1763.
[137] J. Huang, B.G. Sumpter, V. Meunier, Chemistry, 14 (2008) 6614-6626.
[138] E. Raymundo-Piñero, F. Leroux, F. Béguin, Adv. Mater., 18 (2006) 1877-1882.
[139] J. Gambya., P.L. Tabernaa., P. Simona., J.F. Fauvarquea., M. Chesneaub., J. Power Sources, 101 (2001) 109-116.
[140] H. Shen, E. Liu, X. Xiang, Z. Huang, Y. Tian, Y. Wu, Z. Wu, H. Xie, Mater. Res. Bull., 47 (2012) 662-666.
[141] S. Ahmed, A. Ahmed, M. Rafat, J. Saudi Chem. Soc., 22 (2018) 993-1002.

[142] X. Wei, S. Wan, S. Gao, Nano Energy, 28 (2016) 206-215.

[143] X. Yu, Y. Kang, H.S. Park, Carbon, 101 (2016) 49-56.

[144] P. Hao, Z. Zhao, Y. Leng, J. Tian, Y. Sang, R.I. Boughton, C.P. Wong, H. Liu, B. Yang, Nano Energy, 15 (2015) 9-23.

[145] H. Pan, J. Li, Y. Feng, Nanoscale Res. Lett., 5 (2010) 654-668.

[146] M. Kaempgen, C.K. Chan, J. Ma, Y. Cui, G. Gruner, Nano Lett., 9 (2009) 1872-1876.

[147] L.F. Aval, M. Ghoranneviss, G.B. Pour, Heliyon, 4 (2018) e00862.

[148] M.F. El-Kady, Y. Shao, R.B. Kaner, Nat. Rev. Mater., 1 (2016) 1-14.

[149] A.G. Pandolfo, A.F. Hollenkamp, J. Power Sources, 157 (2006) 11-27.

[150] J. Xia, F. Chen, J. Li, N. Tao, Nat. Nanotechnol., 4 (2009) 505-509.

[151] J. Wang, P. Nie, B. Ding, S. Dong, X. Hao, H. Dou, X. Zhang, J. Mater. Chem. A 5 (2017) 2411-2428.

[152] X. Deng, J. Li, L. Ma, J. Sha, N. Zhao, Mater. Chem. Front., 3 (2019) 2221-2245.

[153] H. Lu, X.S. Zhao, Sustain. Energy Fuels 1 (2017) 1265-1281.

[154] K. Kierzek, E. Frackowiak, G. Lota, G. Gryglewicz, J. Machnikowski, Electrochim. Acta, 49 (2004) 515-523.

[155] J. Chmiola, C. Largeot, P.L. Taberna, P. Simon, Y. Gogotsi, Angew. Chem. Int. Ed., 47 (2008) 3392-3395.

[156] Y.-b. Xie, W.-m. Qiao, W.-y. Zhang, G.-w. Sun, L.-c. Ling, New Carbon Mater., 25 (2010) 248-254.

[157] J. Hou, C. Cao, X. Ma, F. Idrees, B. Xu, X. Hao, W. Lin, Sci. Rep., 4 (2014) 7260.

[158] S. Iijima, Nature, 354 (1991) 56-58.

[159] A. Aqel, K.M.M.A. El-Nour, R.A.A. Ammar, A. Al-Warthan, Arab. J. Chem., 5 (2012) 1-23.

[160] S. Iijima, T. Ichihashi, Nature, 363 (1993) 603-605.

[161] X. Fang, A. Shashurin, G. Teel, M. Keidar, Carbon, 107 (2016) 273-280.

[162] Y. Ando, X. Zhao, New diamond and frontier carbon technology, 16 (2006) 123-138.

[163] H.E. Lim, Y. Miyata, R. Kitaura, Y. Nishimura, Y. Nishimoto, S. Irle, J.H. Warner, H. Kataura, H. Shinohara, Nat. Commun., 4 (2013) 2548.

[164] T. Guo, P. Nikolaev, A. Thess, D.T. Colbert, R.E. Smalley, Chem. Phys. Lett., 243 (1995) 49-54.

[165] F. Yang, X. Wang, D. Zhang, J. Yang, D. Luo, Z. Xu, J. Wei, J.Q. Wang, Z. Xu, F. Peng, X. Li, R. Li, Y. Li, M. Li, X. Bai, F. Ding, Y. Li, Nature, 510 (2014) 522-524.

[166] J. Li, C. Papadopoulos, J. Xu, Nature, 402 (1999) 253-254.

[167] T. Tang, X. Chen, X. Meng, H. Chen, Y. Ding, Angew. Chem. Int. Ed., 44 (2005) 1517-1520.

[168] L. Huang, X. Cui, B. White, S.P. O'Brien, J. Phys. Chem. B, 108 (2004) 16451-16456.

[169] M. Jung, K.Y. Eun, J.-K. Lee, Y.-J. Baik, K.-R. Lee, J.W. Park, Diam. Relat. Mater., 10 (2001) 1235-1240.

[170] S. Kumar, M. Nehra, D. Kedia, N. Dilbaghi, K. Tankeshwar, K.-H. Kim, Prog. Energy Combust. Sci., 64 (2018) 219-253.

[171] S. Fan, M.G. Chapline, N.R. Franklin, T.W. Tombler, A.M. Cassell, H. Dai, Science 283 (1999) 512-514.

[172] A. Reina, M. Hofmann, D. Zhu, J. Kong, J. Phys. Chem. C, 111 (2007) 7292-7297.

[173] Y. Chen, J. Zhang, Acc. Chem. Res., 47 (2014) 2273-2281.

[174] C.-M. Seah, S.-P. Chai, A.R. Mohamed, Carbon, 49 (2011) 4613-4635.

[175] Min-Feng Yu, B.S. Files, S. Arepalli, R.S. Ruoff1, Phys. Rev. Lett., 84 (2000) 5552-5555.

[176] Eric Pop, D. Mann, Q. Wang, K. Goodson, H. Dai, Nano Lett., 6 (2006) 96-100.

[177] T.W. Ebbesen, H.J. Lezec, H. Hiura, J.W. Bennett, H.F. Ghaemi, T. Thio, Nature 382 (1996) 54-56.

[178] Z. Yang, J. Ren, Z. Zhang, X. Chen, G. Guan, L. Qiu, Y. Zhang, H. Peng, Chem. Rev., 115 (2015) 5159-5223.

[179] K.H. An, W.S. Kirn, Y.S. Park, H.J. Jeong, Y.C. Choi, J.-M. Moon, D.J. Bae, S.C.

Lim, Y.H. Lee, in: AIP Conference Proceedings, 2001, pp. 241-244.

[180] H. Pan, C.K. Poh, Y.P. Feng, J. Lin, Chem. Mater., 19 (2007) 6120-6125.

[181] A. Izadi-Najafabadi, S. Yasuda, K. Kobashi, T. Yamada, D.N. Futaba, H. Hatori, M. Yumura, S. Iijima, K. Hata, Adv. Mater., 22 (2010) E235-E241.

[182] Y.-T. Kim, T. Mitani, J. Power Sources, 158 (2006) 1517-1522.

[183] L. Li-Xiang, T. Jing, G. Xin, A. Bai-Gang, Acta. Phys. Sin., 29 (2013) 111-116.

[184] D. Gueon, J.H. Moon, ACS Appl. Mater. Interfaces 7(2015) 20083-20089.

[185] V. Khomenko, E. Frackowiak, F. Béguin, Electrochim. Acta, 50 (2005) 2499-2506.

[186] E. Frackowiak, V. Khomenko, K. Jurewicz, K. Lota, F. Béguin, J. Power Sources, 153 (2006) 413-418.

[187] V. Subramanian, H. Zhu, B. Wei, Electrochem. commun., 8 (2006) 827-832.

[188] Z. Sun, Z. Liu, B. Han, S. Miao, J. Du, Z. Miao, Carbon, 44 (2006) 888-893.

[189] A.L.M. Reddy, S. Ramaprabhu, J. Phys. Chem. C, 111 (2007) 7727-7734.

[190] K.S. Novoselov, A.K. Geim, S.V. Morozov, D. Jiang, Y. Zhang, S.V. Dubonos, I.V. Grigorieva, A.A. Firsov, Science 306 (2004) 666-669.

[191] L. Dai, D.W. Chang, J.B. Baek, W. Lu, Small, 8 (2012) 1130-1166.

[192] E.P. Randviir, D.A.C. Brownson, C.E. Banks, Mater. Today, 17 (2014) 426-432.

[193] W. Choi, I. Lahiri, R. Seelaboyina, Y.S. Kang, Crit. Rev. Solid State Mater. Sci., 35 (2010) 52-71.

[194] S.L. Candelaria, Y. Shao, W. Zhou, X. Li, J. Xiao, J.-G. Zhang, Y. Wang, J. Liu, J. Li, G. Cao, Nano Energy, 1 (2012) 195-220.

[195] A.K. GEIM, K.S. NOVOSELOV, Nat. Mater., 6 (2007) 183-191.

[196] K.V. Emtsev, A. Bostwick, K. Horn, J. Jobst, G.L. Kellogg, L. Ley, J.L. McChesney, T. Ohta, S.A. Reshanov, J. Rohrl, E. Rotenberg, A.K. Schmid, D. Waldmann, H.B. Weber, T. Seyller, Nat. Mater., 8 (2009) 203-207.

[197] P. sutter, Nat. Mater., 8 (2009) 171-172.

[198] J.-O. Carlsson, P.M. Martin, (2010).

[199] A. Reina, X. Jia, J. Ho, D. Nezich, H. Son, V. Bulovic, M.S. Dresselhaus, J. Kong,

Nano Lett., 9 (2009) 30-35.

[200] K.S. Kim, Y. Zhao, H. Jang, S.Y. Lee, J.M. Kim, K.S. Kim, J.H. Ahn, P. Kim, J.Y. Choi, B.H. Hong, Nature, 457 (2009) 706-710.

[201] S. Bae, H. Kim, Y. Lee, X. Xu, J.S. Park, Y. Zheng, J. Balakrishnan, T. Lei, H.R. Kim, Y.I. Song, Y.J. Kim, K.S. Kim, B. Ozyilmaz, J.H. Ahn, B.H. Hong, S. Iijima, Nat. Nanotechnol., 5 (2010) 574-578.

[202] X. Li, W. Cai, J. An, S. Kim, J. Nah, D. Yang, R. Piner, A. Velamakanni, I. Jung, E. Tutuc, S.K. Banerjee, L. Colombo, R.S. Ruoff, Science, 324 (2009) 1312-1314.

[203] C.K. Chua, M. Pumera, Commun. Chem., 52 (2016) 72-75.

[204] S. Park, J. An, J.R. Potts, A. Velamakanni, S. Murali, R.S. Ruoff, Carbon, 49 (2011) 3019-3023.

[205] J. Shen, Y. Hu, M. Shi, X. Lu, C. Qin, C. Li, M. Ye, Chem. Mater., 21 (2009) 3514-3520.

[206] H.A. Becerril, J. Mao, Z. Liu, R.M. Stoltenberg, Z. Bao, Y. Chen, ACS Nano 2(2008) 463-470.

[207] X. Wang, L. Zhi, K. Müllen, Nano Lett., 8 (2008) 323-327.

[208] W.S.H. Jr., R.E. Offeman, J. Am. Chem. Soc., 80 (1958) 1339-1339.

[209] D.C. Marcano, D.V. Kosynkin, J.M. Berlin, A. Sinitskii, Z. Sun, A. Slesarev, L.B. Alemany, W. Lu, J.M. Tour, ACS Nano, 4 (2010) 4806-4814.

[210] J. Cao, P. He, M.A. Mohammed, X. Zhao, R.J. Young, B. Derby, I.A. Kinloch, R.A.W. Dryfe, J Am Chem Soc, 139 (2017) 17446-17456.

[211] A.A. Balandin, S. Ghosh, W. Bao, I. Calizo, D. Teweldebrhan, F. Miao, C.N. Lau, Nano Lett., 8 (2008) 902-907.

[212] F. Bonaccorso, L. Colombo, G. Yu, M. Stoller, V. Tozzini, A.C. Ferrari, R.S. Ruoff, V. Pellegrini, Science, 347 (2015) 1246501.

[213] C. Lee, X. Wei, J.W. Kysar, J. Hone, Science, 321 (2008) 385-388.

[214] Y. Liu, X. Dong, P. Chen, Chem. Soc. Rev., 41 (2012) 2283-2307.

[215] Z. Liu, S.P. Lau, F. Yan, Chem. Soc. Rev., 44 (2015) 5638-5679.

[216] F. Perreault, A. Fonseca de Faria, M. Elimelech, Chem. Soc. Rev., 44 (2015)

5861-5896.

[217] K. Chen, S. Song, F. Liu, D. Xue, Chem. Soc. Rev., 44 (2015) 6230-6257.

[218] I.H. Son, J.H. Park, S. Park, K. Park, S. Han, J. Shin, S.G. Doo, Y. Hwang, H. Chang, J.W. Choi, Nat. Commun., 8 (2017) 1561.

[219] C. Liu, Z. Yu, D. Neff, A. Zhamu, B.Z. Jang, Nano Lett., 10 (2010) 4863-4868.

[220] M.D. Stoller, S. Park, Y. Zhu, J. An, R.S. Ruoff, Nano Lett., 8 (2008) 3498-3502.

[221] Y. Chen, X. Zhang, D. Zhang, P. Yu, Y. Ma, Carbon, 49 (2011) 573-580.

[222] Y. Zhu, M.D. Stoller, W. Cai, A. Velamakanni, R.D. Piner, D. Chen, R.S. Ruoff, ACS Nano, 4 (2010) 1227-1233.

[223] Z. Chu, R. He, X. Zhang, Z. Jiang, H. Cheng, Y. Wang, X. Li, Carbon, 48 (2010) 2115-2118.

[224] W. Lv, D.-M. Tang, Y.-B. He, C.-H. You, Z.-Q. Shi, X.-C. Chen, C.-M. Chen, P.-X. Hou, C. Liu, Q.-H. Yang, ACS Nano, 3 (2009) 3730-3736.

[225] S. Stankovich, D.A. Dikin, R.D. Piner, K.A. Kohlhaas, A. Kleinhammes, Y. Jia, Y. Wu, S.T. Nguyen, R.S. Ruoff, Carbon, 45 (2007) 1558-1565.

[226] Yuxi Xu, K. Sheng, C. Li, G. Shi, ACS Nano, 4 (2010) 4324-4330.

[227] Y. Lin, F. Liu, G. Casano, R. Bhavsar, I.A. Kinloch, B. Derby, Adv. Mater., 28 (2016) 7993-8000.

[228] Y. Si, E.T. Samulski, Chem. Mater., 20 (2008) 6792-6797.

[229] X. Yang, J. Zhu, L. Qiu, D. Li, Adv. Mater., 23 (2011) 2833-2838.

[230] X. An, T. Simmons, R. Shah, C. Wolfe, K.M. Lewis, M. Washington, S.K. Nayak, S. Talapatra, S. Kar, Nano Lett., 10 (2010) 4295-4301.

[231] Z. Qin, Z.J. Li, M. Zhang, B.C. Yang, R.A. Outlaw, J. Power Sources, 217 (2012) 303-308.

[232] J. Yan, T. Wei, B. Shao, F. Ma, Z. Fan, M. Zhang, C. Zheng, Y. Shang, W. Qian, F. Wei, Carbon, 48 (2010) 1731-1737.

[233] N.A. Kumar, H.-J. Choi, Y.R. Shin, D.W. Chang, L. Dai, J.-B. Baek, ACS Nano 6(2012) 1715-1723.

[234] L. Qiu, X. Yang, X. Gou, W. Yang, Z.F. Ma, G.G. Wallace, D. Li, Chemistry, 16

(2010) 10653-10658.

[235] K. Zhang, L. Mao, L.L. Zhang, H.S. On Chan, X.S. Zhao, J. Wu, J. Mater. Chem., 21 (2011) 7302-7307.

[236] M.-x. Wang, Q. Liu, H.-f. Sun, E.A. Stach, J. Xie, ECS Trans., 41 (2012) 95-105.

[237] Y. Zhu, S. Murali, M.D. Stoller, K.J. Ganesh, W. Cai, P.J. Ferreira, A. Pirkle, R.M. Wallace, K.A. Cychosz, M. Thommes, D. Su, E.A. Stach, R.S. Ruoff, Science, 332 (2011) 1537-1541.

[238] H.M. Jeong, J.W. Lee, W.H. Shin, Y.J. Choi, H.J. Shin, J.K. Kang, J.W. Choi, Nano Lett., 11 (2011) 2472-2477.

[239] H.-L. Guo, P. Su, X. Kang, S.-K. Ning, J. Mater. Chem. A 1(2013) 2248-2255.

[240] Y. Zhao, C. Hu, Y. Hu, H. Cheng, G. Shi, L. Qu, Angew. Chem. Int. Ed., 124 (2012) 11533-11537.

[241] J. Han, L.L. Zhang, S. Lee, J. Oh, K.-S. Lee, J.R. Potts, J. Ji, X. Zhao, R.S. Ruoff, S. Park, ACS Nano, 7 (2012) 19-26.

[242] C. Wang, Y. Zhou, L. Sun, Q. Zhao, X. Zhang, P. Wan, J. Qiu, J. Phys. Chem. C, 117 (2013) 14912-14919.

[243] H. Wang, H.S. Casalongue, Y. Liang, H. Dai, J. Am. Chem. Soc., 132 (2010) 7472-7477.

[244] K. Zhang, L.L. Zhang, X.S. Zhao, J. Wu, Chem. Mater., 22 (2010) 1392-1401.

[245] Z. Li, J. Wang, L. Niu, J. Sun, P. Gong, W. Hong, L. Ma, S. Yang, J. Power Sources, 245 (2014) 224-231.

[246] G. Han, Y. Liu, L. Zhang, E. Kan, S. Zhang, J. Tang, W. Tang, Sci. Rep., 4 (2014) 4824.

[247] T. Brousse, D. Bélanger, J.W. Long, J. Electrochem. Soc., 162 (2015) A5185-A5189.

[248] E. Herrero, L.J. Buller, H.c.D. Abrun˜a, Chem. Rev., 101 (2001) 1897-1930.

[249] V. Sudha, M.V. Sangaranarayanan, J. Phys. Chem. B, 106 (2002) 2699-2707.

[250] C.-C. Hu, K.-H. Chang, M.-C. Lin, Y.-T. Wu, Nano Lett., 6 (2006) 2690-2695.

[251] M. Huang, F. Li, F. Dong, Y.X. Zhang, L.L. Zhang, J. Mater. Chem. A, 3 (2015)

21380-21423.

[252] H. Zhou, H.-J. Zhai, X. Zhi, Electrochim. Acta, 290 (2018) 1-11.

[253] W. Chen, R.B. Rakhi, H.N. Alshareef, J. Mater. Chem. A 1 (2013) 3315-3324.

[254] B. Saravanakumar, K.K. Purushothaman, G. Muralidharan, ACS Appl. Mater. Interfaces, 4 (2012) 4484-4490.

[255] J.W. Kim, V. Augustyn, B. Dunn, Adv. Energy Mater., 2 (2012) 141-148.

[256] V. Augustyn, J. Come, M.A. Lowe, J.W. Kim, P.L. Taberna, S.H. Tolbert, H.D. Abruna, P. Simon, B. Dunn, Nat. Mater., 12 (2013) 518-522.

[257] O. Mashtalir, M. Naguib, V.N. Mochalin, Y. Dall'Agnese, M. Heon, M.W. Barsoum, Y. Gogotsi, Nat. Commun., 4 (2013) 1716.

[258] M.R. Lukatskaya, O. Mashtalir, C.E. Ren, Y. Dall'Agnese, P. Rozier, P.L. Taberna, M. Naguib, P. Simon, M.W. Barsoum, Y. Gogotsi, Science, 341 (2013) 1502-1505.

[259] B. Anasori, M.R. Lukatskaya, Y. Gogotsi, Nat. Rev. Mater., 2 (2017) 1-17.

[260] X. Zhang, Y. Xia, H. Dou, X. Hao, Y. Wang, B. Ding, S. Dong, J. Wang, Natl. Sci. Rev., 4 (2017) 71-90.

[261] Y. Gogotsi, R.M. Penner, ACS Nano, 12 (2018) 2081-2083.

[262] H. Xia, Y. Shirley Meng, G. Yuan, C. Cui, L. Lu, Electrochem. solid-state lett., 15 (2012) A60-A63.

[263] D. Majumdar, T. Maiyalagan, Z. Jiang, ChemElectroChem, 6 (2019) 4343-4372.

[264] L.Y. Chen, Y. Hou, J.L. Kang, A. Hirata, T. Fujita, M.W. Chen, Adv. Energy Mater., 3 (2013) 851-856.

[265] R.K. Das, B. Liu, J.R. Reynolds, A.G. Rinzler, Nano Lett., 9 (2009) 677-683.

[266] W. Wei, X. Cui, W. Chen, D.G. Ivey, Chem. Soc. Rev., 40 (2011) 1697-1721.

[267] M. Toupin, T. Brousse, D. Be´langer, Chem. Mater., 16 (2004) 3184-3190.

[268] Y. Hu, Y. Wu, J. Wang, Adv. Mater., 30 (2018) 1802569.

[269] O. Sadak, W. Wang, J. Guan, A.K. Sundramoorthy, S. Gunasekaran, ACS Appl. Nano Mater., 2 (2019) 4386-4394.

[270] Z. Wang, F. Wang, J. Mater. Chem. A, 5 (2017) 9709-9716.

[271] Q. Meng, K. Cai, Y. Chen, L. Chen, Nano Energy, 36 (2017) 268-285.

[272] Y. Han, L. Dai, Macromol. Chem. Phys., 220 (2019) 1800355.

[273] X. Zhang, W.J. Goux, S.K. Manoha, J. Am. Chem. Soc. , 126 (2004) 4502-4503.

[274] X. Yu, Y. Li, K. Kalantar-zadeh, Sens. Actuators B Chem., 136 (2009) 1-7.

[275] X. Zhang, S.K. Manohar, J. Am. Chem. Soc. , 127 (2005) 14156-14157.

[276] K. Xie, J. Li, Y. Lai, Z. Zhang, Y. Liu, G. Zhang, H. Huang, Nanoscale, 3 (2011) 2202-2207.

[277] X. Lu, H. Dou, S. Yang, L. Hao, L. Zhang, L. Shen, F. Zhang, X. Zhang, Electrochim. Acta, 56 (2011) 9224-9232.

[278] T. Liu, L. Finn, M. Yu, H. Wang, T. Zhai, X. Lu, Y. Tong, Y. Li, Nano Lett., 14 (2014) 2522-2527.

[279] M. Naguib, M. Kurtoglu, V. Presser, J. Lu, J. Niu, M. Heon, L. Hultman, Y. Gogotsi, M.W. Barsoum, Adv. Mater., 23 (2011) 4248-4253.

[280] W. Yang, J. Yang, J.J. Byun, F.P. Moissinac, J. Xu, S.J. Haigh, M. Domingos, M.A. Bissett, R.A.W. Dryfe, S. Barg, Adv. Mater., 31 (2019) 1902725.

[281] X. Wang, T.S. Mathis, K. Li, Z. Lin, L. Vlcek, T. Torita, N.C. Osti, C. Hatter, P. Urbankowski, A. Sarycheva, M. Tyagi, E. Mamontov, P. Simon, Y. Gogotsi, Nat. Energy, 4 (2019) 241-248.

[282] M. Hu, H. Zhang, T. Hu, B. Fan, X. Wang, Z. Li, Chem. Soc. Rev., 49 (2020) 6666-6693.

[283] M. Naguib, O. Mashtalir, J. Carle, V. Presser, J. Lu, L. Hultman, Y. Gogotsi, M.W. Barsoum, ACS Nano 6 (2012) 1322-1331.

[284] M.R. Lukatskaya, S. Kota, Z. Lin, M.-Q. Zhao, N. Shpigel, M.D. Levi, J. Halim, P.-L. Taberna, M.W. Barsoum, P. Simon, Y. Gogotsi, Nat. Energy, 2 (2017) 1-6..

[285] M. Hu, Z. Li, T. Hu, S. Zhu, C. Zhang, X. Wang, ACS Nano, 10 (2016) 11344-11350.

[286] P. Simon, Y. Gogotsi, Nat. Mater., 19 (2020) 1151-1163.

[287] M. Ghidiu, M.R. Lukatskaya, M.Q. Zhao, Y. Gogotsi, M.W. Barsoum, Nature, 516 (2014) 78-81.

[288] F. Liu, A. Zhou, J. Chen, J. Jia, W. Zhou, L. Wang, Q. Hu, Appl. Surf. Sci., 416

(2017) 781-789.

[289] Y. Xie, M. Naguib, V.N. Mochalin, M.W. Barsoum, Y. Gogotsi, X. Yu, K.W. Nam, X.Q. Yang, A.I. Kolesnikov, P.R. Kent, J. Am. Chem. Soc., 136 (2014) 6385-6394.

[290] Q. Tang, Z. Zhou, P. Shen, J. Am. Chem. Soc., 134 (2012) 16909-16916.

[291] T. Li, L. Yao, Q. Liu, J. Gu, R. Luo, J. Li, X. Yan, W. Wang, P. Liu, B. Chen, W. Zhang, W. Abbas, R. Naz, D. Zhang, Angew. Chem. Int. Ed., 57 (2018) 6115-6119.

[292] W. Sun, S.A. Shah, Y. Chen, Z. Tan, H. Gao, T. Habib, M. Radovic, M.J. Green, J. Mater. Chem. A, 5 (2017) 21663-21668.

[293] S.Y. Pang, Y.T. Wong, S. Yuan, Y. Liu, M.K. Tsang, Z. Yang, H. Huang, W.T. Wong, J. Hao, J. Am. Chem. Soc., 141 (2019) 9610-9616.

[294] W. Du, E.H. Ang, Y. Yang, Y. Zhang, M. Ye, C.C. Li, Energy Environ. Sci., 13 (2020) 3330-3360.

[295] A. Konarov, N. Voronina, J.H. Jo, Z. Bakenov, Y.-K. Sun, S.-T. Myung, ACS Energy Lett., 3 (2018) 2620-2640.

[296] J. Shin, J. Lee, Y. Park, J.W. Choi, Chem. Sci., 11 (2020) 2028-2044.

[297] J.F. Parker, C.N. Chervin, I.R. Pala, M. Machler, M.F. Burz, J.W. Long, D.R. Rolison, Science, 356 (2017) 415-418.

[298] Q. Yang, Q. Li, Z. Liu, D. Wang, Y. Guo, X. Li, Y. Tang, H. Li, B. Dong, C. Zhi, Adv. Mater. , 32 (2020) 2001854.

[299] H. Jia, Z. Wang, B. Tawiah, Y. Wang, C.-Y. Chan, B. Fei, F. Pan, Nano Energy, 70 (2020) 104523.

[300] N. Zhang, X. Chen, M. Yu, Z. Niu, F. Cheng, J. Chen, Chem. Soc. Rev., 49 (2020) 4203-4219.

[301] N. Zhang, F. Cheng, J. Liu, L. Wang, X. Long, X. Liu, F. Li, J. Chen, Nat. Commun., 8 (2017) 405.

[302] B. Jiang, C. Xu, C. Wu, L. Dong, J. Li, F. Kang, Electrochim. Acta, 229 (2017) 422-428.

[303] C. Zhu, G. Fang, J. Zhou, J. Guo, Z. Wang, C. Wang, J. Li, Y. Tang, S. Liang, J. Mater. Chem. A, 6 (2018) 9677-9683.

[304] T.R. Juran, J. Young, M. Smeu, J. Phys. Chem. C 122 (2018) 8788-8795.

[305] K. Alam, N. Seriani, P. Sen, Mater. Res. Express, 6 (2019) 076108.

[306] T. Yamamoto, T. Shoji, Inorganica Chim. Acta, 117 (1986) L27-L28.

[307] C. Xu, B. Li, H. Du, F. Kang, Angew. Chem. Int. Ed., 51 (2012) 933-935.

[308] M.H. Alfaruqi, J. Gim, S. Kim, J. Song, J. Jo, S. Kim, V. Mathew, J. Kim, J. Power Sources, 288 (2015) 320-327.

[309] H. Pan, Y. Shao, P. Yan, Y. Cheng, K.S. Han, Z. Nie, C. Wang, J. Yang, X. Li, P. Bhattacharya, K.T. Mueller, J. Liu, Nat. Energy, 1 (2016) 16039.

[310] B. Lee, H.R. Seo, H.R. Lee, C.S. Yoon, J.H. Kim, K.Y. Chung, B.W. Cho, S.H. Oh, ChemSusChem, 9 (2016) 2948-2956.

[311] W. Sun, F. Wang, S. Hou, C. Yang, X. Fan, Z. Ma, T. Gao, F. Han, R. Hu, M. Zhu, C. Wang, J. Am. Chem. Soc., 139 (2017) 9775-9778.

[312] J. Huang, Z. Wang, M. Hou, X. Dong, Y. Liu, Y. Wang, Y. Xia, Nat. Commun., 9 (2018) 2906.

[313] G. Zampardi, F. La Mantia, Curr. Opin. Electrochem., 21 (2020) 84-92.

[314] K. Hurlbutt, S. Wheeler, I. Capone, M. Pasta, Joule, 2 (2018) 1950-1960.

[315] Z. Liu, G. Pulletikurthi, F. Endres, ACS Appl. Mater. Interfaces, 8 (2016) 12158-12164.

[316] Z. Liu, P. Bertram, F. Endres, J. Solid State Chem., 21 (2017) 2021-2027.

[317] Z. Jia, B. Wang, Y. Wang, Mater. Chem. Phys., 149-150 (2015) 601-606.

[318] R. Trocoli, F. La Mantia, ChemSusChem, 8 (2015) 481-485.

[319] L. Zhang, L. Chen, X. Zhou, Z. Liu, Adv. Energy Mater., 5 (2015) 1400930.

[320] P. Hu, M. Yan, T. Zhu, X. Wang, X. Wei, J. Li, L. Zhou, Z. Li, L. Chen, L. Mai, ACS Appl. Mater. Interfaces, 9 (2017) 42717-42722.

[321] J. Zhou, L. Shan, Z. Wu, X. Guo, G. Fang, S. Liang, Commun. Chem., 54 (2018) 4457-4460.

[322] L. Chen, Z. Yang, Y. Huang, Nanoscale, 11 (2019) 13032-13039.

[323] D. Kundu, B.D. Adams, V. Duffort, S.H. Vajargah, L.F. Nazar, Nat. Energy, 1 (2016) 1-8.

[324] C. Xia, J. Guo, P. Li, X. Zhang, H.N. Alshareef, Angew. Chem. Int. Ed., 57 (2018) 3943-3948.

[325] P. He, G. Zhang, X. Liao, M. Yan, X. Xu, Q. An, J. Liu, L. Mai, Adv. Energy Mater., 8 (2018) 1702463.

[326] M. Yan, P. He, Y. Chen, S. Wang, Q. Wei, K. Zhao, X. Xu, Q. An, Y. Shuang, Y. Shao, K.T. Mueller, L. Mai, J. Liu, J. Yang, Adv. Mater., 30 (2018) 1703725.

[327] A. Muzaffar, M.B. Ahamed, K. Deshmukh, J. Thirumalai, Renew. Sust. Energ. Rev. , 101 (2019) 123-145.

[328] S. Roldan, D. Barreda, M. Granda, R. Menendez, R. Santamaria, C. Blanco, Phys. Chem. Chem. Phys., 17 (2015) 1084-1092.

[329] Y. Zhang, S. Liu, Y. Ji, J. Ma, H. Yu, Adv. Mater., 30 (2018) 1706310.

[330] M. Soltani, S.H. Beheshti, J. Energy Storage, 34 (2021) 102019.

[331] V. Aravindan, M. Ulaganathan, S. Madhavi, J. Mater. Chem. A 4(2016) 7538-7548.

[332] Q. Liu, H. Zhang, J. Xie, X. Liu, X. Lu, Carbon Energy, 2 (2020) 521-539.

[333] Z. Li, Y. An, S. Dong, C. Chen, L. Wu, Y. Sun, X. Zhang, Energy Storage Mater., 31 (2020) 252-266.

[334] L. Dong, X. Ma, Y. Li, L. Zhao, W. Liu, J. Cheng, C. Xu, B. Li, Q.-H. Yang, F. Kang, Energy Storage Mater., 13 (2018) 96-102.

[335] Y. Tian, R. Amal, D.-W. Wang, Front. Energy Res., 4 (2016) 34.

[336] S. Wu, Y. Chen, T. Jiao, J. Zhou, J. Cheng, B. Liu, S. Yang, K. Zhang, W. Zhang, Adv. Energy Mater., 9 (2019) 1902915.

[337] H. Zhang, Q. Liu, Y. Fang, C. Teng, X. Liu, P. Fang, Y. Tong, X. Lu, Adv. Mater., 31 (2019) 1904948.

[338] H. Wang, M. Wang, Y. Tang, Energy Storage Mater., 13 (2018) 1-7.

[339] G.H. An, J. Hong, S. Pak, Y. Cho, S. Lee, B. Hou, S. Cha, Adv. Energy Mater., 10 (2019) 1902981.

[340] P. Yu, Y. Zeng, Y. Zeng, H. Dong, H. Hu, Y. Liu, M. Zheng, Y. Xiao, X. Lu, Y. Liang, Electrochim. Acta, 327 (2019) 134999.

[341] P. Liu, W. Liu, Y. Huang, P. Li, J. Yan, K. Liu, Energy Storage Mater., 25 (2020) 858-865.

[342] S. Chen, L. Ma, K. Zhang, M. Kamruzzaman, C. Zhi, J.A. Zapien, J. Mater. Chem. A 7 (2019) 7784-7790.

[343] Y. Lu, Z. Li, Z. Bai, H. Mi, C. Ji, H. Pang, C. Yu, J. Qiu, Nano Energy, 66 (2019) 104132.

[344] Y. Zheng, W. Zhao, D. Jia, Y. Liu, L. Cui, D. Wei, R. Zheng, J. Liu, Chem. Eng. J., 387 (2020) 124161.

[345] P. Liu, Y. Gao, Y. Tan, W. Liu, Y. Huang, J. Yan, K. Liu, Nano Res., 12 (2019) 2835-2841.

[346] T. Xiong, Y. Shen, W.S.V. Lee, J. Xue, Nano mater. sci., 2 (2020) 159-163.

[347] Z. Pan, Z. Lu, L. Xu, D. Wang, Appl. Surf. Sci., 510 (2020) 145384.

[348] P. Zhang, Y. Li, G. Wang, F. Wang, S. Yang, F. Zhu, X. Zhuang, O.G. Schmidt, X. Feng, Adv. Mater., 31 (2019) 1806005.

[349] L. Han, H. Huang, X. Fu, J. Li, Z. Yang, X. Liu, L. Pan, M. Xu, Chem. Eng. J., 392 (2020) 123733.

[350] G. Sun, Y. Xiao, B. Lu, X. Jin, H. Yang, C. Dai, X. Zhang, Y. Zhao, L. Qu, ACS Appl. Mater. Interfaces 12 (2020) 7239-7248.

[351] Q. Wang, S. Wang, X. Guo, L. Ruan, N. Wei, Y. Ma, J. Li, M. Wang, W. Li, W. Zeng, Adv. Electron. Mater., 5 (2019) 1900537.

# Chapter 2 Characterization Techniques

## 2.1 Characterization

The applications of materials are determined by the properties of the materials which are highly dependent on their structure and compositions as well as morphology. Characterization is critical in understanding the properties of the materials, thus providing guidance in the possible applications of the materials. The work in this thesis will use various electrode materials. Therefore, the characterization and electrochemical techniques used in this thesis will be briefly introduced.

### 2.1.1 X-ray Diffraction

As a rapid and non-destructive technique, X-ray diffraction (XRD) has been widely employed to characterize crystalline materials. The principle of XRD is on the basis of constructive interference between monochromatic incident X-rays and crystal specimens [1]. X-rays are a type of high-energy electromagnetic waves with a wavelength ranging from $10^{-3}$ nm to 10 nm. They can be generated using an X-ray tube in which electrons are generated by heating a tungsten filament under a vacuum, which are then accelerated by a high voltage ranging from 20 kV to 60 kV [2]. The high velocity electrons collide with a metal target called an anode, thus emitting X-rays. Two effects are caused by the incident electrons. The first is to produce X-ray photons with a broad continuous distribution of wavelengths due to the deceleration of the electrons. The second is to induce the ionization of the atoms that the electrons have collided with by ejecting electrons from the inner shells. To maintain a more stable state, electrons from outer shells fall into the inner shells to lower the energy of the system. The extra energy of the incoming electrons (i.e., outer electrons) is emitted in the form of photons. These photons have a characteristic energy value determined by the initial and final energy level occupied by the electrons and the corresponding target materials, shown in Figure 2.1. The characteristic radiation can only be achieved when the minimum

excitation potential of the electrons is met. These minimum excitation potential values are dependent the target material.

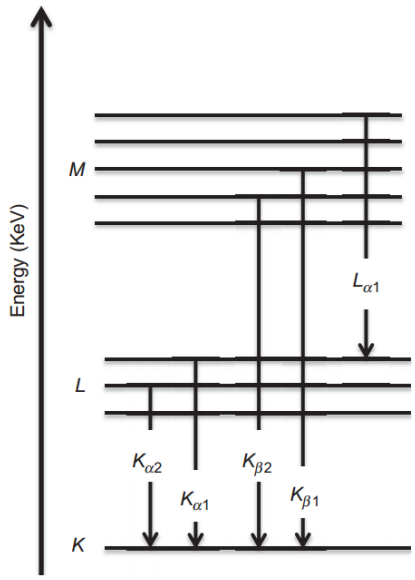


**Figure 2.1.** Schematic of the atomic energy levels and emission of characteristic X-ray radiation. Reproduced from [2].

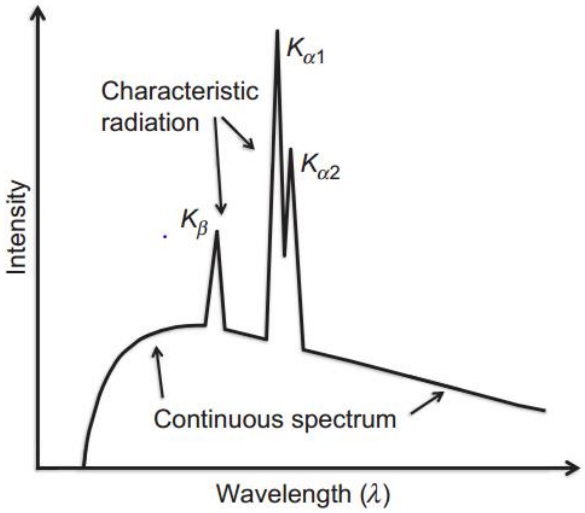


**Figure 2.2.** Intensity over wavelength distribution of the X-ray radiation produced by a sealed tube showing the continuous and the characteristic spectrum. Reproduced from [2].

The generated X-ray radiation is a combination of a continuous spectrum and

characteristic radiation, as shown in Figure 2.2. In practice, only the characteristic radiation (Kα) with the highest intensity is used to characterize the materials by using appropriate filters and monochromators to eliminate most of the remaining radiation. The filter material enables a strong absorption of the continuous spectrum and the $K_\beta$ radiation whilst allowing most of the Kα radiation to pass through. The summary of the common target materials with the corresponding characteristic wavelength, the minimum excitation potential and required filters is exhibited in Table 2.1.

**Table 2.1.** List of several common target materials and corresponding wavelength of $K_\alpha$ and $K_\beta$ radiation in nm together with the minimum excitation potential in kV and the appropriate filter material. Reproduced from [2, 3].

| Target | $K_{\alpha 1}$ | $K_{\alpha 2}$ | $K_{\alpha\ \text{mean}}$ | $K_\beta$ | Excitation potential | Filter |
|---|---|---|---|---|---|---|
| Cr | 0.22897263 | 0.22936513 | 0.22910346 | 0.20848881 | 5.98 | V |
| Mn | 0.21018543 | 0.21058223 | 0.21031770 | 0.19102164 | 6.54 | Cr |
| Fe | 0.19360413 | 0.19399733 | 0.19373520 | 0.17566055 | 7.11 | Mn |
| Co | 0.17889961 | 0.17928351 | 0.17902758 | 0.16208263 | 7.71 | Fe |
| Ni | 0.16579301 | 0.16617561 | 0.16592054 | 0.15001523 | 8.33 | Co |
| Cu | 0.15405929 | 0.15444274 | 0.15418711 | 0.13922346 | 8.98 | Ni |
| Mo | 0.07093000 | 0.07135900 | 0.07107300 | 0.06322880 | 20.0 | Zr |

Several different interactions such as photon absorption and scattering can occur when X-rays interact with matter. Here only elastic scattering will be discussed. The elastic scattering, also named Rayleigh scattering, take places between the photons and the electrons surrounding the atomic nuclei. In this case, the energy of the scattered wave is the same to that of the incident wave. Owing to the periodic nature of a crystal structure, characteristic diffraction patterns are produced. As a result, the X-ray diffraction pattern can be considered as the fingerprint to identify the periodic atomic arrangements of materials. The constructive interference should follow Bragg's law [2]:

$$n\lambda = 2\, d_{hkl} \sin\theta \qquad (2.1)$$

where $n$ is an integer called the order of diffraction, $\lambda$ is the wavelength of the X-ray,

*hkl* are the Miller indices of the diffracting planes, $d_{hkl}$ is the interplanar crystal spacing of a given sample, and the $\theta$ is the diffraction angle. The details about the geometrical condition for diffraction are shown in Figure 2.3,

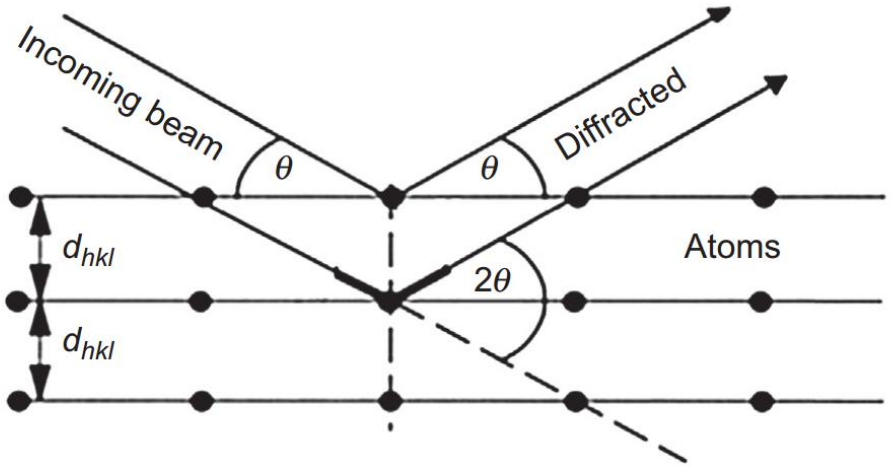


**Figure 2.3.** Geometrical condition for diffraction from lattice planes. Reproduced from [2].

It is expected that all the possible diffraction directions of the lattice can be recorded by scanning a specimen through the 2θ angle range, typically from 5° to 80° in view of the random orientation of the given material. By measuring the diffraction angles, the interplanar distances can be estimated so that the compound can be identified by comparison of d-spacings with reference patterns. Generally, the corresponding diffraction peaks can provide a lot of useful information regarding phases, preferred crystal orientations, crystallinity and averaged grain size.

As real materials are not perfect, the practical shape of the diffracted signal can be affected by various factors, such as instrumental broadening, particle sizes, crystal defects and inhomogeneous strains. Generally, an XRD pattern is displayed as the intensity distribution scattered at different angles as a function of the 2θ angle. The extracted information is shown in Figure 2.4.

The maximum peak intensity ($I_{max}$) and the integrated intensity ($I_{int}$, area under the peak) can be obtained after the background is subtracted. Generally, the peak width can be measured by either the full width at half maximum (FWHM) or the integral breadth.

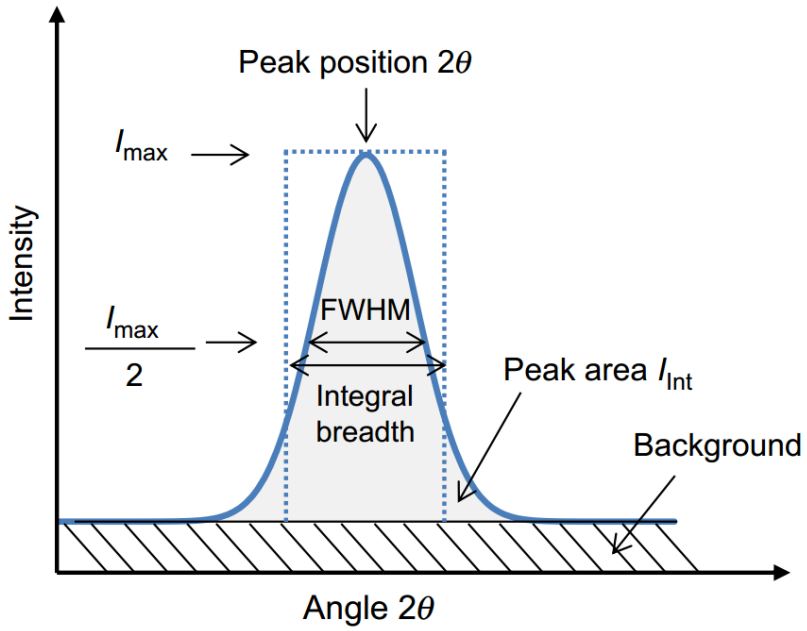


**Figure 2.4.** Extracted diffraction peak and information content from an RXD pattern. Reproduced from [2].

### 2.1.2 Raman Spectroscopy

Raman spectroscopy is a powerful non-destructive technique that can provide useful information on the chemical structure, polymorphs and crystalline phase of materials investigated. The principle is based on the interaction of light with matter. When a beam of incident light interacts with matter, it can be scattered either elastically or inelastically. Most of the scattered light is elastically scattered with the same wavelength as the incident light, as discussed in the previous section for the case of XRD. However, a small fraction of incident light is inelastically scattered and this is called Raman scattering [4]. During the interaction between the incident light and the sample, the electron of the sample is excited to a virtual energy state which is unstable. If the electrons fall back to the initial energy level, the emitted photons have the same energy as the incident photons and thus the frequency of photons do not change. This process is the Rayleigh scattering event, discussed above. When the electrons fall to a new energy level different from the initial energy level, the frequency of the photons

will change. If the energy of the scattered photon is lower than that of the incident photon, the scattering is called Stokes scattering. If the energy is higher, it is called Anti-Stokes scattering. The energy shift of photons can provide information about the vibrational mode of the materials [5]. The inelastic scattering of light was theoretically predicted by Adolf Smekal in 1923 [6] and the experimental phenomenon was first observed by C. V. Raman [7].

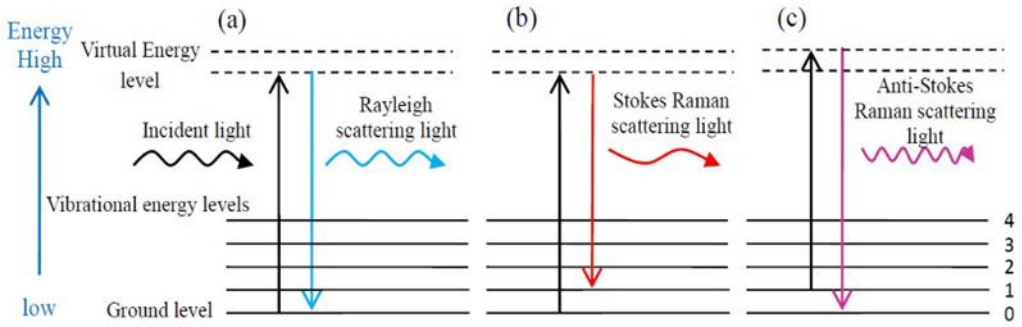


**Figure 2.5.** Diagram of Rayleigh and Raman scattering processes: **(a)** Rayleigh scattering, **(b)** Stokes Raman scattering and **(c)** Anti-Stokes Raman scattering. Reproduced from [8].

The intensity of Raman scattering is determined by the number of the scattered molecules which can be described by the Boltzmann distribution below [8],

$$\frac{N_1}{N_2} = \frac{g_1}{g_2} \exp\left(-\frac{\Delta E}{KT}\right) \qquad (2.2)$$

where $N_1$ and $N_2$ represent the number of molecules in the higher and lower energy level, $g_1$ and $g_2$ represent the degeneracy of higher and lower energy level, $\Delta E$ is the difference in energy before and after scattering, $K$ represents the Boltzmann's constant, and $T$ is the temperature.

The intensity from the Stokes scattered light is much stronger than that from the Anti-Stokes scattering. Thus, Raman scattered light is generally treated as arising from the Stokes scattered light. The Raman spectrum is usually presented as the intensity of the scattered light versus wavenumber. The Raman shift (i.e., wavenumber) is described by the following equation [8]:

$$\text{Raman shift} = \frac{1}{\lambda_i} - \frac{1}{\lambda_s} \quad (2.3)$$

Where $\lambda_i$ and $\lambda_s$ represent the wavelengths of the incident light and scattered light, respectively.

The typical information of a Raman spectrum and the related material information are presented in Figure 2.6.

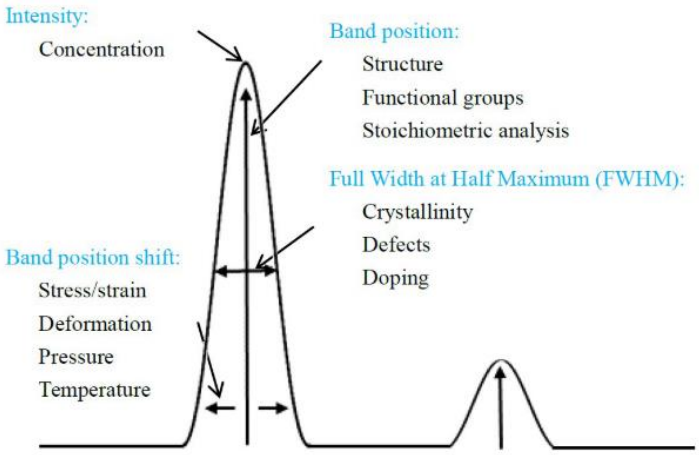


**Figure 2.6.** Typical information of a Raman spectrum and corresponding material information. Reproduced from [8].

Generally, it is suitable to analyze various forms of samples such as solids, liquids and even gases by using Raman spectroscopy. Therefore, as a powerful technique, it is widely employed in a variety of fields such as materials science [9], medicine [10] and environmental monitoring [11].

### 2.1.3 Scanning Electron Microscopy

It is well known that the topography of a material has a significant impact on its properties. Therefore, it is of importance to obtain some information about the morphology of materials used as electrodes. Traditional optical microscopy involves the use of visible light and lenses to produce a magnified image of the sample. Since the resolution is limited by the wavelength of photons, its magnification is usually restricted to between 400-1000 times the original size [12], which impedes the

corresponding applications in the field of nanoscience. Therefore, scanning electron microscopy (SEM) is required to achieve a higher magnification to obtain clear morphology information. Typically, SEM generates images by scanning the specimen surface with a finely focused electron beam. A variety of signals are produced from the interaction of the electron beam with the specimen, including secondary electrons, backscattered electrons, characteristic X-rays, and other photons of various energies [13]. Secondary electrons and backscattered electrons are usually detected in SEM technique. Secondary electrons have low energies in the order of 50 eV, originating from the surface or near-surface regions of the specimen due to the inelastic interactions between the specimen and the primary electron beam. They are very useful in providing information on the surface topography of the specimen. Back-scattered electrons are electrons elastically scattered by the sample. The production of back-scattered electrons varies with the atomic numbers of the elements. Generally, incident electrons are more strongly deflected by heavy elements compared with light elements. Therefore, heavy elements with high atomic numbers tend to be brighter in the image and back-scattered electrons can be employed to differentiate between areas with different chemical compositions. Characteristic X-rays produced by the interaction between the primary electron beam and specimen can also be detected in a SEM instrument with energy-dispersive X-ray spectroscopy (EDS), which is related to the phenomenon used to generate X-rays discussed in the first section of this chapter. EDS is very useful for qualitative and quantitative analysis of elemental distributions within the specimen. We can only obtain information about surface topography of the specimen by SEM without EDS. A schematic of an SEM instrument is shown below:

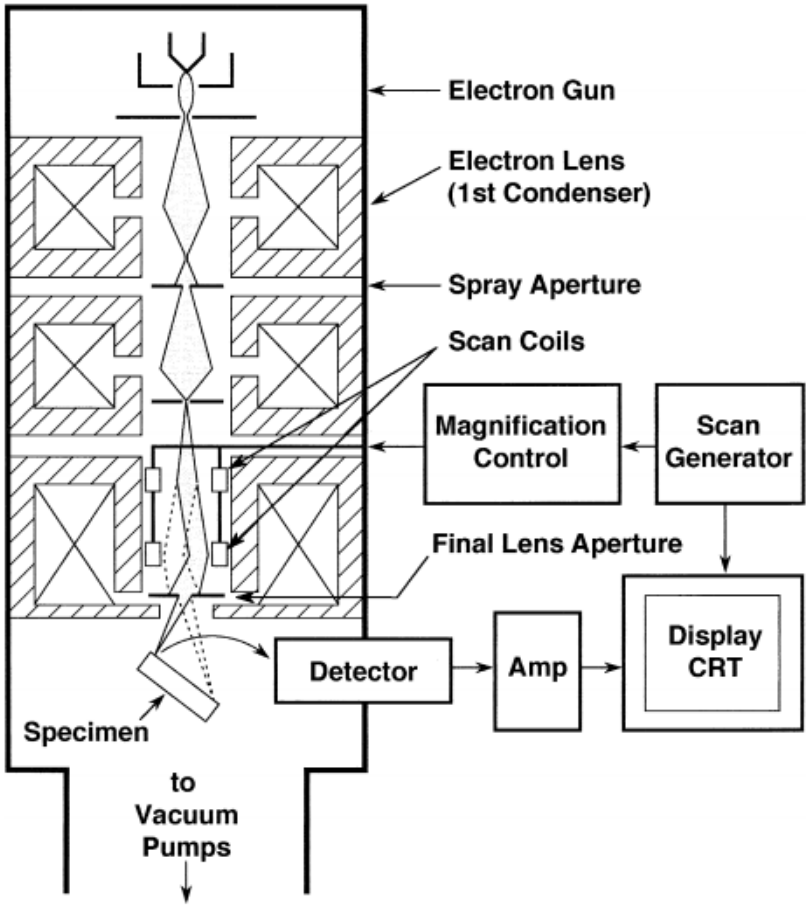


**Figure 2.7.** Schematic drawing of electron column showing the electron gun, lenses, the deflection system, and the electron detector. Reproduced from [13].

In a typical working process of SEM, an electron gun is used to produce the electron beam. Generally, electron guns can be divided into two types: thermionic guns and field emission guns. The thermionic gun uses high current to resistively heat a filament (tungsten or $LaB_6$) to extract electrons off the tip through thermionic emission, while the field emission gun creates a strong electric field to pull electrons away from the atoms. The electron beam is accelerated by a high voltage ranging from 0.1 to 40 kilovolts (kV). Usually, the high accelerating voltage gives rise to deep travelling depth within the specimen. The higher accelerating voltage tends to result in better resolution together with more heat generated within the specimen. If the voltage is too high, the yield of secondary electrons hitting the detector will be lower and detailed surface information will be lost in this case. The specific accelerating voltage is highly

dependent on the nature of the observed specimens. Generally, it is empirically recommended to employ 5 kV or 10 kV. Lenses inside the SEM instrument consist of electromagnets aimed at focusing and controlling the path of electrons. Scan coils are employed to deflect the focused electron beam in the X and Y axes so that the electron beam can scan the specimen surface in a raster pattern. When the beam interacts with the specimen in the vacuum chamber, a variety of signals are generated. Therefore, different detectors are required to collect and distinguish signals from the scanned specimen. If a positive voltage is applied to the collector screen, secondary and back-scattered electrons will be collected. In case of negative voltage applied to the collector screen, only backscattered electrons will be collected. The signals then are displayed on the viewing screen to obtain the images.

It should be noted that samples for SEM must possess good electronic conductivity. For non-conductive samples, they tend to collect charge during the scanning process of the electron beam, thus leading to scanning faults or imaging artifacts. Therefore, they need to be coated by an ultrathin coating of conductive materials under high-vacuum evaporation. The common conductive materials used for coating include gold, platinum, gold/palladium alloy and carbon.

### 2.1.4 Transmission Electron Microscopy

Transmission electron microscopy (TEM) is a very popular and powerful technique in the fields of materials science and nanotechnology. TEM is a microscopic characterization tool in which a high-energy electron beam is transmitted through a thin specimen to form an image, allowing the microscopic analysis of specimens at the atomic level. The main techniques of TEM can be divided into three categories, including imaging, diffraction and spectroscopy [14]. The investigation of topography can be accomplished by high magnification imaging, including high resolution TEM, scanning transmission electron microscopy (STEM) imaging and 3D electron tomography technique. The examination of local crystal structure can be achieved by selected area electron diffraction (SAED) or nano-beam electron diffraction. The

elemental composition can be analyzed by spectroscopic techniques including X-ray energy dispersive spectroscopy (EDS) and electron energy-loss spectroscopy. The schematic diagram of TEM is illustrated as follows:

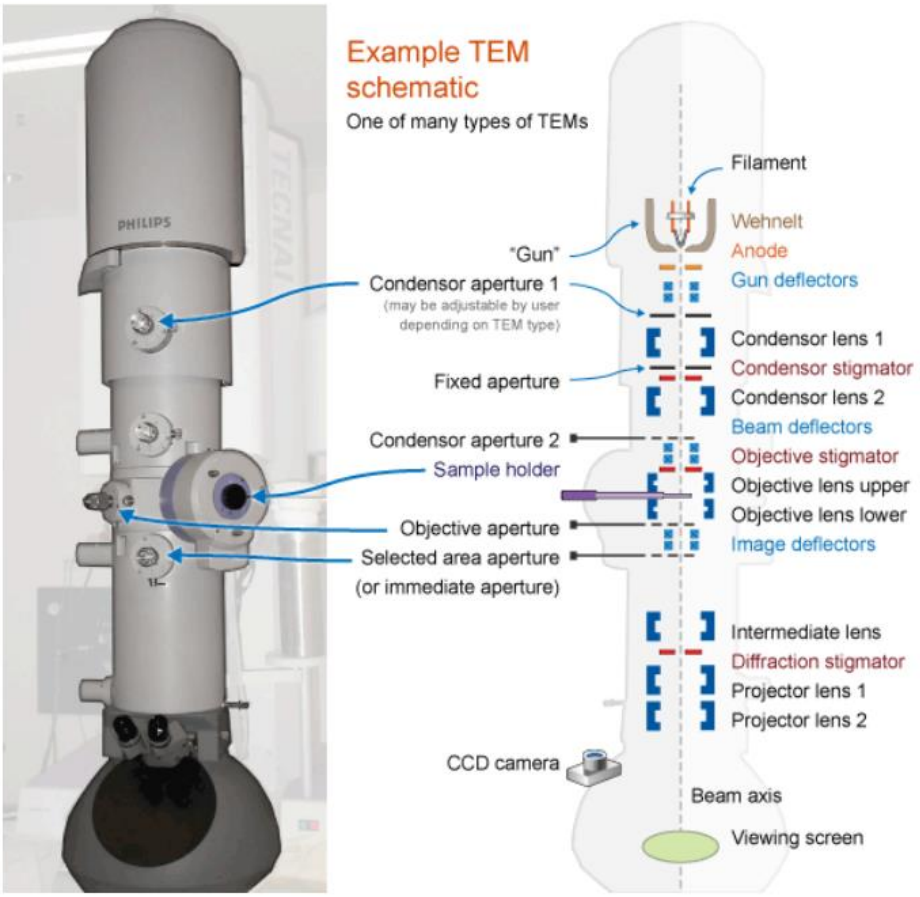


**Figure 2.8.** A general cut-away diagram of the internal structure of a transmission electron microscope. Reproduced from this website: https://myscope.training/legacy/tem/introduction/

The main components of TEM include a vacuum system, electron gun, electron column, electromagnetic lenses, specimen chamber, cooling system, detectors and viewing screen. The imaging is performed under high vacuum to minimize the interference between the electron beam and molecules from the air. An electron gun located at the top of the column is employed to generate the electron beam. A high accelerating voltage, ranging from 100-300 kV, is usually used in TEM to obtain high-energy

electron beams. Electromagnetic lenses which are made up of copper coils are employed to modulate the electron beam generated by the electron gun. A set of adjustable apertures within the column consist of small metallic discs which are thick enough to block the passage of most electrons and only permit the pass of axial electrons. For example, the purpose of the condenser lens aperture is to reduce aberration and control the spot size of the beam. The other apertures below the object lens and project lens are related to imaging. The image is projected on the screen in the viewing chamber which is located at the bottom of the column. A temporary image can be viewed on the screen. A charge-coupled device camera can be inserted into the path of the electron beam to obtain a permanent image in a digital form. One of the most common detectors equipped in TEM is the EDS for composition analysis.

Specimen preparation is a critical step to obtain high quality images in TEM, thus facilitating the result analysis. TEM specimens should be sufficiently thin (< 100 nm) to allow sufficient transmission of electrons through them to produce images with minimum energy loss. For nanomaterials such as powders, they can be deposited on the copper grid by using the corresponding dilute solution. For thick samples, ion milling is the common technique used to prepare specimens, in which argon ions are accelerated to etch the specimen surface to achieve a suitable thickness for imaging.

Compared with SEM, TEM provides more information on morphology, structures and compositions of specimens on the nanoscale with high resolution. Therefore, it has been widely used in materials science, environmental science, biological materials and geology [15]. It also should be noted that TEM is rather expensive and requires special maintenance.

### 2.1.5 X-ray Photoelectron Spectroscopy

As a surface sensitive analysis technique, X-ray photoelectron spectroscopy (XPS) is widely used to identify the elements and their chemical states on the surface of the investigated materials. The basic principle is based on the photoelectric effect. When a

beam of photons is irradiated to the surface of the sample, the photons can be absorbed by electrons on the atomic orbital of an element in the sample. If the excitation energy is high enough for the electrons to overcome the work function of the solid, the excited electrons will be freed from the nucleus of atom with a certain kinetic energy to escape into the vacuum and the atom itself becomes an excited ion. According to Einstein's law of photoelectric emission [16],

$$E_b = h\nu - E_k - \phi \qquad (2.4)$$

Where $E_b$ is the binding energy of the electron measured relative to the chemical potential, $h\nu$ is the incident photon energy, $E_k$ represents the kinetic energy of the electron measured by the instrument and $\phi$ denotes the work function for the specific surface of the material.

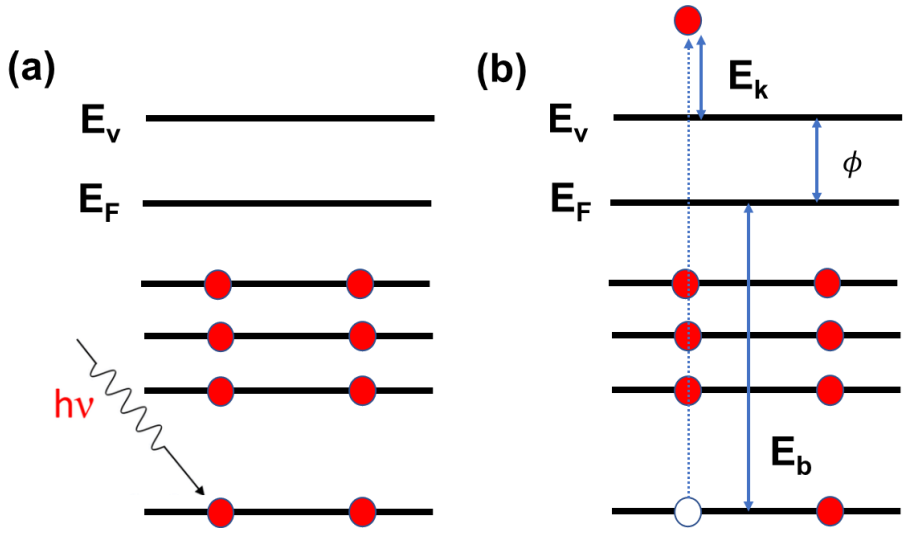


**Figure 2.9.** The photoemission process: **(a)** initial state of the element and **(b)** excited state of the element.

The binding energy ( $E_b$ ) can provide us the information about the chemical composition of the sample and different chemical environments can lead to the shift of $E_b$. For a specific monochromatic excitation source and a specific atomic orbital, the binding energy is characteristic. When the excitation source energy is fixed, the energy of the photoelectron is related to the type of element and the atomic orbital excited by ionization. Therefore, we can qualitatively analyze the element types of substances

based on the binding energy of photoelectrons. Furthermore, the electron binding energy of the inner shell will vary with different chemical environments of the atom. This change is shown as the shift of the peak (chemical shift) on the spectrum.

The common excitation source used in the photoelectron spectroscopy is a Mg or Al anode. The produced photons have a fixed energy of 1253.6 eV and 1486.6 eV for Mg Kα emission and Al Kα emission, respectively. Due to the limited mean free path of the photoelectrons caused by internal collisions, the depth of XPS analysis is usually restricted from 1 nm to 10 nm [16]. A typical XPS test is usually carried out under ultrahigh vacuum (< $10^{-7}$ Pa) conditions and the measured samples need to be dry and have clean surfaces. In some cases, the ion sputtering can be used for surface cleaning in the chamber. XPS can detect all elements in the periodic table except hydrogen and helium. The general detection limit is 0.1% (atomic percentage).

### 2.1.6 Gas Physisorption Measurements

Specific surface area and pore size distribution of solids, especially porous materials, are critical parameters in determining their electrochemical performance when used as electrode materials. These properties can be characterized by using gas physisorption. The commonly used gases are $N_2$, Ar, Kr and $CO_2$ and among them $N_2$ is widely employed due to the easy accessibility. When a solid is exposed to nitrogen gas at 77 K at a given pressure, the solid surface will adsorb an amount of $N_2$ gas molecules due to van der Waals forces. The amount of $N_2$ gas adsorbed is dependent on the temperature, pressure and characteristics of the investigated solid.

Basically, a specimen with a measured mass is placed into a tube which is then evacuated to a high vacuum to ensure a clean and uncovered surface. Then a small dose of gas is introduced into the tube, the gas molecules would form a thin monolayer on the solid surface at a low relative pressure. As more gas molecules are continuously added into the tube, it results in the formation of multiple layers on the top of each other. The un-adsorbed gas within the tube reaches a dynamic equilibrium. Eventually, a curve describing the amount of gas adsorbed as a function of relative pressure is obtained and

this curve is known as an isotherm. According to the shape of isotherm, the most common physisorption isotherms are classified into six types as shown in Figure 2.10.

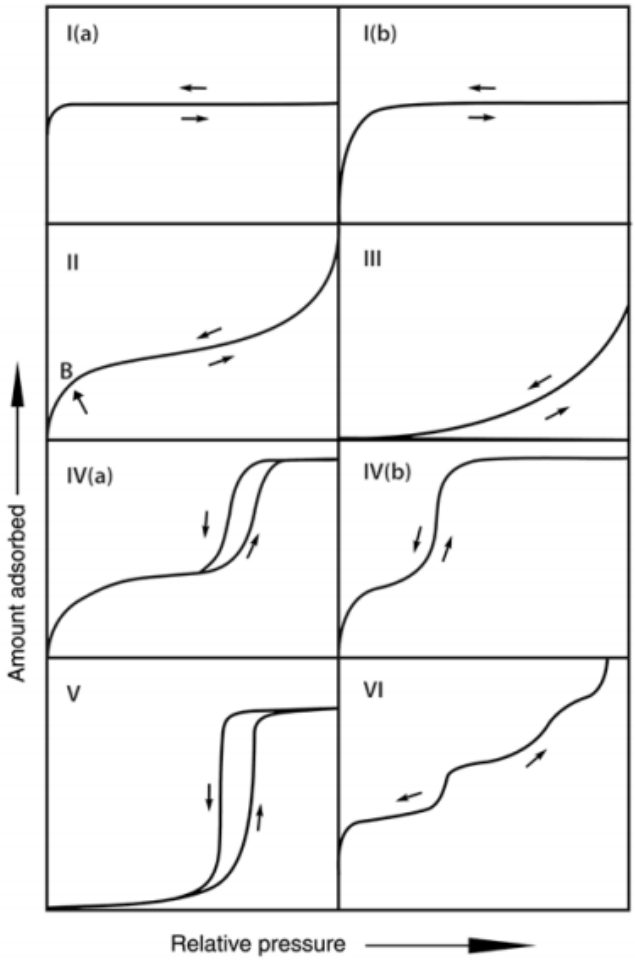


**Figure 2.10.** Classification of physisorption isotherms. Reproduced from [17].

Langmuir theory is widely used to understand the physisorption of gas molecules on a solid surface, however, it only describes an ideal situation for monolayer molecular adsorption. The Langmuir theory is extended to multilayer adsorption by the Brunauer-Emmett-Teller (BET) theory in which all layers are in equilibrium without interactions among them. Molecules underneath the layers can serve as the sites to adsorb new molecules. The BET equation can be described below [17, 18]:

$$\frac{P/P_0}{n(1-\frac{P}{P_0})} = \frac{1}{n_m C} + \frac{C-1}{n_m C}\left(\frac{P}{P_0}\right) \qquad (2.5)$$

Where $n$ denotes the specific amount of the adsorbed gas at the relative pressure $P/P_0$, $n_m$ represents the monolayer capacity of the adsorbed gas, $P$ is the pressure, $P_0$

denotes the saturation pressure of adsorbates at the adsorption temperature, and $C$ denotes the BET constant described as follows:

$$C = \exp\left(\frac{E_1 - E_L}{RT}\right) \quad (2.6)$$

Where $E_1$ is the heat of adsorption for the first layer and $E_L$ is heat of adsorption for the second and higher layers and is equal to the heat of liquefaction or vaporization.

To calculate the BET specific surface area, $\left(\frac{P}{P_0}\right)/[n(1-\left(\frac{P}{P_0}\right)]$ as a function of $\left(\frac{P}{P_0}\right)$ is plotted. To obtain a good linear relationship of this equation, the standard relative pressure $\left(\frac{P}{P_0}\right)$ range is often recommended to be between 0.05 - 0.3. According to the slope and the intercept, $n_m$ and $C$ can be calculated.

After $n_m$ is obtained, the BET specific surface area (SSA) can be estimated by using the formula below:

$$\text{SSA} = \frac{n_m \times N_A \times S_c}{m} \quad (2.7)$$

Where $N_A$ is Avogadro's number, $S_c$ represents the molecular cross-sectional area and $m$ denotes the mass of the sample.

It is worth pointing out that the practical pressure range used to fit the equation may be significantly different from the standard pressure range, especially in the case of microporous materials. Therefore, some criteria must be met during the practical operation. The parameter $C$ resulting from the linear regression must be positive and a high regression coefficient should be guaranteed (exceeding 0.999) when the relative pressure range is selected.

According to the IUPAC classification [19], pores can be classified into three categories: micropores (< 2 nm), mesopores (2 - 50 nm) and macropores (> 50 nm). Pore size analysis by gas physisorption is often limited to pores which are less than 100 nm. Nitrogen isotherms measured at 77 K are widely used to analyze micropores and mesopores present in solids. However, due to the quadrupole moment and relatively big kinetic diameter (3.6 Å) of diatomic $N_2$ molecules, it is not ideal for analyzing solids with ultramicropores (below 7 Å) [20]. Therefore, Ar at 87 K has been used as an acceptable alternative to precisely analyze ultramicropores due to the relatively small

kinetic diameter (3.4 Å) and the absence of the quadrupole moment. If pores are close to the kinetic diameter of $N_2$ or Ar, these gas molecules cannot overcome the activation energy barrier to enter the pores below 4.5 Å at cryogenic temperatures [18]. Therefore, $CO_2$, with a kinetic diameter of 3.3 Å at 273 K, is often chosen as an alternative way to probe such materials to obtain reliable results [21].

To determine the pore size distribution, various models have been used. The semi-empirical method like Horvath and Kawazoe (HK method) is widely used for analyzing slit-shaped micropores but cannot be employed in the mesopore range due to the drawback of underestimating the pore size [17]. The conventional Barrett-Joyner-Halenda (BJH) model is based on the Kelvin equation associated with the pore condensation. This model is only applicable for analysis of mesopores and may cause inaccurate analysis in narrow mesopores (< 10 nm) [17]. Therefore, in the case of materials including both micropores and mesopores, at least two different models are required to obtain the complete pore size distribution. It is worth noting that the inaccuracy in the conventional models is caused by the assumption that the pore fluid has similar thermodynamic properties as the bulk fluid. To overcome the drawbacks of the conventional models, more advanced models like non-local density functional theory (NLDFT) or Monte Carlo simulation methods are proposed to achieve a more realistic description of the sorption phenomena. These theories are based on statistical mechanics, connecting macroscopic properties to the molecular level. The NLDFT method has been shown to obtain superior results in pore size analysis and thus is recommended by an IUPAC technical report [17]. In the NLDFT method, pores of different size are assumed to have the same geometry such as slits, cylinders and spheres, and behave independently. The adsorbate is regarded as an inhomogeneous fluid which is described by its density profile across the pore. The pore filling is controlled by the solid-fluid and fluid-fluid interactions. In view of the assumption of homogeneous adsorbent surface, the pore size distribution can be reflected by the derived energetic heterogeneity [22]. Since the NLDFT method covers both micropores and mesopores, it is widely used in the literature for pore size analysis [23, 24].

## 2.2 Electrochemical Measurements

### 2.2.1 Cyclic Voltammetry

Cyclic voltammetry (CV) is a powerful and popular technique to obtain information on electrochemical behaviour, such as the thermodynamics of redox process and the kinetics of electron transfer reactions of the investigated materials [25]. Generally, a CV experiment is performed in a three-electrode system consisting of a working electrode, a reference electrode and a counter electrode, as shown in Figure 2.11. Both the working electrode and the counter electrode must be good electrical conductors and they must be inert without inducing any chemical reactions with the electrolyte solution. Also, the counter electrode should have a large surface area to allow the circuit current to easily flow between the working and counter electrode. The reference electrode is designed with a known potential which is constant during the CV experiment. In a CV experiment, all electrochemical processes are recorded relative to the reference potential.

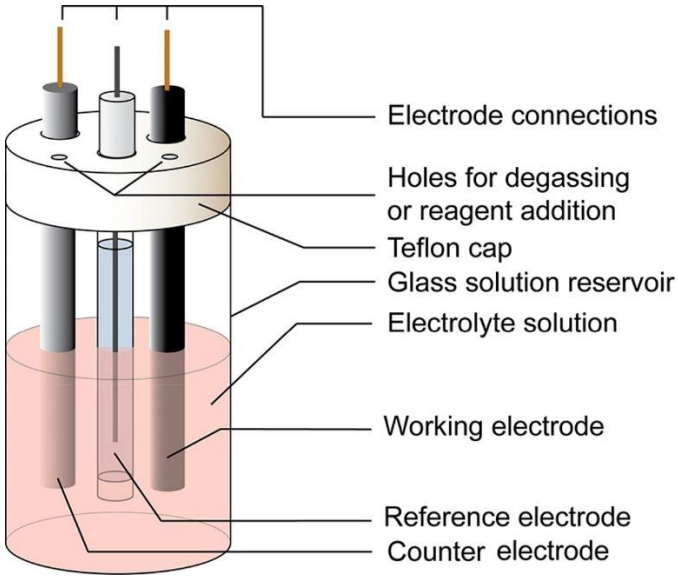


**Figure 2.11.** Schematic of an electrochemical cell for CV experiments. Reproduced from [25].

By controlling the scan rate of the working electrode potential, the periodic charge and

discharge process occurs alternately on the electrode, and the reaction process is studied by recording the current-potential curve. The working potential is varied linearly as a function of time during a CV experiment, as shown in Figure 2.12. The cycle can be repeated multiple times as required. When the current measured at the working electrode is plotted with respect to the applied potential, we can obtain the so-called voltammogram. The typical voltammogram is a duck-shaped plot, as shown in Figure 2.13H.

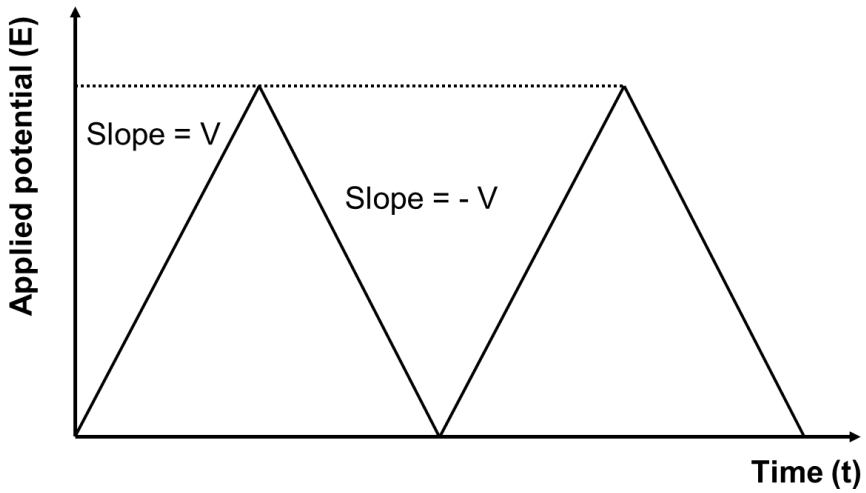


**Figure 2.12.** Schematic of the potential profile in a typical CV.

In order to understand the "duck-shape" of the cyclic voltammogram, the equilibrium between ferricenium ($Fc^+$) and ferrocene (Fc) is adopted as a typical example, which can be described by using the Nernst equation [25]. The Nernst equation describes a correlation of the potential of electrochemical reaction ($E$) with the standard electrode potential ($E^0$), activities of the reactive species and temperature of a system at equilibrium, as shown below [25]:

$$E = E^0 - \frac{RT}{nF} ln \frac{a(Red)}{a(Ox)} \qquad (2.8)$$

Where $R$ represents the universal gas constant (8.314 J $K^{-1}$ $mol^{-1}$), $T$ (K) represents the temperature, $n$ represents the number of electrons transferred per molecule, $F$ is the Faraday's constant (96485 C $mol^{-1}$), $a(Red)$ is the activity of the reduced analyte and $a(Ox)$ is the activity of oxidized analyte.

In a practical situation, the activities and $E^0$ are usually replaced by the corresponding concentrations of the analytes and the formal potential ($E^{0\prime}$), respectively. When the Nernst equation is applied to the reduction of $Fc^+$ to Fc with one electron transfer, the equation above can be rewritten in the following form:

$$E = E^{0\prime} - \frac{RT}{F} ln \frac{[Fc]}{[Fc^+]} \qquad (2.9)$$

The formal potential varies with the experimental conditions investigated and is usually evaluated by using the experimental value $E_{1/2}$ which is the mean potential between point F and point C in Figure 2.13H. The Nernst equation is useful in predicting the corresponding responses caused by any changes in the electrode potential or the analyte concentration. If the applied potential is varied, the concentrations of the analytes in solution near the electrode surface will respond according to the Nernst equation.

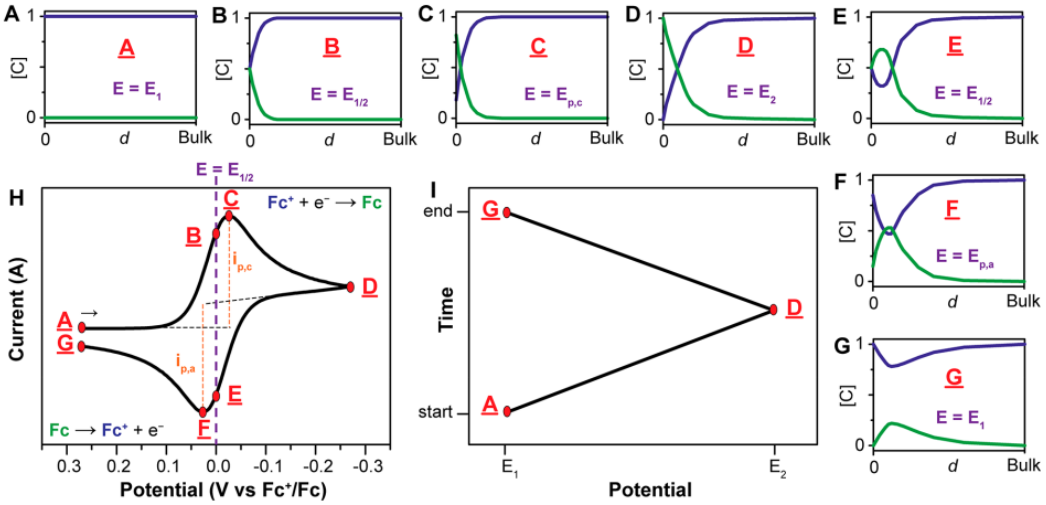


**Figure 2.13. (A−G)** Concentration profiles for $Fc^+$ (blue) and Fc (green) as a function of the distance from the electrode (d, from the electrode surface to the bulk solution, e.g., 0.5 mm) at various points during the voltammogram. **(H)** Voltammogram of the reversible reduction of a 1 mM $Fc^+$ solution to Fc at 100 mV $s^{-1}$. **(I)** Applied potential as a function of time in a general CV experiment, with the initial, switching, and end potentials represented (A, D, and G, respectively). Reproduced from [25].

As shown in Figure 2.13(A-G), the concentration-distance profiles for $Fc^+$ (denoted as blue line) and Fc (denoted as green line) at different stages in the voltammogram are

depicted, which are impacted by the applied potential and the diffusion of the species between the bulk solution and the electrode surface. When it is negatively scanned from point A to point D shown in Figure 2.13, $Fc^+$ is reduced to Fc, leading to the consumption and even depletion of $Fc^+$ near the electrode surface. As the potential is scanned from point A to point C approaching the formal potential, the cathodic current is produced and increases with the potential to result in a peak current at point C. From point C to point D, the current begins to decrease due to the limitation of mass transport. The transport of the species to the electrode surface is mainly achieved by diffusion in a quiescent solution. The region of solution containing the reduced Fc at the electrode surface is known as the diffusion layer and it keeps growing during the negative scan process. The rate of mass transport of $Fc^+$ to the electrode surface will be decelerated by the diffusion layer. As the potential is scanned more negatively, the depletion of $Fc^+$ will give rise to the decrease of measured current from point C to point D. The concentration of Fc will increase accordingly with the depletion of $Fc^+$. After it reaches point D (i.e., the switching potential), the scan direction is switched. During the positive scan direction from point D to point G, the Fc at the electrode surface is oxidized back to $Fc^+$ with the applied potential becoming more positive.

The thickness of the diffusion layer is dependent on the experimental timescale and it is usually in the range of ~μm. Faster scan rates give rise to a decrease in the thickness of the diffusion layer and thus higher peak currents are observed at higher scan rates. For a reversible electrochemical process with free diffusion, the peak current ($i_p$) can be estimated by the Randles-Sevcik equation shown below [25]:

$$i_p = 0.446nFAC^0\left(\frac{nFvD_0}{RT}\right)^{\frac{1}{2}} \qquad (2.10)$$

where $n$ denotes the electron transfer number, $F$ is the Faraday constant (96485 C $mol^{-1}$), $A$ ($cm^2$) denotes the electrode surface area, $C^0$ (mol $cm^{-3}$) is the bulk concentration of the analyte, $v$ denotes the scan rate (V $s^{-1}$), $D_0$ ($cm^2$ $s^{-1}$) denotes the diffusion coefficient of the oxidized analyte, $R$ is the ideal gas constant (8.314 J $K^{-1}$ $mol^{-1}$), and $T$ (K) represents the temperature. This equation can provide information about whether the electrolysis of an analyte is diffusion-controlled in solution. The diffusion-

controlled process exhibits a liner relationship between $i_p$ and $v^{1/2}$, while the current response for adsorbed species is expected to vary linearly with the scan rate.

Additionally, the CV is usually used to determine supercapacitor behaviour. The CV exhibits a rectangular shape in a typical electric double-layer capacitor, while there are redox peaks observed in a typical pseudocapacitor. The characteristic CVs of an electric double layer capacitor and a pseudocapacitor are shown in Figure 2.14. Based on the CV results, the specific capacitance ($C_s$) can be calculated by using the following equation:

$$C_s = \frac{2\int_{V_1}^{V_2} I\, dV}{vm(V_1 - V_2)} \qquad (2.11)$$

where $\int_{V_1}^{V_2} I\, dV$ is the integral area of the CV, $v$ is the scan rate, $m$ is the mass of the electrode, $V_1$ and $V_2$ are the lower and upper potential limits of the CV curve, respectively.

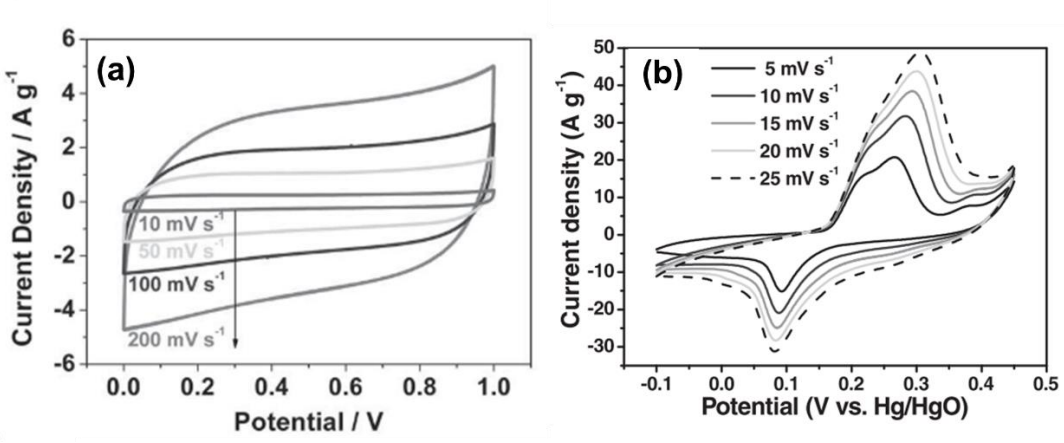


**Figure 2.14. (a)** CVs of the graphene-cellulose paper electrode at different scan rates in 1 M $H_2SO_4$, reproduced from [26]. **(b)** CVs of $Ni(OH)_2$/graphene composite at various scan rates in 6 M KOH, reproduced from [27].

### 2.2.2 Electrochemical Impedance Spectroscopy

Electrochemical impedance spectroscopy (EIS) is a powerful characterization technique widely used in various fields such as corrosion, plating, batteries, fuel cells, etc [28-30]. It is an application of a frequency-domain measurement to a complex

system that is difficult to be visualized and is regarded as a black box. The aim of use of impedance spectroscopy is to attempt to understand the properties of the box. Generally, a low amplitude oscillating voltage (1-10 mV) is applied to the system and the corresponding alternating current response is measured. With such a small voltage signal, the relationship between current and potential can be approximately linear. EIS investigates the impedance characteristics of an electrochemical system over a range of frequency which is usually from 100 kHz to 0.01 mHz. The first step is to understand the theory of impedance.

As is known to us, Ohm' law formulates the correlation between voltage and direct current flowing through a resistor as follows:

$$E = I R \quad (2.12)$$

When an alternating voltage is applied in a circuit, the concept of resistance is extended to impedance which is generally denoted as Z. Therefore, the corresponding relationship can be formulated as follows:

$$E = I Z \quad (2.13)$$

As is mentioned above, a low oscillating voltage is applied to the given system to measure the oscillating current response. The corresponding oscillating voltage is shown as below:

$$E(t) = |E| \sin(\omega t) \quad (2.14)$$

Where |E| represents the amplitude of the applied voltage, ω represents the angular frequency (ω=2πf). The response current can be described as follows:

$$I(t) = |I| \sin(\omega t + \theta) \quad (2.15)$$

Due to the presence of capacitance or inductance, a phase shift in current can be observed. The impedance can be described as following:

$$Z = \frac{E(t)}{I(t)} = \frac{|E| \sin(\omega t)}{|I| \sin(\omega t+\theta)} = |Z| \frac{\sin(\omega t)}{\sin(\omega t+\theta)} \quad (2.16)$$

According to Euler's formula,

$$e^i = cos(x) + isin(x) \quad (2.17)$$

Where $i$ is the imaginary unit ($i = \sqrt{-1}$).

Then the above formulae can be transformed by using complex numbers:

$$Z = |\mathrm{Z}|e^{i\theta} = \frac{|\mathrm{E}|e^{iwt}}{|\mathrm{I}|e^{iwt+\theta}} \qquad (2.18)$$

$$\text{Or } E = IZ = I|Z|e^{i\theta} \qquad (2.19)$$

Considering that the impedance can be represented by a magnitude $|Z|$ and a phase angle $\theta$, it can be further expressed using a polar coordinate. Usually, the impedance spectroscopy is displayed by using a complex plane as follows:

$$Z = Z_{Re} - iZ_{Im} \qquad (2.20)$$

Where $Z_{Re}$ and $Z_{Im}$ are real and imaginary parts, respectively.

$$Z = \sqrt{{Z_{Re}}^2 + {Z_{Im}}^2} \qquad (2.21)$$

The phase angle can be calculated by using the following equation:

$$\theta = \arctan\left(\frac{Z_{Im}}{Z_{Re}}\right) \qquad (2.22)$$

The phase angle can provide useful information about the investigated device. If the phase angle is equal to 0°, the device exhibits purely resistive behavior. If the phase angle ranges from 0° to 90°, the device shows both resistive and capacitive behaviors. If the phase angle is 90°, the device exhibits purely capacitive behavior. When Z is represented on an Argand diagram, a single point for a single frequency is obtained. An impedance spectroscopy usually contains a series of points, which is also called Nyquist plot composed of the real and imaginary parts of the impedance, as shown in Figure 2.15.

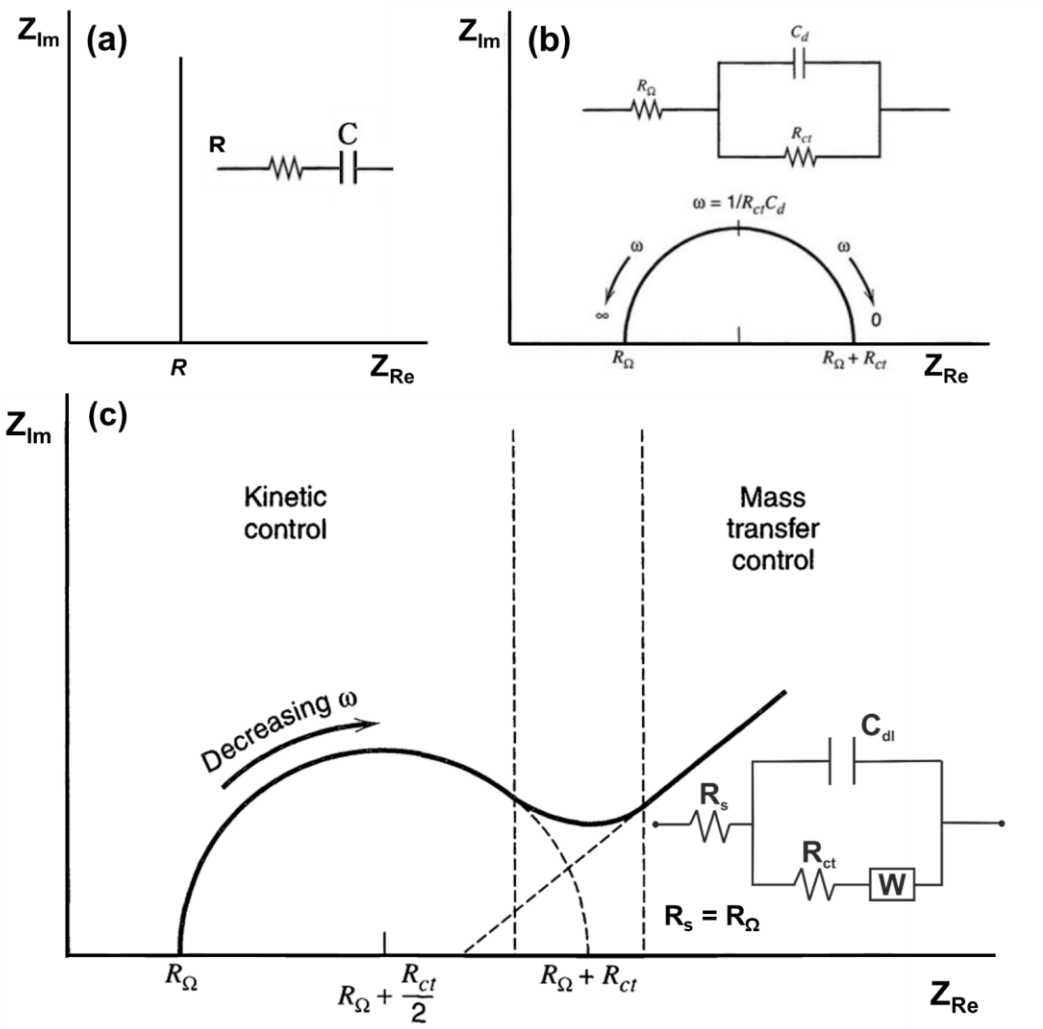


**Figure 2.15.** Typical Nyquist plots and the corresponding equivalent circuits. Reproduced from [31].

As shown in Figure 2.15c, the smallest impedance |Z| is obtained at the highest frequency. With the frequency decreasing, the shape of the spectrum is composed of a semicircle followed by a straight line. The shape in the Nyquist plot exhibits features of certain circuit elements or a combination of circuit elements. Therefore, the electrochemical process can be visualized by using equivalent circuits to analyze the investigated system. It should be noted that when an equivalent circuit is used to mimic the real electrochemical process, each component should have a potential physical meaning. Some key information can be drawn from the Nyquist plot. The semicircle intersects with the x axis at the highest frequency region, which means the imaginary component is zero. This point is denoted as $R_s$ (equivalent series resistance), including

solution resistance, electrode resistance and the contact resistance. With the frequency decreasing, the charge transfer semicircle is present at high and medium frequencies and the extrapolated diameter of the semicircle is known as charge transfer resistance ($R_{ct}$). The straight line at the low frequency region is known as the mass transport region, also known as the Warburg region. The mass diffusion can give rise to the retardation of overall processes of the diffusion-limited reactions. The decrease in the reaction rate caused by diffusion shows a resistive trait, which can be represented by a complex resistive element, i.e., the Warburg element ($W$).

Additionally, the EIS can be used to measure the capacitances of a system. The capacitances include real and imaginary components which are dependent on the applied frequency. The real and imaginary capacitances can be calculated by the following formulae [32],

$$C_{Re} = \frac{-Z_{Im}}{w|Z|^2} \quad (2.23)$$

$$C_{Im} = \frac{Z_{Re}}{w|Z|^2} \quad (2.24)$$

The real capacitance ($C_{Re}$) is usually used to reflect the charge storage capability at the given frequency. Generally, the representative capacitance is chosen at the phase angle close to 90°. The imaginary capacitance ($C_{Im}$) is related to the energy dissipation in the charge storage process.

**References**

[1] A.A. Bunaciu, E.G. Udristioiu, H.Y. Aboul-Enein, Crit. Rev. Anal. Chem., 45 (2015) 289-299.

[2] J. Epp, X-ray diffraction (XRD) techniques for materials characterization, in: Materials Characterization Using Nondestructive Evaluation (NDE) Methods, 2016, pp. 81-124.

[3] E. Prince, A.J.C. Wilson, International tables for crystallography, Kluwer., 2004.

[4] R.R. Jones, D.C. Hooper, L. Zhang, D. Wolverson, V.K. Valev, Nanoscale Res. Lett., 14 (2019) 231.

[5] R.S. Das, Y.K. Agrawal, Vib. Spectrosc., 57 (2011) 163-176.

[6] A. Smekal, Naturwissenschaften, 11 (1923) 873-875.

[7] C.V. RAMAN, K.S. KRISHNAN, Nature 121 (1928) 501-502.

[8] Z. Xu, Z. He, Y. Song, X. Fu, M. Rommel, X. Luo, A. Hartmaier, J. Zhang, F. Fang, Micromachines 9 (2018) 361.

[9] H. Zhang, C. Wang, H.L. Sun, G. Fu, S. Chen, Y.J. Zhang, B.H. Chen, J.R. Anema, Z.L. Yang, J.F. Li, Z.Q. Tian, Nat. Commun., 8 (2017) 15447.

[10] K.J.I. Ember, M.A. Hoeve, S.L. McAughtrie, M.S. Bergholt, B.J. Dwyer, M.M. Stevens, K. Faulds, S.J. Forbes, C.J. Campbell, NPJ Regen. Med., 2 (2017) 12.

[11] K. Wang, M. Huang, J. Chen, L. Lin, L. Kong, X. Liu, H. Wang, M. Lin, J. Raman Spectrosc., 49 (2018) 493-498.

[12] A. Mohammed, A. Abdullah, Proceedings of 2018 International Conference on Hydraulics and Pneumatics- HERVEX, (2019) ISSN 1454 - 8003.

[13] J.I. Goldstein, D.E. Newbury, P. Echlin, D.C. Joy, C.E. Lyman, E. Lifshin, L. Sawyer, J.R. Michael, in: K. Academic (Ed.), Springer, 2003.

[14] D. Su, Green Energy Environ., 2 (2017) 70-83.

[15] D.J. Smith, Chapter 1. Characterization of Nanomaterials Using Transmission Electron Microscopy, in: Nanocharacterisation, 2015, pp. 1-29.

[16] J.F. Watts, J. Wolstenholme, Wiley, New York, (2003).

[17] M. Thommes, K. Kaneko, A.V. Neimark, J.P. Olivier, F. Rodriguez-Reinoso, J. Rouquerol, K.S.W. Sing, Pure Appl. Chem., 87 (2015) 1051-1069.

[18] F. Ambroz, T.J. Macdonald, V. Martis, I.P. Parkin, Small Methods, 2 (2018) 1800173.

[19] K.S.W. Sing, D.H. Everett, R.A.W. Haul, L. Moscou, R.A. Pieroti, J. Rouquerol, T. Siemieniewska, Pure Appl. Chem., 57 (1985) 603-619.

[20] K.A. Cychosz, R. Guillet-Nicolas, J. Garcia-Martinez, M. Thommes, Chem. Soc. Rev., 46 (2017) 389-414.

[21] D. Lozano-Castelló, D. Cazorla-Amorós, A. Linares-Solano, Carbon, 42 (2004) 1233-1242.

[22] K. Sing, Colloids Surf. A: Physicochem. Eng. Asp., 187 (2001) 3-9.

[23] M. Luisa Ojeda, J. Marcos Esparza, A. Campero, S. Cordero, I. Kornhauser, F. Rojas, Phys. Chem. Chem. Phys. , 5 (2003) 1859-1866.

[24] J. Landers, G.Y. Gor, A.V. Neimark, Colloids Surf. A: Physicochem. Eng. Asp., 437 (2013) 3-32.

[25] N. Elgrishi, K.J. Rountree, B.D. McCarthy, E.S. Rountree, T.T. Eisenhart, J.L. Dempsey, J. Chem. Educ., 95 (2017) 197-206.

[26] Z. Weng, Y. Su, D.-W. Wang, F. Li, J. Du, H.-M. Cheng, Adv. Energy Mater., 1 (2011) 917-922.

[27] J. Yan, Z. Fan, W. Sun, G. Ning, T. Wei, Q. Zhang, R. Zhang, L. Zhi, F. Wei, Adv. Funct. Mater., 22 (2012) 2632-2641.

[28] Z. He, F. Mansfeld, Energy Environ. Sci., 2 (2009) 215-219.

[29] P.M. Gomadam, J.W. Weidner, Int. J. Energy Res., 29 (2005) 1133-1151.

[30] Q. Mohsen, S.A. Fadl-allah, N.S. El-Shenawy, Int. J. Electrochem. Sci., 7 (2012) 4510-4527.

[31] J.B. Allen, R.F. Larry, Electrochemical methods fundamentals and applications, John Wiley & Sons, 2001.

[32] C. Portet, P.L. Taberna, P. Simon, E. Flahaut, C. Laberty-Robert, Electrochim. Acta, 50 (2005) 4174-4181.

# Part II

# Experimental Results

# Chapter 3 Unravelling the Mechanism of Rechargeable Aqueous Zn–$MnO_2$ Batteries: Implementation of Charging Process by Electrodeposition of $MnO_2$

**Jie Yang,[a, b] Jianyun Cao,[c] Yudong Peng,[c] Wenji Yang,[c] Suelen Barg,[c] Zhu Liu,[c]Ian A. Kinloch,[c] Mark A. Bissett,*[c] and Robert A. W. Dryfe*[a, b]**

[a] Department of Chemistry, University of Manchester, Manchester M13 9PL, UK

[b] National Graphene Institute, University of Manchester, Manchester M13 9PL, UK

[c] Department of Materials, University of Manchester, Manchester M13 9PL, UK

**Corresponding authors: mark.bissett@manchester.ac.uk, robert.dryfe@manchester.ac.uk**

**Published in ChemSusChem 2020, 13, 4103–4110.**



**Author Contributions**:

The synthesis, characterization, and electrochemical measurement were carried out by J. Yang. The TEM characterization was performed by Y. Peng and J. Yang. The article was written by J. Yang with comments from Dr. M. A. Bissett and Prof. R. A. W. Dryfe. All authors discussed the results and commented on the manuscript.

**Abstract:** Poor cycling stability and mechanistic controversies have hindered the wider application of rechargeable aqueous Zn-$MnO_2$ batteries. Herein, we provide direct evidence of the importance of $Mn^{2+}$ in this type of battery by using a bespoke cell. Without pre-addition of $Mn^{2+}$, the cell exhibits an abnormal discharge-charge profile, meaning it functions as a primary battery. By adjusting the $Mn^{2+}$ content in the electrolyte, the cell recovers its charging ability, via electrodeposition of $MnO_2$. Additionally, a dynamic pH variation has been observed during the discharge-charge process, with a precipitation of $Zn_4(OH)_6(SO_4)\cdot 5H_2O$ buffering the pH of the electrolyte. Contrary to the conventional $Zn^{2+}$ intercalation mechanism, $MnO_2$ is first converted into MnOOH, which reverts to $MnO_2$ via disproportionation, resulting in the dissolution of $Mn^{2+}$. The charging process occurs by the electrodeposition of $MnO_2$, thus improving the reversibility through the availability of $Mn^{2+}$ ions in the solution.

## *Introduction*

Electrochemical energy storage devices, i.e., batteries, supercapacitors and hybrid devices ("supercapatteries"), play a crucial role in exploiting the electricity generated from renewable but intermittent energy sources such as wind and solar energy [1-5]. Li-ion batteries have achieved great commercial success in the rechargeable battery market because of their high energy density and good cycling stability [6, 7]. However, their cost along with concerns about safety and environmental impact significantly hinder their wider penetration to yield large-scale applications [8], hence the drive to develop alternative battery chemistries such as Na-ion batteries [9], K-ion batteries [10], Mg-ion batteries [11, 12], and Al-ion batteries [13]. Most of these alternative batteries still use flammable and toxic electrolytes, which motivates the study of aqueous batteries, in principle combining low cost, high safety, and environmetal friendliness. The alkaline primary Zn-$MnO_2$ batteries have been commercialized and widely used for many years [14]. However, this type of battery suffers from poor reversibility in alkaline electrolyte due to the irreversible formation of byproducts on the cathode (i.e., $Mn(OH)_2$, $Mn_2O_3$, and $Mn_3O_4$) and the anode (i.e.,

$Zn(OH)_2$ and ZnO) [15-19]. Therefore, mild aqueous electrolytes used in the Zn-$MnO_2$ battery are expected to enhance the electrochemical performance.

Recently, rechargeable aqueous Zn-$MnO_2$ batteries have attracted attention: the above attributes of aqueous batteries add to their high theoretical specific capacity of 308 mAh $g^{-1}$ [20-22]. To date, there have been notable developments in achieving high performance Zn-$MnO_2$ batteries in mild aqueous electrolytes. However, the mechanism of the Zn-$MnO_2$ battery is far from being fully understood and remains highly controversial. Various reaction mechanisms in Zn-$MnO_2$ batteries have been proposed. The earliest reports of rechargeable Zn-$MnO_2$ batteries, described a mechanism based on reversible $Zn^{2+}$ insertion/extraction into/from the tunnels of α-$MnO_2$ [19, 20]. Subsequently, Liu et al. proposed an alternative mechanism based on conversion between α-$MnO_2$ and $H^+$ without zinc ion intercalation and de-intercalation [23]. Wang et al. proposed that both processes operated, i.e., the $MnO_2$ cathode underwent successive $H^+$ and $Zn^{2+}$ insertion/extraction [24]. Also, a precipitation of zinc hydroxide sulfate on the surface of α-$MnO_2$ was reported without zinc intercalation into the tunnels of $MnO_2$ [25]. Recently, a reversible chloride storage in Zn-ion-trapped $Mn_3O_4$ has been proposed by Ji and co-wokers [26]. In-depth understanding of the mechanism in Zn-$MnO_2$ batteries is important in optimizing this battery chemistry in terms of performance and lifetime and thus promoting the large-scale application of this type of battery.

As well as the differences in mechanism, various crystallographic polymorphs of manganese dioxide exist, such as α-$MnO_2$ (2×2), β-$MnO_2$ (1×1), δ-$MnO_2$ (1×∞) and todorokite-$MnO_2$ (3×3), which may also be responsible for the variety in reported charge storage mechanisms when the material is employed as an electrode [23-25, 27-30]. Among them, α-$MnO_2$ with 2×2 tunnels have been of particular interest for Mn-based Zn-ion batteries. In common with other batteries, the performance of Zn-$MnO_2$ batteries is generally investigated in coin cells with a small amount of electrolyte (ca. 100 μL), which complicates in operando measurement of mechanistically relevant parameters such as local variations in electrolyte pH and composition. Consequently,

in this work, a custom cell was designed and used to reveal the reaction mechanism of the rechargeable aqueous Zn-$MnO_2$ batteries, which enables monitoring of variations in electrode potential and pH value of the electrolyte. The effect of solution phase $Mn^{2+}$ on cell reversibility is explored: it is found that this species significantly changes the ability to charge the cell. The potential of the electrodes and pH of the electrolyte was monitored in-situ during the discharge/charge process. The morphological and structural evolution of the α-$MnO_2$ cathode has also been investigated during discharge/charge using scanning electron microscopy (SEM), X-ray diffraction (XRD), transmission electron microscopy (TEM), scanning TEM energy dispersive spectroscopy (STEM–EDS) and Raman spectroscopy. This combined structural and electrochemical study sheds light on the reaction mechanism of rechargeable aqueous Zn-$MnO_2$ batteries.

## *Results and Discussion*

The sample was synthesized by using a typical hydrothermal method (shown in the Experimental section), which is widely employed for the nano-materials preparation due to its facile operation. Figure 3.1a shows the XRD pattern of as-prepared sample used as the cathode for Zn-$MnO_2$ batteries, which is well indexed into the crystalline phase of α-$MnO_2$ (JCPDS: 44-0141). The corresponding space group is $I_4/m$ with cell parameters (a=9.785 Å, b= 9.785 Å, c=2.863 Å and α= β=γ=90°). The morphology was first observed by SEM in Figure 3.1b, showing a homogeneous nanorod structure, with length ranging between 1 μm and 5 μm. The TEM further shows the detailed structure of nanorods with a diameter of 40 ± 8 nm in Figure 3.1c. The high-resolution transmission electron microscopy (HRTEM) image shows the α-$MnO_2$ nanorod with a well-defined lattice constant of 0.310 nm for the (310) crystal plane, indicating its high degree of crystallinity. As shown in Figure 3.1(d-f), the corresponding scanning transmission electron microscopy–energy dispersive spectroscopy (STEM–EDS) mapping reveals abundant Mn, O, and a low K content in the nanorod. The residual K is introduced into the $MnO_2$ tunnels by the synthetic conditions due to the $KMnO_4$

starting material. Figure 3.1g shows a profile of elements across the nanorod by linear scanning. The intensity profiles of the three elements (Mn, O and K) indicates a homogeneous distribution.

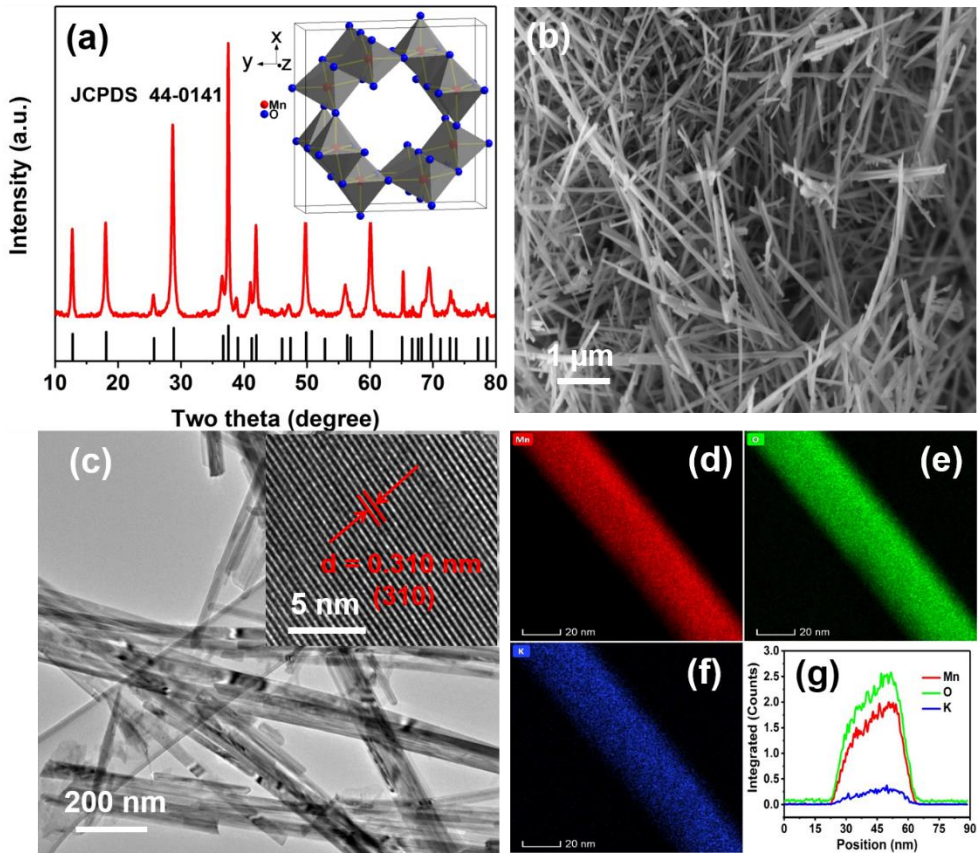


**Figure 3.1.** Characterizations of α-$MnO_2$. **(a)** X-ray diffraction pattern. (b) Representative SEM image. **(c)** Representative TEM image (inset showing the HRTEM image with a lattice distance of 0.310 nm corresponding to (310) plane). **(d-f)** STEM–EDS mappings of the elemental distributions of Mn, O and K in the $MnO_2$. **(g)** Line profiles of Mn, O and K across the $MnO_2$ nanorod.

Figure 3.2a illustrates how the reaction mechanism was investigated by using a home-made cell composed of α-$MnO_2$ as the cathode, Zn foil as the anode and 2 M $ZnSO_4$ with different concentrations of $MnSO_4$ as the electrolyte without separator. Although the cycling stability of the $MnO_2$ electrode has been improved by adding $Mn^{2+}$ to the

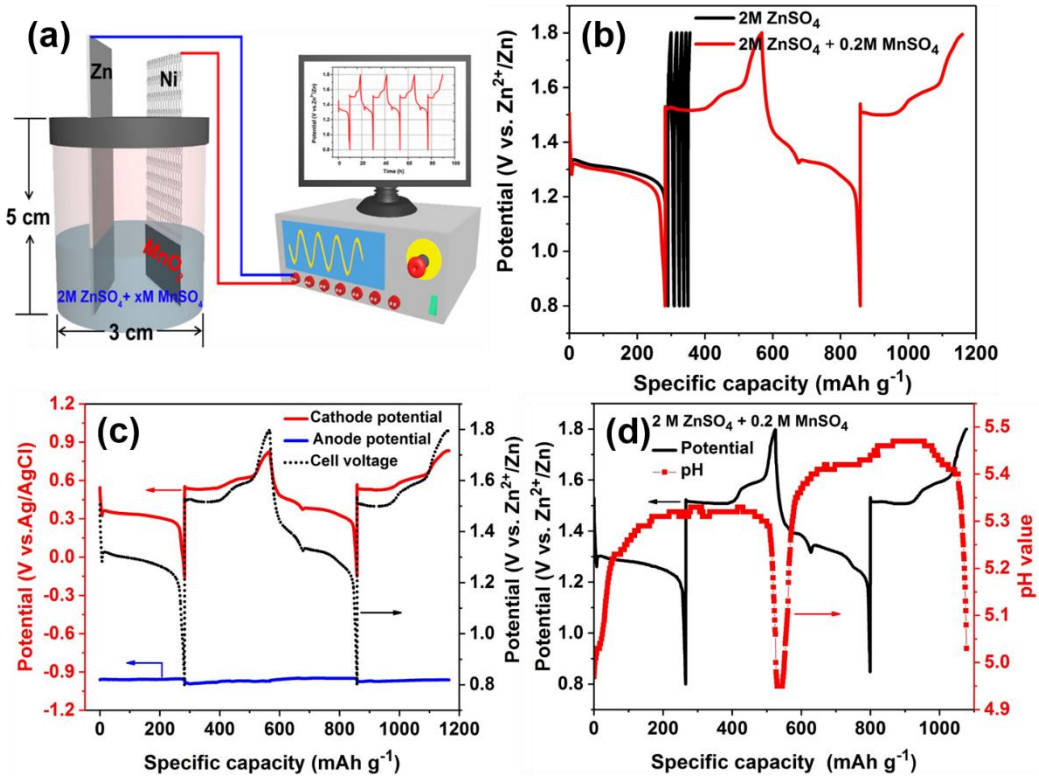


**Figure 3.2.** Tests in a home-made cell composed of a working electrode (α-$MnO_2$), counter electrode (Zn) and electrolyte without separator: **(a)** Schematic diagram of the cell, **(b)** Galvanostatic discharge and charge curves in 2 M $ZnSO_4$ and 2 M $ZnSO_4$ + 0.2 M $MnSO_4$, **(c)** In-situ potential monitoring, **(d)** In-situ pH monitoring.

electrolyte. Interestingly, we found that the cell was able to discharge with a high specific capacity of ~283 mAh $g^{-1}$ and almost lost the ability to charge, shown in Figure 3.2b. The subsequent cycles show a quite low revesible capacity of about 9 mAh $g^{-1}$ (discharging for 0.3 h at 30 mA $g^{-1}$) without the addition of $MnSO_4$. Also a brown deposit was observed on the current collector after charging, indicating the formation of $MnO_2$, shown in Figure S3.(1-3). Since there is no $Mn^{2+}$ in the electrolyte, it is inferred that $Mn^{2+}$ dissolves into the solution during the discharge process. The dissolved $Mn^{2+}$ in the first discharge process was measured by Inductively Coupled Plasma Optical Emission Spectroscopy (ICP-OES). The amount of $Mn^{2+}$ in the electrolyte was calcucated to be 0.774 mg, which is less than half of the total mass of Mn in the $MnO_2$ cathode (2.8 mg), shown in Figure S3.4. Also previous literature has reported that the dissolution of $Mn^{2+}$ results in a rapid capacity fade [23].Consequently,

various concentrations of $MnSO_4$ were added to the 2 M $ZnSO_4$ electrolyte, as shown in Figure S3.5. Significantly, there is no difference in the first discharge curve, but the charging curve begins to recover to a normal state compared with that using 2 M $ZnSO_4$ electrolyte and the cell can then be cycled normally, as shown in Figure 3.2b. This direct comparative experiment reveals that $Mn^{2+}$ plays a vital role in the charging behavior of the cell, not simply enhancing the cycling ability of the $MnO_2$ electrode. This abnormal phenomenon requires us to reconsider the discharge and charge processes. If the discharge product is MnOOH or $ZnMn_2O_4$ as previously reported in the literature, then the cell should be charged normally to extract the inserted ions without addition of $MnSO_4$, leading to a relatively high reversible capacity, contrary to what is observed in our study.

It is well-known that manganese dioxide can be electrodeposited from $Mn^{2+}$ aqueous solution by the following generalized reaction [31]:

$$Mn^{2+} + 2H_2O \rightarrow MnO_2 + 4H^+ + 2e^- \quad (E°=1.23\ V) \qquad (3.1)$$

Based on the Nernst equation, the theoretical potential to form $MnO_2$ by electrodeposition in 0.2 M $MnSO_4$ solution is calculated to be 1.413 V (vs. $Zn^{2+}/Zn$), as shown in the Supporting Information. An in-situ potential monitoring of each electrode was performed by using an Ag/AgCl reference electrode shown in Figure 3.2c. The potential on the zinc anode is fairly consistent during the discharge-charge process. The potential on the cathode changes gradually during the discharge process, while it dramatically jumps to 1.523 V (1st cycle) or 1.520 V ( 2nd cycle) (vs. $Zn^{2+}/Zn$) at the beginning of the charge process. This potential is consistent with the required theoretical potential of $MnO_2$ electrodeposition, suggesting a possible electrodeposition of $MnO_2$. Also the electrodeposition of $MnO_2$ would cause pH variations in the solution. So an in-situ pH monitoring of the electrolyte during the discharge–charge process was also carried out. As shown in Figure 3.2d, the electrolyte pH value increases as

discharge proceeds. It reaches a pH of 5.33 at the end of discharge with a plateau region around this value. Upon charging, there is a slow decrease in the pH value and it goes back to the initial value at the end of the charge process. During the charge process, the variation in pH provides evidence that the charging process is probably based on the electrodeposition of $MnO_2$. To give further support for this, the electrodeposition of $MnO_2$ was investigated with a bare nickel mesh as working electrode, a Zn foil as counter electrode and 2 M $ZnSO_4$ + 0.2 M $MnSO_4$ as electrolyte.

As shown in Figure S3.6a, the charge-discharge profile for the bare nickel mesh is quite similar to that in the Zn-$MnO_2$ battery although there is no active material loaded on the cathode. Without $MnSO_4$ additive, the bare nickel mesh only exhibits a capacitor-like behaviour in Figure S3.6b, indicating that the $MnO_2$ electrodeposited from the solution acts as the active material. Considering that the cell cannot normally charge without the $Mn^{2+}$ as additive and the onset charging potential is quite close to the electrodeposition potential of $MnO_2$ coupled with the trend in pH value during the charging process, it is speculated that charging is based on the electrodeposition of $MnO_2$ on the cathode. The pre-addition of $MnSO_4$ in the solution can provide enough Mn for electrodeposition of $MnO_2$ to compensate for the loss of $MnO_2$ from the electrode.

Ex-situ XRD and SEM data was acquired for the α-$MnO_2$ cathode in the 2 M $ZnSO_4$ + 0.2 $MnSO_4$ electrolyte to reveal the phase and morphology evolution, respectively. As shown in Figure 3.3a-b, some emerging peaks at around 8.0°, 16.0°, 21.1°, 24.4°, 27.3°, 32.7°, and 34.7° are well matched to $Zn_4(OH)_6(SO_4)\cdot 5H_2O$ (JCPDS: 78–0246) during the discharging process. The zinc hydroxide sulfate hydrate ($Zn_4(OH)_6(SO_4)\cdot nH_2O$, n=0, 0.5, 1, 3, 4, and 5, ZHSH) consists of stacked zinc hydroxide layers. The interlayer space is filled with zinc sulfate and different numbers of water molecules, resulting in an interlayer distance of 7-11 Å [25, 32-34]. When the cell is further discharged to 0.8 V, the corresponding peak intensity of $Zn_4(OH)_6(SO_4)\cdot 5H_2O$ shows an upward trend,

indicating its growth. During the subsequent charging process, the intensity of $Zn_4(OH)_6(SO_4)\cdot 5H_2O$ peaks gradually decreases and finally the corresponding peaks disappear, suggesting a reversible precipitation/dissolution of $Zn_4(OH)_6(SO_4)\cdot 5H_2O$. As shown in Figure 3.3c, the original $MnO_2$ electrode exhibits a clean surface. After discharging, some large flakes emerge on the electrode surface in Figure 3d and 3e. Energy-dispersive spectroscopy (EDS) analysis shows that the flake-like product contains abundant Zn, O and S, in Figure S3.7. During the subsequent charging process, the large flakes gradually disappear in Figure 3.3f-3.3h. The reversible morphological evolution during the discharge/charge process is consistent with the XRD results. In fact, the formation of this material has been independently reported by other groups [23, 25, 35]. It is worth noting that the formation of zinc hydroxide sulfate has been rationalised in various ways. Liu et al. [23] think that with the consumption of $H^+$ in the electrolyte, the increasing concentration of $OH^-$ leads to the formation of zinc hydroxide sulfate hydrate. On this basis they proposed a new mechanism based on the conversion reaction between $MnO_2$ and $H^+$ without zinc ion intercalation and de-intercalation. Oh et al. [25] attribute the precipitation of zinc hydroxide sulfate hydrate to the disproportionation of the unstable trivalent manganese. The dissolution of $Mn^{2+}$ into the solution leads to an increase in the pH of the solution, thus triggering precipitation of zinc hydroxide sulfate hydrate on the electrode surface. There is no doubt that the formation of zinc hydroxide sulfate hydrate is intimately bound to variation in solution pH, but the reason for the pH variation is unclear.

Also, the point at which the zinc hydroxide sulfate forms has not been mentioned. According to ex situ XRD results from Xia's group [35], the zinc hydroxide sulfate hydrate flakes do not form in the potential region from 1.8 V to 1.35 V (vs. $Zn^{2+}/Zn$) and start to emerge with further discharging to 1 V (vs. $Zn^{2+}/Zn$). During the subsequent charging, the zinc hydroxide sulfate hydrate gradually vanishes. To confirm that the formation of zinc hydroxide sulfate hydrate is pH-dependent, the discharged electrode was washed with acetic acid. As shown in Figure S3.8, it is found that the flakes on the electrode surface can be totally removed, verifying the pH-dependent property of zinc

hydroxide sulfate hydrate. It is also observed that there are far fewer $MnO_2$ nanorods on the surface, indicating the consumption of $MnO_2$ during the discharge process.

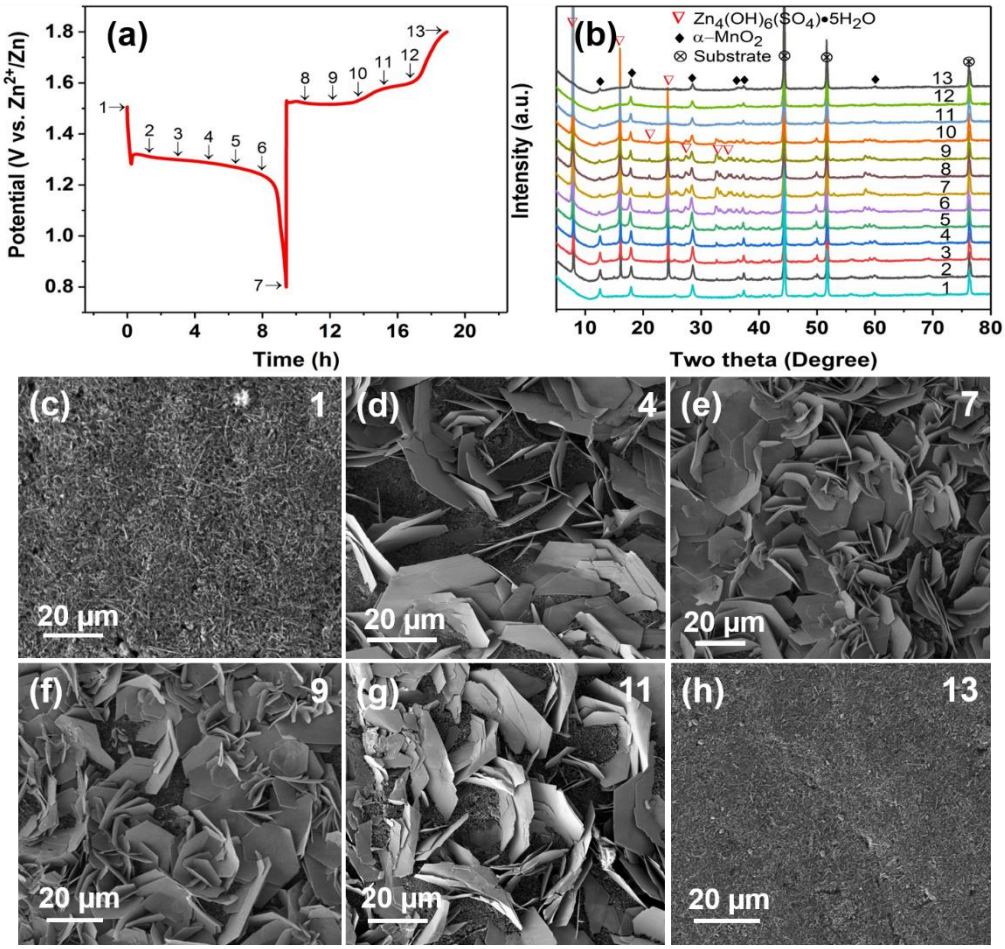


**Figure 3.3. (a)** A typical profile during the first discharge-charge process at 30 mA $g^{-1}$, **(b)** Evolution of ex-situ XRD patterns of $MnO_2$ electrodes recorded at different states denoted in a, **(c-h)** Corresponding SEM images of $MnO_2$ electrodes collected at states denoted by 1, 4, 7, 9, 11, 13.

Also, the XRD pattern of the discharged product was compared with the pure $ZnMn_2O_4$, which does not demonstrate a good match with reported intercalated phases in the literature, shown in Figure S3.9 (a-b). Further, the XRD pattern of the discharged product was compared with pure MnOOH, shown in Figure S3.9 (c-d). It was previously reported that the MnOOH phase as a discharged product was submerged in the strong characteristic peaks of current collector (carbon paper) and resultant products [23]. However, the strongest peak of MnOOH at 26.3° was not detected in our study.

The peaks from zinc hydroxide sulfate hydrate dominate the XRD patterns of the discharged product and neither MnOOH nor $ZnMn_2O_4$ can be detected. Since the electrode surface is covered by the zinc hydroxide sulfate hydrate, the complex peaks complicate the determination of the structural evolution of $MnO_2$. So the fully discharged electrode was washed with acetic acid to remove the precipitated zinc hydroxide sulfate hydrate. Surprisingly, only α-$MnO_2$ can be observed, and no evidence for $Zn^{2+}$ or proton intercalation into α-$MnO_2$ can be found, as shown in Figure S10. This is consistent with Oh et al.'s report [25]. So it is more likely that the Zn ions cannot intercalate into the tunnels of α-$MnO_2$ to form intercalated phases: this point was further investigated by TEM and Raman spectroscopy (see below). The phase and morphology evolution of α-$MnO_2$ with pure 2 M $ZnSO_4$ electrolyte was also investigated, shown in Figure S3.11. With regard to MnOOH, it is probably unstable due to the Jahn-Teller effect of $Mn^{3+}$ ion, thus forming solid $MnO_2$ and aqueous $Mn^{2+}$ [25, 36, 37]. This shows a good match with the observation that there is a brown deposit on the current collector during the charge process although $Mn^{2+}$ is not pre-added to the solution. Additionally, this is consistent with the XRD result after the zinc hydroxide sulfate hydrate flakes are removed with the weak acid. A previous report suggested that there is a phase transformation between α-$MnO_2$ and Zn-buserite [29]. However, it should be noted that XRD pattern of zinc hydroxide sulfate hydrate phase is quite similar to the previously reported Zn-birnessite [25, 30]. So more attention should be paid to analyse the XRD results and other techniques are required to further elucidate the reaction mechanism of α-$MnO_2$.

TEM was used to gain further insight into the structural evolution of α-$MnO_2$ during discharge process. As shown in Figure 3.4a (also in Figure S3.12), the morphology of α-$MnO_2$ electrode is well maintained when it is first discharged to 0.8 V. The corresponding scanning transmission electron microscopy-energy dispersive spectroscopy (STEM-EDS) mapping reveals various elements such as Mn, O, K, Zn and S in the discharge products, shown in Figure 3.4(b-f). The Mn, O and K elements

simultaneously coexist in the same region while Zn, O and S elements simultaneously coexist in a different region. Previous papers reported that zinc ions intercalate into the tunnel of $MnO_2$ to form the spinel $ZnMn_2O_4$, or a tunnel or layered $Zn_xMnO_2$ phase [19, 20, 29]. However, it is found that Zn is not homogeneously distributed in the bulk of

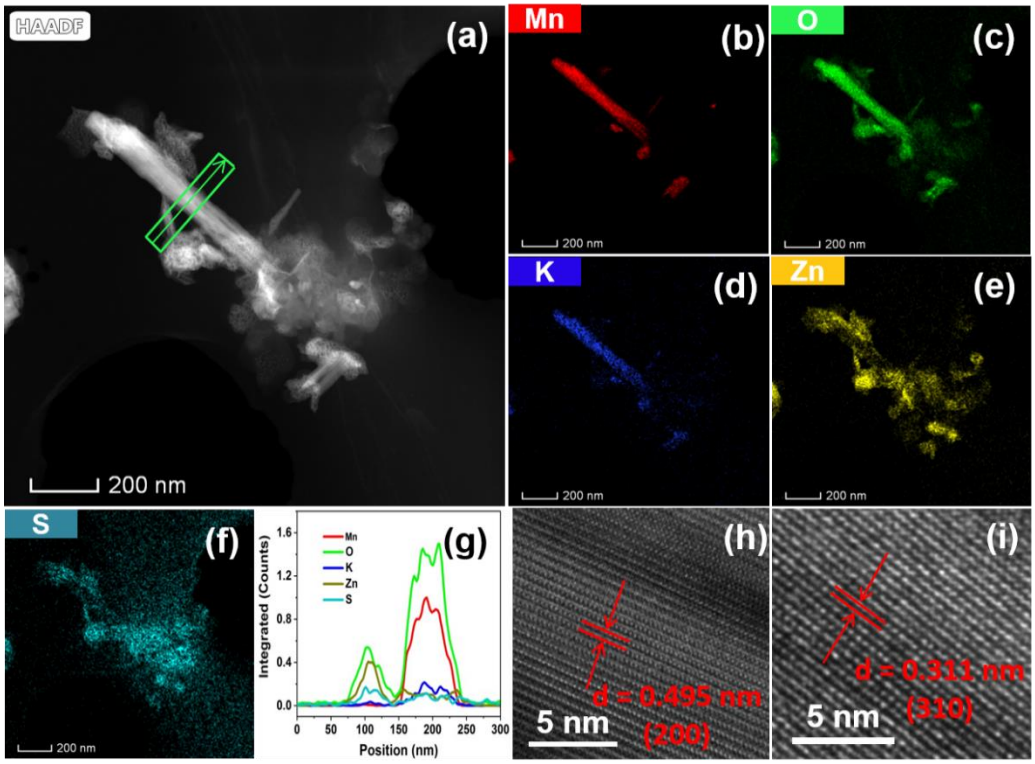


**Figure 3.4.** TEM/HRTEM images of $MnO_2$ electrodes after 1st discharge: **(a)** STEM-HAADF image of short nanorods, **(b-f)** STEM-EDS mappings of different elements, **(g)** Line profiles of different elements across the α-$MnO_2$ nanorod, **(h-i)** HRTEM images.

$MnO_2$ and only exists on the surface of the $MnO_2$ nanorod. The Zn element shows a similar distribution to that of S, indicating the formation of zinc hydroxide sulfate, which is consistent with results of SEM and XRD. To further confirm the localized elemental distribution, the corresponding linear scanning position is shown in the highlighted rectangle. As shown in Figure 3.4g, Mn, O and K clearly exhibit a synchronous trend while Zn, S show a different synchronous trend, indicating that the

zinc ions do not intercalate into the tunnel of $MnO_2$. The HR-TEM was further used to reveal the lattice distance of the discharged products, shown in Figure 3.4(h, i). A larger lattice distance of 0.495 nm is indexed to the (200) plane of α-$MnO_2$ and a smaller lattice distance of 0.311 nm is consistent with the (310) plane of α-$MnO_2$. The TEM results showed that the lattice fringes from the discharged products do not match the reported intercalated phases in the literature. Also the synthesized pure $ZnMn_2O_4$ (Figure S3.13) was investigated by TEM. The corresponding STEM–EDS mapping shows a homogeneous distribution of Zn, Mn and O, shown in Figure S3.(14-15). The lattice distance was revealed by HR-TEM, showing a 0.485 nm corresponding to the (101) plane of $ZnMn_2O_4$, shown in Figure S3.16. Furthemore, the electrochemical performance of the $ZnMn_2O_4$ was investigated by galvanostatic charge-discharge method. It is found that the $ZnMn_2O_4$ does not exhibit electrochemical activity with an extremely low specific capacity of 15 mAh $g^{-1}$, as shown in Figure S3.17. The charge-discharge profile, showing a capacitor-like behaviour, suggests that the zinc ions in the spinel $ZnMn_2O_4$ cannot be extracted from the tunnel, which provides an indirect proof to support our conclusion that the mechanism does not involve the insertion of zinc ions. Steingart et al. reported that $ZnMn_2O_4$ is electrochemically inert, which is consistent with our results [38]. Although $Zn^{2+}$ has a relatively small ionic radius of 0.75 Å, it is still difficult to find ideal cathode materials to accomodate $Zn^{2+}$ due to the strong electrostatic interaction between divalent $Zn^{2+}$ and solid framework of host materials as well as the difficulty in redistributing the multiple charges of the inserted cations in the host [25, 39]. Additionally, the high ionic radius of hydrated $Zn^{2+}$ (Table S3.1) will add an additional barrier for the intercalation process despite the partial charge shielding of the solvation shell [30]. Therefore, our conclusion is that it is difficult for zinc ions to intercalate into the tunnel of α-$MnO_2$.

Although the test capacity may be affected by various factors such as the properties (defects, surface area) of $MnO_2$, the composition of the electrode, and measurement conditions like discharge current and electrolyte, the capacity obtained at a low current

density is more likely to approach the theoretical capacity of the electrode materials. The practical specific capacity of $MnO_2$ reported by most researchers is less than the theoretical capacity of 308 mAh $g^{-1}$ [22, 40-42], which is consistent with our results. Although the $MnO_2$/a-CNT nanocomposites displayed an ultrahigh capacity of 665 mAh $g^{-1}$ at 0.1 A $g^{-1}$, the improved capacity was attributed to the numerous oxidative functional groups in the acid-treated carbon nanotubes, which could act as additional storage sites [43]. Based on the statistical principle and experimental errors, the Faradaic reaction is more likely based on one electron transfer reaction ($Mn^{4+} + e^- \rightarrow Mn^{3+}$) in this battery system. It means that the $MnO_2$ will not directly transform into $Mn^{2+}$ although we have directly observed the dissolution of $Mn^{2+}$ into the solution. The intermediate is likely to be MnOOH. Previous observations showed that MnOOH dissolved significantly below pH 6 via an acidic disproportionation due to the high-spin electronic configuration [36, 44]. It will form dissolved $Mn^{2+}$ and solid $MnO_2$ [$2Mn^{3+} \rightarrow Mn^{2+}(aq) + Mn^{4+}(s)$] due to the Jahn-Teller effect [25, 37]. During the whole discharge process, the pH of the solution is always below 6, which will facilitate the transformation of MnOOH into $Mn^{2+}$ and $MnO_2$. This is probably the reason for the difficulty in detecting the intermediate MnOOH. It should be noted that this disproportionation involves a localized electron transfer without contributing any capacity.

Based on the above analysis, the reaction mechanism of this battery during the discharge process including the intermediate $Mn^{3+}$ can described as follows:

Reductive half-reaction:

$$MnO_2(s) + H^+(aq) + e^- \rightarrow MnOOH(s) \qquad (3.2)$$

$$2MnOOH(s) + 2H^+(aq) \rightarrow MnO_2(s) + Mn^{2+}(aq) + 2H_2O(l) \qquad (3.3)$$

$$4Zn^{2+}(aq) + 6OH^-(aq) + SO_4^{2-}(aq) + 5H_2O(l) \rightarrow Zn_4(OH)_6(SO_4)\cdot 5H_2O(s)\downarrow \qquad (3.4)$$

Oxidative half-reaction: $Zn(s) \rightarrow Zn^{2+}(aq) + 2e^-$ (3.5)

Overall: $4MnO_2(s) + 10H^+(aq) + 4Zn(s) + SO_4^{2-}(aq) + 3H_2O(l) \rightarrow 4Mn^{2+}(aq) + Zn_4(OH)_6(SO_4)\cdot 5H_2O(s)\downarrow$ (3.6)

During the charge process, the reaction mechanism can be formulated as follows:

Oxidative half-reaction: $Mn^{2+}(aq) + 2H_2O(l) \rightarrow MnO_2(s) + 4H^+(aq) + 2e^-$ (3.7)

$Zn_4(OH)_6(SO_4)\cdot 5H_2O(s) + 6H^+(aq) \rightarrow 4Zn^{2+}(aq) + SO_4^{2-}(aq) + 11H_2O(l)$ (3.8)

Reductive half-reaction: $Zn^{2+}(aq) + 2e^- \rightarrow Zn(s)$ (3.9)

Overall: $4Mn^{2+}(aq) + Zn_4(OH)_6(SO_4)\cdot 5H_2O(s) \rightarrow 4MnO_2(s) + 10H^+(aq) + 4Zn(s) + SO_4^{2-}(aq) + 3H_2O(l)$ (3.10)

Although this aqueous battery is safe and environmentally friendly compared with organic-based batteries, the key conversion reaction is more complicated than that in intercalation chemistry since it is accompanied by MnOOH disproportionation and a precipitation reaction. The accessibility of $Mn^{2+}$ in the solution is crucial to improving the reversibility of this battery and the pH of the electrolyte need to be controlled. The precipitation reaction plays a vital role in dynamically tunning the pH of the solution. If the pH is higher than ~7 (alkaline solution), this type of battery functions as an alkaline primary battery. If the pH is lower than ~3 (acid solution), the zinc metal is unstable with respect to the generation of hydrogen gas. This fundamental research is expected to provide useful guidance in promoting the practical application of rechargeable aqueous Zn-$MnO_2$ batteries.

## *Conclusions*

In summary, we have provided direct evidence of the importance of $Mn^{2+}$ in rechargeable aqueous Zn-$MnO_2$ batteries by studying their discharge-charge behaviour. The reaction mechanism was studied with a home-made cell containing a large amount of electrolyte (ca. 12 mL) without separator, which enables monitoring of variations in electrode potential and pH value of the electrolyte. In the absence of pre-added $Mn^{2+}$ in the electrolyte, the dissolved $Mn^{2+}$ ions are not easily returned to the electrode, leading

to the instantaneous failure of the cell. This provides a direct way to identify the degradation mechanism of the rechargeable aqueous Zn-$MnO_2$ batteries, thus helping to reveal the underlying reaction mechamism. By increasing the content of $Mn^{2+}$ in the electrolyte, the loss of $MnO_2$ from the eletrode can be replenished by electrodeposition of $MnO_2$ from the pre-addition $Mn^{2+}$ in the electrolyte, leading to a normal charging behaviour. This degradation and charging mechanism also applies to other manganese oxides such as β-$MnO_2$. More interestingly, the in-depth investigation of morphology and structure of the discharged cathode reveals that there is a conversion reaction between $MnO_2$ and MnOOH without zinc ion intercalation into the tunnel of α-$MnO_2$ to form $ZnMn_2O_4$ or $Zn_xMnO_2$ phase. The dissolution of $Mn^{2+}$ was caused by the acidic disproportionation of MnOOH. The precipitation of zinc hydroxide sulfate hydrate is essential to buffer the pH value of the solution. These findings shed light on the degradation and reaction mechanism of rechargeable aqueous Zn-$MnO_2$ batteries and provide useful guidance in designing high performance rechargeable aqueous Zn-$MnO_2$ batteries.

## *Acknowledgements*

We thank the President's Doctoral Scholarship (PDS) Award from the University of Manchester for providing a studentship for J.Y. We thank the EPSRC (UK) for support (EP/R023034/1). Further support for equipment, funded via EPSRC grants to the Sir Henry Royce Institute (grant references EP/S019367/1 and EP/P025021/1), is gratefully acknowledged.

## *Conflict of interest*

The authors declare no conflict of interest.

**Keywords:** Aqueous Zn-$MnO_2$ batteries • conversion • $Mn^{2+}$ dissolution • degradation • electrodeposition

## *References*

[1] M. Armand, J.-M. Tarascon, Nature, 451 (2008) 652-657.

[2] J. Li, Y. Zhang, X. Zhang, J. Huang, J. Han, Z. Zhang, X. Han, P. Xu, B. Song, ACS Appl. Mater. Interfaces, 9 (2017) 398-405.

[3] S. Kelly-Richards, N. Silber-Coats, A. Crootof, D. Tecklin, C. Bauer, Energy Policy, 101 (2017) 251-264.

[4] G. Ren, J. Liu, J. Wan, Y. Guo, D. Yu, Appl. Energy, 204 (2017) 47-65.

[5] G.Z. Chen, Int. Mater. Rev., 62 (2016) 173-202.

[6] J.B. Goodenough, K.S. Park, J. Am. Chem. Soc., 135 (2013) 1167-1176.

[7] D. Deng, ENERGY SCI ENG., 3 (2015) 385-418.

[8] G. Zubi, R. Dufo-López, M. Carvalho, G. Pasaoglu, Renew. Sust. Energ. Rev., 89 (2018) 292-308.

[9] J. Yang, J. Hu, M. Zhu, Y. Zhao, H. Chen, F. Pan, J. Power Sources, 365 (2017) 362-371.

[10] J.C. Pramudita, D. Sehrawat, D. Goonetilleke, N. Sharma, Adv. Energy Mater., 7 (2017) 1602911.

[11] S. Tepavcevic, Y. Liu, D. Zhou, B. Lai, J. Maser, X. Zuo, H. Chan, P. Kral, C.S. Johnson, V. Stamenkovic, N.M. Markovic, T. Rajh, ACS Nano, 9 (2015) 8194-8205.

[12] M. Mao, T. Gao, S. Hou, C. Wang, Chem. Soc. Rev., 47 (2018) 8804-8841.

[13] M.C. Lin, M. Gong, B. Lu, Y. Wu, D.Y. Wang, M. Guan, M. Angell, C. Chen, J. Yang, B.J. Hwang, H. Dai, Nature, 520 (2015) 325-328.

[14] E. Faegh, T. Omasta, M. Hull, S. Ferrin, S. Shrestha, J. Lechman, D. Bolintineanu, M. Zuraw, W.E. Mustain, J. Electrochem. Soc., 165 (2018) A2528-A2535

[15] Y. Shen, K. Kordesch, J. Power Sources, 87 ( 2000) 162-166.

[16] F.R. McLarnon, E.J. Cairns, J. Electrochem. Soc., 138 (1991) 645-656.

[17] C.-C. Yang, S.-J. Lin, J. Power Sources, 112 (2002) 174-183.

[18] N. Tang, X. Tian, C. Yang, Z. Pi, Q. Han, J. Phys. Chem. Solids, 71 (2010) 258-262.

[19] M.H. Alfaruqi, J. Gim, S. Kim, J. Song, J. Jo, S. Kim, V. Mathew, J. Kim, J. Power

Sources, 288 (2015) 320-327.

[20] C. Xu, B. Li, H. Du, F. Kang, Angew. Chem. Int. Ed., 51 (2012) 933-935.

[21] N. Zhang, F. Cheng, J. Liu, L. Wang, X. Long, X. Liu, F. Li, J. Chen, Nat. Commun, 8 (2017) 405.

[22] J. Ming, J. Guo, C. Xia, W. Wang, H.N. Alshareef, Mater. Sci. Eng. R Rep., 135 (2019) 58-84.

[23] H. Pan, Y. Shao, P. Yan, Y. Cheng, K.S. Han, Z. Nie, C. Wang, J. Yang, X. Li, P. Bhattacharya, K.T. Mueller, J. Liu, Nat. Energy, 1 (2016) 16039.

[24] W. Sun, F. Wang, S. Hou, C. Yang, X. Fan, Z. Ma, T. Gao, F. Han, R. Hu, M. Zhu, C. Wang, J. Am. Chem. Soc., 139 (2017) 9775-9778.

[25] B. Lee, H.R. Seo, H.R. Lee, C.S. Yoon, J.H. Kim, K.Y. Chung, B.W. Cho, S.H. Oh, ChemSusChem, 9 (2016) 2948-2956.

[26] H. Jiang, X. Ji, Carbon Energy, (2020) 1-6.

[27] K. Zhang, X. Han, Z. Hu, X. Zhang, Z. Tao, J. Chen, Chem. Soc. Rev., 44 (2015) 699-728.

[28] B. Lee, C.S. Yoon, H.R. Lee, K.Y. Chung, B.W. Cho, S.H. Oh, Sci. Rep., 4 (2014) 6066.

[29] B. Lee, H.R. Lee, H. Kim, K.Y. Chung, B.W. Cho, S.H. Oh, Commun. Chem., 51 (2015) 9265-9268.

[30] M. Song, H. Tan, D. Chao, H.J. Fan, Adv. Funct. Mater., 28 (2018) 1802564.

[31] A.J. Gibson, B. Johannessen, Y. Beyad, J. Allen, S.W. Donne, J. Electrochem. Soc., 163 (2016) H305-H312.

[32] A. Moezzi, M.B. Cortie, A.M. McDonagh, Dalton Trans, 42 (2013) 14432-14437.

[33] W. Liang, W. Li, H. Chen, H. Liu, L. Zhu, Electrochim. Acta, 156 (2015) 171-178.

[34] S.A. Morin, A. Forticaux, M.J. Bierman, S. Jin, Nano Lett, 11 (2011) 4449-4455.

[35] J. Huang, Z. Wang, M. Hou, X. Dong, Y. Liu, Y. Wang, Y. Xia, Nat. Commun., 9 (2018) 2906.

[36] M. Ramstedt, S. Sjöberg, Aquatic Geochemistry, 11 (2005) 413-431.

[37] T. Takashima, K. Hashimoto, R. Nakamura, J. Am. Chem. Soc., 134 (2012) 18153-

18156.

[38] B.J. Hertzberg, A. Huang, A. Hsieh, M. Chamoun, G. Davies, J.K. Seo, Z. Zhong, M. Croft, C. Erdonmez, Y.S. Meng, D. Steingart, Chem. Mater., 28 (2016) 4536-4545.

[39] E. Levi, M.D. Levi, O. Chasid, D. Aurbach, J. Electroceramics, 22 (2007) 13-19.

[40] Y. Zhang, S. Deng, M. Luo, G. Pan, Y. Zeng, X. Lu, C. Ai, Q. Liu, Q. Xiong, X. Wang, X. Xia, J. Tu, Small, 15 (2019) 1905452.

[41] Y. Zhang, S. Deng, G. Pan, H. Zhang, B. Liu, X.L. Wang, X. Zheng, Q. Liu, X. Wang, X. Xia, J. Tu, Small Methods, 4 (2020) 1900828.

[42] Y. Zhang, S. Deng, Y. Li, B. Liu, G. Pan, Q. Liu, X. Wang, X. Xia, J. Tu, Energy Storage Mater., 29 (2020) 52-59.

[43] D. Xu, B. Li, C. Wei, Y.-B. He, H. Du, X. Chu, X. Qin, Q.-H. Yang, F. Kang, Electrochim. Acta, 133 (2014) 254-261.

[44] M. Sun, B. Lan, T. Lin, G. Cheng, F. Ye, L. Yu, X. Cheng, X. Zheng, CrystEngComm, 15 (2013) 7010.

# ChemSusChem
# Supporting Information

## Unravelling the Mechanism of Rechargeable Aqueous Zn-$MnO_2$ Batteries: Implementation of Charging Process by Electrodeposition of $MnO_2$

**Jie Yang,[a, b] Jianyun Cao,[c] Yudong Peng,[c] Wenji Yang,[c] Suelen Barg,[c] Zhu Liu,[c]Ian A. Kinloch,[c] Mark A. Bissett,*[c] and Robert A. W. Dryfe*[a, b]**

### 1. Experimental Procedures

**1.1 Synthesis of $MnO_2$ and $ZnMn_2O_4$.** α-$MnO_2$ nanorods were prepared by a typical hydrothermal method [1]. Briefly, 0.50 g of $KMnO_4$ and 0.21 g of $MnSO_4{\cdot}H_2O$ were added to 32 mL deionized water to form a homogeneous solution under magnetic stirring for about 30 min. The solution was then transferred to a Teflon-lined stainless steel autoclave with a volume of 50 mL and heated in an oven at 160 °C for 12 h. The obtained product was collected by filtration, washed with deionized water, and dried at 80 °C in an oven overnight. The corresponding reaction can be formulated as follows [2]:

$$2KMnO_4 + 3MnSO_4 + 2H_2O \rightarrow 5MnO_2 + K_2SO_4 + 2H_2SO_4 \qquad (S3.1)$$

The $ZnMn_2O_4$ was prepared by a self-propagating combustion method [3]. Typically, zinc nitrate hexahydrate (14.874 g) and manganese nitrate (17.895 g) were dissolved into 100 mL water containing citric acid (43.228 g) to form a homogeneous solution with stirring. Then the solution was heated to obtain a gel precursor which was further heat-treated using a hotplate, with a set temperature of 300 °C, until it combusted. After a self-propagating combustion, the precursor was further treated in a muffle furnace under 700 °C for 2 h to obtain a fine powder.

**1.2 Characterization.** The crystal structure of the materials was characterized by Powder X-ray diffraction (XRD) using a Bruker D8 Advanced diffractometer with Cu-Kα radiation (λ = 1.5406 Å). The morphologies and structures were characterized by field-emission scanning electron microscopy (FESEM, TESCAN Mira3) and transmission electron microscopy (TEM, FEI Talos F200X). The Raman spectra were obtained by using a Renishaw inVia Raman instrument with an excitation wavelength of 532 nm. Elemental analysis of Mn in the electrolyte was conducted by Inductively Coupled Plasma Optical Emission Spectroscopy (ICP-OES) using a "PlasmaQuant" model PQ 9000.

**1.3 Electrochemical tests.** Electrodes were prepared by mixing 70 wt% of $MnO_2$ as active material with 20 wt% of carbon black ("Super-P", conductive additive) and 10 wt% of binder polytetrafluoroethylene (PTFE). The $MnO_2$ powder and carbon black were firstly dispersed and mixed in isopropanol. Then PTFE was added to get a paste which was rolled into a uniform film with thickness about 50 μm and dried at 80 °C for 24 h. Afterwards, the film was cut into smaller pieces 0.8 cm × 0.8 cm in size and about 3-4 mg in weight. The areal loading density of $MnO_2$ is 5-6 mg $cm^{-2}$. Finally, the small films were pressed on a nickel mesh as working electrode (Nickel mesh, Advent Research Materials). The electrolyte was deoxygenated by using nitrogen gas for 1h before use. For the mechanistic investigation, a home-made cell (glass cell) is composed of a working electrode ($MnO_2$, 0.8 cm × 0.8 cm), counter electrode (zinc foil 1.5 cm × 1.5 cm with a mass loading of about 191 mg $cm^{-2}$) and electrolyte (2 M $ZnSO_4$ or 2 M $ZnSO_4$ + 0.2 M $MnSO_4$, about 12 mL) without separator. The distance between

electrodes is about 2 cm. For the in-situ test, an Ag/AgCl reference electrode and a pH meter were placed between the working electrode and the counter electrode. During the discharge-charge process, the pH value of the electrolyte was recorded by using a digital pH meter per minute. Galvanostatic charge/discharge performances were conducted on a battery test system (Basytec, Germany). Cyclic voltammetry measurements were carried out using an AUTOLAB potentiostat. All the tests were performed at room temperature.

## 2. Results and Discussion

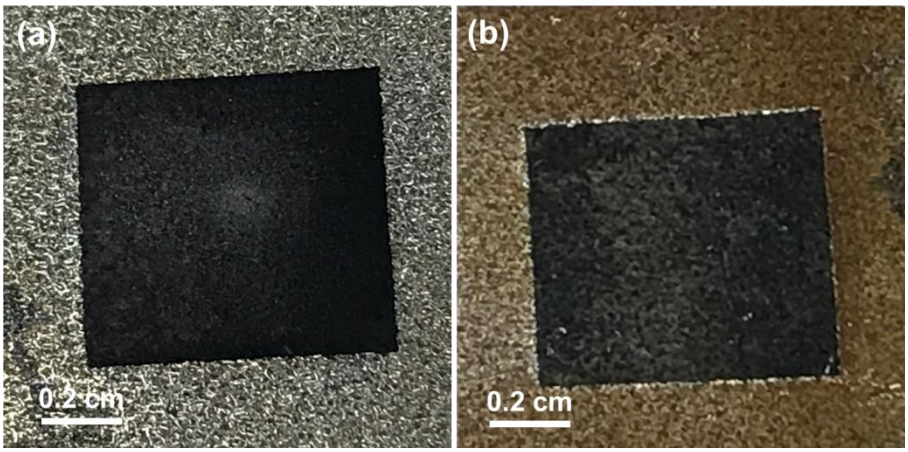


**Figure S3.1.** Digital images of the electrode: **(a)** after 1st discharge, **(b)** after 1st charge After charging, the bare nickel mesh is covered by the brown deposit.

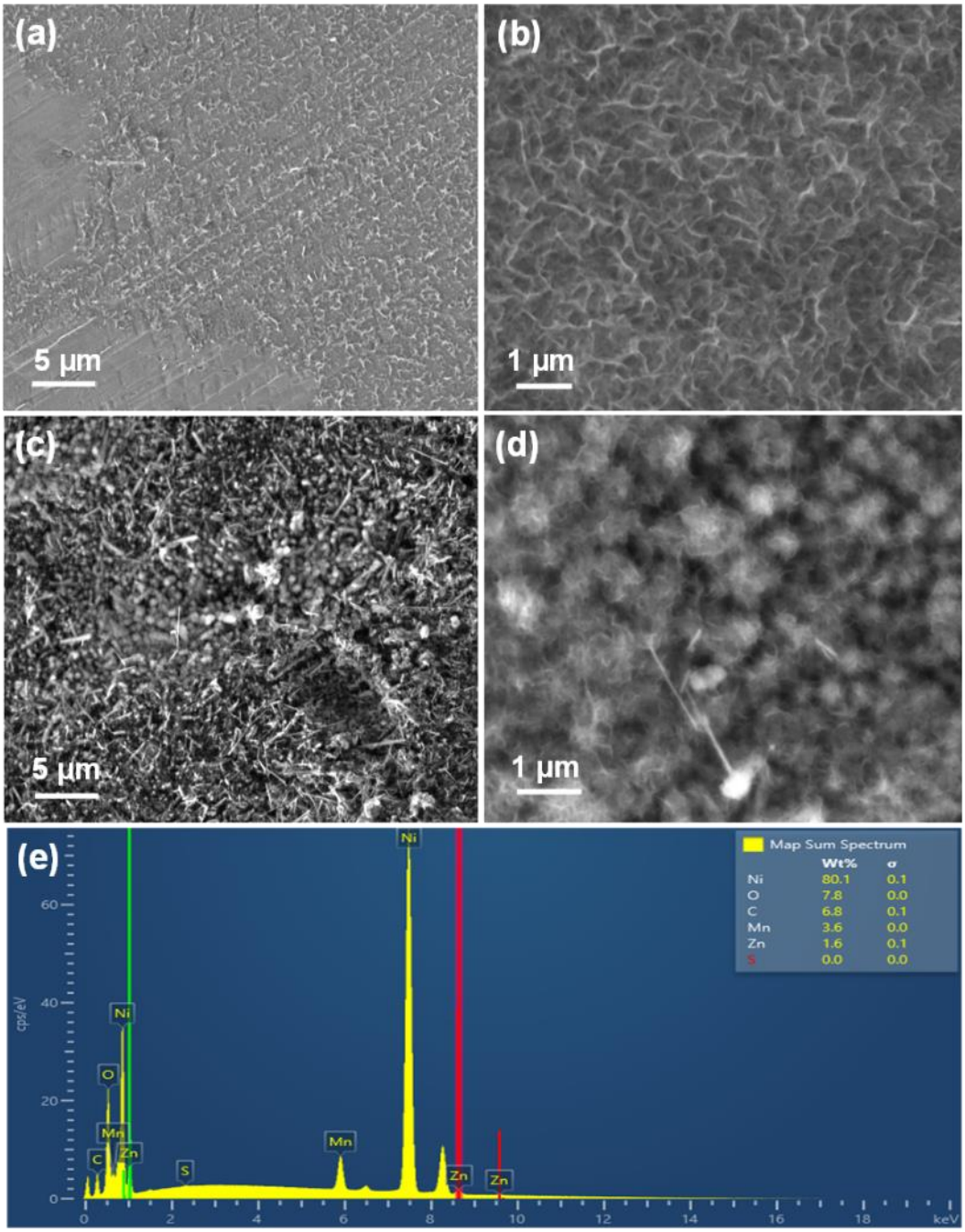


**Figure S3.2.** SEM images of the charged electrode: (a-b) the surface of bare current collector, (c-d) the surface of α-$MnO_2$ electrode, (e) energy-dispersive spectroscopy (EDS) analysis of brown deposit.

The brown deposit was investigated by SEM, exhibiting a spongiform structure in Figure S3.2. The corresponding morphology is quite common in $MnO_2$ [4]. Based on the colour and morphology as well as the elemental composition, it is inferred that this

brown deposit is $MnO_2$. Furthermore, the brown deposit was investigated by Raman spectroscopy.

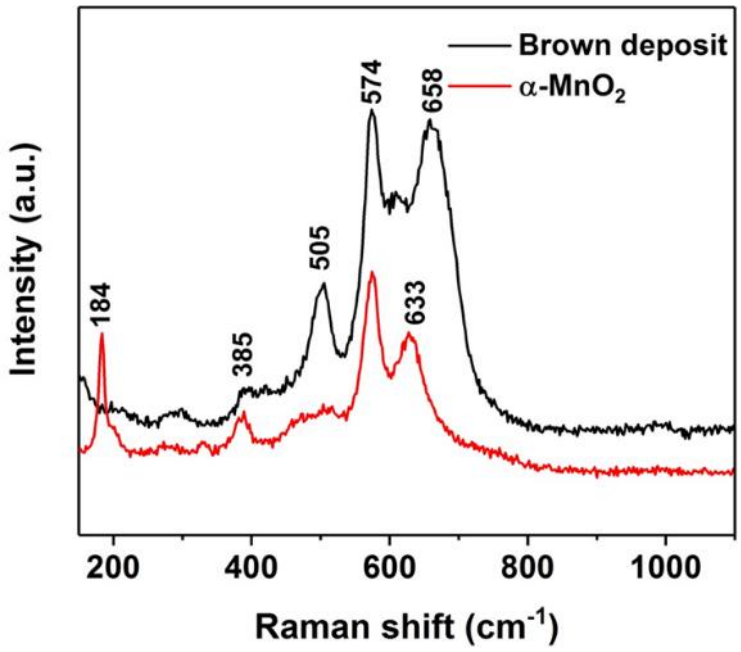


**Figure S3.3.** Raman spectra of brown deposit and α-$MnO_2$.

According to the Raman spectrum, the brown deposit formed on the current collector can be ascribed to birnessite-type $MnO_2$ [5, 6].

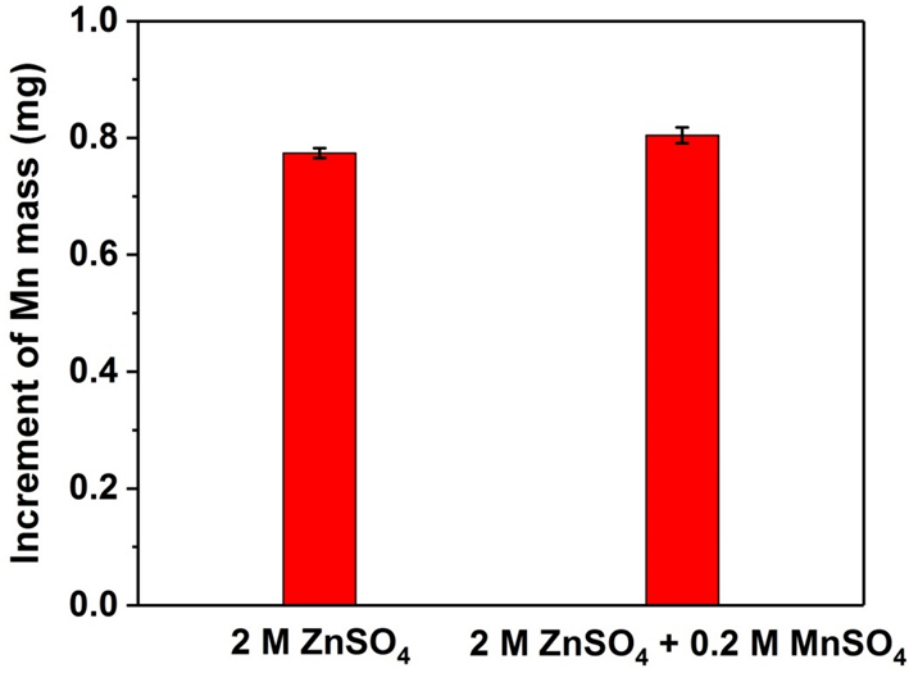


**Figure S3.4.** The increment of $Mn^{2+}$ in the solution after 1st discharge.

It has been reported that the pre-addition of $Mn^{2+}$ to the electrolyte enables the improved cycling stability of $MnO_2$ electrode by inhibiting the dissolution of $Mn^{2+}$ [7]. This is not the case in our experiments. Since the dissolution of $Mn^{2+}$ is caused by disproportionation due to high-spin electronic configuration of $Mn^{3+}$ [8], the pre-addition of $Mn^{2+}$ in the solution will not affect the configuration of $Mn^{3+}$, thus is unable to suppress the dissolution of $Mn^{2+}$. The pre-addition of $Mn^{2+}$ in the solution can provide enough $Mn^{2+}$ for electrodeposition into $MnO_2$ to compensate the loss of $MnO_2$ from the electrode.

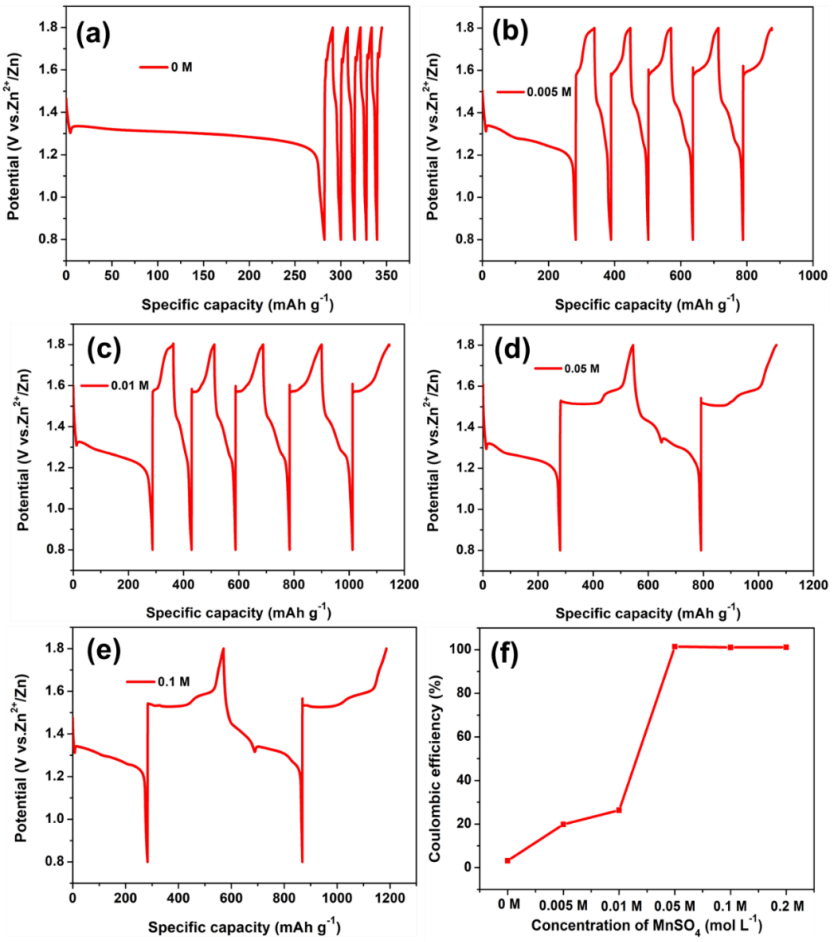


**Figure S3.5.** Typical galvanostatic charge-discharge curves of the cells with different concentrations of $MnSO_4$ in the electrolyte at 30 mA $g^{-1}$, **(a)** 0 M, **(b)** 0.005 M, **(c)** 0.01 M, **(d)** 0.05 M, **(e)** 0.1 M, **(f)** the corresponding coulombic efficiency in the first cycle under different concentrations of $MnSO_4$ as additive.

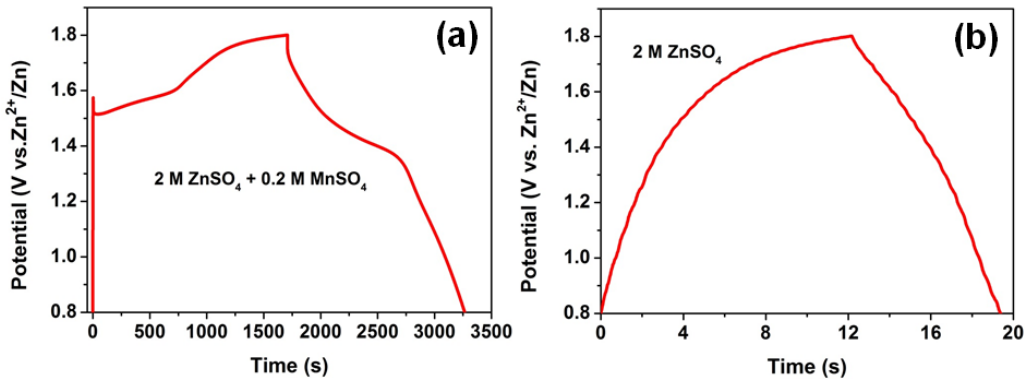


**Figure S3.6.** Typical galvanostatic charge-discharge curves of bare nickel mesh at current of 100 μA in **(a)** 2 M $ZnSO_4$ + 0.2 M $MnSO_4$ and **(b)** 2 M $ZnSO_4$.

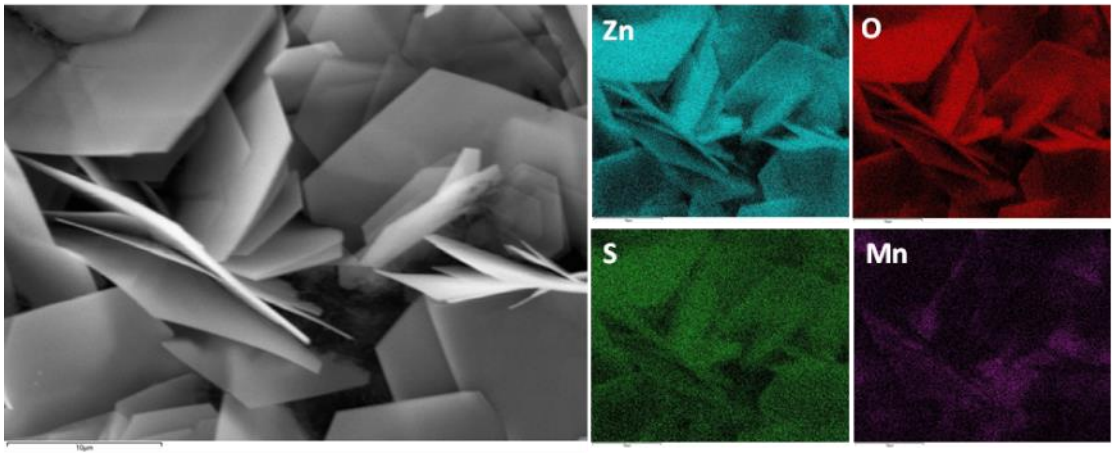


**Figure S3.7.** Energy-dispersive spectroscopy (EDS) analysis of the flake-like product on the electrode surface.

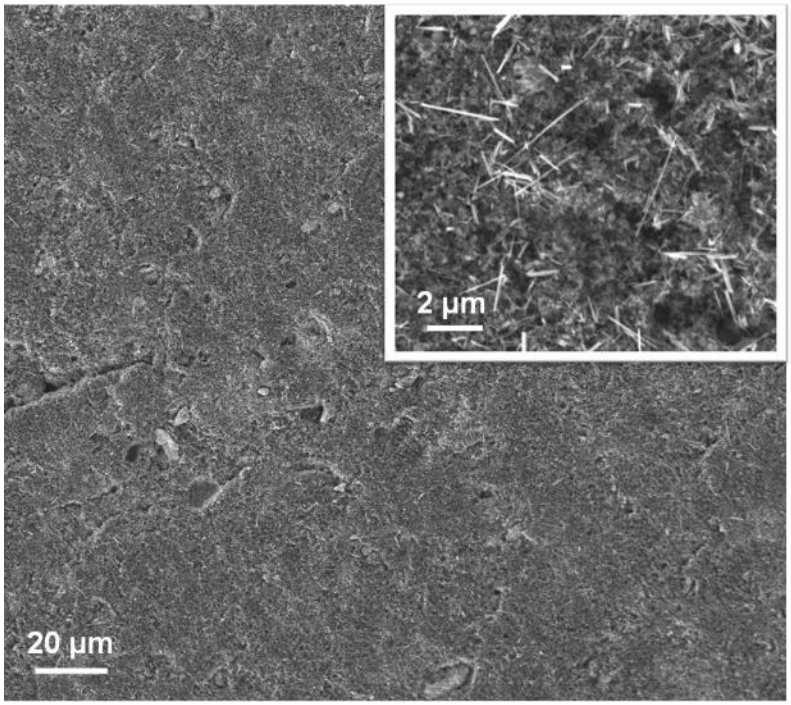


**Figure S3.8.** SEM images of electrode after the 1st discharge to 0.8 V and subsequent washing with acetic acid to remove the precipitate.

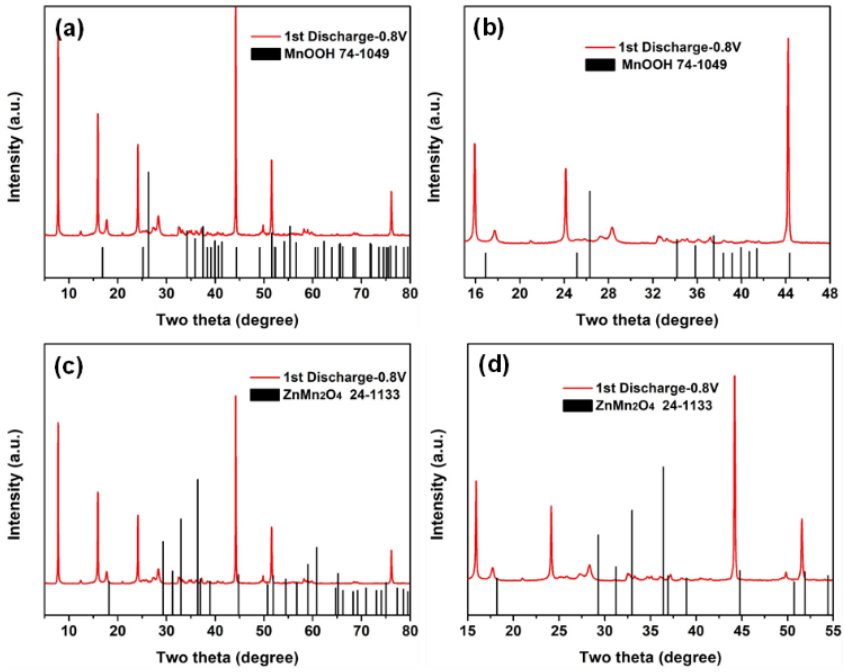


**Figure S3.9.** XRD pattern of discharged electrode compared with **(a-b)** MnOOH and **(c-d)** $ZnMn_2O_4$.

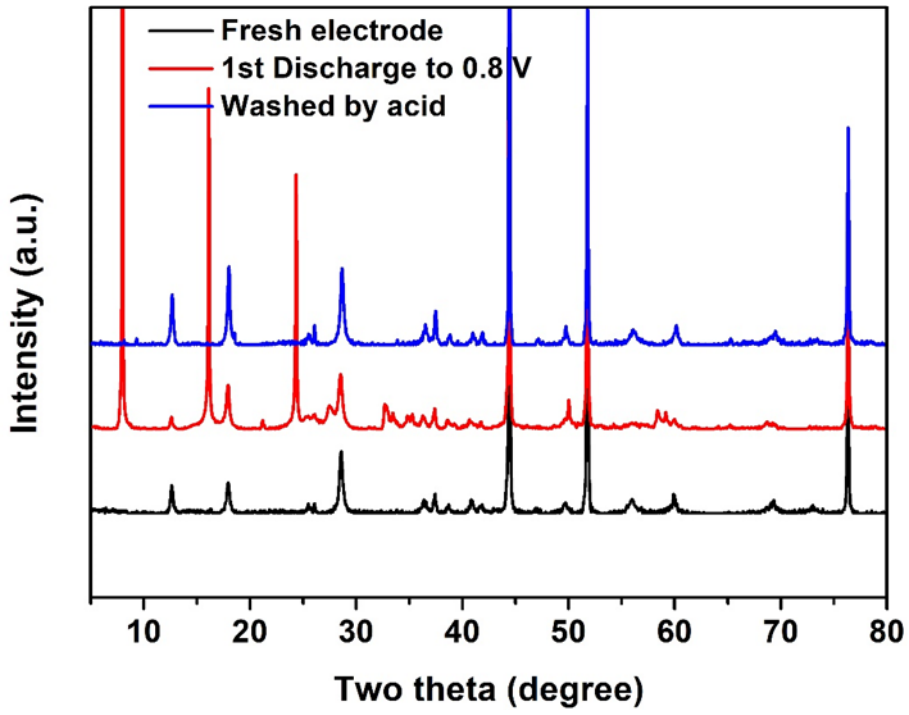


**Figure S3.10.** XRD patterns of fresh electrode and discharged electrode. The black line represents the fresh electrode. The red line is the electrode first discharged to 0.8 V.

After full discharge to 0.8 V, the discharged electrode was washed by weak acid to remove the precipitation on the electrode surface. The electrode washed by acid shows a similar XRD pattern to that of the fresh electrode. Surprisingly, only α-$MnO_2$ can be observed, and no evidence for $Zn^{2+}$ or proton intercalation into α-$MnO_2$ can be found.

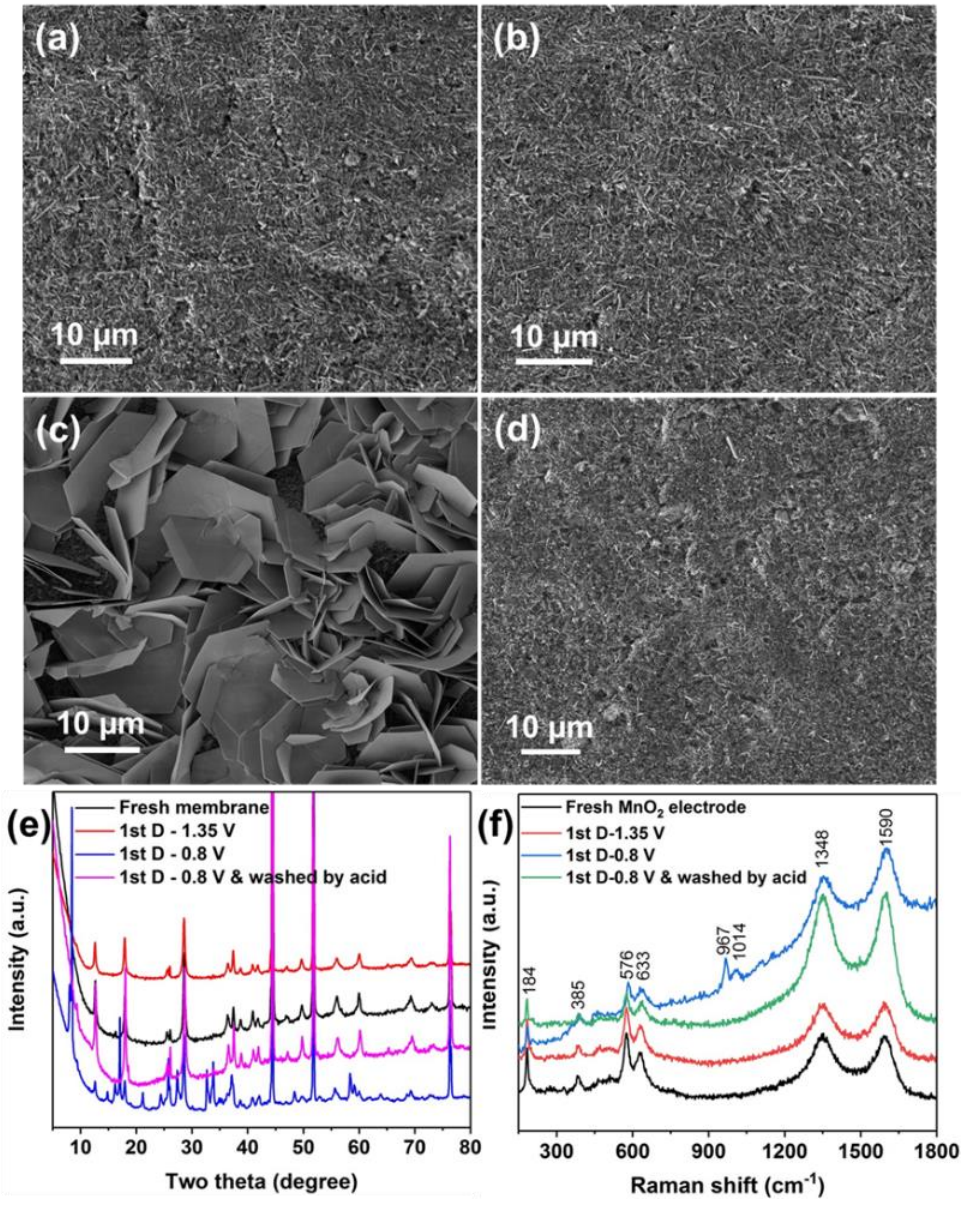


**Figure S3.11. (a-b)** SEM images of electrode in 2 M $ZnSO_4$ electrolyte: **(a)** original α-$MnO_2$, **(b)** 1st discharge to 1.35 V, **(c)** 1st discharge to 0.8 V, **(d)** 1st discharge to 0.8 V and washing with acetic acid to remove the precipitation, **(e)** XRD patterns of original α-$MnO_2$ electrode and discharged electrodes, **(f)** Raman spectra of the original α-$MnO_2$ electrode and discharged electrodes.

The morphology of the $MnO_2$ electrode during the first discharge process in 2 M $ZnSO_4$ electrolyte was also observed by SEM. Figure S3.11a shows the morphology of the original $MnO_2$ electrode, exhibiting a clean surface. When the cell is discharged to 1.35 V, there is no obvious change on the electrode surface, shown in Figure S3.11b. But when the cell is further discharged to 0.8 V, some large flakes emerge on the electrode surface in Figure S3.11c. As shown in Figure S3.10d, the flakes on the electrode surface can be totally removed by acid. XRD analysis of the discharge product was conducted during the first discharge process. As shown in Figure S3.11e, when the cell is discharged to 1.35 V, there is no obvious variation compared with the XRD pattern of the fresh electrode. However, when the cell is further discharged to 0.8 V, the characteristic peaks of $Zn_4(OH)_6(SO_4)\cdot 5H_2O$ appear, which is consistent with the XRD results in 2 M $ZnSO_4$ + 0.2 M $MnSO_4$. After the discharged electrode was treated by acid, the characteristic peaks belonging to $Zn_4(OH)_6(SO_4)\cdot 5H_2O$ disappeared. Only α-$MnO_2$ can be observed, and no evidence for $Zn^{2+}$ or proton intercalation into α-$MnO_2$ can be found. The discharge product was further investigated by Raman spectroscopy to reveal the structural evolution. As shown in Figure S3.11f, the original α-$MnO_2$ exhibits four main peaks at 184, 385, 576, and 633 $cm^{-1}$ [1, 9, 10]. The peaks at 633 $cm^{-1}$ and 576 $cm^{-1}$ arise from the symmetric Mn-O stretching vibrations in $MnO_6$ units [6, 9]. The translational motion of $MnO_6$ leads to an external vibration at 184 $cm^{-1}$. The peak located at 385 $cm^{-1}$ is caused by the Mn-O bending vibrations [9]. The peaks at 1348 $cm^{-1}$ and 1590 $cm^{-1}$ are assigned to the D band and G band of the conductive carbon added in the electrode. When the α-$MnO_2$ electrode is first discharged to 1.35 V, there is no significant change in the Raman spectrum. When it is further discharged to 0.8 V, two new peaks emerge at 967 $cm^{-1}$ and 1014 $cm^{-1}$, which belongs to the vibrations of $SO_4^{2-}$ in the zinc hydroxide sulfate hydrate [11-13]. After the discharged electrode is washed with acid, the peaks corresponding to $SO_4^{2-}$ disappears and the whole spectrum is similar to that of the original $MnO_2$ electrode. No signals corresponding to MnOOH and $ZnMn_2O_4$ can be detected.

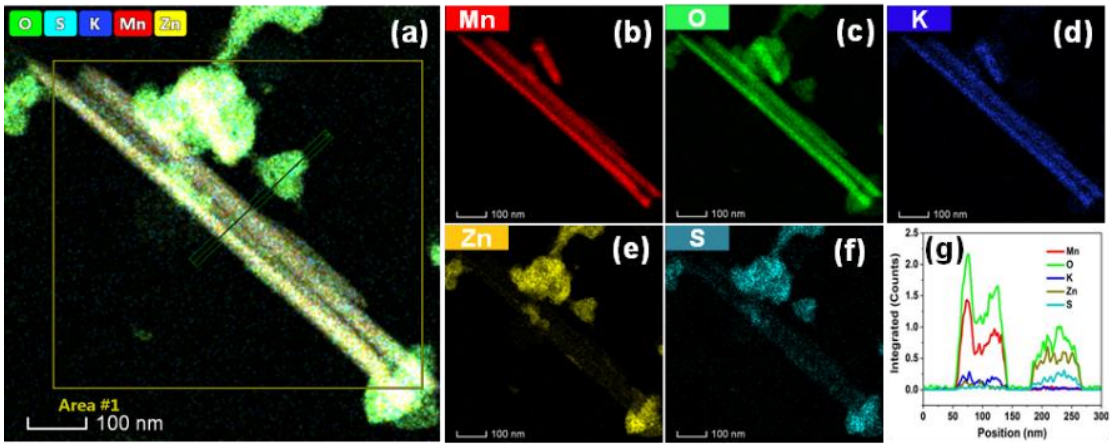


**Figure S3.12. (a)** STEM-HAADF image of $MnO_2$ electrode after 1st discharge, **(b-f)** STEM–EDS mappings of the elemental distributions of Mn, O, K, Zn and S, **(g)** line profiles of Mn, O, K, Zn and S extracted from the green rectangle in (a).

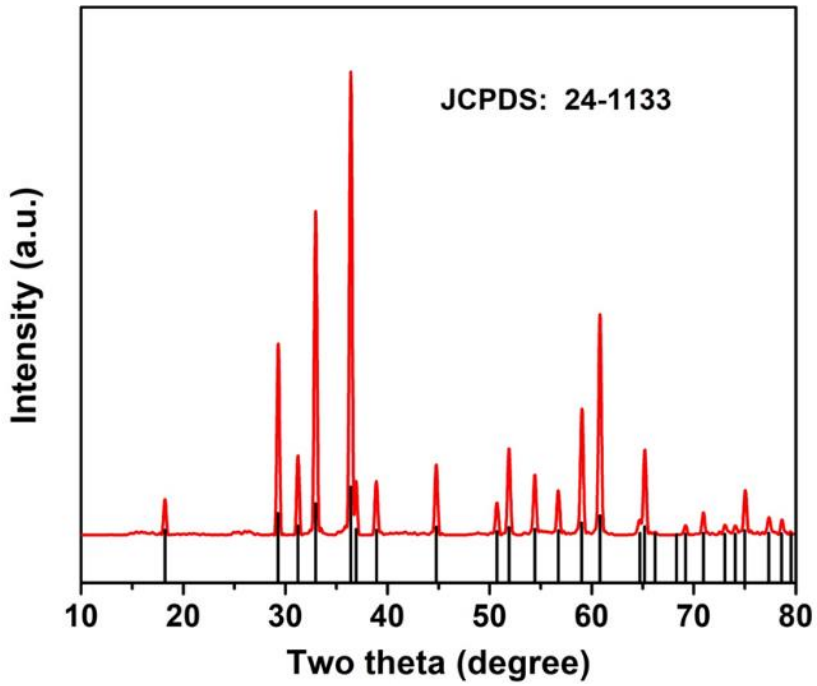


**Figure S3.13.** XRD pattern of the synthesized $ZnMn_2O_4$.

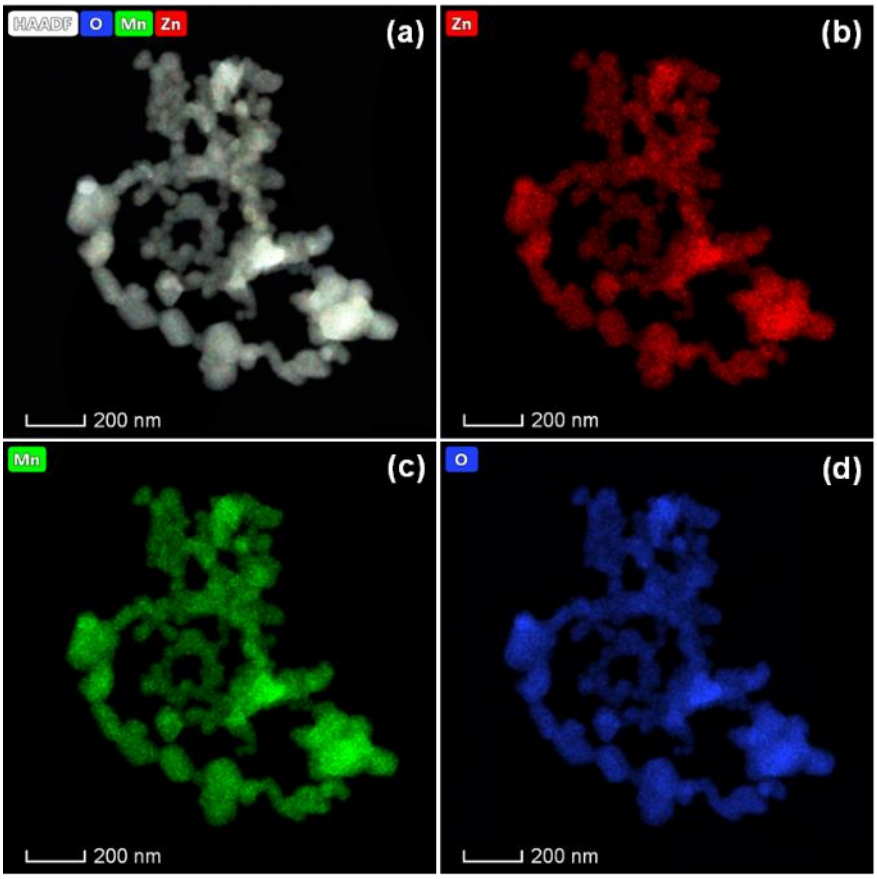


**Figure S3.14. (a)** STEM-HAADF image of $ZnMn_2O_4$ and **(b-d)** STEM–EDS mappings of the elemental distributions of Mn, O and Zn in the $ZnMn_2O_4$.

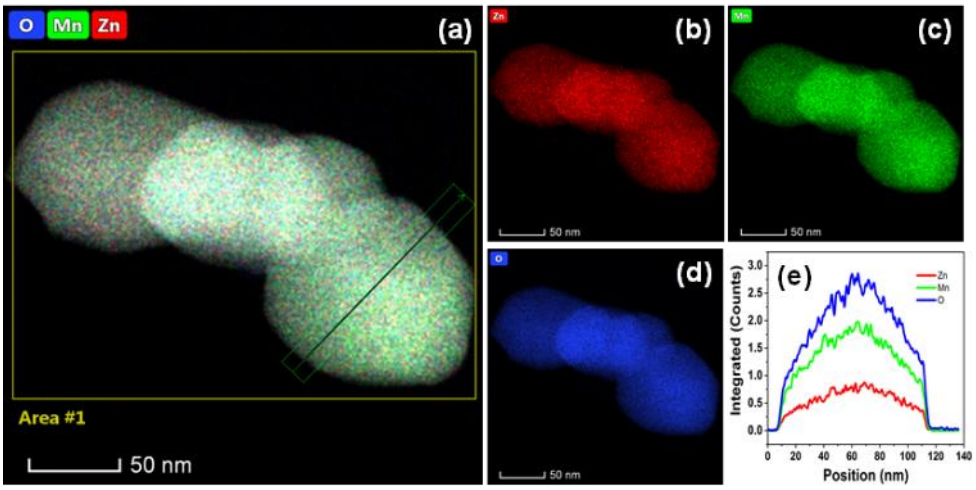


**Figure S3.15. (a)** STEM-HAADF image of $ZnMn_2O_4$, **(b-d)** STEM-EDS mappings of the elemental distributions of Zn, Mn and O, **(e)** line profiles of Zn, Mn and O extracted from green rectangle in (a).

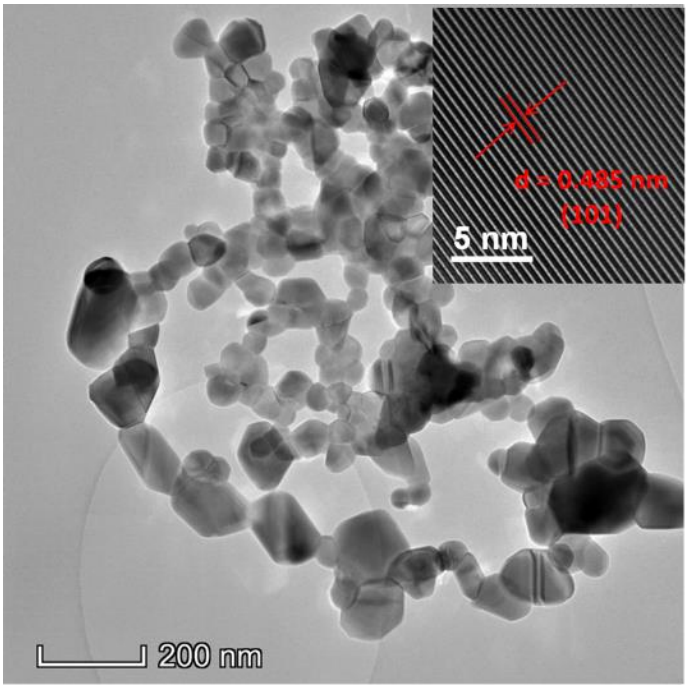


**Figure S3.16.** Representative TEM image of $ZnMn_2O_4$ (inset showing the HRTEM image).

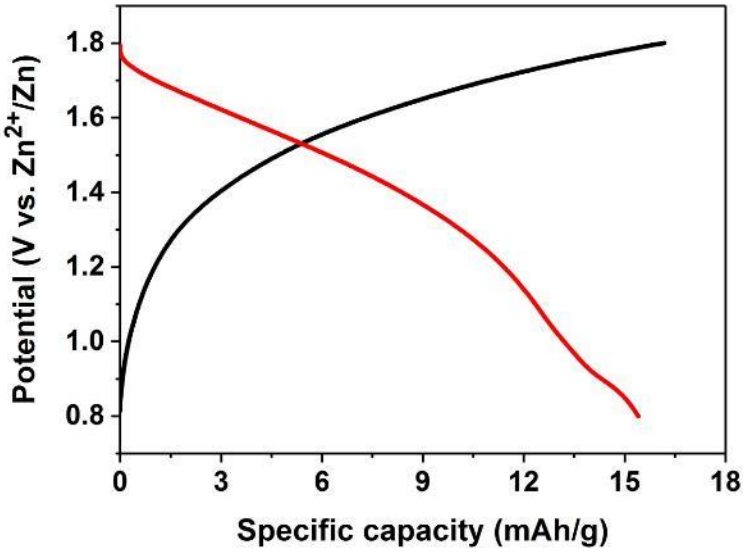


**Figure S3.17.** Typical galvanostatic charge-discharge curves of $ZnMn_2O_4$ electrode at a current density of 30 mA $g^{-1}$.

**Table S3.1.** Comparison of different monovalent and multivalent metals [14]

| Element | Standard potential (V vs. SHE) | Ionic radius (Å) | Hydrated ionic radius (Å) | Specific capacity (mAh/g) | Capacity density (mAh/cm$^3$) |
|---|---|---|---|---|---|
| Li | −3.040 | 0.76 | 3.40-3.82 | 3860 | 2061 |
| Na | −2.713 | 1.02 | 2.76-3.60 | 1166 | 1129 |
| K | −2.924 | 1.38 | 2.01-3.31 | 685 | 610 |
| Mg | −2.356 | 0.72 | 3.00-4.70 | 2206 | 3834 |
| Ca | −2.840 | 1.00 | 4.12-4.20 | 1337 | 2072 |
| Zn | −0.763 | 0.75 | 4.04-4.30 | 820 | 5855 |
| Al | −1.676 | 0.53 | 4.80 | 2980 | 8046 |

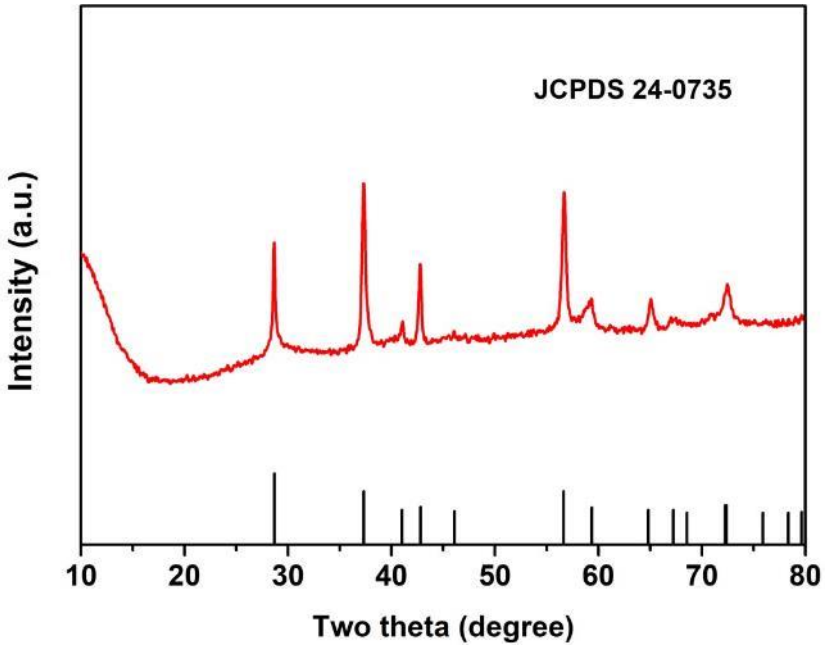


**Figure S3.18.** XRD Pattern of beta-$MnO_2$.

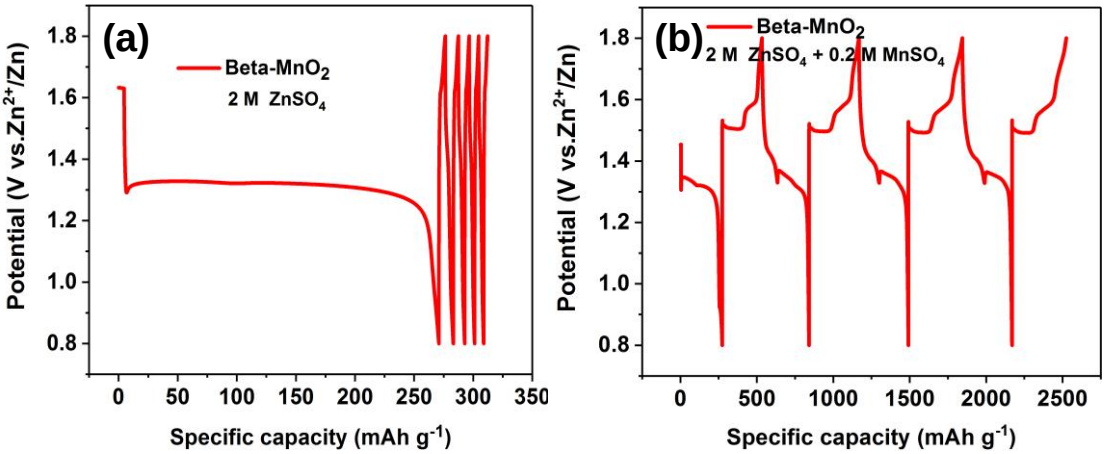


**Figure S3.19.** Typical galvanostatic charge-discharge curves of beta-$MnO_2$ **(a)** 2 M $ZnSO_4$ and **(b)** 2 M $ZnSO_4$ + 0.2 M $MnSO_4$.

### 3. Potential conversion

$$MnO_2 + 4H^+ + 2e^- \rightleftharpoons Mn^{2+} + 2H_2O \ (E° = 1.23 \text{ V}) \qquad \text{(S3.2)}$$

The concentration of $Mn^{2+}$ is 0.2 M and the pH is measured to be about 5. So:

$$E = E° - \frac{RT}{nF}\ln\frac{[Mn^{2+}]}{[H^+]^4} = 1.23 - \frac{8.314\times298.15}{2\times96485}\times\ln\frac{0.2}{[10^{-5}]^4} = 0.659 \text{ V} \qquad \text{(S3.3)}$$

$$Zn^{2+} + 2e^- \rightleftharpoons Zn \ (E° = -0.762 \text{ V}) \qquad \text{(S3.4)}$$

$$E = E° - \frac{RT}{nF}\ln\frac{[Zn]}{[Zn^{2+}]} = -0.762 - \frac{8.314\times298.15}{2\times96485}\times\ln\frac{1}{2} = -0.754 \text{ V} \qquad \text{(S3.5)}$$

So the required theoretical potential to electrodeposit $MnO_2$ is about 1.413 V (vs. $Zn^{2+}$/Zn) under our experimental conditions.

References

[1] S. Liang, F. Teng, G. Bulgan, R. Zong, Y. Zhu, J. Phys. Chem., 112 (2008) 5307-5315.

[2] X. Wang, Y. Li, Chem. Eur. J., 9 (2003) 300.

[3] R. Liu, Y. Yan, C. Ma, Front Chem, 6 (2018) 69.

[4] W. Wei, X. Cui, W. Chen, D.G. Ivey, Chem. Soc. Rev., 40 (2011) 1697-1721.

[5] R.M. Freitas, T.A.G. Perilli, A.C.Q. Ladeira, J. Chem., 2013 (2013) 1-8.

[6] S.-B. Ma, K.-Y. Ahn, E.-S. Lee, K.-H. Oh, K.-B. Kim, Carbon, 45 (2007) 375-382.

[7] H. Pan, Y. Shao, P. Yan, Y. Cheng, K.S. Han, Z. Nie, C. Wang, J. Yang, X. Li, P. Bhattacharya, K.T. Mueller, J. Liu, Nat. Energy, 1 (2016) 1-7.

[8] T. Takashima, K. Hashimoto, R. Nakamura, J. Am. Chem. Soc., 134 (2012) 18153-18156.

[9] T. Gao, M. Glerup, F. Krumeich, R. Nesper, H. Fjellvåg, P. Norby, J. Phys. Chem. C, 112 (2008) 13134-13140.

[10] T. Gao, H. Fjellvag, P. Norby, Anal Chim Acta, 648 (2009) 235-239.

[11] Z. Du, J. Chen, W. Ye, J. Guo, X. Zhang, R. Zheng, Sensors (Basel), 15 (2015) 12377-12388.

[12] S.M. Angel, N.R. Gomer, S.K. Sharma, C. McKay, Appl Spectrosc., 66 (2012) 137-150.

[13] K. Ben Mabrouk, T.H. Kauffmann, H. Aroui, M.D. Fontana, J. Raman Spectrosc.,44 (2013) 1603-1608.

[14] M. Song, H. Tan, D. Chao, H.J. Fan, Adv. Funct. Mater., 28 (2018) 1802564.

# Chapter 4 Investigation of Voltage Range and Self-Discharge in Aqueous Zinc-Ion Hybrid Supercapacitors

**Jie Yang,[a, b] Mark A. Bissett,*[b, c] and Robert A. W. Dryfe*[a, b]**

[a] Department of Chemistry, University of Manchester, M13 9PL Manchester (UK)

[b] National Graphene Institute, University of Manchester, M13 9PL Manchester (UK)

[c] Department of Materials, University of Manchester, M13 9PL Manchester (UK)

Corresponding authors: mark.bissett@manchester.ac.uk; robert.dryfe@manchester.ac.uk

**Published in ChemSusChem 2021, 14, 1700–1709.**



**Author Contributions**:

The characterization and electrochemical measurement were carried out by J. Yang. The article was written by J. Yang with the comments from Dr. M. A. Bissett and Prof. R. A. W. Dryfe. All authors discussed the results and commented on the manuscript.

**Abstract:** Aqueous zinc-ion hybrid supercapacitors are a promising energy storage technology, owing to their high safety, low cost, and long-term stability. At present, however, there is a lack of understanding of the potential window and self-discharge of this aqueous energy storage technology. This study concerns a systematic investigation of the potential window of this device by cyclic voltammetry and galvanostatic charge–discharge. Hybrid supercapacitors based on commercial activated carbon (AC) demonstrate a wide and stable potential window (0.2 V to 1.8 V), high specific capacitances (308 F $g^{-1}$ at 0.5 A $g^{-1}$ and 110 F $g^{-1}$ at 30 A $g^{-1}$), good cycling stability (10000 cycles with 95.1 % capacitance retention), and a high energy density (104.8 Wh $kg^{-1}$ at 383.5 W $kg^{-1}$), based on the active materials. The mechanism involves simultaneous adsorption–desorption of ions on the AC cathode and zinc ion plating/stripping on the Zn anode. This work leads to better understanding of such devices and will aid future development of practical high-performance aqueous zinc-ion hybrid supercapacitors based on commercial carbon materials, thus accelerating the deployment of these hybrid supercapacitors and filling the gap between supercapacitors and batteries.

## *Introduction*

The use of clean renewable energy sources such as solar and wind are of prime importance to the sustainable development of modern society with respect to pressing environmental issues related to our energy use [1, 2]. To achieve this goal, effective and efficient energy storage devices such as batteries and supercapacitors are required. The general properties of different storage devices are determined by the corresponding mechanism of energy storage [3]. Batteries are able to store large amounts of energy but deliver it slowly, resulting in their high energy densities and low power densities [4]. Unlike batteries, supercapacitors (especially electric double-layer capacitors, EDLCs) store charges at the surface, or near surface, of the active materials and can deliver energy in a short time, thus providing high power densities and low energy

densities [5]. Additionally, supercapacitors have much better cycling stability than batteries. Supercapacitors as energy storage devices are very promising in various fields, such as hybrid electric vehicles, smart grids and aircraft, in which high power densities and long lifetimes are needed [6]. However, their wider application has been limited by their relatively low energy densities (<10 Wh $kg^{-1}$) [7, 8]. Therefore, various strategies have been adopted to enhance the energy densities of supercapacitors without sacrificing the merits in terms of power densities and cyclability.

The energy density, *E*, of a supercapacitor is determined by the specific capacitance of active materials (*C*) and the square of operating voltage (*U*) based on the energy equation ($E = \frac{1}{2}\ C\ U^2$). To increase the specific capacitance, many different strategies have been used to develop nanostructured carbon materials with high surface area and hierarchical pores, since the specific capacitance of carbon materials is highly dependent on these properties [9-13]. Additionally, another common way to improve the capacitance is to make composites by combining carbon materials with metal oxides or conductive polymers [14-16]. Compared with the methods to improve the electrode capacitance, widening the cell voltage is a more efficient means in terms of the improvement of energy density. Essentially, the operating voltage is determined by the stability of the electrolytes. Although a high ionic conductivity can be obtained in acidic and basic aqueous electrolyte, they are highly corrosive and the voltage is usually restricted to 1.0 V due to decomposition of water [17]. Organic electrolytes have been widely used in commercial supercapacitors, because they possess a wider voltage window of 2.5–2.7 V. Environmental and safety issues, along with cost, are major concerns for organic electrolytes [18]. Although the operating window can be further widened to more than 3 V in ionic liquids, and a much higher energy density can be achieved, the device loses the high power due to the high viscosity and associated low ionic conductivity of ionic liquids [17]. Neutral aqueous electrolytes such as group 1 salts of sulfate and nitrate have been considered as promising electrolytes over the past few years due to the wider operating voltage, up to 1.6 V–2.0 V, and less corrosive

nature, thus reducing the environmental impact and providing a higher energy density [17, 19-23].

Constructing better energy storage devices not only relies on the properties of the electrode materials and electrolytes but also depends significantly on the configuration of the devices [2, 24-26]. Therefore, much effort has been devoted to combining the advantages of battery-type electrodes with capacitor-type electrodes to obtain high energy and power densities as well as good cyclability [27, 28]. Recently, a novel hybrid supercapacitor with a zinc metal anode has been reported by several groups [29-31]. For example, Dong et al. [29] reported a novel energy storage system of zinc-ion hybrid supercapacitors in which activated carbon materials, Zn metal and $ZnSO_4$ aqueous solution serve as cathode, anode and electrolyte, respectively. A very high energy density of 84 Wh $kg^{-1}$ and excellent cycling stability were achieved. Wu et al. [31] used porous carbon derived from chemically activated graphene as the cathode with 3 M $Zn(CF_3SO_3)_2$ electrolyte in zinc ion hybrid supercapacitors, demonstrating an energy density of 106.3 Wh $kg^{-1}$ and a power density of 31.4 kW $kg^{-1}$. Although there have been great advances in achieving high-performance zinc ion hybrid supercapacitor devices by developing various carbon-based materials, to the best of our knowledge, no detailed study to optimise the potential window has been performed on aqueous hybrid supercapacitors, nor has the effect of self-discharge processes been considered. Considering that the potential window is critical to the energy output and lifespan of supercapacitors, and high self-discharge rates compromise their practical value, it is necessary to perform a comprehensive and systematic investigation of the potential window and self-discharge in the zinc ion hybrid supercapacitors.

In this work, we systematically study the voltage range and self-discharge in aqueous zinc ion hybrid supercapacitors comprised of activated carbon cathode, Zn foil anode and $ZnSO_4$ aqueous electrolyte solution. The corresponding mechanism and advantages of the hybrid supercapacitor have also been discussed. Furthermore, the self-discharge

is found to be dependent on the initial voltage and it can be significantly suppressed to enhance the charge storage efficiency in this hybrid device compared with symmetric supercapacitors. The hybrid supercapacitor exhibits a wide operating voltage window from 0.2 V to 1.8 V with high specific capacitance (308 F $g^{-1}$ at 0.5 A $g^{-1}$ and 110 F $g^{-1}$ at 30 A $g^{-1}$) as well as good stability with 95.1% capacitance retention over 10,000 cycles. A much higher energy density of about 104.8 Wh $kg^{-1}$ is achieved at the power density of 383.5 W $kg^{-1}$, based on the mass of the active materials. The combination of cost-effective and non-toxic electrode materials (commercially available zinc metal and activated carbon) with non-flammable aqueous electrolyte is expected to open a new avenue for next-generation energy storage devices.

## *Results and Discussion*

The structure of the activated carbon (AC) denoted as YEC-8A was characterized by X-ray diffraction (XRD), shown in Figure 4.1a. The XRD pattern only shows a relatively broad peak located at 43.1°, which can be ascribed to the (101) plane reflection [13]. The relatively broad peaks indicate the highly amorphous characteristic of the sample. The Raman spectrum shown in the inset of Figure 4.1a also revealed the highly disordered characteristics of the material. The D band at 1346 $cm^{-1}$ corresponds to the breathing mode vibration at free edges and the G band at 1589 $cm^{-1}$ is ascribed to the in-plane stretching vibration [13, 32, 33]. The morphology of YEC-8A was characterized by SEM, shown in Figure 4.1b. The shape of the particles is irregular with relatively coarse surfaces and a particle size in the range from 5 μm to 20 μm. The surface composition was further identified by XPS, shown in Figure 4.1c. The elemental composition of the sample surface is comprised of C (~90.17 at.%) and O (~9.83 at.%). The high-resolution C1s spectrum shown in Figure 4.1c (inset) further confirms the presence of surface functional groups such as C-O (~286.2 eV) and C=O (~288.7 eV) [34-36]. The presence of abundant oxygen-containing groups at the surface of carbon should give rise to hydrophilic properties of the carbon materials, thus

facilitating the wettability of electrode and promoting the transport of electrolyte ions [37].

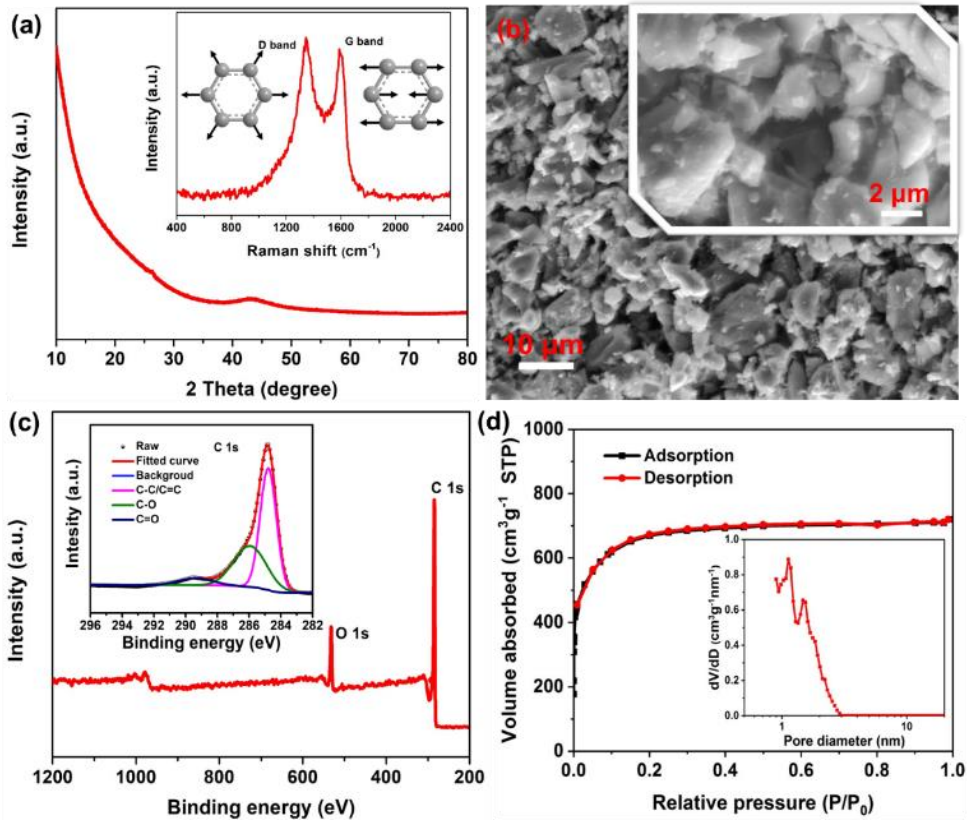


**Figure 4.1.** Characterization of YEC-8A **(a)** XRD pattern and Raman spectrum in the inset, **(b)** SEM images, **(c)** XPS spectra and high resolution C 1s XPS spectrum in the inset, and **(d)** Nitrogen physisorption isotherms and pore size distribution derived from NLDFT calculations.

The specific surface area and pore structure of YEC-8A were probed by nitrogen adsorption/desorption technique. The nitrogen adsorption/desorption isotherm of YEC-8A is shown in Figure 4.1d, showing the typical characteristics of a type I isotherm [38]. The significant nitrogen adsorption at a relative pressure below 0.01 represents typical feature of micropores (< 2 nm), indicating abundant micropores exist in the material. The slight increase in nitrogen adsorption at the relative pressure between 0.05 and 0.3 suggests the lack of abundant mesopores (2 nm - 50 nm) in the sample. The specific surface area was calculated to be about 2390 $m^2 g^{-1}$ based on the Brunauer-Emmett-Teller (BET) model [39]. Such a high specific surface area should provide effective

surface sites for ion adsorption and desorption. The pore size distribution was derived from non-local density functional theory (NLDFT) based on a slit-pore model [40]. The corresponding pore size distribution is in the range from 0.87 nm to 3.03 nm shown in the inset of Figure 4.1d. The summary is that the pores inside the material consist of many micropores and a small amount of mesopores**.** Generally, it is believed that both the micropores and mesopores are responsible for charge accumulation and ion adsorption. Furthermore, mesopores can act as channels to transport ions from bulk electrolyte to the electrode/electrolyte interface, facilitating the fast mass transport [41, 42]. In order to effectively and efficiently utilize the surface of the carbon, the relation between the pore size of the carbon electrode and the electrolyte ions should also be considered [43].

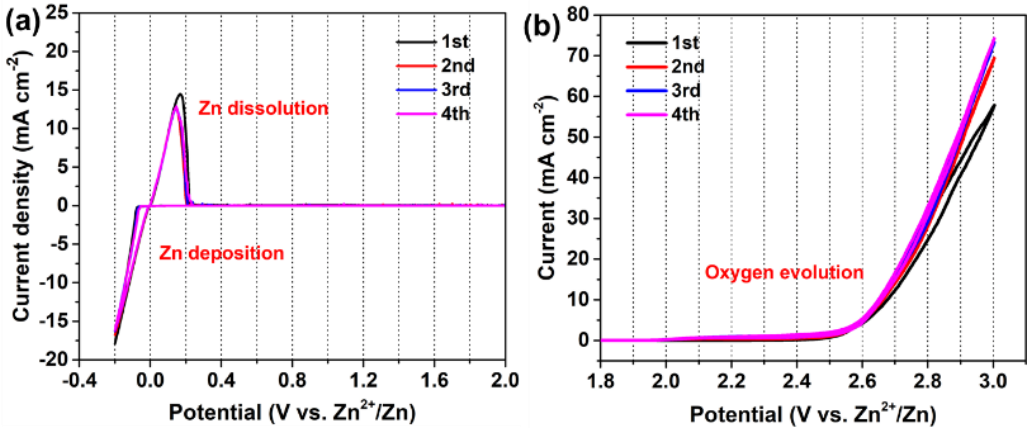


**Figure 4.2.** Electrochemical potential window in 2 M $ZnSO_4$ electrolyte investigated by cyclic voltammetry at a scan rate of 0.5 mV $s^{-1}$.

The performance of supercapacitors is not only affected by the electrode materials, but also is dependent on the electrolytes used. The electrochemical stability of the electrolytes is critical in determining the operating voltage and lifespan of the supercapacitors. In aqueous supercapacitors with Zn foil electrodes, strong alkaline electrolytes such as KOH solution are not suitable due to the formation of ZnO which is detrimental to the cyclability of the cell. Meanwhile, strongly acidic electrolytes, such as $H_2SO_4$, can react with the Zn metal to generate $H_2$. Considering the strongly corrosive and limited electrochemical potential window of alkaline and acidic electrolyte, a mild (neutral) zinc salt is chosen as the electrolyte. To optimize the

electrolyte, $ZnSO_4$ solutions with different concentrations were prepared and the corresponding ionic conductivities were directly measured by using a ready-to-measure conductivity meter from METTLER TOLEDO, shown in Figure S4.1. As the concentration of $ZnSO_4$ increases from 1 M to 2 M, the ionic conductivity increases from 49.1 mS $cm^{-1}$ to 58.7 mS $cm^{-1}$. When the concentration is further increased to 3 M, it begins to decrease to 46.5 mS $cm^{-1}$ due to the high viscosity and extensive ion-pairing outweighing the effect of additional charge carriers, so 2 M $ZnSO_4$ is used as the electrolyte for further experiments. The potential window of 2 M $ZnSO_4$ was investigated in a three-electrode system with stainless steel as the working electrode and Zn foil as both the reference electrode and the counter electrode. As shown in Figure 4.2, the cyclic voltammetry (CV) indicates that the deposition/dissolution of $Zn^{2+}$ is reversible in $ZnSO_4$ solutions. From the CV response, we can roughly determine a stable electrochemical window from 0.2 V to 2.4 V (vs. $Zn^{2+/}Zn$). The oxygen evolution reaction is significantly suppressed up to 2.4 V in this electrolyte. When the potential is higher than 2.4 V, the parasitic oxygen evolution reaction begins to become quite obvious accompanied by the vigorous generation of gas bubbles. The widened potential window can be explained by the strong ion solvation of $Zn^{2+}$ and $SO_4^{2-}$ [22]. We adopt a conservative estimation of the stable window which should be stable in the range of 0.2−2.2 V since there are no detectable side reactions in this range.

In practical applications, the device is usually employed in a two-electrode configuration. The available maximum operating voltage was further studied in a two-electrode configuration (i.e., coin cell) with YEC-8A as the cathode, zinc foil as the anode and 2 M $ZnSO_4$ as the electrolyte. The operating voltage was first investigated by CV over various voltage ranges, shown in Figure 4.3a. It is observed that a quasi-rectangular shape of the CV curve is maintained in the range from 0.2 V to 1.8 V. However, when the upper cut-off voltage is increased to 1.9 V, the current at higher voltage shows a significant increase due to the oxidation of carbon surface functional groups or oxidation of the carbon bulk [44, 45]. Also a “hump” located at around 1.2 V

is observed, which is attributed to the electrochemical reduction of quinone surface functionalities to hydroquinone [45-47]. As the upper cut-off voltage is further increased to 2.0 V, the hump is more pronounced owing to more quinone being generated at high potentials during the anodic sweep. The carbon materials, especially the nanoporous carbon materials with abundant defects, are able to undergo electrochemical oxidation to generate surface oxides (e.g., carboxyl, carbonyl) and even

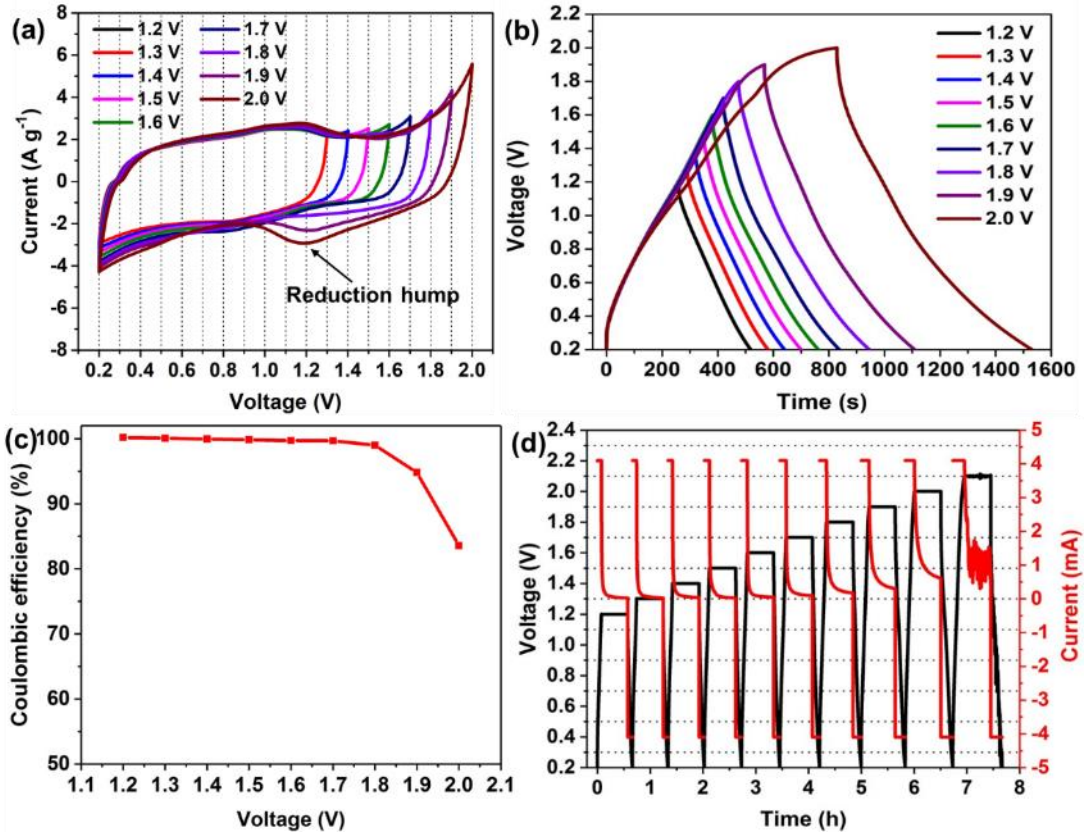


**Figure 4.3.** Electrochemical characterizations of AC//$ZnSO_4$ (aq)//Zn hybrid supercapacitor **(a)** Cyclic voltammogram (10 mV $s^{-1}$) of with stepwise increase in positive cell voltage limits, **(b)** GCD characteristics (1 A $g^{-1}$) at different voltage ranges, **(c)** Coulombic efficiencies at different voltage ranges, and **(d)** GCD and potentiostatic aging profiles at various voltages.

$CO/CO_2$ at high potentials [44, 45, 48]. The highest operation voltage for carbon-based electrodes can be restricted by such carbon oxidation processes which can occur before

the oxygen evolution reaction [48]. Alhough the supercapacitor can still operate beyond the maximum voltage range, the cycle life and the safety are significantly compromised.

The electrochemical potential window was further studied by galvanostatic charge-discharge (GCD) at a current density of 1 A $g^{-1}$ shown in Figure 4.3b. When the voltage is below 1.9 V, the charge-discharge curves are highly symmetrical, indicating a typical capacitive behavior. As the voltage is further increased to 2.0 V, the linearity of the charge curve is not retained at the highest voltage due to the oxidation of the carbon surface groups. These results are in a good agreement with the CV results. Additionally, the corresponding coulombic efficiencies at different voltages were also calculated, shown in Figure 4.3c. The coulombic efficiency is defined as the ratio of the discharge capacity to the charge capacity and it is noted that the coulombic efficiency decreases as the voltage increases. The coulombic efficiency is nearly 100% in the voltage range from 1.2 V to 1.8 V, indicating excellent charge and discharge reversibility of the supercapacitors. In contrast, when the voltage exceeds 1.9 V, the coulombic efficiency drops to 83.6%. A coulombic efficiency significantly lower than 100% indicates that additional irrevisible reactions occur at the high voltage range in the charging process. Generally, the practical coulombic efficiency is expected to approach 100%. Otherwise, both the lifespan and the safety would be undermined because of the irreversible side-reactions: the operational voltage window should therefore be restricted from 0.2 V to 1.8 V.

The CV and GCD tests can reveal the point at which a side reaction has started to take place. However, if the reaction is thermodynamically feasible, but kinetically controlled, it is difficult to discern the reaction immediately. For this reason, the electrochemical potential window was further confirmed by a combination of GCD and potentiostatic aging. The cell was charged to a set voltage and kept at the corresponding voltage for 30 minutes to observe the current response and then discharged, as shown in Figure 4.3d. The final dwell current response during the potentiostatic dwell was employed to evaluate the electrode stability. If the final dwell current is negligible, it indicates an ideal electric double layer behavior and no Faradaic current. When the cell is kept in

the voltage range from 1.2 V to 1.8 V, the final current during the dwell period tends to zero. As the voltage increases to 2.0 V, the response current is much higher than zero, suggesting a slow pseudocapacitive current under this voltage. As the voltage is further increased to 2.1 V, the strong oscillation of the response current indicates a drastic Faradaic reaction and the failure of the cell under this high voltage.

After confirmation that the stable operating voltage range of the cell is from 0.2 V to 1.8 V, the electrochemical behavior was further investigated by CV at various scan rates, shown in Figure 4.4a. The CVs show no distinct redox peaks, suggesting it displays the approximate characteristics of a classical double layer capacitor. The CVs

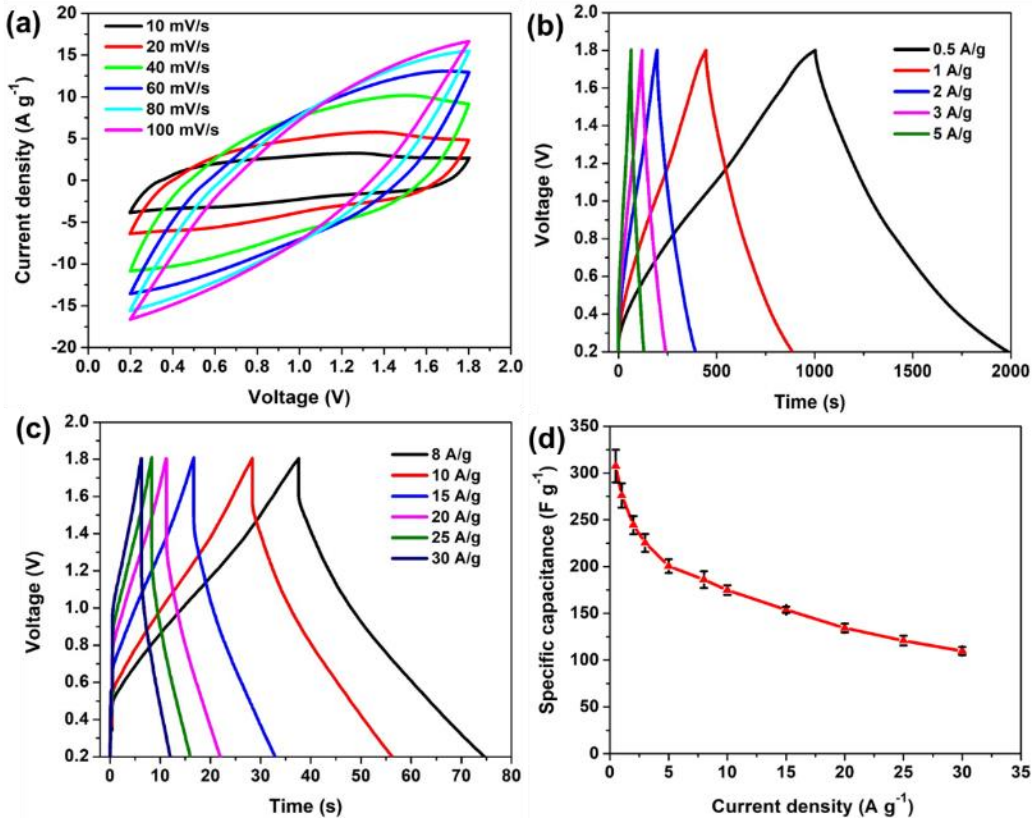


**Figure 4.4. (a)** Cyclic voltammograms as a function of scan rate, **(b-c)** GCD curves at various current densities, and **(d)** Specific capacitances at various current densities.

do not coincide at different scan rates due to the diffusion limitation of the ions. Moreover, the corresponding GCD curves are shown in Figure 4.4b and Figure 4.4c.

The linearity of the responses obtained at various current densities demonstrates that the device shows typical capacitive behavior. The increase in IR drop with current density also has a detrimental influence on the electrochemical performance. The specific capacitances at different current densities were calculated based on the discharge process. As shown in Figure 4.4d, a high specific capacitance, of about 308 F $g^{-1}$, is obtained at a low current density of 0.5 A $g^{-1}$. As the current density increases to 1, 2, 3, and 5 A $g^{-1}$, the capacitance decreases to 276, 244, 225 and 201 F $g^{-1}$, respectively. At higher current densities of 8, 10, 15, 20, 25 and 30 A $g^{-1}$, the corresponding specific capacitances are 186, 175, 154, 134, 121 and 110 F $g^{-1}$, respectively. The low capacitance retention of 35.69% at 30 A $g^{-1}$ should be ascribed to the slow ionic diffusion in the $ZnSO_4$ solution as well as relatively slow stripping and plating process on the Zn electrode.

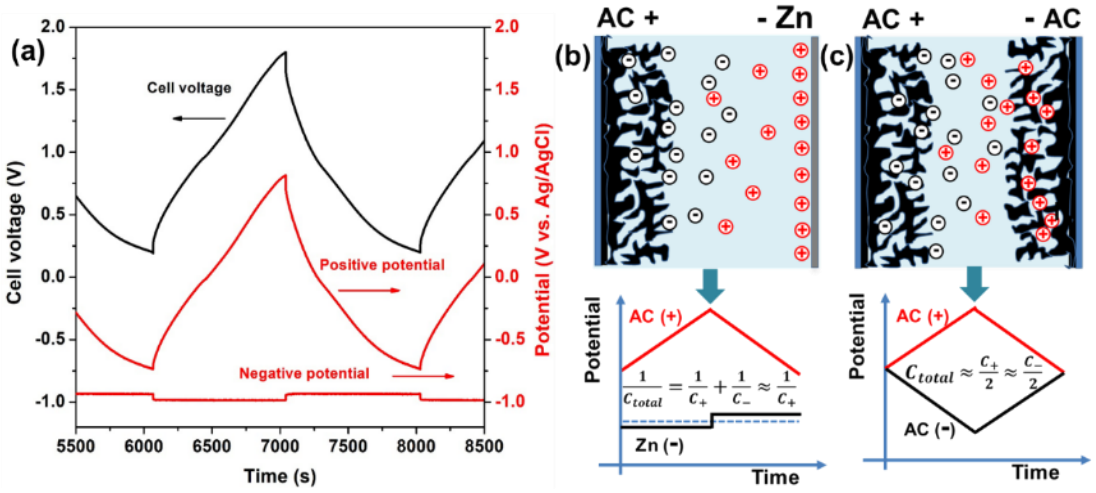


**Figure 4.5. (a)** GCD profiles recorded at 0.5 A $g^{-1}$ in a two-electrode system with a Ag/AgCl reference electrode, and schematic diagram for **(b)** AC-Zn hybrid supercapacitors and **(c)** AC-AC symmetric supercapacitors.

In order to understand the mechanism of the hybrid supercapacitors, the potential profiles of both the AC electrode and Zn electrode were simultaneously recorded by using a Ag/AgCl reference electrode in an open two-electrode system. The zinc ion

hybrid supercapacitor was characterized using GCD at 0.5 A $g^{-1}$, shown in Figure 4.5a. The potential profile of the AC cathode exhibited an approximately linear behavor with the charge time, indicating a capacitive behavior. The zinc metal anode shows a constant potential of −0.983 V (vs. Ag/AgCl) for deposition of $Zn^{2+}$ and −0.933 V (vs. Ag/AgCl) for stripping of Zn. The behavior of the zinc metal electrode is similar to that of a battery electrode. Considering that the potential range of the zinc electrode is almost unchanged, its specific capacitance can be considered as semi-infinite compared with the specific capacitance of the AC electrode. As this hybrid capacitor consists of an AC electrode and zinc electrode connected in series, the total capacitance is dominated by the capacitance of the smaller (i.e., AC) electrode [49]. So the total capacitance of this device is approximately equal to that of the AC electrode: if the weight and thickness of zinc anode is optimised, this leads to the effective utilization of the capacitance of the AC electrode in this hybrid supercapacitor. By contrast, in the case of a symmetric supercapacitor, the specific capacitance of a cell is restricted to approximately 25% of that of a single electrode, since the cell capacitance is half of a single electrode and the cell is twice the mass of a single electrode. Since the AC electrodes consist of the activated carbon, conductive carbon, binder and current collector, we can directly use zinc metal to replace one of the AC electrodes in a symmetric supercapacitor to construct a hybrid supercapacitor in which the zinc metal can serve as the active material and current collector without additional binders and conductive agent. Therefore, this strategy may provide a possibility to fully utilize the capacitance of AC electrode at the cell level and potentially reduce the total weight of the cell. To further confirm that the specific capacitance is dominated by AC electrode, we have chosen another kind of activated carbon known as C9157 with a low specific surface area of 915 $m^2$ $g^{-1}$ as the cathode, shown in Figure S4.4. As shown in Figure S4.6, it delivers a relatively low specific capacitance of 100 F $g^{-1}$ at a current density of 0.5 A $g^{-1}$, which testifies that the performance of the cell is dominated by the AC electrode and the corresponding specific capacitance is highly dependent on the specific surface area of the activated carbon. The physical and chemical nature of carbon

materials clearly has a great influence on the adsorption/desorption of ions at the interface between the carbon and electrolyte. Therefore, the rational design of nanostructured carbon materials is expected to optimize the performance of the hybrid supercapacitors.

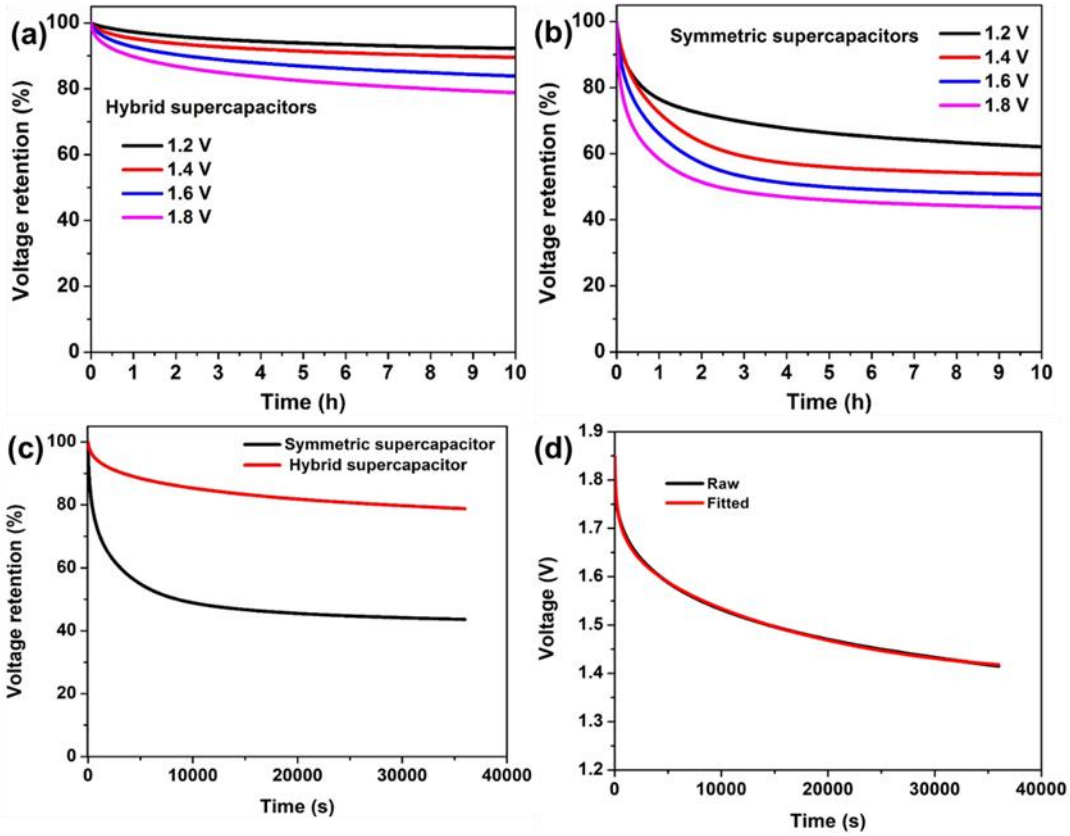


**Figure 4.6.** Voltage retention of **(a)** zinc ion hybrid supercapacitors and **(b)** symmetric supercapacitors at different initial voltages under the open-circuit conditions, **(c)** Comparison of the voltage retention at initial voltage of 1.8 V between zinc ion hybrid supercapacitors and symmetric supercapacitors, **(d)** Fitting of the self-discharge of zinc ion hybrid supercapacitors based on mixed mechanism.

Although considerable efforts have been made to improve the energy and power densites of supercapacitors, the self-discharge of hybrid supercapacitor has been comparatively overlooked. Self-discharge means the spontaneous voltage drop of energy storage devices over a period of storage time, thus resulting in energy loss of the devices [50, 51]. In batteries, the self-discharge rate is relatively slow due to the energy being stored through the bulk of the electrode materials. In electrical double-

layer capacitors, the mechanism is usually based on the electrostatic adsorption of ions on the interface between the electrode and electrolyte, leading to a much faster self-discharge rate. Considering that self-discharge is a significant concern in the practical application of supercapacitors, the self-discharge phenomenon of this hybrid supercapacitor were systematically investigated. The cell was charged to a given volage with a low current density of 0.5 A $g^{-1}$ and then held for 20 minutes to keep it fully charged. The self-discharge voltage profiles for various initial voltages are shown in Figure 4.6a. When the zinc ion hybrid supercapacitors are charged to 1.2, 1.4, 1.6 and 1.8 V, the retention of voltage is 92.29%, 89.53%, 83.86% and 78.79%, respectively, after 10 h under open circuit conditions. For comparison in Figure 4.6b, the symmetric supercapacitors are also charged to 1.2, 1.4, 1.6 and 1.8 V, respectively. The corresponding retentions of voltage are 62.04%, 53.70%, 47.53% and 43.64%, respectively. As shown in Figure 4.6c, a distinct difference in the voltage rentention can be noted between the zinc ion hybrid supercapacitor and the symmetric supercapacitor, indicating effective suppression of self-discharge in this hybrid supercapacitor due to the higher energy barrier for spontaneous stripping/plating of zinc in comparison with the electrostatic adsorption/desorption of ions. The self-discharge is driven by the system minimsing its Gibbs energy and is sensitive to the initial voltage [52, 53]. Considering that supercapacitors will lose 75% of the stored energy once their voltage drops to half of the initial voltage, the rapid loss of voltage can cause fatal damage to the performance of supercapacitors [51]. These results prove that the self-discharge phenomena were substantially suppressed in the hybrid supercapacitors. The merit of this hybrid configuration in suppressing self-discharge has also been demonstrated by Zhi et al. [54-56]. For instance, the voltage retention in the phosphorene-Zn hybrid capacitor was 72.73% within 15 h under the initial voltage of 2.2 V and the voltage retention was 65.93% after 72 h in the $Ti_3C_2$-Zn hybrid capacitor fully charged to 1.35 V. Since self-discharge is an inevitable issue in supercapacitors, various methods have been used to suppress it by tailoring the electrode [57], introducing additives to the electrolyte [53, 58, 59], and using ion-exchange membranes

as separators [58]. Compared with the methods reported in the literature, this hybrid configuration proves to be a simpler and more effective strategy, without side effects, to alleviate the self-discharge phenomena in supercapacitors.

Generally, three different self-discharge mechanisms have been proposed based on electric double-layer capacitors. The first one is ohmic leakage which takes place through internal resistance present in the device [51, 52]. The second one is charge redistribution due to the diffusion of ions adsorbed on the electrode surface [60-63]. The third one is faradaic process owing to the oxidation or reduction of redox species and impurities on the electrode surface [51, 64]. As to ohmic leakage, the relationship between voltage and time is in a similar way as a dielectric capacitor. The relevant equation is [52, 65]:

$$U_t = U_0 \exp\left(-\frac{t}{RC}\right) \qquad (4.1)$$

$$\text{or} \quad \ln U_t = \ln U_0 - \frac{t}{RC} \qquad (4.2)$$

where $U_t$ is the device voltage during the self-discharge process, $U_0$ is the initial voltage, $t$ is the self-discharge time, $C$ is the capacitance of the cell, and $R$ is internal resistance present in the cell.

For self-discharge under diffusion-control, the voltage variation is assumed to be a function of the square root of time [50, 52, 53]:

$$U_t = U_0 - m\sqrt{t} \qquad (4.3)$$

where $m$ is a constant related to the diffusion parameter of the ions near the electrode surface.

For self-discharge caused by Faradaic reactions, which may be attributed to local overcharging or impurities, the voltage variation can be expressed by following equation [50, 52, 60, 65]:

$$U_t = U_0 - \frac{RT}{\alpha F}\ln\frac{\alpha F i}{RTC} - \frac{RT}{\alpha F}\ln\left(t + \frac{CK}{i}\right) \qquad (4.4)$$

where $R$ is ideal gas constant, $T$ is temperature, α represents charge transfer coefficient, $F$ is the Faraday constant, $i$ is the exchange current, and $K$ represents an integration constant.

In conventional dielectric capacitors, the self-discharge is dominated by the leakage mechanism, but voltage changes may be caused by hybrid mechanisms in electrochemical capacitors. Combining the three possible mechanisms, the general relation of voltage and time can be described as following [50, 53]:

$$U_t = U_0 \exp\left(-\frac{t}{RC}\right) - m\sqrt{t} - a\ln(t + \frac{CK}{i}) + b \quad (4.5)$$

where $a$, and $b$ are constants.

When the ohmic leakage model is used to fit the self-discharge curve, it is found that the self-discharge phenomenon cannot be entirely attributed to ohmic leakage, since the self-discharge does not exhibit a purely exponential decrease, shown in Figure S4.7. Addtionally, the diffusion process and faradaic process are also considered to explain the self-discharge process. As shown in Figure S4.8 and Figure S4.9, it is difficult to match a single model with the practical self-discharge behavior. When the three mechanisms are combined, it is possible to obtain a good match between the test curve and fitting results in the whole period, as shown in Figure 4.6d. This implies that the self-discharge can be ascribed to the joint effect of the three mechanisms.

The Ragone plot based on the mass of active materials is also shown in Figure 4.7a. A high energy density of 104.8 Wh $kg^{-1}$ was achieved at the power density of 383.5 W $kg^{-1}$ and a high power density of 19.0 kW $kg^{-1}$ was obtained at the energy density of 30.8 Wh $kg^{-1}$, which are superior to those of most reported zinc-based hybird supercapacitors [29-31, 66-69]. This level of performance confirms the effectiveness of the hybrid configuration design to enhance energy storage. In view of the total weight of the device including active materials, binder, current collectors, electrolyte, separator and packaging, the Ragone plots merely based on the mass of active materials could not realistically present the practical performance in energy and power. Generally, the

proportion of the active materials is about 30% of the total mass in a packaged commercial supercapacitor. So a factor of 3 to 4 is usually employed to reappraise the practical performance of the active materials in energy and power [4]. Therefore, the energy densities of the assumed packaged supercapacitors are expected to be about 25 to 30 Wh $kg^{-1}$, which are higher than those of commercial activated carbon based supercapacitors (5 to 10 Wh $kg^{-1}$). Additionally, the cycling stability of the cell was evaluated by using the GCD method at 4 A $g^{-1}$, shown in Figure 4.7b. The inset of Figure 4.7b demonstrates the typical GCD profile after long-term cycling. This hybrid supercapacitor has exhibited excellent long-term stability with a capacitance retention of about 95.1% over 10,000 cycles with almost 100% coulombic efficiency. Considering that the aqueous mild electrolyte is non-flammable, non-corrosive and eco-friendly, aqueous zinc ion hybrid supercapacitors are expected to hold great potential in future practical applications to fill the gap between electrochemical capacitors and batteries.

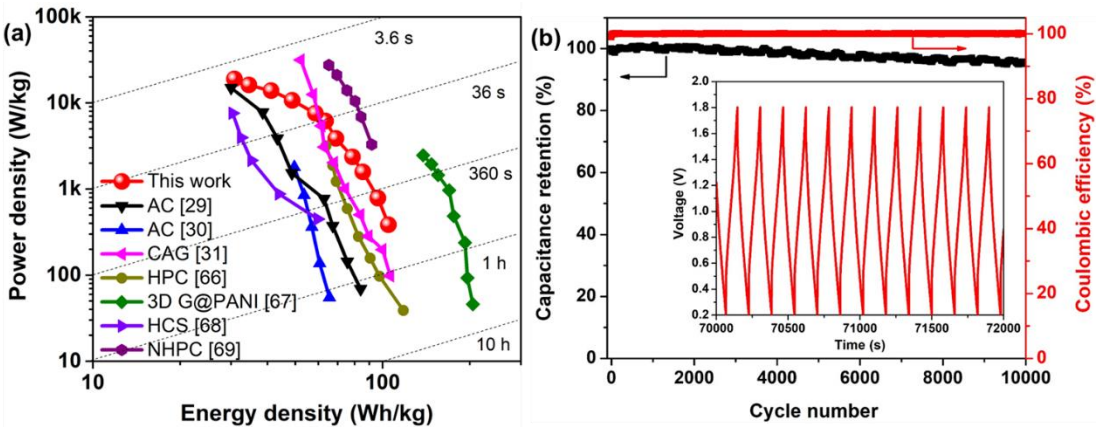


**Figure 4.7. (a)** Ragone plots of the Zn-ion hybrid supercapacitor based on the mass of active materials compared to the reported results, AC represents activated carbon, CAG represents chemical activated graphene, HPC represents hierarchical porous carbon, 3D G@PANI represents 3-dimensional graphene@ polyaniline composite hydrogel, HCS represents hollow carbon sphere and NHPC represents N-doped hierarchically porous carbon. **(b)** Cycling stability at 4 A $g^{-1}$ for 10,000 cycles and the typical GCD profile shown in inset.

## *Conclusions*

In summary, the voltage range and self-discharge phenomena have been systematically investigated in aqueous zinc ion hybrid supercapacitors, which leads to a better understanding of this hybrid device. Three universal approches based on CV and GCD techniques were employed to thoroughly investigate the voltage window in this aqueous zinc ion hybrid supercapacitor based on 2 M $ZnSO_4$. The corresponding mechanism and configuration advantages of this hybrid supercapacitor have also been discussed. The mechanism of the zinc ion hybrid supercapacitor involves the simultaneous adsorption/desorption of ions on the AC cathode and zinc ion plating/stripping on the Zn anode. Constructed by the large capacity of the Zn metal negative electrode, with its relatively low standard redox potential of −0.76 V (*vs.* standard hydrogen electrode) and neutral aqueous electrolyte, the hybrid supercapacitors have demonstrated excellent electrochemical performances including high specific capacitance (308 F $g^{-1}$ at 0.5 A $g^{-1}$ and 110 F $g^{-1}$ at 30 A $g^{-1}$), good cycling stability (10,000 cycles with 95.1% capacitance retention) and a high energy density 104.8 Wh $kg^{-1}$ at 383.5 W $kg^{-1}$ (30.8 Wh $kg^{-1}$ at 19.0 kW $kg^{-1}$) based on the active materials, which exceed those of most reported zinc-based hybrid supercapacitors and symmetrical supercapacitors. Additionally, the self-discharge was substantially suppressed in the hybrid supercapacitors compared with the symmetric supercapacitors, a phenomenon which is highly dependent on the initial voltage. Since the zinc foil can be simultaneously used as both current collector and active material, the unnecessary weight and volume of the devices can potentially be reduced to some extent. The performance of this device can be further boosted by developing novel advanced carbon-based materials or other composites. This work is expected to provide more insight into the hybrid supercapacitors and accelerate industrial development of high-voltage aqueous hybrid supercapacitors for next-generation energy storage devices.

## *Experimental Section*

### 1) Materials and chemicals

The activated carbon (AC) (YEC-8A) was purchased from Fuzhou Yihuan Carbon Co.,Ltd (China). Zinc foil (thickness of 180 μm), $ZnSO_4 \cdot 7H_2O$, conductive carbon black (Super P with sizes from 40 to 100 nm) and cellulose separator were purchased from Alfa Aesar manufacturer. Activated charcoal (C9157) and 60 wt% polytetrafluoroethylene (PTFE) dispersion in $H_2O$ were purchased from Sigma-Aldrich Company. After polishing, Zinc foil (15 mm diameter) was directly used as the anode. The cathode was composed of activated carbon, conductive carbon black and PTFE in the mass ratio of 8 : 1: 1. *Iso*-propanol was added to the above mixture and the resultant suspension was rolled into thin sheets of about 100 μm thickness. The sheets were then punched into electrodes of 12 mm diameter. All the electrodes were dried in an oven at 80 °C for 24 h. The mass loading of the activated carbon is about 4 mg $cm^{-2}$.

**2) Materials characterization**

The structure of the materials was investigated by powder X-ray diffraction (Bruker D8 Advanced diffractometer) with Cu-Kα radiation (λ = 1.5406 Å) at 40 kV. The morphology of the materials was observed by using a Philips XL30 Field Emission Scanning Electron Microscope (FESEM) at 5 kV. Raman spectroscopy was recorded using a Renishaw inVia microscope with an excitation wavelength of 532 nm at a power of ~1 mW. X-ray photoelectron spectroscopy (XPS) analysis was performed by using a Kratos Axis Ultra spectrometer with a mono-chromatic Al-Kα X-ray source. Nitrogen adsorption/desorption measurements were used to characterize the pore structure on a Micromeritics ASAP 2020 analyzer at 77 K. The specific surface area was derived from the Brunauer-Emmett-Teller (BET) model and the pore size distribution (PSD) was derived from a non-local density functional theory (NLDFT) model [39, 40].

**3) Electrochemical measurements**

The cyclic voltammetry (CV) was carried out in a PGSTAT302N potentiostat (Metrohm Autolab). The galvanostatic charge-discharge (GCD) tests were performed in a Battery Test System (BaSyTec GmbH, Germany). The three-electrode tests were performed with a stainless steel (Type 316, ~2 $cm^2$) working electrode, zinc foil as both

the reference electrode and as the counter electrode. The stainless steel working electrode was employed to make the three electrode experiments consistent with the conditions of the coin cell work, where a stainless steel casing can come into contact with the electrolyte. For the hybrid supercapacitors, the cells were assembled into a CR2032 coin-cell type device with activated carbon electrode as cathode, a zinc anode and 2 M $ZnSO_4$ aqueous electrolyte. The cyclic voltammetry was performed at various scan rates ranging from 10 to 100 mV $s^{-1}$. GCD tests were carried out with a voltage range from 0.2 V to 1.8 V at various current densities. Moreover, the cyclic stability was performed at a current density of 4 A $g^{-1}$ for 10,000 cycles. All the electrochemical tests were carried out at room temperature.

According to the galvanostatic discharge curve, the gravimetric capacitance ($C$) was calculated by the following equation:

$$C = \frac{I\Delta t}{m\Delta V} \quad (4.6)$$

where $I$ is the discharge current, $\Delta t$ represents the discharge time, $m$ is the mass of the activated carbon and $\Delta V$ is potential range.

The corresponding energy density (E) and power density (P) were calculated via the following equations:

$$E = \int_0^{\Delta t} V(t) I dt \quad (4.7)$$

$$P = \frac{E}{\Delta t} \quad (4.8)$$

Where $\Delta t$ is the discharge time, $V(t)$is the voltage and $I$ is the current density. The detailed calculation procedure is provided in the Supporting Information.

## *Acknowledgements*

We thank the University of Manchester for providing the President's Doctoral Scholarship (PDS) Award for J. Yang and the EPSRC for further financial support

(grant reference EP/R023034/1). We thank Dr. Ben Spencer for assistance in obtaining the XPS data. J. Yang would like to thank Dr. Lewis W. Le Fevre and Dr. Richard Fields for their induction and technical support in the Energy Lab of the National Graphene Institute.

## *Conflict of interest*

The authors declare no conflict of interest.

**Keywords:** aqueous zinc ion hybrid supercapacitors • voltage range • self-discharge • high performance

## *References*

[1] B. Dunn, H. Kamath, J.-M. Tarascon, Science, 334 (2011) 928-935.

[2] W. Zuo, R. Li, C. Zhou, Y. Li, J. Xia, J. Liu, Adv. Sci., 4 (2017) 1600539.

[3] W. Sun, F. Wang, S. Hou, C. Yang, X. Fan, Z. Ma, T. Gao, F. Han, R. Hu, M. Zhu, C. Wang, J. Am. Chem. Soc., 139 (2017) 9775-9778.

[4] Y.G.a.P. Simon, Science 334 (2011) 917-918.

[5] P. Simon, Y. Gogotsi, Nat. Mater., 7 (2008) 845-854.

[6] B.K. Kim, S. Sy, A. Yu, J. Zhang, Electrochemical Supercapacitors for Energy Storage and Conversion, in: Handbook of Clean Energy Systems, 2015, pp. 1-25.

[7] Y. Jin, K. Tian, L. Wei, X. Zhang, X. Guo, J. Mater. Chem. A, 4 (2016) 15968-15979.

[8] J. Xu, Z. Tan, W. Zeng, G. Chen, S. Wu, Y. Zhao, K. Ni, Z. Tao, M. Ikram, H. Ji, Y. Zhu, Adv. Mater., 28 (2016) 5222-5228.

[9] T. Kim, G. Jung, S. Yoo, K.S. Suh, R.S. Ruoff, ACS Nano, 7 (2013) 6899-6905.

[10] Y. Zhu, S. Murali, M.D. Stoller, K.J. Ganesh, W. Cai, P.J. Ferreira, A. Pirkle, R.M. Wallace, K.A. Cychosz, M. Thommes, D. Su, E.A. Stach, R.S. Ruoff, Science, 332 (2011) 1537-1541.

[11] L. Estevez, R. Dua, N. Bhandari, A. Ramanujapuram, P. Wang, E.P. Giannelis, Energy Environ. Sci., 6 (2013) 1785-1790.

[12] T. Lin, I.W. Chen, F. Liu, C. Yang, H. Bi, F. Xu, F. Huang, Science, 350 (2015) 1508-1513.

[13] J. Yang, H. Wu, M. Zhu, W. Ren, Y. Lin, H. Chen, F. Pan, Nano Energy, 33 (2017) 453-461.

[14] Q. Wang, Z.H. Wen, J.H. Li, Adv. Funct. Mater., 16 (2006) 2141-2146.

[15] R. Liu, S.B. Lee, J. Am. Chem. Soc., 130 (2008) 2942-2943.

[16] E. Lim, C. Jo, J. Lee, Nanoscale, 8 (2016) 7827-7833.

[17] C. Zhong, Y. Deng, W. Hu, J. Qiao, L. Zhang, J. Zhang, Chem. Soc. Rev., 44 (2015) 7484-7539.

[18] A. González, E. Goikolea, J.A. Barrena, R. Mysyk, Renew. Sust. Energ. Rev., 58 (2016) 1189-1206.

[19] Q. Gao, L. Demarconnay, E. Raymundo-Piñero, F. Béguin, Energy Environ. Sci., 5 (2012) 9611.

[20] L. Demarconnay, E. Raymundo-Piñero, F. Béguin, Electrochem. Commun., 12 (2010) 1275-1278.

[21] M.P. Bichat, E. Raymundo-Piñero, F. Béguin, Carbon, 48 (2010) 4351-4361.

[22] K. Fic, G. Lota, M. Meller, E. Frackowiak, Energy Environ. Sci., 5 (2012) 5842-5850.

[23] J. Yang, J. Hu, M. Zhu, Y. Zhao, H. Chen, F. Pan, J. Power Sources, 365 (2017) 362-371.

[24] M. Armand, J.M. Tarascon, Nature, 451 (2008) 652-657.

[25] L. Kong, C. Zhang, S. Zhang, J. Wang, R. Cai, C. Lv, W. Qiao, L. Ling, D. Long, J. Mater. Chem. A, 2 (2014) 17962-17970.

[26] C. Zhang, M. Beidaghi, M. Naguib, M.R. Lukatskaya, M.-Q. Zhao, B. Dyatkin, K.M. Cook, S.J. Kim, B. Eng, X. Xiao, D. Long, W. Qiao, B. Dunn, Y. Gogotsi, Chem. Mater., 28 (2016) 3937-3943.

[27] K. Naoi, S. Ishimoto, J.-i. Miyamoto, W. Naoi, Energy Environ. Sci., 5 (2012) 9363-9373.

[28] D.P. Dubal, O. Ayyad, V. Ruiz, P. Gomez-Romero, Chem. Soc. Rev., 44 (2015) 1777-1790.

[29] L. Dong, X. Ma, Y. Li, L. Zhao, W. Liu, J. Cheng, C. Xu, B. Li, Q.-H. Yang, F. Kang, Energy Stor. Mater., 13 (2018) 96-102.

[30] H. Wang, M. Wang, Y. Tang, Energy Stor. Mater., 13 (2018) 1-7.

[31] S. Wu, Y. Chen, T. Jiao, J. Zhou, J. Cheng, B. Liu, S. Yang, K. Zhang, W. Zhang, Adv. Energy Mater., 9 (2019) 1902915.

[32] A.C. Ferrari, J. Robertson, Phys. Rev. B, 61 (2000) 14095-14107.

[33] F. Tuinstra, J.L. Koenig, J. Chem. Phys., 53 (1970) 1126-1130.

[34] Y. Li, Y. Zhao, H. Cheng, Y. Hu, G. Shi, L. Dai, L. Qu, J. Am. Chem. Soc., 134 (2012) 15-18.

[35] Y.S. Yun, S. Lee, N.R. Kim, M. Kang, C. Leal, K.-Y. Park, K. Kang, H.-J. Jin, J. Power Sources, 313 (2016) 142-151.

[36] T.I.T. Okpalugo, P. Papakonstantinou, H. Murphy, J. McLaughlin, N.M.D. Brown, Carbon, 43 (2005) 153-161.

[37] Q. Li, R. Jiang, Y. Dou, Z. Wu, T. Huang, D. Feng, J. Yang, A. Yu, D. Zhao, Carbon, 49 (2011) 1248-1257.

[38] Z. Alothman, Materials, 5 (2012) 2874-2902.

[39] S. Brunauer, P.H. Emmett, E. Teller, J. Am. Chem. Soc., 60 (1938) 309-319.

[40] M. Thommes, K. Kaneko, A.V. Neimark, J.P. Olivier, F. Rodriguez-Reinoso, J. Rouquerol, K.S.W. Sing, Pure Appl. Chem., 87 (2015) 1051-1069.

[41] Y. Gong, Z. Wei, J. Wang, P. Zhang, H. Li, Y. Wang, Sci. Rep., 4 (2014) 6349.

[42] Q. Wang, J. Yan, Y. Wang, T. Wei, M. Zhang, X. Jing, Z. Fan, Carbon, 67 (2014) 119-127.

[43] H. Zhang, G. Cao, Y. Yang, Z. Gu, Carbon, 46 (2008) 30-34.

[44] M. He, K. Fic, E. Frąckowiak, P. Novák, E.J. Berg, Energy Environ. Sci., 9 (2016) 623-633.

[45] B. Avasarala, R. Moore, P. Haldar, Electrochim. Acta, 55 (2010) 4765-4771.

[46] J.-S. Ye, X. Liu, H.F. Cui, W.-D. Zhang, F.-S. Sheu, T.M. Lim, Electrochem. Commun., 7 (2005) 249-255.

[47] Y. Yang, Z.G. Lin, J Appl Electrochem., 25 (1995) 259-266.

[48] X. Zang, C. Shen, M. Sanghadasa, L. Lin, ChemElectroChem, 6 (2019) 976-988.

[49] H.D. Yoo, I. Shterenberg, Y. Gofer, R.E. Doe, C.C. Fischer, G. Ceder, D. Aurbach, J. Electrochem. Soc., 161 (2014) 410-415.

[50] A. Lewandowski, P. Jakobczyk, M. Galinski, M. Biegun, Phys. Chem. Chem. Phys., 15 (2013) 8692-8699.

[51] H.A. Andreas, J. Electrochem. Soc., 162 (2015) 5047-5053.

[52] B.E. Conway, W.G. Pell, T.-C. Liu, J. Power Sources, 65 (1997) 53-59.

[53] M. Xia, J. Nie, Z. Zhang, X. Lu, Z.L. Wang, Nano Energy, 47 (2018) 43-50.

[54] Q. Yang, Z. Huang, X. Li, Z. Liu, H. Li, G. Liang, D. Wang, Q. Huang, S. Zhang, S. Chen, C. Zhi, ACS Nano, 13 (2019) 8275-8283.

[55] Z. Huang, A. Chen, F. Mo, G. Liang, X. Li, Q. Yang, Y. Guo, Z. Chen, Q. Li, B. Dong, C. Zhi, Adv. Energy Mater., 10 (2020) 2001024.

[56] Z. Huang, T. Wang, H. Song, X. Li, G. Liang, D. Wang, Q. Yang, Z. Chen, L. Ma, Z. Liu, B. Gao, J. Fan, C. Zhi, Angew. Chem. Int. Ed., 60 (2020) 1011-1021.

[57] T. Tevi, H. Yaghoubi, J. Wang, A. Takshi, J. Power Sources, 241 (2013) 589-596.

[58] L. Chen, H. Bai, Z. Huang, L. Li, Energy Environ. Sci., 7 (2014) 1750-1759.

[59] K. Fic, G. Lota, E. Frackowiak, Electrochim. Acta, 55 (2010) 7484-7488.

[60] J. Black, H.A. Andreas, Electrochim. Acta, 54 (2009) 3568-3574.

[61] M. Kaus, J. Kowal, D.U. Sauer, Electrochim. Acta, 55 (2010) 7516-7523.

[62] J. Black, H.A. Andreas, J. Power Sources, 195 (2010) 929-935.

[63] J. Kowal, E. Avaroglu, F. Chamekh, A. Šenfelds, T. Thien, D. Wijaya, D.U. Sauer, J. Power Sources, 196 (2011) 573-579.

[64] B.W. Ricketts, C.T.-T. , J. Power Sources, 89 (2000) 64-69.

[65] J. Niu, B.E. Conway, W.G. Pell, J. Power Sources, 135 (2004) 332-343.

[66] P. Yu, Y. Zeng, Y. Zeng, H. Dong, H. Hu, Y. Liu, M. Zheng, Y. Xiao, X. Lu, Y. Liang, Electrochim. Acta, 327 (2019) 134999.
[67] J. Han, K. Wang, W. Liu, C. Li, X. Sun, X. Zhang, Y. An, S. Yi, Y. Ma, Nanoscale, 10 (2018) 13083-13091.
[68] S. Chen, L. Ma, K. Zhang, M. Kamruzzaman, C. Zhi, J.A. Zapien, J. Mater. Chem. A, 7 (2019) 7784-7790.
[69] H. Zhang, Q. Liu, Y. Fang, C. Teng, X. Liu, P. Fang, Y. Tong, X. Lu, Adv. Mater., 31 (2019) 1904948.

# ChemSusChem

# Supporting Information

## Investigation of Voltage Range and Self-Discharge in Aqueous Zinc-Ion Hybrid Supercapacitors

Jie Yang,[a, b] Mark A. Bissett,*[b, c] and Robert A. W. Dryfe*[a, b]

[a] Department of Chemistry, University of Manchester, M13 9PL Manchester (UK)

[b] National Graphene Institute, University of Manchester, M13 9PL Manchester (UK)

[c] Department of Materials, University of Manchester, M13 9PL Manchester (UK)

Corresponding authors: mark.bissett@manchester.ac.uk;

robert.dryfe@manchester.ac.uk

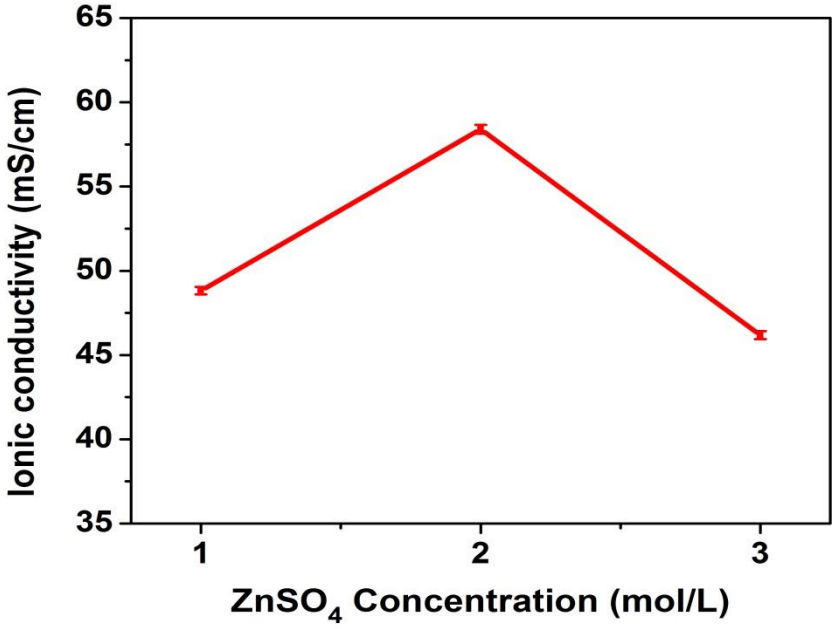


**Figure S4.1.** Ionic conductivities of $ZnSO_4$ measured for the concentrations used in this study.

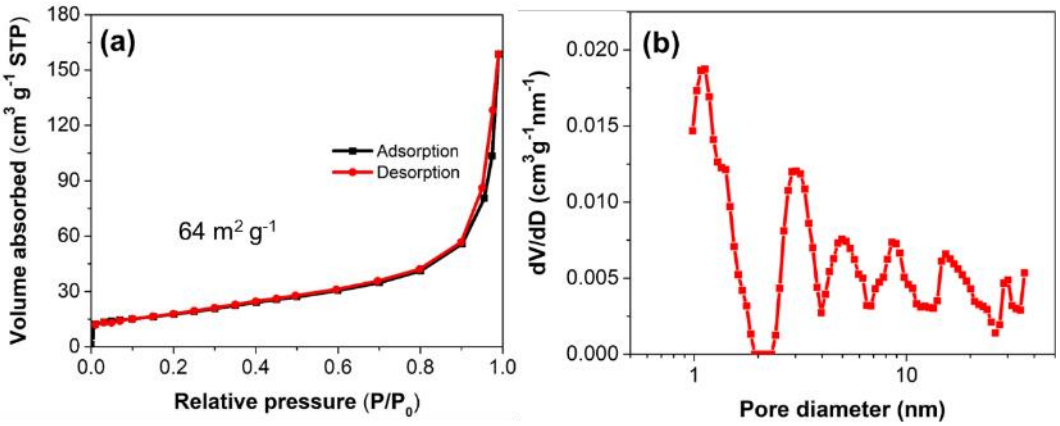


**Figure S4.2.** Conductive carbon black (Super P): **(a)** Nitrogen physisorption isotherms and **(b)** NLDFT-derived pore size distribution.

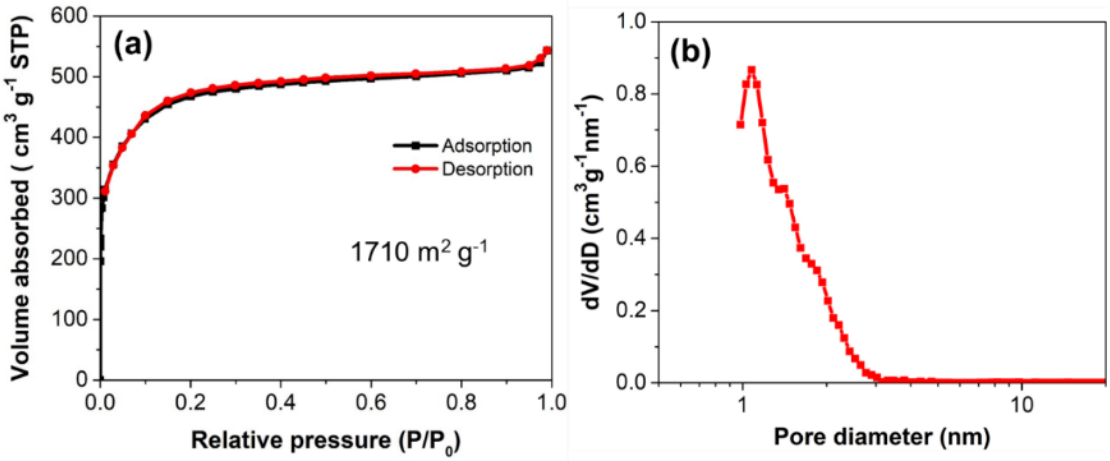


**Figure S4.3.** Fabricated electrode using the activated carbon (YEC-8A) as active materials: **(a)** Nitrogen physisorption isotherms and **(b)** NLDFT-derived pore size distribution.

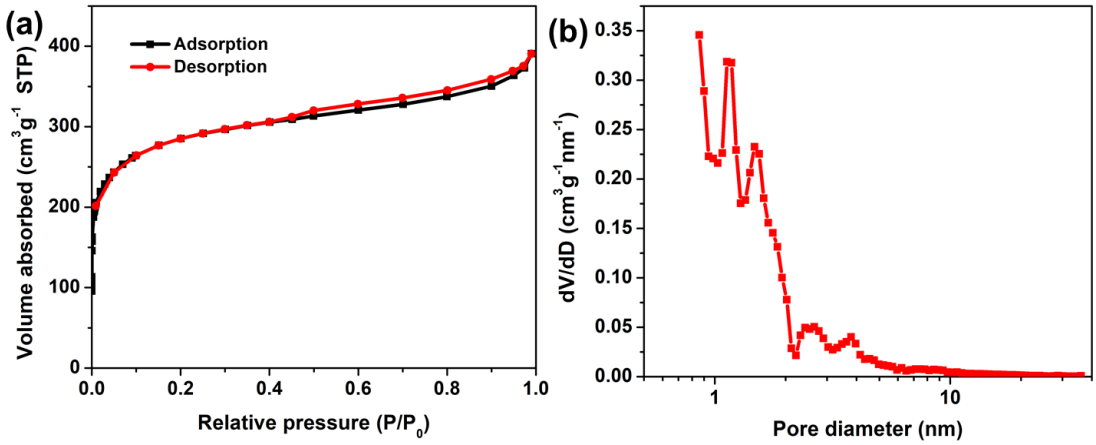


**Figure S4.4.** Activated charcoal (C9157): **(a)** Nitrogen physisorption isotherms and **(b)** NLDFT-derived pore size distribution.

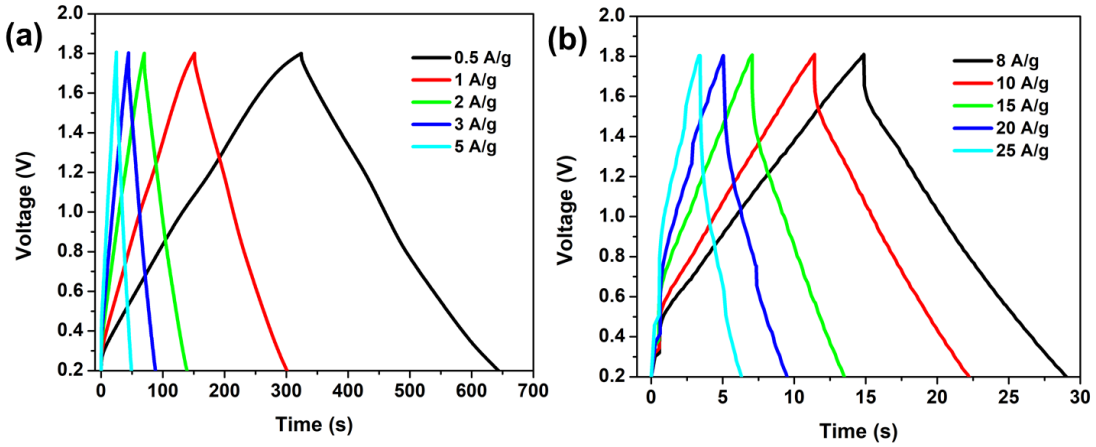


**Figure S4.5.** Representative galvanostatic charge-discharge profiles of zinc ion hybrid supercapacitors based on activated charcoal (C9157).

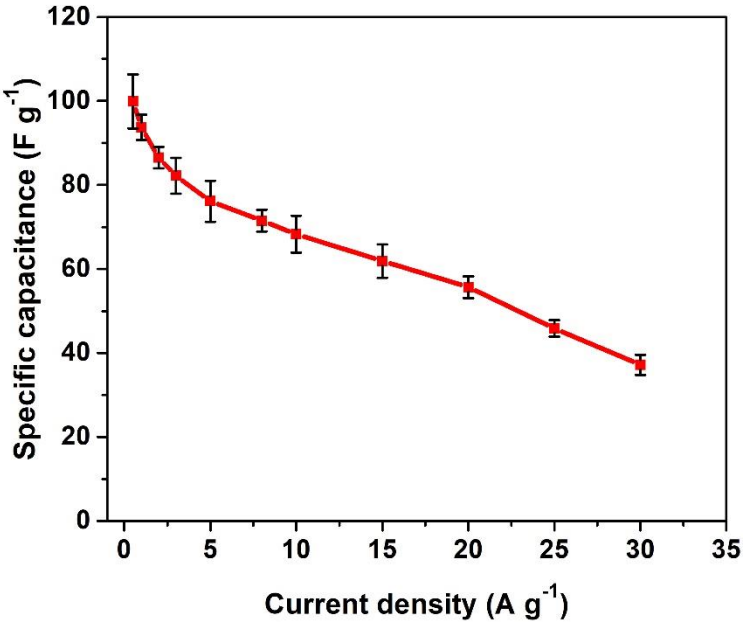


**Figure S4.6.** Specific capacitances of activated charcoal (C9157) at various current densities

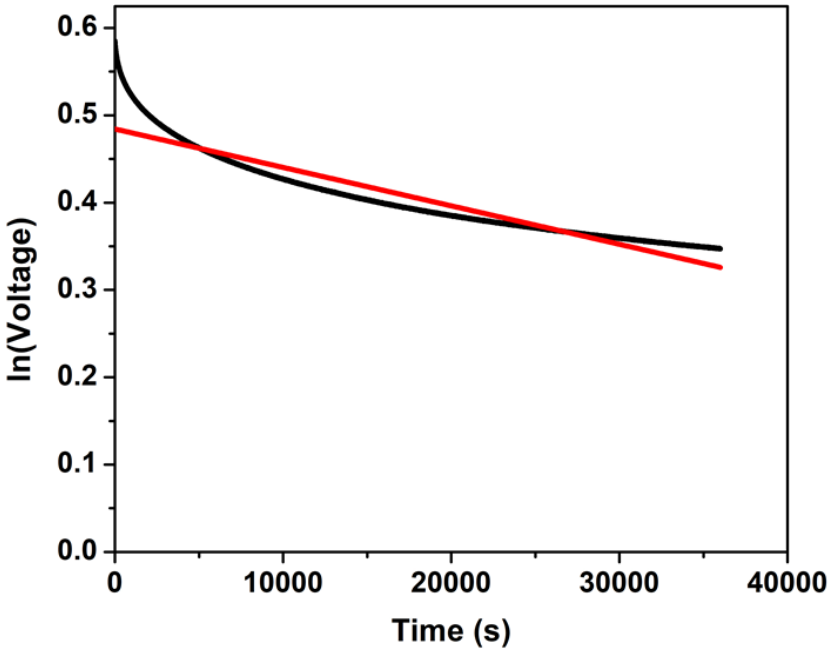


**Figure S4.7.** Fitting of self-discharge process based on ohmic leakage model.

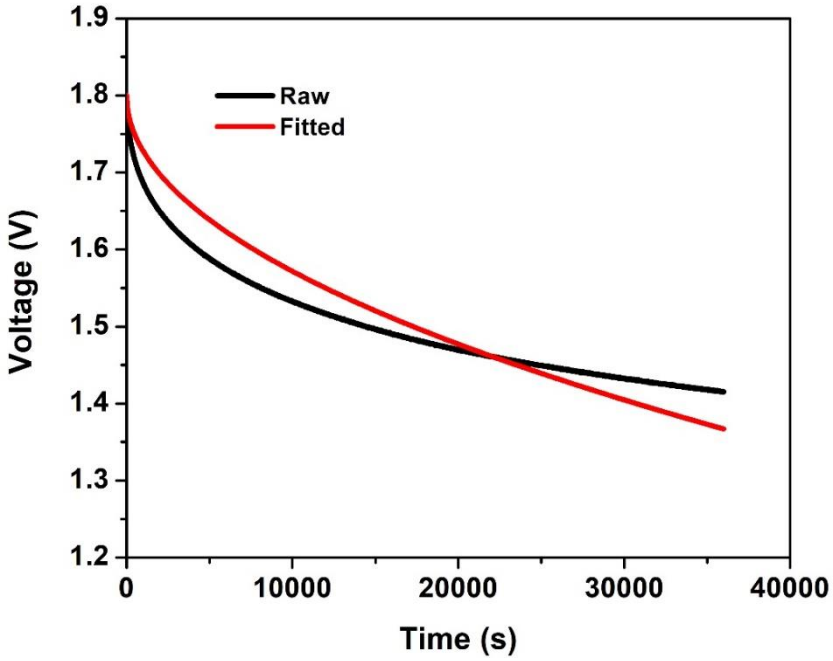


**Figure S4.8.** Fitting of self-discharge process based on ion diffusion model.

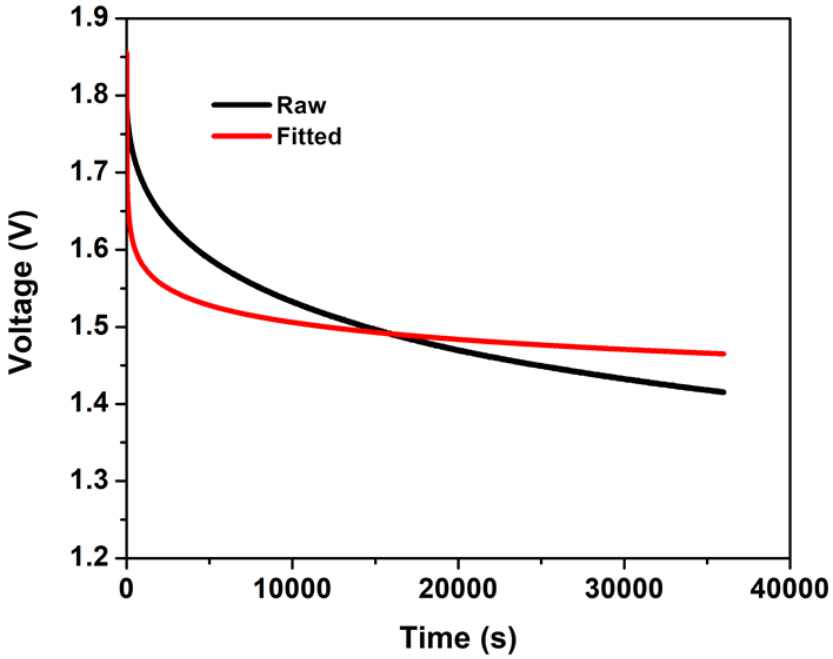


**Figure S4.9.** Fitting of self-discharge behavior based on faradaic process.

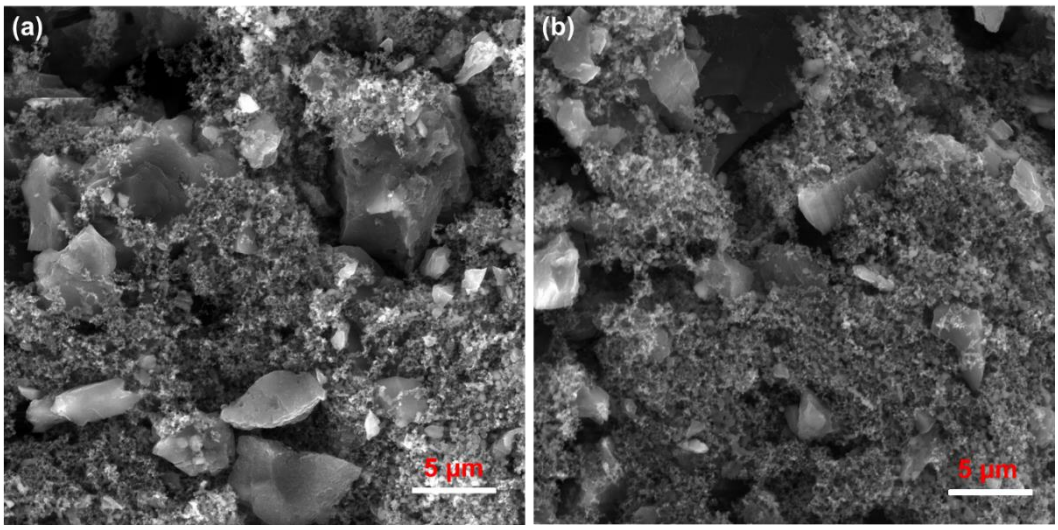


**Figure S4.10.** SEM images of the AC electrode **(a)** before and **(b)** after cycles.

#**Potential conversion**

The standard redox potential of $Zn^{2+}$/Zn is as follows:

$$Zn^{2+} + 2e^{-} \rightleftharpoons Zn \ (E° = -0.762 \text{ V vs. SHE}) \qquad \text{(S4.1)}$$

The practical concentration of $Zn^{2+}$ is 2 mol $L^{-1}$. According to the Nernst equation, the practical potential of $Zn^{2+}$/Zn can be calculated as following:

$$E = E° - \frac{RT}{nF}\ln\frac{[Zn]}{[Zn^{2+}]} = -0.762 - \frac{8.314\times298.15}{2\times96485}\times\ln\frac{1}{2} = -0.754 \text{ V (vs. SHE)} \qquad \text{(S4.2)}$$

The standard potential of reference electrode (Ag/AgCl with saturated KCl solution) is 0.222 V (vs. SHE). Therefore, the required theoretical potential of ($Zn^{2+}$/Zn) relative to the reference electrode (Ag/AgCl) is estimated to be -0.976 V (Vs. Ag/AgCl). This value is consistent with the experimentally obtained values.

# **The calculation of energy density and power density**

Generally, the energy density of supercapacitors can be estimated by numerically integrating the discharge curves [1]:

$$E = \int_{t_1}^{t_2} IVdt \qquad \text{(S4.3)}$$

Where $t_1$and $t_2$ are time, $I$ is the current density, $V$ is the discharge voltage.

If $V$ is a liner function of time t, then

$$E = \int_{t_1}^{t_2} IVdt = \frac{1}{2}C({V_2}^2 - {V_1}^2) \qquad \text{(S4.4)}$$

where $V_1$ is minimum voltage at time $t_1$, $V_2$ is maximum voltage at time $t_2$ and C is the capacitance of the device.

If $V_1$ is set to be 0 V which is the common minimum voltage in symmetric supercapacitors, then equation (2) can be transformed into the most common equation widely used to calculate energy density in supercapacitors,

$$E = \frac{1}{2}C{V_2}^2 = \frac{1}{2}C\Delta V^2 \qquad \text{(S4.5)}$$

Where $\Delta V$ is the voltage window($\Delta V = V_2 - V_1$).

However, in the case of a hybrid supercapacitor, the minimum voltage $V_1$ for capacitive behavior is usually larger than 0 V. Therefore, the equation (S4.4) can be used to calculate the corresponding energy density. It should be noted that the voltage is not an ideal linear behavior with time in hybrid supercapacitors. If the equation is directly used to calculate the energy density in a hybrid device, the corresponding energy density will be overestimated. Therefore, the direct numerically integrating the discharge curves is highly recommended. We have compared the differences of these two methods, shown in Table S4.1.

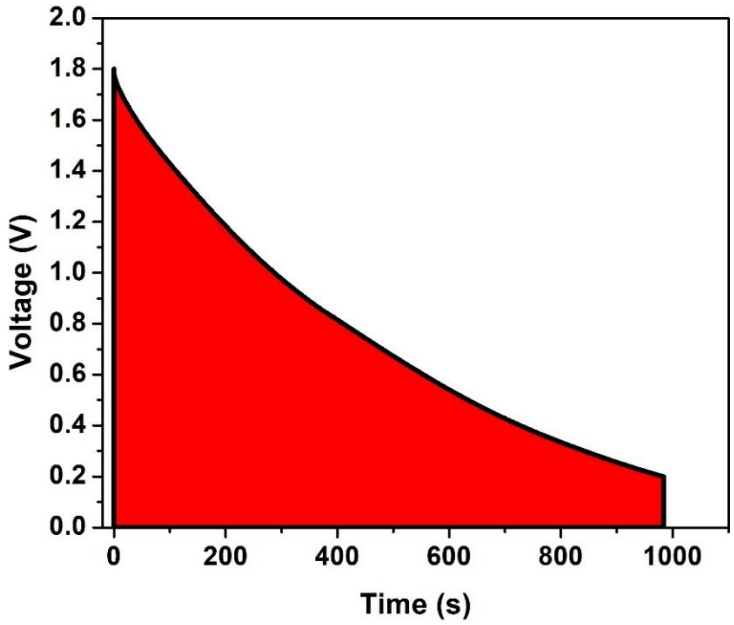


**Figure S4.11.** The typical discharge curve of zinc ion hybrid supercapacitor at 0.5 A $g^{-1}$.

The energy density ($E$) is calculated by using the following equation:

$$E = \int_0^{\Delta t} V(t) I dt = A_S I \quad \text{(S4.6)}$$

Where $\Delta t$ is the discharge time, $V(t)$ is the voltage, I is the current density, $A_S$ is the integral area denoted in the red area.

The energy density ($P$) is calculated by:

$$P = \frac{E}{\Delta t} \quad \text{(S4.7)}$$

**Table S4.1.** Comparison of two methods to calculate the energy density and power density.

| Direct integral | | Formula method | |
|---|---|---|---|
| $E = \int_{t_1}^{t_2} IVdt$ | | $E = \frac{1}{2}C({V_2}^2 - {V_1}^2)$ | |
| Energy density (Wh $kg^{-1}$) | Power density (W $kg^{-1}$) | Energy density (Wh $kg^{-1}$) | Power density (W $kg^{-1}$) |
| 104.8 | 383.5 | 136.7 | 500 |
| 96.4 | 785.6 | 122.7 | 1000 |
| 85.6 | 1575.2 | 108.6 | 2000 |
| 78.7 | 2358.0 | 100.2 | 3000 |
| 69.0 | 3869.7 | 89.1 | 5000 |
| 63.5 | 6147.9 | 82.7 | 8000 |
| 58.7 | 7549.6 | 77.7 | 10000 |

References

[1] Y. Wang, Y. Song, Y. Xia, Chem. Soc. Rev., 45 (2016) 5925-5950.

# Chapter 5 Unlocking the energy storage potential of polypyrrole via electrochemical graphene oxide for high performance zinc-ion hybrid supercapacitors

Jie Yang[a,c,1], Jianyun Cao[b,c,*,1], Yudong Peng[b], Mark Bissett[b,c], Ian A. Kinloch[b,c,*], Robert A. W. Dryfe[a,c]

[a] *Department of Chemistry, University of Manchester, Oxford Road, Manchester, M13 9PL, U.K.*

[b] *Department of Materials, University of Manchester, Oxford Road, Manchester, M13 9PL, U.K.*

[c] *National Graphene Institute and Henry Royce Institute, University of Manchester, Oxford Road, M13 9PL, U.K.*

* Corresponding authors.

*E-mail addresses:*

jianyun.cao@manchester.ac.uk (J. Cao); ian.kinloch@manchester.ac.uk (I. Kinloch)

[1] These authors contributed equally to this work.

**Published in *Journal of Power Sources, 2021, 516: 230663.***



## Author contributions:

The synthesis, characterization, and electrochemical measurement were carried out by J. Yang under the guidance from Dr. J. Cao. The TEM characterization was performed by Y. Peng and J. Yang. The article was written by J. Yang with comments from Dr. J. Cao and Prof. R. A. W. Dryfe. All authors discussed the results and commented on the manuscript.

**Abstract**

Safe, low-cost and environmentally benign zinc-ion hybrid supercapacitors based on neutral aqueous electrolytes are promising for large scale and high power energy storage. A key challenge for Zn-ion hybrid supercapacitors is to increase their energy density without sacrificing the high power performance. Herein, we report a Zn-ion hybrid supercapacitor using a polypyrrole/electrochemical graphene oxide (PPy/EGO) composite cathode and aqueous zinc halide electrolyte (i.e., 1 M $ZnCl_2$ or $ZnBr_2$). We used the recently reported EGO to prepare conducting polymer composite because of its low degree of oxidation and good integrity in conjugated structure, which are favoured for electron conduction. The water dispersible EGO further allows one-step co-electrodeposition of PPy/EGO composite that has a porous structure for fast ion diffusion in pores. Moreover, the small-sized and monovalent anions in the optimized zinc halides electrolytes are highly mobile in bulk PPy for fast anion insertion/de-insertion. Hence, the PPy/EGO composite showed high specific capacitances > 440 F $g^{-1}$ and good rate capability in either 1 M $ZnCl_2$ or $ZnBr_2$. The as-fabricated Zn-PPy/EGO system that had an operation cell voltage from 0.5 to 1.5 V exhibited high energy and high power densities of 117.7 Wh $kg^{-1}$ and 72.1 Wh $kg^{-1}$ at 0.34 kW $kg^{-1}$ and 12.4 kW $kg^{-1}$, respectively, with 81% capacity retention over 5000 cycles. Electrochemical characterization and *ex-situ* X-ray photoelectron spectroscopy confirmed the anion dominated charge storage mechanism of PPy cathode in Zn-PPy system, rather than the reported insertion/de-insertion of divalent $Zn^{2+}$ cations.

**Keywords:** zinc-ion hybrid supercapacitor; polypyrrole; electrochemical graphene oxide; zinc halides; monovalent anions

## 1. Introduction

The rapid development of modern society has accelerated the consumption of fossil fuels and the consequent emission of greenhouse gases. Sustainability for the future depends largely on the replacement of fossil fuels by renewable energy resources, such as solar, wind and tidal energy [1]. Advanced energy storage devices including batteries and supercapacitors play a critical role in the effective storage and utilization of the intermittent electrical energy generated by these renewable resources [2, 3]. Compared with batteries, supercapacitors, also called electrochemical capacitors, are known for their fast charge/discharge rates (i.e., high power density) and ultra-long cycle life. In principle, supercapacitors include (1) electrical double-layer capacitors (EDLCs) that store charges by ion adsorption/desorption at the electrode/electrolyte interface and (2) pseudocapacitors that use fast reversible redox reactions at the surface or near-surface of active materials [4, 5]. However, the relatively low energy density (ca. 10 Wh $kg^{-1}$) of supercapacitors compared with batteries restricts their wide application [6]. Various strategies, including the design of electrode materials [7-10] or device configuration [11, 12] and the selection of electrolytes [13, 14], have been adopted to boost the energy density of supercapacitors without sacrificing their inherent merits of high power and long cycle-life.

The integration of a battery-type electrode with a capacitor-type electrode to construct a hybrid supercapacitor is considered as an effective strategy to improve the energy density of supercapacitors [15]. Recently, aqueous Zn-ion hybrid supercapacitors are emerging as a type of promising energy storage devices, which comprise a capacitor-type carbon-based electrode as cathode, a battery-type metallic Zn anode and aqueous $Zn^{2+}$-containing solution as the electrolyte [16-18]. The integration of the respective merits of supercapacitors and batteries in this hybrid Zn-ion system is expected to fill the performance gap between supercapacitors and batteries. In detail, the rapid reversible adsorption/desorption of ions on carbon cathode endows a superior power density while the high-capacity Zn metal anode (820 mAh $g^{-1}$) guarantees a high energy density. Moreover, the Zn anode is safe, nontoxic, abundant in the Earth's crust and

easily manufactured and recycled [19-21]. These attractive merits have triggered extensive research interest in developing high performance zinc-ion hybrid supercapacitors [22-27]. Currently, most of the cathode materials used in Zn-ion hybrid supercapacitors are carbon-based materials and the reported energy densities (ca. 100 Wh $kg^{-1}$) are significantly higher compared with the conventional symmetrical supercapacitors (ca. 10 Wh $kg^{-1}$) [16-18, 22-26]. Nevertheless, further enhancement in the performance of zinc-ion hybrid supercapacitors is limited by the relatively low specific capacitance (generally, 200-300 F $g^{-1}$) of carbon-based materials. The development of new cathode materials that have high specific capacitance and rate capability is expected to further improve the performance of Zn-ion hybrid devices.

As an important type of electrode materials, conducting polymers including polypyrrole (PPy), polyaniline (PANI), polythiophene (PTh) and their derivatives have been widely studied in supercapacitors due to their good electrical properties, large specific capacitances, light weight and/or flexibility in processing [28-30]. Among them, PPy is of particular interest due to its high theoretical specific capacitance of 620 F $g^{-1}$ (assuming the doping level is 0.33, i.e., one in three pyrrole units involve in the redox reaction, and a potential window of 0.8 V), good electrical conductivity (10-50 S $cm^{-1}$), low cost and ease of processing in aqueous media [31-33]. However, the practical application of PPy in supercapacitors is still limited by two major issues [33]. One of them is the inferior cycling stability in long-term operation due to the volume swelling and shrinkage caused by electrolyte ions insertion/de-insertion [34]. The other issue is the large gap between the measured specific capacitances and the theoretical value due to the dense growth of PPy, which to some extent restricts the effective exposure of active sites and the transport of electrolyte ions [32]. Constructing various composites of PPy with carbon-based materials or metal oxides is considered as one of the effective strategies to overcome the undesirable shortcomings of PPy [31, 33, 34].

PPy has a stable operating potential window from –0.5 to 0.5 V vs saturated calomel electrode (SCE) in neutral aqueous electrolyte (e.g., KCl) [35], and thus is a candidate cathode material for constructing aqueous Zn-ion hybrid supercapacitor that uses a Zn

metal anode (the redox potential of $Zn^{2+}$/Zn is about −1.0 V vs. SCE) [17]. In addition, the most widely accepted charge storage mechanism of PPy is through the reversible insertion/de-insertion of monovalent anions ($Cl^-$, $ClO_4^-$) into the polymer chain [36]; therefore, the tuning of cation species in the electrolytes (i.e., addition of $Zn^{2+}$ to enable electrochemistry of Zn anode) should have a minimum impact on the performance of PPy. Despite these promising prospects, only a few attempts have been tried to develop Zn-PPy hybrid supercapacitors/batteries and the reported performance (e.g., rapid decay of capacity to 38% after 200 cycles) requires further improvement [37-39]. In fact, the choice of electrolyte formulation affects significantly on the specific capacitance, rate capability and cycling stability of PPy electrode. The earlier reported Zn-PPy batteries using zinc acetate salt as $Zn^{2+}$ source imported large sized acetate anion which is likely the reason for the poor cycling stability (i.e., a low capacity retention of 60% was obtained after 50 cycles) [39]. Larger anions as dopants are less mobile in bulk PPy [40], and also likely to cause more severe volume change upon charging-discharging compared with smaller anions (e.g., $Cl^-$). Hence, for the Zn-PPy system, the understanding of charge storage mechanism needs further improvement to guide the selection of electrolyte; whilst the performance of the PPy cathode requires further enchantment to achieve the promising high energy density and power density of the Zn-PPy system. In view of PPy as a typical pseudocapacitive material, a Zn-PPy device composed of a battery-type electrode (Zn) and a capacitor-type electrode (PPy) is referred to as a hybrid supercapacitor within this paper.

Compositing PPy with carbon nanomaterials has been demonstrated as a powerful strategy to enhance its electrochemical performance [35, 40, 41]. Carbon nanomaterials act not only as mechanical and electrical reinforcements but also as building blocks/skeletons to guide the nucleation and growth of PPy to form composites with porous structures [35, 42]. Generally, nanocarbons are functionalized with oxygen groups to allow good dispersibility in aqueous media and easy processing. Earlier studies have demonstrated that the electrochemical polymerization of pyrrole monomer in aqueous dispersions of oxidized carbon nanotubes (CNTs) or graphene oxide (GO)

leads to co-deposition of nanocarbon and PPy with a three-dimensional (3D) porous structure [35, 42]. Nevertheless, the GO used in these previous works is chemical GO (CGO) prepared by oxidation of graphite using potassium permanganate in concentrated sulfuric acid [43, 44]. In general, the CGO is highly oxidized (oxygen content > 20 at.%), and thus its conjugated structure is heavily disrupted [45]. The recently reported electrochemical GO (EGO), prepared by two-step electrochemical intercalation and oxidation approaches [46, 47], has shown tunable oxidation degree via the control of second-step electrolyte formulation/concentration. In comparison to CGO, EGO obtained in 0.1 M $(NH_4)_2SO_4$ aqueous solution has a relatively low oxygen content (ca. 18 at. %) and a much less disrupted graphene lattice structure, the latter is a result of the lower abundance of the un-restorable carbonyl and carboxylic groups compared with CGO. The EGO flakes are most monolayer (ca. 90%) with a thickness of about 1 nm [46]. The less disruption in the conjugated structure of EGO is expected to benefit the π-π interaction between EGO and PPy, leading to enhanced electrical conductivity in the composite [35, 48]. Moreover, EGO can be reduced much easier than CGO [46, 49], which will potentially allow effective reduction of EGO in the EGO/PPy composites by facile electrochemical reduction.

In this work, we have produced PPy/EGO composite electrodes for the first time by using a one-step electrochemical co-deposition approach. The incorporation of EGO nanosheets transformed the compact and dense morphology of the pure PPy electrode to a porous structure of the composite electrode. The facilitated ionic and electronic transport in the composite electrodes lead to high specific capacitance of 444.2 F $g^{-1}$ at 0.35 A $g^{-1}$, equivalent to 633.0 mF $cm^{-2}$ at 0.5 mA $cm^{-2}$. The combination of the PPy/EGO composite cathode with Zn metal anode in 1 M $ZnCl_2$ aqueous electrolyte leads to a Zn-PPy hybrid supercapacitor that has a high energy density of 117.7 Wh $kg^{-1}$ at 0.34 kW $kg^{-1}$. The Zn-PPy hybrid supercapacitor also demonstrates high power performance by retaining the energy density at 72.1 Wh $kg^{-1}$ at 12.4 kW $kg^{-1}$, as well as long-term cycling stability with 81% capacitance retention after 5000 cycles. The high energy and high-power performance of this Zn-PPy/EGO hybrid system

outperforms most of the recently reported Zn-ion supercapacitors/batteries. Moreover, we decoupled of the effects of ion type (cation and anion) and ion valence (monovalent and divalent) by electrochemical characterization and *ex-situ* X-ray photoelectron spectroscopy (XPS); the results indicate a charge storage mechanism of the PPy/EGO cathode in the Zn-ion capacitor by insertion/de-insertion of monovalent anions (e.g., $Cl^-$, $Br^-$) instead of $Zn^{2+}$ cations. This proposed mechanism clarifies the current confusion in understanding the charge storage mechanism in Zn-PPy system and will guide the further development of both electrode materials and electrolytes.

## 2. Results and discussion

### 2.1 Materials preparation and characterization

Figure 5.1 illustrates the process of preparing the PPy/EGO composites. EGO flakes were prepared by the two-step electrochemical intercalation and oxidation approach as reported previously by our group (Figure 5.1a) [46]. The as-prepared EGO dispersion was formulated with pyrrole monomer and supporting electrolyte ($LiClO_4$) for electrochemical co-deposition (Figure 5.1b). The PPy/EGO composite electrode was deposited on a Ti substrate and used as the cathode in the hybrid Zn-PPy/EGO supercapacitor (Figure 5.1c). Detailed descriptions of experimental procedures are available in the electronic supplementary information.

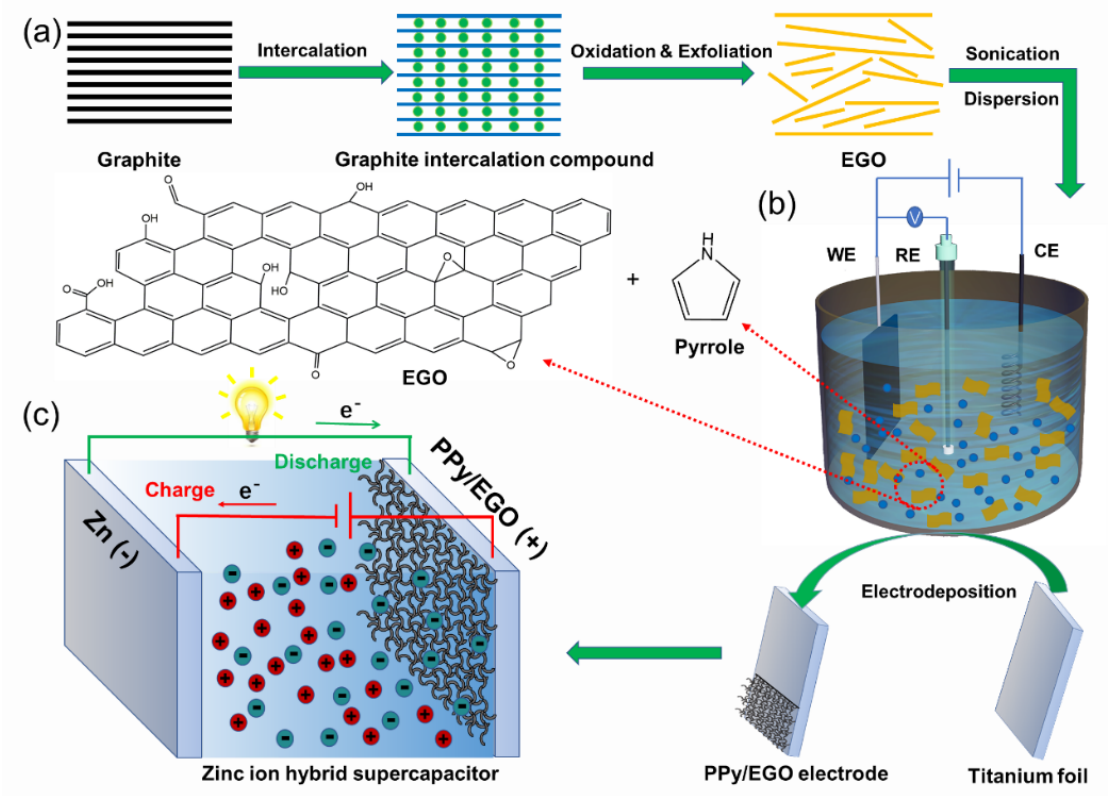


**Figure 5.1.** Electrochemical fabrication of PPy/EGO composite electrodes: schematic illustration of **(a)** two-step electrochemical production of EGO; **(b)** electrochemical co-deposition of EGO/PPy composites on titanium foil substrate, molecular structures of EGO and pyrrole monomer are marked by red arrows; **(c)** cell configuration of Zn-PPy/EGO hybrid supercapacitor using zinc halides electrolytes.

Figure 5.2a shows the scanning electron microscopy (SEM) image of the as-prepared EGO flakes, and statistical analysis of 100 flakes suggests an average flake size of 0.56 ± 0.24 μm (Figure S5.1). As shown in Figure 5.2b and 5.2c, as well as in Figure S5.2, the morphologies of the PPy/EGO composite electrode exhibit a highly porous architecture formed by random interconnection of PPy coated EGO flakes, which would facilitate the penetration of electrolyte and shorten the solid-phase ion diffusion pathways. In contrast, the surface of pure PPy electrode (Figure S5.3) shows a dense and compact morphology made of the large PPy particles with size ~ 1 μm. The SEM characterization indicates that EGO addition has a significant influence on the morphology of the resulting product of the electrochemical deposition. Additionally,

the transmission electron microscopy (TEM) image of the PPy/EGO composite further suggests that the EGO flakes are uniformly coated with PPy shown in Figure 5.2d. Fourier-transform infrared (FT-IR) spectra of the pure PPy and PPy/EGO composite were performed to characterize the functional groups. As shown in Figure 5.2e, the full FT-IR spectra of pure PPy and PPy/EGO composite exhibit similar characteristics. Considering that most useful information is located at the fingerprint region denoted in the dashed rectangle, the located spectrum is further represented in Figure 5.2f. The absorption band at 1550 $cm^{-1}$ arises from the stretching vibration of C−C, while the band at 1036 $cm^{-1}$ is corresponding to the deformation vibration of C−H [35]. The weak absorption bands located at 1745 and 1097 $cm^{-1}$ can be assigned to the stretching vibrations of C=O and C−O, respectively. The bands at 1457 and 1305 $cm^{-1}$ are attributed to the stretching vibrations of C−N bond [50]. The weak band at 1384 $cm^{-1}$ corresponding to C−O group suggests mild overoxidation of PPy occurs during the electrochemical polymerization process. In addition, the strong bands at 1183 and 912 $cm^{-1}$ confirm that the PPy is in a doped state [35]. The bands at 965 and 774 $cm^{-1}$ are related to polymerized pyrrole [51].

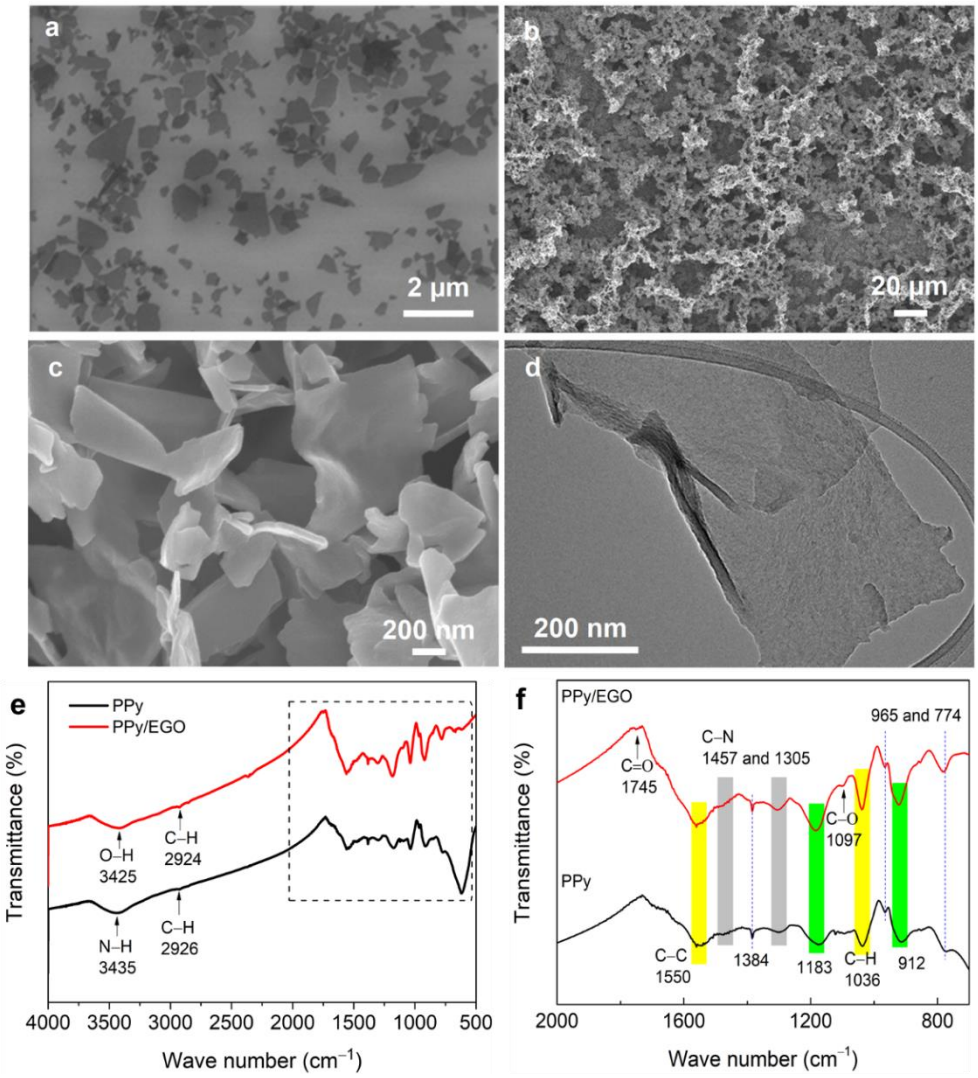


**Figure 5.2.** Characterization of the electrodeposited PPy/EGO composite film. **(a)** SEM image of the starting EGO flakes on Si wafer substrate. **(b-c)** SEM images of the PPy/EGO-1200 s composite film at different magnifications. **(d)** TEM image of the PPy coated EGO flakes. **(e)** Full FT-IR spectra for the pure PPy and PPy/EGO composite. **(f)** Located FT-IR spectra denoted in the dotted rectangle in (e).

## 2.2 Single-electrode electrochemical performance

The basic electrochemistry of the PPy/EGO composite was studied initially using a three-electrode configuration with Pt and SCE as counter and reference electrodes, respectively; the working electrode is a PPy/EGO-1200 s composite electrode prepared at an electrodeposition time of 1200 s. Potassium halides solutions, namely, 1 M KF,

KCl, KBr and KI, were used as electrolytes to identify the most suitable monovalent halide anion for constructing the Zn-PPy system. Since $ZnSO_4$ are the most widely used electrolyte for Zn-ion supercapacitor based on carbon cathodes, the electrochemistry of PPy/EGO in aqueous 1 M $K_2SO_4$ was also investigated to understand the effect of divalent sulfate anions on the charge balancing mechanism of PPy.

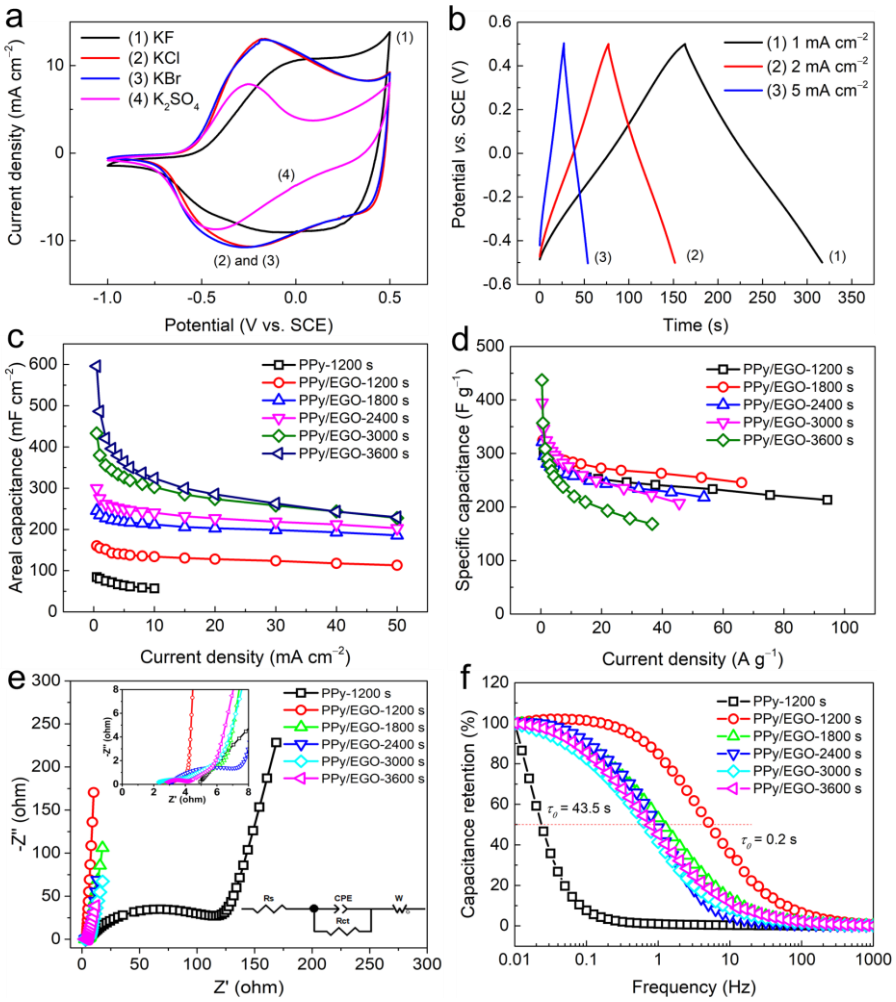


**Figure 5.3.** Electrochemical performance of the PPy/EGO composite electrodes in a three-electrode cell configuration. **(a)** Comparison of CVs at 50 mV $s^{-1}$ in different aqueous potassium halides electrolytes. **(b)** Galvanostatic charge-discharge curves of PPy/EGO-1200 s electrode in 1 M KCl aqueous electrolyte at different current densities. **(c-d)** Comparison of areal capacitances and specific capacitances at increasing current density for the PPy/EGO electrodes prepared at different deposition times in 1 M KCl electrolyte, respectively. **(e-f)** Comparison of EIS Nyquist and Bode plots for PPy/EGO composites electrodes prepared at varying deposition time in 1 M KCl electrolyte.

Figure 5.3a compares the as-recorded cyclic voltammograms (CVs) in different electrolytes at a scan rate of 50 mV $s^{-1}$, the CV recorded in 1 M KI aqueous solution is shown in Figure S5.4 as the oxidation of iodide anion to iodine occurs in the measured potential range. From Figure 5.3a, it is obvious that both the 1 M KCl and KBr aqueous solutions show equally good electrochemical performance with nearly overlapped CVs. In contrast, the CV recorded in 1 M KF aqueous solution exhibits a smaller responsive current density compared with that of 1 M KCl and KBr, and the responsive current density decays rapidly with increasing number of CV scans (Figure S5.5). This fast decay in current density is due to the strong interaction of fluoride anions with the hydrogen atoms at the pyrrole nitrogen of PPy, which localizes the positive charges (i.e., carriers) on the hydrogen atoms [52]. Therefore, the PPy is in an oxidized, but nearly nonconductive state [52].

Compared with the CVs in electrolytes with monovalent anions (1 M KCl and KBr), the PPy/EGO-1200 s electrode shows a distinctly different CV in 1 M $K_2SO_4$ electrolyte with divalent anions (Figure 5.3a). In detail, the responsive current density is very low particularly at potential > 0 V vs. SCE, and thus the enclosed area of CV in 1 M $K_2SO_4$ is much smaller than that in 1 M KCl or KBr. In addition, the pair of redox peaks of the PPy/EGO-1200 s electrode in 1 M $K_2SO_4$ occur at more negative potentials than seen in 1 M KCl and KBr. These differences in peak potential and responsive current density clearly indicate different charge balancing mechanisms for PPy/EGO composite in 1 M KCl (or KBr) and $K_2SO_4$ electrolytes, respectively. According to the previous report [36], the small sized (ion radius ~0.180 nm [53]) and monovalent $Cl^-$ counterions introduced into the PPy chains under our experimental conditions are unlikely to be replaced by the relatively large (radius ~0.242 nm [53]) and divalent $SO_4^{2-}$ anions during the cathodic scan process. Instead of achieving anion exchange, the monovalent $K^+$ cations are inserted into the PPy/$Cl^-$ chains to maintain the electro-neutrality in the polymer [36]. It is worth noting that the freshly deposited PPy/EGO composite is doped by $ClO_4^-$, the spontaneous exchange of $ClO_4^-$ by $Cl^-$ occurs during the storage of

electrodes in 1 M KCl solution [35]. Therefore, in 1 M $K_2SO_4$ aqueous solution, the charge balancing mechanism can be described as follow [36]:

$$n\mathrm{K}^+(aq) + \mathrm{PPy}^{n+}/(\mathrm{Cl}^-)_n(\mathrm{s}) + n\mathrm{e}^- \leftrightarrow (\mathrm{K}^+)_n\mathrm{PPy}/(\mathrm{Cl}^-)_n(\mathrm{s}) \qquad (5.1)$$

In contrast, the exchange of the inherently doped $Cl^-$ in the PPy chains can be efficiently achieved by the monovalent halides anions in the 1 M KCl or KBr electrolytes. Take 1 M KCl as an example, the following reaction represents the charge balancing mechanism:

$$\mathrm{PPy}^{n+}/(\mathrm{Cl}^-)_n(\mathrm{s}) + n\mathrm{e}^- \leftrightarrow \mathrm{PPy}(\mathrm{s}) + n\mathrm{Cl}^-(aq) \qquad (5.2)$$

The galvanostatic charge-discharge (GCD) profiles recorded with the PPy/EGO-1200 s composite electrode in 1 M KCl aqueous electrolyte (Figure 5.3b) show a well-defined symmetric triangular shape in the potential range of -0.5 to 0.5 V vs SCE, suggesting good capacitive behaviour. Figure 5.3c plots the areal capacitance as a function of current density for the pure PPy-1200 s and PPy/EGO composite electrodes prepared at different electrodeposition times in 1 M KCl electrolyte. The pure PPy-1200 s electrode has an areal capacitance of 84.3 mF $cm^{-2}$ at 0.5 mA $cm^{-2}$ and the capacitance drops to 56.9 mF $cm^{-2}$ at 10 mA $cm^{-2}$. In comparison, the PPy/EGO-1200 s electrode exhibits an enhanced areal capacitance of 160.3 mF $cm^{-2}$ at 0.5 mA $cm^{-2}$ about twice as large as that of the pure PPy-1200 s electrode and maintains an areal capacitance of 112.9 mF $cm^{-2}$ at a high current density of 50 mA $cm^{-2}$. This enhanced performance of PPy/EGO composite compared to pure PPy is attributed to the favourable liquid-phase ion diffusion through the interconnected porous structure of the composite electrode and the short solid-phase ion diffusion path in the thin PPy coating on EGO flakes as well as the improved conductive network within the composite. The latter is because the EGO is likely to be reduced (at least partially) during the initial CV scans in a potential window from −1.0 to 0.5 V vs SCE (see the CV scans, X-ray diffraction and Raman spectroscopy results of the electrochemical reduction of EGO film in Figure S5.6, supporting information), and thus is electrically conductive. Note the initial CV scans (−1.0 to 0.5 V vs SCE) at 50 mV $s^{-1}$ for 20 cycles were performed to all electrodes before further electrochemical measurements. Therefore, the conductive network

realized by the electrochemical reduced EGO flakes and their conjugated structure with PPy rings further benefit the high-rate capability of the EGO/PPy composite electrodes. In comparison to the PPy/EGO-1200 s electrode, the composite electrode of PPy and CGO prepared under identical conditions has lower rate performance (Figure S5.7), confirming the advantage of the less defective and easily reduced EGO in developing PPy based nanocomposites.

The mass loading of PPy/EGO composite electrode can be well-controlled by the electrodeposition time, exhibiting a quasi-linear relationship with it, shown in Figure S5.8a. The increased mass loading of PPy/EGO composite electrode prepared at extended deposition time directly contributes to a higher responsive current density during the CV scans (Figure S5.8c). The ease of controlling the mass loading allows one to tailor electrode performance for different purposes in the energy storage devices. For example, thick electrodes can be used for high energy density devices, while thin electrodes can be employed for high power density devices. As shown in Figure 5.3c, the areal capacitances of PPy/EGO composite electrodes at low current densities keep increasing with the deposition time due to the increased mass loading. It is also noted that the areal capacitances of PPy/EGO-3000 s electrode and PPy/EGO-3600 s electrode tend to approach the same values at high current densities (> 20 mA $cm^{-2}$), likely due to the ion diffusion limitation which starts to dominate. The areal capacitance of PPy/EGO-3600 s electrode reaches a large value of 595.8 mF $cm^{-2}$ at 0.5 mA $cm^{-2}$ and maintains at 229.3 mF $cm^{-2}$ at a high current density of 50 mA $cm^{-2}$.

Figure 5.3d compares the gravimetric specific capacitances (F $g^{-1}$) of the as-prepared PPy-EGO composites at various current densities (A $g^{-1}$). All the PPy/EGO composites show high specific capacitances over 300 F $g^{-1}$ at low current densities, namely < 1 A $g^{-1}$. Particularly, the PPy/EGO-3600 s composite exhibits the highest specific capacitance up to 437.1 F $g^{-1}$ at a current density of 0.37 A $g^{-1}$, together with good rate capability by maintaining a specific capacitance of 168.3 F $g^{-1}$ at 36.7 A $g^{-1}$. The highest specific capacitance obtained from the PPy/EGO-3600 s electrode is attributed to the smallest discharge current density normalized by mass (0.37 A $g^{-1}$), i.e., all the

electrodes are charged and discharged at same areal current densities while the PPy/EGO-3600 s electrode has the highest mass loading. It is noted that, because of the known dependence of electrode performance on the thickness of electrodes [54], the thin and low mass loading PPy/EGO-1200 s electrode shows the best rate capability among the measured electrodes with a high specific capacitance of 213.1 F $g^{-1}$ at an extremely high current density of 94.3 A $g^{-1}$.

The resistance and frequency response of the PPy/EGO composite electrodes were further studied by electrochemical impedance spectroscopy (EIS). As shown in Figure 5.3e, the Nyquist plot of pure PPy-1200 s electrode has a large semicircle at high frequencies, corresponding to a large charge transfer resistance (~ 99.75 Ω) due to the sluggish ion migration in the densely grown PPy electrode. In comparison, all the PPy/EGO composite electrodes have much smaller charge transfer resistances (i.e., 0.54 Ω for PPy/EGO-1200 s, 1.81 Ω for PPy/EGO-1800 s, 5.06 Ω for PPy/EGO-2400 s, 1.96 Ω for PPy/EGO-3000 s and 1.40 Ω for PPy/EGO-3600 s) than that of pure PPy because of the porous structure of PPy/EGO composite electrodes. In addition, the nearly vertical Nyquist plots of PPy/EGO composites at low frequencies suggest an ideal capacitive behaviour. Bode plots of capacitance retentions versus frequency (Figure 5.3f) directly reveal that the incorporation of EGO into the PPy electrode significantly improves its rate capability. For the pure PPy-1200 s electrode, the real part of capacitance drops dramatically with the increasing frequency with a relaxation time constant of 43.5 s (determined by the frequency of 50% capacitance retention). In contrast, the PPy/EGO-1200 s electrode has a much more stable capacitance with the increasing frequency and exhibits a short relaxation time constant of 0.2 s (two orders of magnitude smaller than that of the pure PPy-1200 s electrode). For the other PPy/EGO composite electrodes with increasing deposition time from 1800 to 3600 s, the relaxation time constant increases slightly and reaches 1.0 s. The relaxation time constant of the PPy/EGO-3600 s composite electrode (~1.0 s) with high mass loading and areal capacitance is superior to that of the previously reported PPy/GO composites (6.3 s) [35] and the PPy/electrochemical exfoliated graphene composite (2.6 s) [40].

The PPy/EGO-3600 s electrode was selected for the fabrication of the zinc-ion hybrid supercapacitor due to its best overall performance, namely, high areal and gravimetric specific capacitances as well as good rate capability.

### 2.3 Performance of Zn-PPy/EGO hybrid supercapacitors

To investigate the operating principle of the Zn-PPy/EGO hybrid capacitor, the electrochemical behaviour of PPy/EGO composite as working electrode was studied in the 1 M $ZnCl_2$ aqueous electrolyte using a three-electrode cell with two pieces of Zn foil acting as counter and quasi-reference electrodes, respectively. The behaviour of Zn plating/stripping was also investigated using a piece of Ti foil ($1 \times 1$ $cm^2$) as working electrode in the same three-electrode configuration. As revealed by the CV of the PPy/EGO cathode shown in Figure 5.4a, the pair of broad and nearly symmetric redox peaks located at ~ 0.75 V vs $Zn^{2+}/Zn$ (equivalent to ~ −0.25 V vs SCE) is consistent with the peak potential of the CV displayed in Figure 5.3a that was recorded in 1 M KCl using the conventional three-electrode configuration. This similarity in the CV peak potential suggests a charge storage mechanism via the insertion/de-insertion of $Cl^-$ anions into PPy. The broad peak in the CV for $Cl^-$ insertion seems to be composed of two peaks, indicating a possible two-step insertion process. In addition, the CV of the Zn anode confirms its charge storage mechanism of electro-plating and -stripping of metallic Zn occurring at ~ 0 V vs $Zn^{2+}/Zn$.

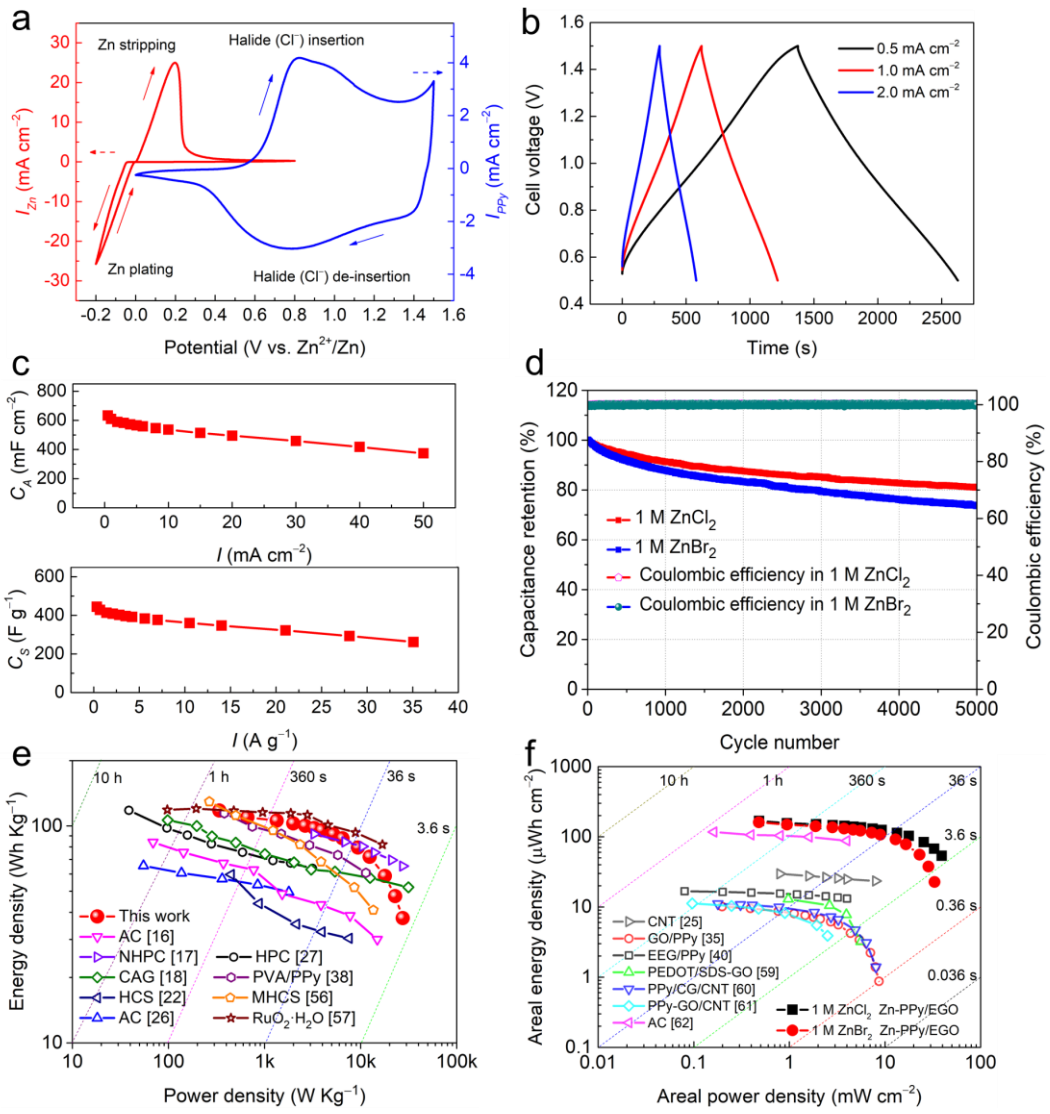


**Figure 5.4.** Electrochemical performance of the Zn-PPy/EGO hybrid supercapacitors using aqueous zinc halides electrolytes. **(a)** CVs showing the Zn plating/stripping at anode (Ti substrate) and $Cl^-$ insertion/de-insertion at PPy/EGO-3600s cathode, recorded using two pieces of Zn foil as quasi-reference and counter electrodes, respectively, at 5 mV $s^{-1}$ in 1 M $ZnCl_2$ aqueous electrolyte. **(b)** Galvanostatic charge-discharge curves of the Zn-PPy/EGO hybrid supercapacitor at different current densities. **(c)** Areal and specific capacitances at various current densities. **(d)** Cycling stability of the Zn-PPy/EGO hybrid supercapacitors in 1 M $ZnCl_2$ and $ZnBr_2$ electrolytes, respectively. **(e-f)** Ragone plots benchmarking the specific and areal energy densities of the Zn-PPy/EGO hybrid supercapacitors with literature values. (AC represents activated carbon, NHPC represents N-doped hierarchically porous carbon,

CAG represents chemical activated graphene, HCS represents hollow carbon sphere, HPC represents hierarchical porous carbon, PVA/PPy represents polyvinyl alcohol/polypyrrole, MHCS represents mesoporous hollow carbon spheres, CNT represents carbon nanotube, GO represents graphene oxide, EEG represents electrochemical exfoliated graphene and PEDOT/SDS represents poly(3,4-ethylenedioxythiophene/ sodium dodecyl sulfate.)

Subsequently, two-electrode hybrid supercapacitor devices were assembled using Zn foil as anode and PPy/EGO-3600 s composite as cathode with aqueous 1 M $ZnCl_2$ or $ZnBr_2$ as electrolytes, respectively. Figure 5.4b shows the charge-discharge profiles of the Zn-PPy/EGO hybrid supercapacitor using 1 M $ZnCl_2$ electrolyte at an operation cell voltage range from 0.5 to 1.5 V. The charge-discharge profiles exhibit a symmetric triangular shape with linear characteristic, corresponding to capacitive behaviour. It is worth noting that we refer to this Zn-PPy energy storage device as a hybrid supercapacitor in this work, since PPy is known as a typical pseudocapacitive material and no plateau is observed in the galvanostatic charge-discharge profiles, although it has been named as a battery in previous reports [37-39]. Moreover, the charge-discharge profiles at high current densities up to 50 mA $cm^{-2}$ (Figure S5.9) display relatively small IR drops, indicating small internal resistance and high rate capability. Figure 5.4c displays the calculated areal capacitances (upper panel) and gravimetric specific capacitances (lower panel) of the PPy/EGO-3600 s composite at various current densities. The areal capacitance reaches a high value of 633.0 mF $cm^{-2}$ at 0.5 mA $cm^{-2}$ and retains 373.7 mF $cm^{-2}$ at a high current density of 50 mA $cm^{-2}$. For gravimetric capacitance, the corresponding values are 444.2 F $g^{-1}$ at 0.35 A $g^{-1}$ and 262.3 F $g^{-1}$ at 35 A $g^{-1}$, respectively. The high areal and gravimetric capacitances of PPy/EGO-3600 s composite measured from the two-electrode hybrid device are consistent with the results obtained from the conventional three-electrode configuration. The electrochemical performance of the Zn-PPy/EGO hybrid supercapacitor using 1 M $ZnBr_2$ electrolyte was also tested. The charge-discharge profiles, plots of areal and specific capacitance versus charge-discharge current density are available in Figure

S5.10. The Zn-PPy/EGO hybrid supercapacitor using 1 M $ZnBr_2$ electrolyte exhibits 447.2 F $g^{-1}$ at a low current density of 0.37 A $g^{-1}$ and 228.5 F $g^{-1}$ at a high current density of 36.7 A $g^{-1}$. Compared with the high rate performance achieved by using 1 M $ZnCl_2$, the slightly inferior rate capacity using 1 M $ZnBr_2$ electrolyte is likely because of the $Br^-$ anions (radius: ~ 0.198 nm [53]) being less mobile in bulk PPy compared with the smaller sized $Cl^-$ anions (radius: ~ 0.180 nm [53]).

For comparison, the electrochemical behaviour of a Zn-PPy/EGO supercapacitor using 1 M $ZnSO_4$ electrolyte was also investigated. The corresponding CVs (Figure S5.11) exhibited low responsive current densities because the active sites were not accessible by the divalent anions. The areal capacitances of PPy/EGO-3600 s electrode in 1 M $ZnSO_4$ obtained from charge-discharge profiles (Figure S5.12) indicate ~ 5 times smaller areal capacitance and severely deteriorated rate capability compared to that in 1 M $ZnCl_2$ or $ZnBr_2$. The distinct differences in electrochemical performance between 1 M $ZnCl_2$ and $ZnSO_4$ electrolytes can be ascribed to the larger ion size of $SO_4^{2-}$ (radius ~0.242 nm) [53], the stronger electrostatic interaction between the divalent $SO_4^{2-}$ and the positively charged bulk PPy/EGO, as well as the more difficult redistribution of the multiple charges carried by $SO_4^{2-}$ within the host structure compared with the counterpart of monovalent $Cl^-$ (radius ~ 0.180 nm) [53, 55].

Cycling stability of the Zn-PPy/EGO hybrid capacitors was tested by GCD method with an operation cell voltage ranging from 0.5 to 1.5 V at a current density of 5 mA $cm^{-2}$. As displayed in Figure 5.4d, the Zn-PPy/EGO hybrid supercapacitor with 1 M $ZnCl_2$ aqueous electrode shows good cycling stability with capacitance retention of 81% after 5000 cycles, which is slightly higher than that in 1 M $ZnBr_2$ electrolyte (73% after 5000 cycles). This discrepancy in cycling stability between 1 M $ZnCl_2$ and $ZnBr_2$ electrolytes is possibly due to the relatively larger ion size of $Br^-$, which causes more significant volume change when inserted/de-inserted into/from the polymer chain of PPy. Nevertheless, the cycling stability of the Zn-PPy/EGO hybrid supercapacitor using aqueous 1 M $ZnCl_2$ electrolyte (81% after 5000 cycles) is obviously superior to the previously reported Zn-PPy systems [37-39], among them the best result being 71%

retention after 1000 cycles. This enhanced cycling stability is likely because of the extra mechanical support provided by the EGO skeleton; and the intermolecular interactions (i.e., hydrogen bonding, π-π interaction) between EGO support and PPy that would restrain the volume change during charge-discharge. In addition, the porous structure of the PPy/EGO composite electrodes can allow extra space for the volume change caused by anion insertion/de-insertion.

Energy density and power density are the key figures of merit to evaluate the performance of an energy storage device. Figure 5.4e compares the gravimetric energy density and power density (Ragone plot) of the Zn-PPy/EGO (1 M $ZnCl_2$) hybrid supercapacitor with the state-of-the-art, recently reported aqueous Zn anode-based supercapacitors/batteries. Note that the data compared in Figure 5.3e are all normalized to the mass of cathode material only. The Zn-PPy/EGO system has a high energy density of 117.7 Wh $kg^{-1}$ at 0.34 kW $kg^{-1}$, and the energy density maintains at 72.1 Wh $kg^{-1}$ at a high power density of 12.4 kW $kg^{-1}$. The Zn-PPy/EGO system outperforms the Zn-ion hybrid supercapacitors using different types of carbon cathodes [16-18, 22, 26, 27, 56], and even comparable to the Zn-$RuO_2$ system using high-cost $RuO_2$ cathode [57]. It is worth mentioning that, for the most recently reported Zn-ion battery using a PPy composite aerogel cathode, the energy density of 64 Wh $kg^{-1}$ at a power density of 11.7 kW $kg^{-1}$ are calculated based the mass of PPy and Zn excluding the mass of graphite nanoplatelets aerogel scaffold [38]. In the present work, the energy density and powder density of the PPy/EGO cathode were calculated based on the total mass of EGO and PPy. According to the thermogravimetric results (shown in Figure S5.13), the weight percentage of PPy in the composite is estimated to be about 90%. Considering that the Zn metal foil is used as both active materials and current collector without additional conductive additive and binder, it can potentially reduce the total weight of the cell by minimizing the weight and thickness of zinc anode with appropriate engineering means. We further estimated the energy density and power density of the Zn-PPy/EGO unit cell by assuming that twice the mass of theoretically needed Zn is used at the anode side [58]. Based on the same amount of charge passing through the

anode and cathode, the theoretically needed mass of Zn metal is calculated by using the specific capacitance of PPy/EGO cathode at the lowest used charge-discharge current density (0.5 mA $cm^{-2}$), see supporting information for the calculation details. As a result, the estimated Zn-PPy/EGO cell exhibits an energy density of 90 Wh $kg^{-1}$ at a power density of 0.26 kW $kg^{-1}$ and maintains at 45 Wh $kg^{-1}$ at 13.8 kW $kg^{-1}$ (Figure S5.14). The energy density and power density of Zn-PPy/EGO hybrid supercapacitors using 1 M $ZnBr_2$ electrolyte are comparable to those using 1 M $ZnCl_2$ but exhibit slightly deteriorating performance at high power region (Figure S5.14).

Areal energy density and power density are important for practical application, particularly for the electrodes prepared using electrodeposition methods, where a high mass loading is relatively difficult to achieve. Figure 5.4f shows the areal energy density and power density of the Zn-PPy/EGO system compared with the recently reported PPy-based symmetric supercapacitors and the state-of-the-art Zn-ion hybrid supercapacitors using carbon cathodes. Attributed to the large areal capacitance (up to 633 mF $cm^{-2}$), good rate capability and high operation cell voltage (0.5 to 1.5 V), the Zn-PPy/EGO (1 M $ZnCl_2$) system exhibits a high areal energy density of 156.1 μWh $cm^{-2}$ at a power density of 0.9 mW $cm^{-2}$ and 39 μWh $cm^{-2}$ at 54 mW $cm^{-2}$. This high performance surpasses that of the previously reported symmetric supercapacitors based on PPy and its composites [35, 40, 59-61]. Moreover, the Zn-PPy/EGO system also shows superior areal energy density and power density than the most recently developed micro-supercapacitors based on Zn anode and activated carbon or CNTs cathodes, respectively [25, 62]. This excellent areal normalized performance indicates the great potential of this electrodeposited PPy/EGO composite film in Zn-based hybrid micro-supercapacitors.

### 2.4 Charge-discharge mechanism

*Ex-situ* XPS was conducted to study the charge-discharge mechanism of the PPy/EGO cathode in the Zn-PPy/EGO hybrid system. As depicted in Figure 5.5a, the PPy/EGO composite electrodes at four different charge-discharge states were selected for XPS

characterization, namely, fully charged state (1.5 V), half discharged state (1.0 V cathodic), fully discharged state (0.5 V) and half charged state (1.0 V anodic). As shown in Figure 5.5b, the XPS survey spectra show that the four selected PPy/EGO composite samples at different charge-discharge states are all abundant in elements of C, O and N, together with the presence of minor Cl and Zn elements. The corresponding contents of different elements were quantitatively analysed, shown in Table S5.1.

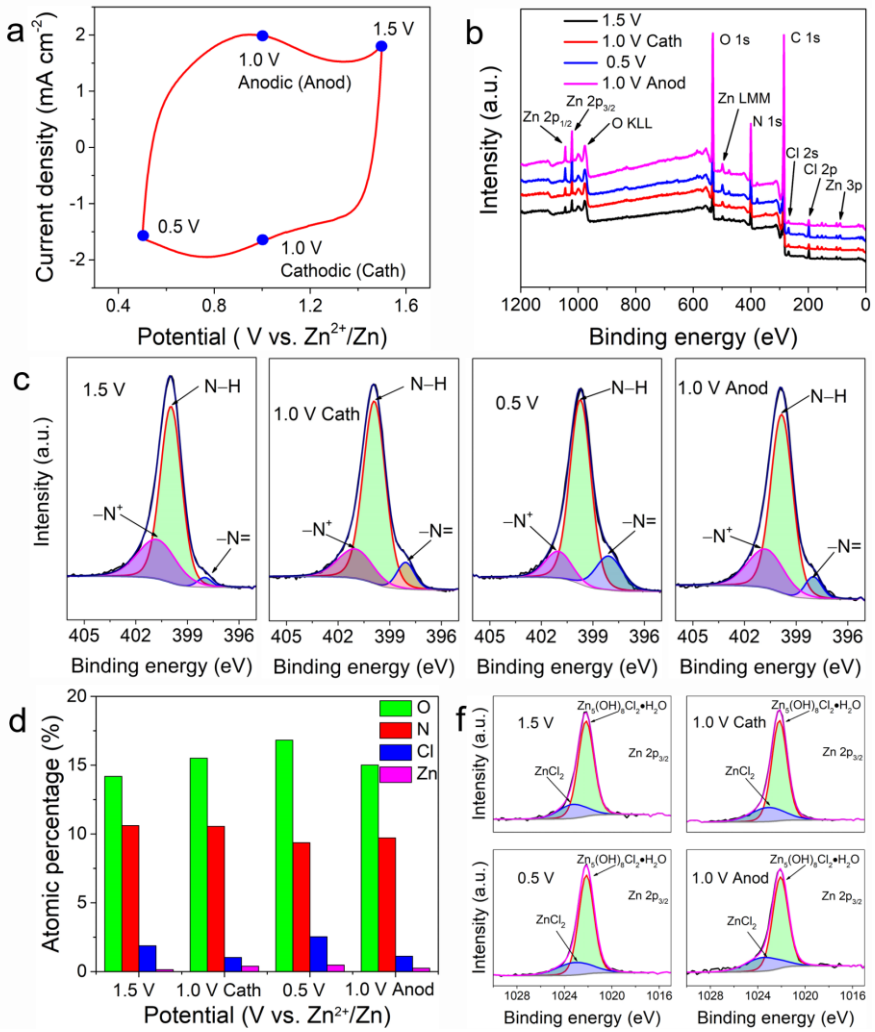


**Figure 5.5.** *Ex-situ* XPS characterization of the PPy/EGO composite electrode. **(a)** Typical CV of Zn-PPy/EGO hybrid supercapacitor at 5 mV $s^{-1}$ using 1 M $ZnCl_2$; **(b)** *Ex-situ* XPS survey spectra corresponding to the states denoted in (a); Evolution of **(c)** high resolution of N 1s spectrum, **(d)** atomic percentages of various elements and **(e)** high resolution of Zn $2p_{3/2}$ spectra during charge-discharge process.

The doping state of PPy, i.e., charge-discharge state, is closely related to the chemical state of the pyrrole nitrogen. Therefore, the deconvolution of N 1s core-level spectra of the PPy/EGO composites recorded at different charge-discharge states can provide useful information related to the charge storage mechanism. In detail, the positively charged nitrogen $–N^+$ with a binding energy of 400.8 eV is reduced to imine −N= at 397.6 eV during the cathodic scan (discharge), vice versa [35, 63]. Figure 5.5c displays the detailed deconvolution of N 1s core-levels at the four different states; the corresponding quantified percentages of the three types of N components at each state are shown in Figure S5.15 and Table S5.2. The major component at 399.5 eV of the N 1s core-level is corresponding to the neutral amine (N−H). Obviously, the percentage of $–N^+$ has the maximum value of 27.9% ($-N^+$/N ratio of 0.28) at the fully charged state (1.5 V) and drops to the minimum value of 10.6% at the fully discharged state (0.5 V). The potential-dependent –N= component follows the opposite trend as the $–N^+$ component. These results directly suggest that the charge-storage of PPy/EGO composite cathode in the Zn-PPy/EGO hybrid system is realized by the oxidation and reduction of pyrrole nitrogen.

Nevertheless, the evolution of N 1s core-level itself cannot reveal the charge-balancing mechanism of PPy/EGO composite. To get insights into the charge-balancing mechanism and the charge-storage reactions occurring at the PPy/EGO cathode, the atomic percentages of N, O, Cl and Zn elements at different stages are analysed and compared in Figure 5.5d. At the fully charged state (1.5 V), the positively charged $–N^+$ species are balanced dominantly by the $Cl^–$ anions, confirmed by the Cl/N ratio of 0.21 being close to that of the $–N^+$/N ratio (0.28). The rest of the $–N^+$ is possibly balanced by the negatively charged, residual oxygen functionalities on the EGO nanosheets. At the half-discharged state (1.0 V cathodic), there is a drop in the atomic percentage of Cl (1.0 at.%) compared to that of the fully charged 1.5 V state (2.2 at.%), corresponding to the de-insertion of $Cl^–$ from PPy. Ideally, with the further reduction of $–N^+$ to neutral –N=, more doped $Cl^–$ would be extracted from the PPy so that the atomic percentage of Cl should be the lowest at the fully discharged state (0.5 V). In contrast, an increase in

the atomic percentage of Cl occurs at 0.5 V, together with simultaneous increases in the atomic percentages of Zn and O elements (Figure 5.5d). Interestingly, at the half-charged state (1.0 V anodic), the atomic percentage of Cl, Zn and O elements return to the level similar to that in the half discharge state (1.0 V cathodic). This simultaneous change of Cl, Zn and O elements during the charge-discharge process strongly indicates the unexpected high content of Cl at the fully discharge state (0.5 V) is likely because of side reactions at the electrode surface.

To identify the possible side reaction, we studied the bonding environment of Zn element by deconvolution of the Zn 2p core-level spectra. As shown in Figure 5.5e, the Zn $2p_{3/2}$ core-level spectra recorded at different states can be deconvoluted into two components at 1022.2 and 1023.16 eV, corresponding to $Zn_5(OH)_8Cl_2{\cdot}H_2O$ [64] and $ZnCl_2$ [65], respectively. Unlike the variation of Zn atomic percentage, the chemical state of Zn element does not vary significantly during the charge-discharge process. The existence of minor $ZnCl_2$ can be attributed the adsorbed residual trace electrolyte, while the presence of the $Zn_5(OH)_8Cl_2{\cdot}H_2O$ phase is likely a result of the local pH change during the charge-discharge process. In detail, as a small portion of the positive charged of $–N^+$ in PPy/EGO composite are balanced by the immobile and negatively charged EGO nanosheets as discussed earlier, and it is reasonable to suspect that minor $Cl^-$ anions remains in the bulk PPy even at the fully-discharged state; consequently, the insertion of protons into the PPy could occur at the fully discharged state to balance the negative charges of the EGO nanosheets and/or the remaining $Cl^-$; the consumption of $H^+$ leads to a local pH rise at the electrode surface and thus the precipitate of the complex hydroxide of $Zn_5(OH)_8Cl_2{\cdot}H_2O$ phase. The corresponding reactions are proposed and listed as follow:

$$\mathrm{PPy^{n+}/(A^-)_n(s) + nH_2O}(l) + \mathrm{ne^-} \leftrightarrow (\mathrm{H^+})_n/\mathrm{PPy^0/(A^-)_n}(s) + \mathrm{nOH^-}(aq) \quad (5.3)$$

$$5\mathrm{Zn^{2+}}(aq) + 8\mathrm{OH^-}(aq) + 2\mathrm{Cl^-}(aq) + \mathrm{H_2O}\ (l) \leftrightarrow \mathrm{Zn_5(OH)_8Cl_2 \cdot H_2O}(s) \quad (5.4)$$

where $A^-$ represents the negatively charge EGO nanosheets and/or residual $Cl^-$ anions in the PPy/EGO composite. It is worth noting that similar phenomena of precipitation of complex Zn hydroxides at the cathode surface have been also reported in the aqueous

Zn-ion batteries [20, 66]. In comparison to the aqueous Zn-$MnO_2$ battery, the precipitation of complex Zn hydroxides at cathode surface is much less severe as revealed by the absence of clear precipitates in SEM images (Figure S5.16).

The electrochemical characterization discussed earlier identifies the essential role of monovalent anions, e.g., $Cl^-$ or $Br^-$, in the electrolytes for achieving high specific capacitance; the *ex-situ* XPS characterization of the evolution of elemental composition and their chemical states during charge-discharge process indicates the observed increased of Zn element at fully discharged state is likely because of the precipitation of complex $Zn_5(OH)_8Cl_2 \cdot H_2O$ phase. Therefore, it is reasonable to propose that the charge balancing in PPy based electrodes in the Zn-PPy hybrid supercapacitors/batteries is via insertion/de-insertion of monovalent anions, instead of the $Zn^{2+}$ ion insertion/de-insertion proposed recently [39].

## 3. Conclusions

In summary, for the first time, binder free composite electrodes of EGO and PPy have been prepared by a facile one-step electrochemical co-deposition method and used in combination with Zn halide electrolytes for aqueous Zn-PPy hybrid supercapacitors. This electrochemical co-deposition leads to device-ready composite electrodes that have a porous structure formed by the PPy coated EGO nanoflakes. The porous structure and the thin PPy coating on EGO allow fast transport of electrolyte ions in electrode pores and short diffuse pathway in the solid phase of PPy, respectively. The structural integrity and easy electrochemical reduction of EGO via initial CV cycling ensure good electronic conduction in the composites. The enhanced electronic and ionic conduction in the PPy/EGO composite electrodes lead to a high specific capacitance of 444.2 F $g^{-1}$ at 0.35 A $g^{-1}$ (633.0 mF $cm^{-2}$ at 0.5 mA $cm^{-2}$). The Zn-PPy hybrid supercapacitor based on the PPy/EGO cathode and the 1 M $ZnCl_2$ aqueous electrolyte exhibits high energy densities of 117.7 and 72.1 Wh $kg^{-1}$ at 0.34 and 12.4 kW $kg^{-1}$, respectively, together with good cycling stability (81% retention after 5000 cycles). Experimental evidence indicates that the charge-discharge mechanism of the PPy/EGO

composite cathode in Zn-PPy/EGO hybrid device mainly involves fast monovalent anion (e.g., $Cl^-$) insertion/de-insertion into/from the PPy. This high performance, yet safe and low cost, aqueous Zn-PPy hybrid supercapacitor is particularly promising for large scale energy storage that requires a combination of high energy density and power density. Furthermore, the insights into the charge storage mechanism of the Zn-PPy system proposed in this work would potentially guide its future designs of high-performance electrodes and electrolytes.

## Conflicts of interest

There are no conflicts to declare.

## Acknowledgements

J.Y. acknowledges the Presidential Doctoral Scholarship provided by the University of Manchester. The authors thank Dr. Ben Spencer for obtaining the XPS data. The authors are grateful to Morgan Advanced Materials/Royal Academy of Engineering, the Engineering and Physical Sciences Research Council (EPSRC), grant reference EP/K016954/1, EP/R023034/1, ROYCE GRANT, and EP/L020742/1 for supporting this work. J.C. and I.A.K. acknowledge the European Union's Horizon 2020 research and innovation program under grant agreements no. 785219 and 881603.

## Supplementary information

Supplementary data related to this article can be found at http://dx.doi.org

## References

[1] T.M. Gür, Energy Environ. Sci., 11 (2018) 2696-2767.

[2] B. Dunn, H. Kamath, J.-M. Tarascon, Science 334 (2011) 928-935.

[3] J.B. Goodenough, Energy Environ. Sci., 7 (2014) 14-18.

[4] P. Simon, Y. Gogotsi, Nat. Mater., 7 (2008) 845-854.

[5] J. Yang, H. Wu, M. Zhu, W. Ren, Y. Lin, H. Chen, F. Pan, Nano Energy, 33 (2017) 453-461.

[6] L.L. Zhang, X.S. Zhao, Chem. Soc. Rev., 38 (2009) 2520-2531.

[7] S. Chen, W. Xing, J. Duan, X. Hu, S.Z. Qiao, J. Mater. Chem. A, 1 (2013) 2941-2954.

[8] M. Yang, Z. Zhou, Adv. Sci., 4 (2017) 1600408.

[9] Y. Yang, C. Han, B. Jiang, J. Iocozzia, C. He, D. Shi, T. Jiang, Z. Lin, Mater. Sci. Eng. R Rep., 102 (2016) 1-72.

[10] J. Yang, J. Hu, M. Zhu, Y. Zhao, H. Chen, F. Pan, J. Power Sources, 365 (2017) 362-371.

[11] E. Lim, C. Jo, M.S. Kim, M.-H. Kim, J. Chun, H. Kim, J. Park, K.C. Roh, K. Kang, S. Yoon, J. Lee, Adv. Funct. Mater., 26 (2016) 3711-3719.

[12] W. Lu, J. Shen, P. Zhang, Y. Zhong, Y. Hu, X.W.D. Lou, Angew.Chem. Int.Ed. , 58 (2019) 15441-15447.

[13] L. Yu, G.Z. Chen, Front. Chem., 7 (2019) 272.

[14] B. Pal, S. Yang, S. Ramesh, V. Thangadurai, R. Jose, Nanoscale Advances, 1 (2019) 3807-3835.

[15] D.P. Dubal, O. Ayyad, V. Ruiz, P. Gomez-Romero, Chem. Soc. Rev., 44 (2015) 1777-1790.

[16] L. Dong, X. Ma, Y. Li, L. Zhao, W. Liu, J. Cheng, C. Xu, B. Li, Q.-H. Yang, F. Kang, Energy Stor. Mater., 13 (2018) 96-102.

[17] H. Zhang, Q. Liu, Y. Fang, C. Teng, X. Liu, P. Fang, Y. Tong, X. Lu, Adv. Mater., 31 (2019) 1904948.

[18] S. Wu, Y. Chen, T. Jiao, J. Zhou, J. Cheng, B. Liu, S. Yang, K. Zhang, W. Zhang, Adv. Energy Mater., 9 (2019).

[19] M. Song, H. Tan, D. Chao, H.J. Fan, Adv. Funct. Mater., 28 (2018) 1802564.

[20] J. Yang, J. Cao, Y. Peng, W. Yang, S. Barg, Z. Liu, I.A. Kinloch, M.A. Bissett, R.A.W. Dryfe, ChemSusChem, 13 (2020) 4103-4110.

[21] D. Chao, W. Zhou, F. Xie, C. Ye, H. Li, M. Jaroniec, S.-Z. Qiao, Sci. Adv., 6 (2020) 1-19.
[22] S. Chen, L. Ma, K. Zhang, M. Kamruzzaman, C. Zhi, J.A. Zapien, J. Mater. Chem. A, 7 (2019) 7784-7790.
[23] J. Han, K. Wang, W. Liu, C. Li, X. Sun, X. Zhang, Y. An, S. Yi, Y. Ma, Nanoscale, 10 (2018) 13083-13091.
[24] P. Liu, Y. Gao, Y. Tan, W. Liu, Y. Huang, J. Yan, K. Liu, Nano Res., 12 (2019) 2835-2841.
[25] G. Sun, H. Yang, G. Zhang, J. Gao, X. Jin, Y. Zhao, L. Jiang, L. Qu, Energy Environ. Sci., 11 (2018) 3367-3374.
[26] H. Wang, M. Wang, Y. Tang, Energy Stor. Mater., 13 (2018) 1-7.
[27] P. Yu, Y. Zeng, Y. Zeng, H. Dong, H. Hu, Y. Liu, M. Zheng, Y. Xiao, X. Lu, Y. Liang, Electrochim. Acta, 327 (2019) 134999.
[28] Y. Shi, L. Pan, B. Liu, Y. Wang, Y. Cui, Z. Bao, G. Yu, J. Mater. Chem. A, 2 (2014) 6086-6091.
[29] H.-P. Cong, X.-C. Ren, P. Wang, S.-H. Yu, Energy Environ. Sci., 6 (2013) 1185-1191.
[30] D. Ni, Y. Chen, H. Song, C. Liu, X. Yang, K. Cai, J. Mater. Chem. A, 7 (2019) 1323-1333.
[31] C. Peng, J. Jin, G.Z. Chen, Electrochim. Acta, 53 (2007) 525-537.
[32] G.A. Snook, P. Kao, A.S. Best, J. Power Sources, 196 (2011) 1-12.
[33] Y. Huang, H. Li, Z. Wang, M. Zhu, Z. Pei, Q. Xue, Y. Huang, C. Zhi, Nano Energy, 22 (2016) 422-438.
[34] K. Wang, H. Wu, Y. Meng, Z. Wei, Small, 10 (2014) 14-31.
[35] J. Cao, Y. Wang, J. Chen, X. Li, F.C. Walsh, J.-H. Ouyang, D. Jia, Y. Zhou, J. Mater. Chem. A, 3 (2015) 14445-14457.
[36] C. Weidlich, K.M. Mangold, K. Jüttner, Electrochim. Acta, 50 (2005) 1547-1552.

[37] J. Wang, J. Liu, M. Hu, J. Zeng, Y. Mu, Y. Guo, J. Yu, X. Ma, Y. Qiu, Y. Huang, J. Mater. Chem. A, 6 (2018) 11113-11118.

[38] X. Li, X. Xie, R. Lv, B. Na, B. Wang, Y. He, Energy Technology, 7 (2019) 1801092.

[39] A. Lahiri, L. Yang, G. Li, F. Endres, ACS Appl. Mater. Interfaces, 11 (2019) 45098-45107.

[40] S. Ji, J. Yang, J. Cao, X. Zhao, M.A. Mohammed, P. He, R.A.W. Dryfe, I.A. Kinloch, ACS Appl. Mater. Interfaces, 12 (2020) 13386-13399.

[41] G.Z. Chen, M.S.P. Shaffer, D. Coleby, G. Dixon, W. Zhou, D.J. Fray, A.H. Windle, Adv. Mater., 12 (2000) 522-526.

[42] M. Hughes, G.Z. Chen, M.S.P. Shaffer, D.J. Fray, A.H. Windle, Compos Sci Technol, 64 (2004) 2325-2331.

[43] W.S.H. Jr., R.E. Offeman, J. Am. Chem. Soc. , 80 (1958) 1339.

[44] Y. Li, Y. Wu, J. Am. Chem. Soc. , 131 (2009) 5851-5857.

[45] S. Eigler, A. Hirsch, Angew. Chem. Int. Ed., 53 (2014) 7720-7738.

[46] J. Cao, P. He, M.A. Mohammed, X. Zhao, R.J. Young, B. Derby, I.A. Kinloch, R.A.W. Dryfe, J. Am. Chem. Soc. , 139 (2017) 17446-17456.

[47] S. Pei, Q. Wei, K. Huang, H.M. Cheng, W. Ren, Nat. Commun., 9 (2018) 145.

[48] S. Bose, T. Kuila, M.E. Uddin, N.H. Kim, A.K.T. Lau, J.H. Lee, Polymer, 51 (2010) 5921-5928.

[49] Y. Peng, J. Cao, J. Yang, W. Yang, C. Zhang, X. Li, R.A.W. Dryfe, L. Li, I.A. Kinloch, Z. Liu, Adv. Funct. Mater., 30 (2020) 2001756.

[50] J. Zhang, X.S. Zhao, J. Phys. Chem. C, 116 (2012) 5420-5426.

[51] V. Selvaraj, M. Alagar, K. Kumar, Appl. Catal. B, 75 (2007) 129-138.

[52] O. Schneider, G. Schwitzgebel, Synth. Met., 93 (1998) 219-225.

[53] Y. Marcus, Chem. Rev., 88 (1988) 1475-1498.

[54] Y. Xia, T.S. Mathis, M.Q. Zhao, B. Anasori, A. Dang, Z. Zhou, H. Cho, Y. Gogotsi, S. Yang, Nature, 557 (2018) 409-412.

[55] E. Levi, M.D. Levi, O. Chasid, D. Aurbach, J. Electroceramics, 22 (2007) 13-19.

[56] P. Liu, W. Liu, Y. Huang, P. Li, J. Yan, K. Liu, Energy Stor. Mater., 25 (2020) 858-865.

[57] L. Dong, W. Yang, W. Yang, C. Wang, Y. Li, C. Xu, S. Wan, F. He, F. Kang, G. Wang, Nano-Micro Lett., 11 (2019) 94.

[58] J. Zheng, Q. Zhao, T. Tang, J. Yin, C.D. Quilty, G.D. Renderos, X. Liu, Y. Deng, L. Wang, D.C. Bock, C. Jaye, D. Zhang, E.S. Takeuchi, K.J. Takeuchi, A.C. Marschilok, L.A. Archer, Science, 366 (2019) 645-648.

[59] H. Zhou, G. Han, D. Fu, Y. Chang, Y. Xiao, H.-J. Zhai, J. Power Sources, 272 (2014) 203-210.

[60] H. Zhou, H.-J. Zhai, X. Zhi, Electrochim. Acta, 290 (2018) 1-11.

[61] H. Zhou, G. Han, Electrochim. Acta, 192 (2016) 448-455.

[62] P. Zhang, Y. Li, G. Wang, F. Wang, S. Yang, F. Zhu, X. Zhuang, O.G. Schmidt, X. Feng, Adv. Mater., 31 (2019) 1806005.

[63] H. Zhou, G. Han, Y. Xiao, Y. Chang, H.-J. Zhai, J. Power Sources, 263 (2014) 259-267.

[64] J. Winiarski, W. Tylus, K. Winiarska, I. Szczygieł, B. Szczygieł, J. Spectrosc., 2018 (2018) 1-14.

[65] R.F. Mulligan, A.A. Iliadis, P. Kofinas, J. Appl. Polym. Sci., 89 (2003) 1058-1061.

[66] J. Huang, Z. Wang, M. Hou, X. Dong, Y. Liu, Y. Wang, Y. Xia, Nat. Commun., 9 (2018) 2906.

# Supplementary Information

## Unlocking the energy storage potential of polypyrrole via electrochemical graphene oxide for high performance zinc-ion hybrid supercapacitors

Jie Yang,‡ [ac] Jianyun Cao,‡*[bc] Yudong Peng,[b] Mark Bissett,[bc] Ian A. Kinloch*[bc] and Robert A. W. Dryfe[ac]

[a] *Department of Chemistry, University of Manchester, Oxford Road, Manchester, M13 9PL,*

*U.K.*

[b] *Department of Materials, University of Manchester, Oxford Road, Manchester, M13 9PL,*

*U.K. E-mail: jianyun.cao@manchester.ac.uk; ian.kinloch@manchester.ac.uk*

[c] *National Graphene Institute and Henry Royce Institute, University of Manchester, Oxford Road, M13 9PL, U.K.*

‡ These authors contributed equally to this work.

## Materials and chemicals

Electrochemical graphite oxide (EGO) was prepared using the two-step electrochemical method reported previously by our group [1]. Chemical graphene oxide (CGO) was prepared by Hummers' method following the method reported previously [2, 3]. Graphite foil with thickness of 0.5 mm was purchased from Gee Graphite LTD, England. Ti foil (thickness, 25 μm) was purchased from Alfa Aesar. Sulfuric acid (> 95%) was ordered from Fisher Scientific. Ammonium sulfate was purchased from VWR International. Pyrrole was purchased from Acros Organics (99%, extra pure). Lithium perchlorate (98%) was ordered from Alfa Aesar. Potassium fluoride (≥ 99%), potassium chloride (≥ 99%), potassium bromide (≥ 99%) and potassium iodide (≥ 99%) were purchased from Sigma Aldrich. Zinc chloride (≥ 98%), Zinc bromide (≥ 98%) and zinc sulfate heptahydrate (≥ 98%) were purchased from Alfa Aesar. Deionized water with a resistivity of 18.2 MΩ cm was used for all the experiments.

## Electrodeposition of EGO/PPy composite electrodes

The method for electrodeposition of EGO/PPy composite electrodes was modified from that reported in the literature [4]. An aqueous electrolyte precursor solution with 0.1 mg $mL^{-1}$ EGO, 20 mM $LiClO_4$ and 5 vol.‰ (72 mM) pyrrole monomer was used for the electrodeposition of PPy/EGO composites. Ti foil was cut into strips with 1 cm width and sealed with insulating tape to allow $1 \times 1$ $cm^2$ area to be exposed to precursor electrolyte for deposition. The co-electrodeposition of PPy/EGO composite electrodes was conducted using an IviumStat potentiostat (Ivium, Netherlands) with a three-electrode configuration; Pt and saturated calomel electrode (SCE) were used as counter and reference electrodes, respectively. The electrodeposition was performed at a constant potential of 0.8 V *vs.* SCE for different deposition times. If not specified, the electrodes used in this work were prepared with an electrodeposition time of 3600 s. The as-prepared PPy/EGO composite electrodes were rinsed with de-ionized water and then stored in 1 M KCl for further experiments.

## Materials characterization

PPy/EGO composites for the characterization were rinsed with deionized water and dried at ambient conditions for 24 h. Scanning electron microscopy characterization was performed using a ULTRA 55 microscope (Carl Zeiss AG). Transmission electron microscopy (TEM) was conducted with a Talos F200X TEM (Thermo Scientific). Fourier transform infrared spectra (FT-IR) of the samples were collected using a Nicolet 5700 spectrometer. X-ray photoelectron spectroscopy (XPS) was performed with a Kratos Axis Ultra X-ray photoelectron spectrometer meter; CasaXPS software was used for the curve fitting and data analysis. Raman spectra were collected by using a Renishaw inVia microscope with a laser wavelength of 532 nm. Thermogravimetric analysis (TGA) was performed by using Mettler Toledo instrument under $N_2$ atmosphere with a ramp rate of 10 °C $min^{-1}$. The XRD patterns were obtained by using X-ray diffraction (Bruker D8 Advanced diffractometer) with Cu-Kα radiation (λ = 1.5406 Å) at 40 kV. The mass loading of each PPy/EGO composite electrodes was measured using a balance with accuracy of 0.001 mg. The PPy/EGO composites were scratched from the Ti foil substrate using a scalpel.

**Electrochemical measurement**

A three-electrode cell configuration with Pt and SCE as reference and counter electrodes was used to study the electrochemical performance of PPy/EGO composites in different potassium halides (KF, KCl, KBr and KI) electrolytes with a concentration of 1 M. For the fabrication of prototype Zn-PPy hybrid supercapacitor, Zn foil was used as anode and PPy/EGO composite electrode was used as cathode, 1 M $ZnCl_2$, $ZnBr_2$ or $ZnSO_4$ aqueous solution was used as electrolyte. The anode and cathode were sandwiched between two PTFE plates with a piece of PTFE filter membrane as separator. The prototype supercapacitor device was sealed with Parafilm before measurement. All electrochemical measurements were conducted with an IviumStat electrochemical workstation.

For the three-electrode measurements, the areal capacitance ($C_A$; mF cm$^{-2}$) of the PPy/EGO electrodes was calculated according to the galvanostatic charge-discharge profiles using the equation:

$$C_A = \frac{I\Delta t}{A\Delta V} \qquad \text{(S5.1)}$$

where $I$ is the discharge current (mA), $\Delta t$ is the discharge time (s), $A$ is the geometric area of the electrode (cm$^2$), $\Delta V$ is the potential range (−0.5 to 0.5 V vs SCE) excluded the IR drop (V). The specific capacitance ($C_S$; F g$^{-1}$) of the electrode was calculated from the below equation:

$$C_S = \frac{C_A}{m} \qquad \text{(S5.2)}$$

where $m$ is the mass loading of PPy/EGO electrode.

For the two-electrode cell (hybrid supercapacitor device) using PPy/EGO as cathode and Zn metal foil as anode, the $C_A$ of PPy/EGO cathode was calculated according to equation (1) with cell voltage range $\Delta V$ of 1.0 V (0.5 to 1.5 V vs $Zn^{2+}$/Zn) excluding the IR drop. The $C_S$ (F g$^{-1}$) of PPy/EGO composite is calculated according to equation (2) with the mass loading of PPy/EGO on the cathode.

The energy density of the PPy/EGO cathode ($E_{PPy/EGO}$; Wh kg$^{-1}$) was calculated from the galvanostatic charge-discharge curves based on the equation:

$$E_{PPy/EGO} = \frac{I\int V(t)dt}{3.6m} \qquad \text{(S5.3)}$$

where $I$ is the discharge current (A), $t$ is the discharge time (s), $V(t)$ is the cell voltage (V) of the device at the corresponding discharge time of $t$, $m$ is the mass loading (g) PPy/EGO composite on the cathode. The power density of the PPy/EGO cathode ($P_{cathode}$; W kg$^{-1}$) is calculated according to

$$P_{PPy/EGO} = \frac{3600E_{PPy/EGO}}{t} \qquad \text{(S5.4)}$$

To estimate the energy density of two-electrode cell ($E_{cell}$) based on the total mass of the Zn anode and PPy/EGO cathode, the mass of Zn involved in the charge storage was estimated from the theoretical capacity of Zn anode (820 mAh g$^{-1}$) and the measured

capacity of PPy/EGO composite cathode, at the smallest used charge-discharge current density (0.5 mA $cm^{-2}$). According to charge conservation

$$Q_{\text{anode}} = Q_{\text{cathode}} \qquad \text{(S5.5)}$$

where $Q_{\text{anode}}$ and $Q_{\text{cathode}}$ is the electric charge stored in anode and cathode, respectively. Therefore, the mass of Zn ($m_{\text{Zn}}$; g) in the anode involved in the charge storage can be calculated according to

$$m_{\text{Zn}} C_{\text{Zn; theo}} = m_{\text{PPy/EGO}} C_{\text{PPy/EGO}} \qquad \text{(S5.6)}$$

where $C_{\text{Zn; theo}}$ is the theoretical capacity of Zn (820 mAh $g^{-1}$), $m_{\text{PPy/EGO}}$ is the mass loading (g) of PPy/EGO composite in the cathode, $C_{\text{PPy/EGO}}$ is the measured capacity (mAh $g^{-1}$) of PPy/EGO composites at the smallest charge-discharge current density of 0.5 mA $cm^{-2}$.

Based on the calculated $m_{\text{Zn}}$, assuming twice of the mass of theoretically need Zn is loaded on the anode (capacity ratio of anode to cathode is 2:1), as the theoretical capacity is difficult to reach in practical experiments. The $E_{\text{cell}}$ can be estimated as follows:

$$E_{\text{cell}} = \frac{I \int V(t) \mathrm{d}t}{3.6 \times (2 \times m_{\text{Zn}} + m_{\text{PPy/EGO}})} \qquad \text{(S5.7)}$$

Note that a coefficient of 2 was applied to the $m_{\text{Zn}}$, corresponding to the twice of theoretically needed Zn. The estimated power density of the cell ($P_{\text{cell}}$; W $kg^{-1}$) was therefore calculated using

$$P_{\text{cell}} = \frac{3600 E_{\text{cell}}}{t} \qquad \text{(S5.8)}$$

**Supplementary Figures**

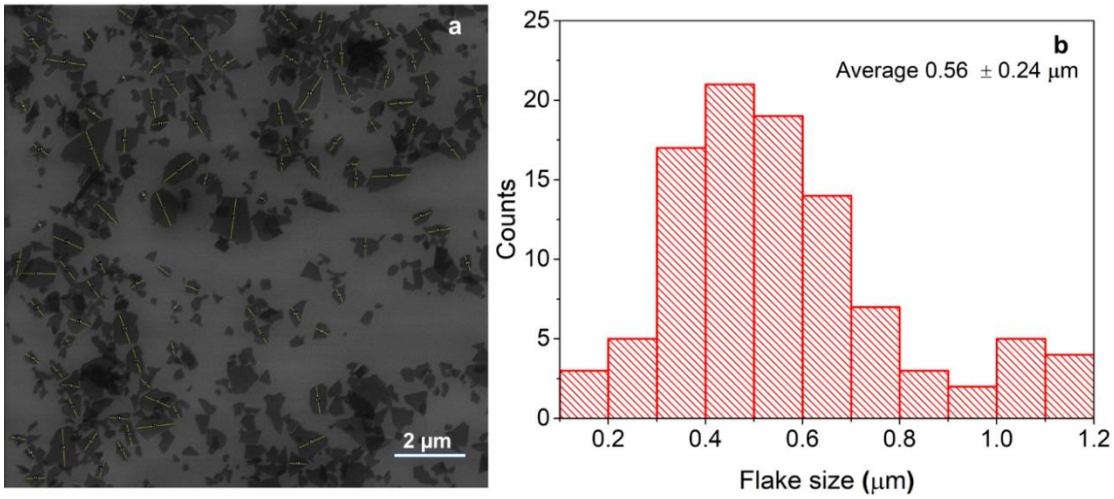


**Figure S5.1. (a)** SEM image of EGO (the flakes marked by the yellow line are considered to measure the corresponding lateral sizes) and **(b)** Flake size distribution of EGO.

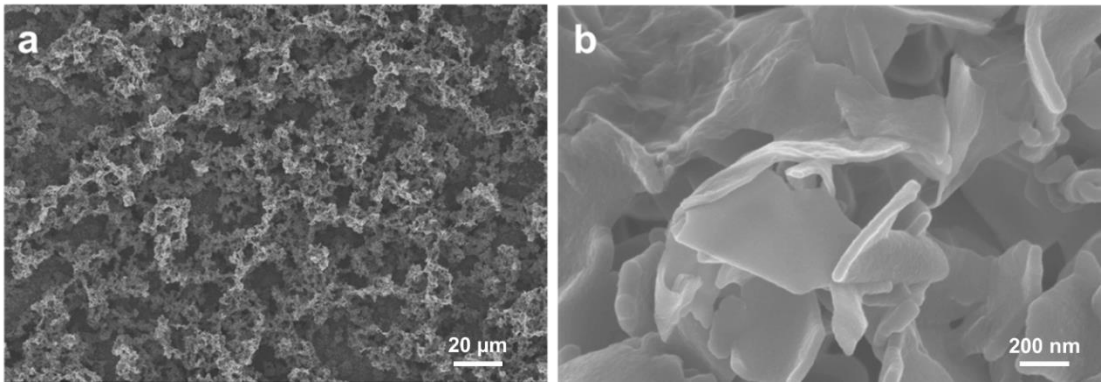


**Figure S5.2.** SEM images of the PPy/EGO electrodes with different magnifications **(a)** Magnification 1000 × and **(b)** Magnification 100k×.

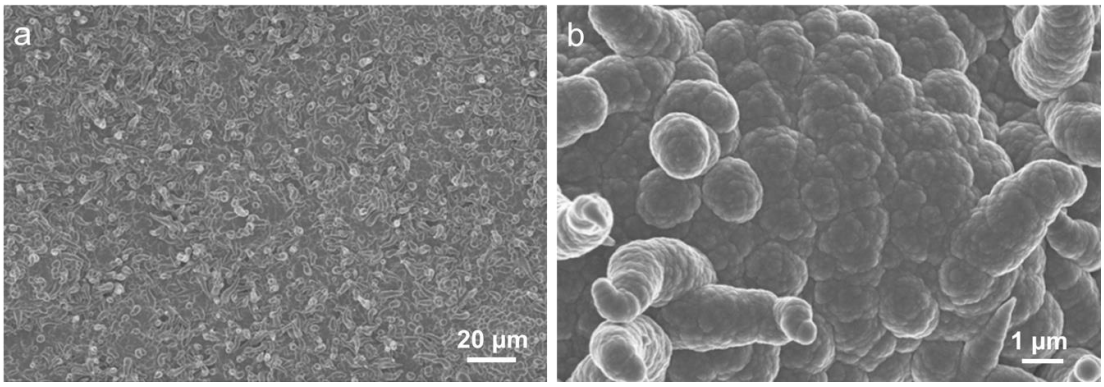


**Figure S5.3.** SEM images of the pure PPy electrodes showing the surface morphology. **(a)** Magnification 2000 × and **(b)** Magnification 20000 ×.

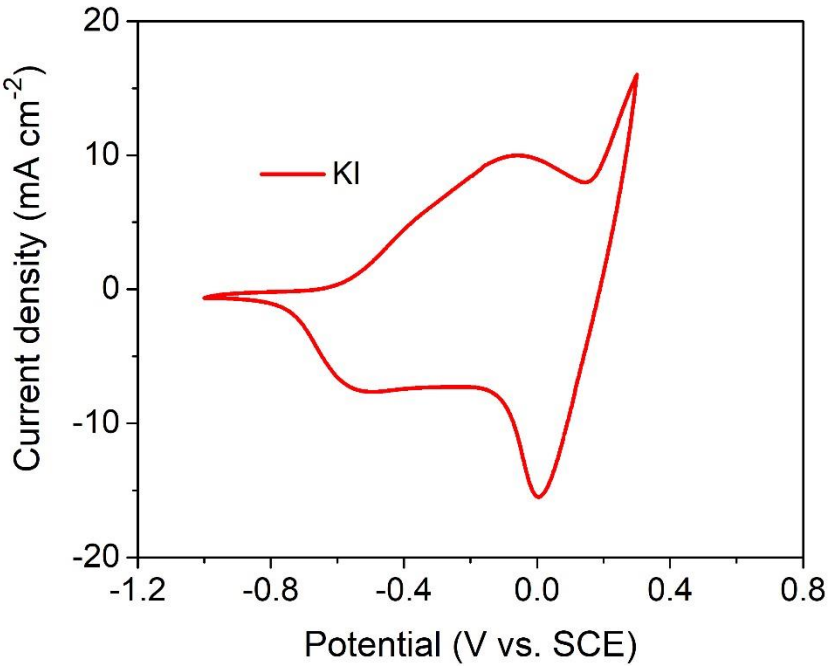


**Figure S5.4.** CV at 50 mV $s^{-1}$ from PPy/EGO-1200s in 1 M KI.

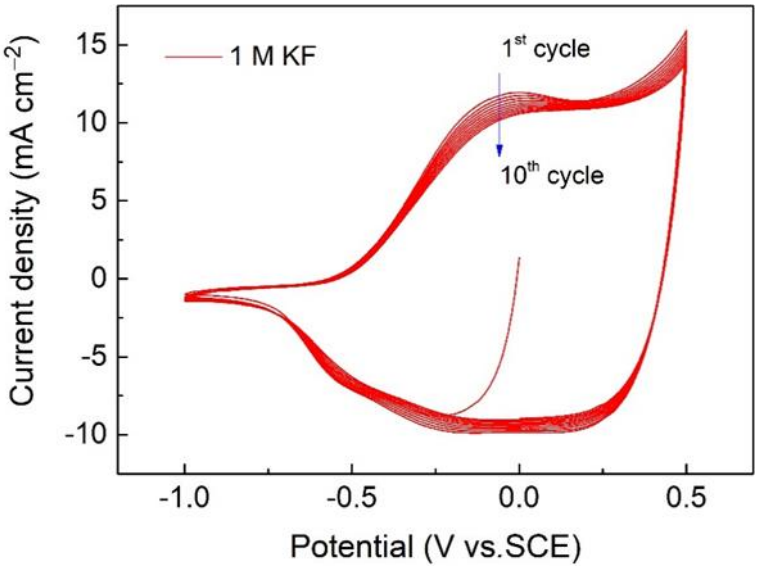


**Figure S5.5.** CVs of the PPy/EGO-1200s composite electrode recorded in 1 M KF aqueous electrolyte, showing the rapid decay of responsive current density with the increase of scan cycles.

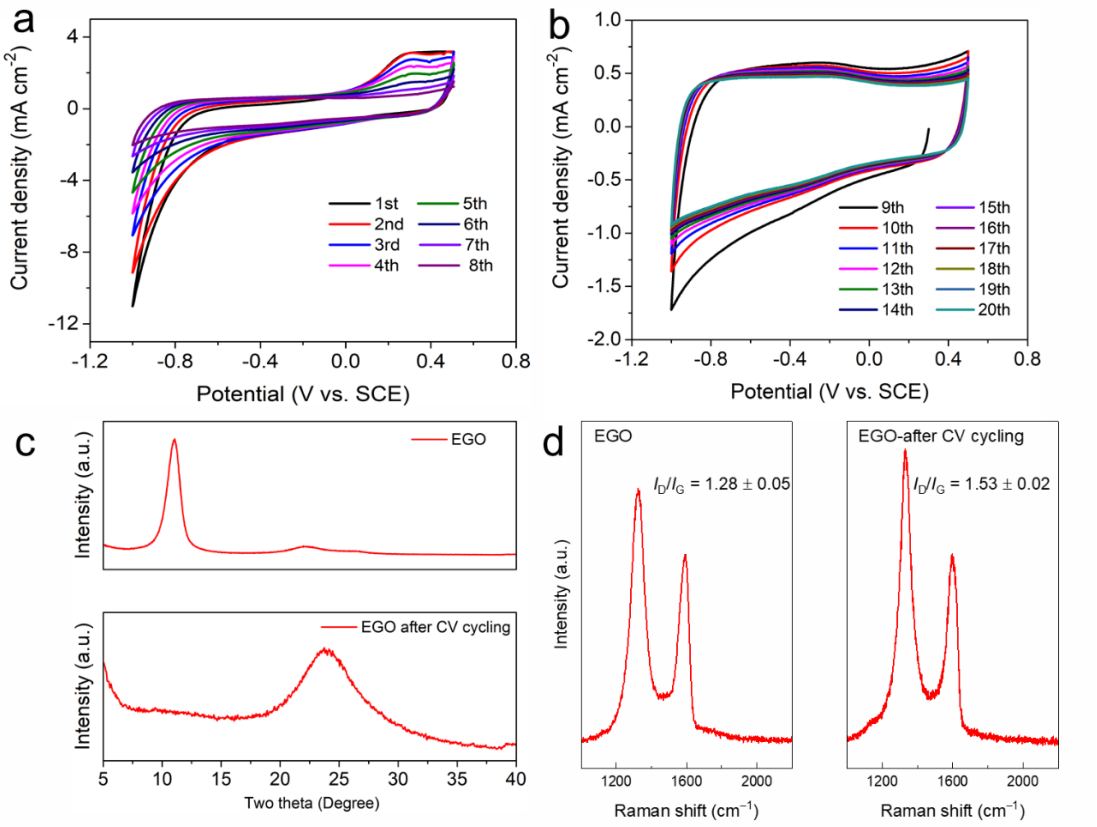


**Figure S5.6. (a-b)** Cyclic voltammograms of the electrochemical reduction of EGO at 50 mV $s^{-1}$ in 1 M KCl, **(c)** XRD patterns of EGO and EGO after electrochemical reduction, **(d)** Raman spectra of EGO and EGO after electrochemical reduction.

The EGO solution (0.5 mL) with a concentration of 1 mg $mL^{-1}$ was stepwise cast on the Ti foil placed on a hot plate heated to 60 °C. After the solution had dried, 100 µL 0.05 wt% Nafion solution was cast on the top of the film and allowed to dry in air. The electrochemical reduction of EGO was performed in the potential range from 0.5 to −1.0 V vs SCE in 1 M KCl at 50 mV $s^{-1}$ in a standard three-electrode configuration with Pt as counter electrode, SCE as reference electrode, respectively.

After electrochemical reduction of EGO, the diffraction peak of EGO at 11.1° shifts to a higher 2θ angle of 24.0°, indicating the decrease in the interlayer distance and thus successful reduction of EGO (removal of oxygen groups). The intensity ratio of D to G band ($I_D/I_G$) is associated with the defect distance ($L_D$, average distance between two

defects) in the graphene lattice and has a maximum value at the $L_D$ of 3~4 nm [5, 6]. For highly defective graphene materials, such as EGO and reduced EGO under mild conditions, the $L_D$ values are well below 3 nm, and thus the $I_D/I_G$ ratio of EGO will increase and becomes close to the maxima after reduction (partially restoration of the graphene lattice). This increase of $I_D/I_G$ ratio of EGO after reduction has been reported in our previous works [1, 7]. In the present work, EGO was reduced after electrochemical CV cycling, as confirmed by the XRD results, and thus the Raman $I_D/I_G$ ratio of the reduced EGO is higher than the pristine one.

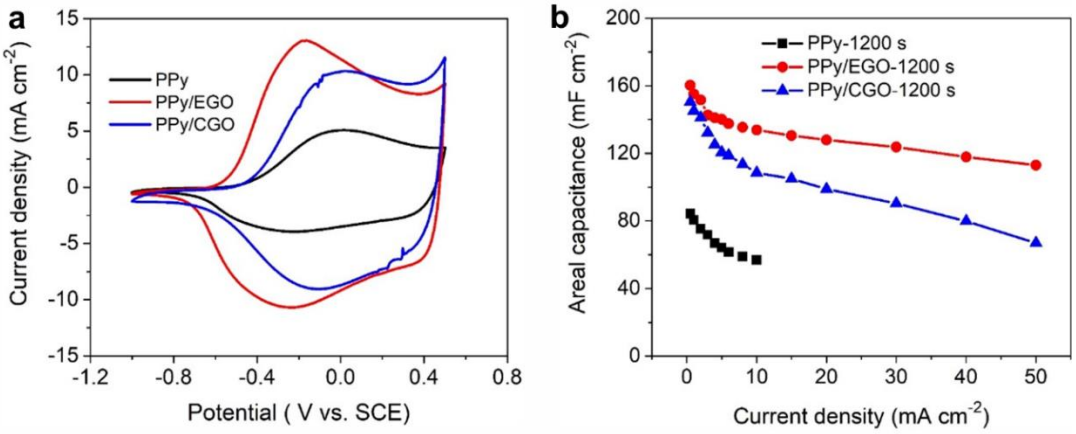


**Figure S5.7.** Comparison of **(a)** CVs at 50 mV $s^{-1}$ and **(b)** rate capability for PPy-1200s, PPy/EGO-1200 s and PPy/CGO-1200 s in 1 M KCl electrolyte.

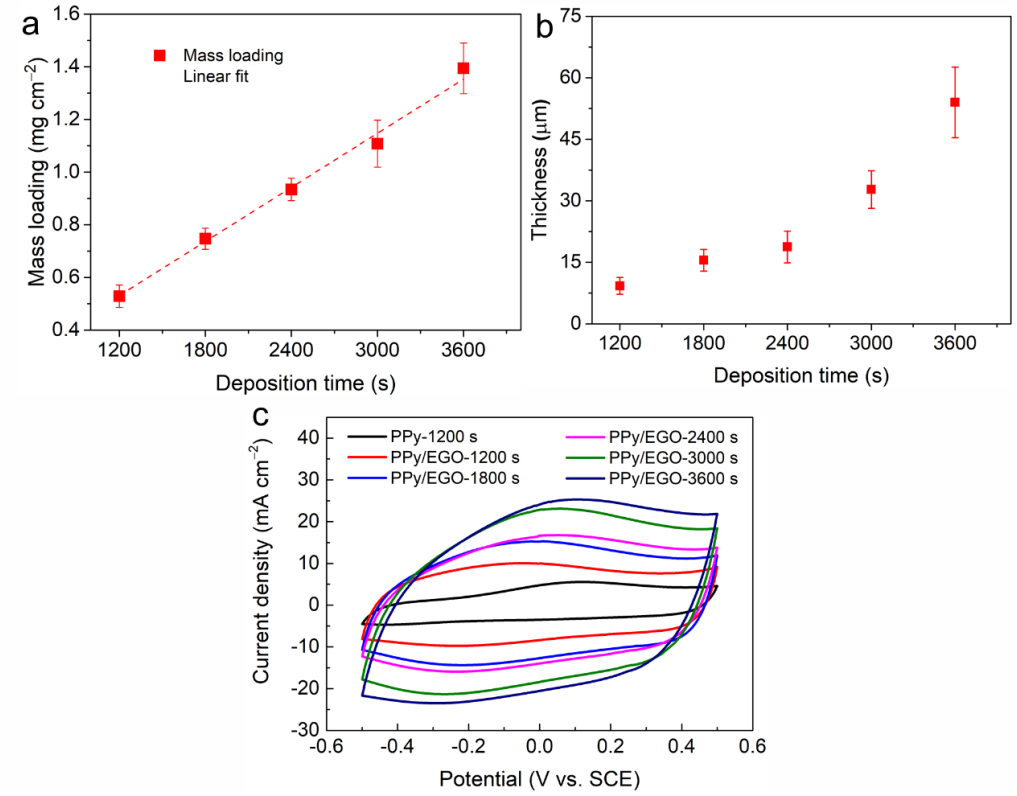


**Figure S5.8. (a)** Mass loading versus deposition time for the PPy/EGO composite electrodes. **(b)** Thickness versus deposition time for the PPy/EGO composite electrodes. **(c)** CVs recorded at 50 mV $s^{-1}$ using a three-electrode configuration for the PPy and PPy/EGO composites electrodes with different deposition times in 1 M KCl.

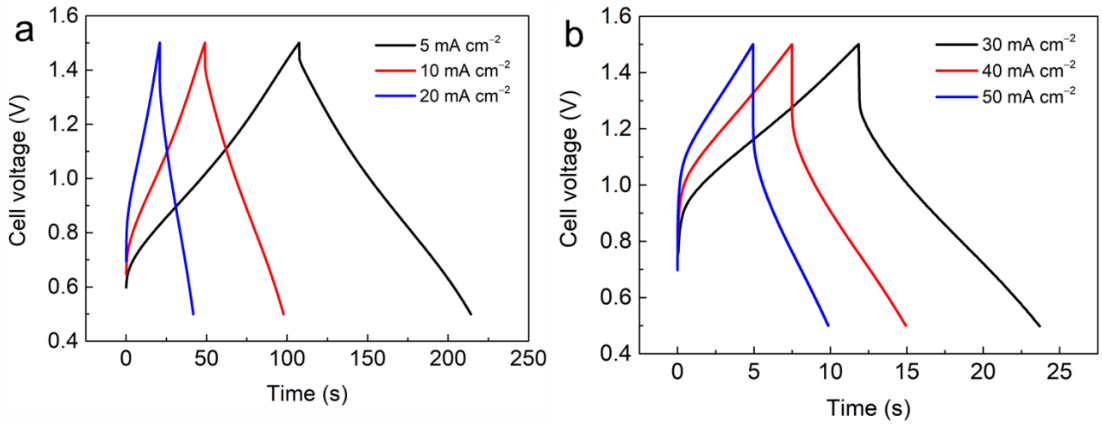


**Figure S5.9.** Galvanostatic charge-discharge profiles at various current densities in Zn-PPy/EGO supercapacitor using 1 M $ZnCl_2$.

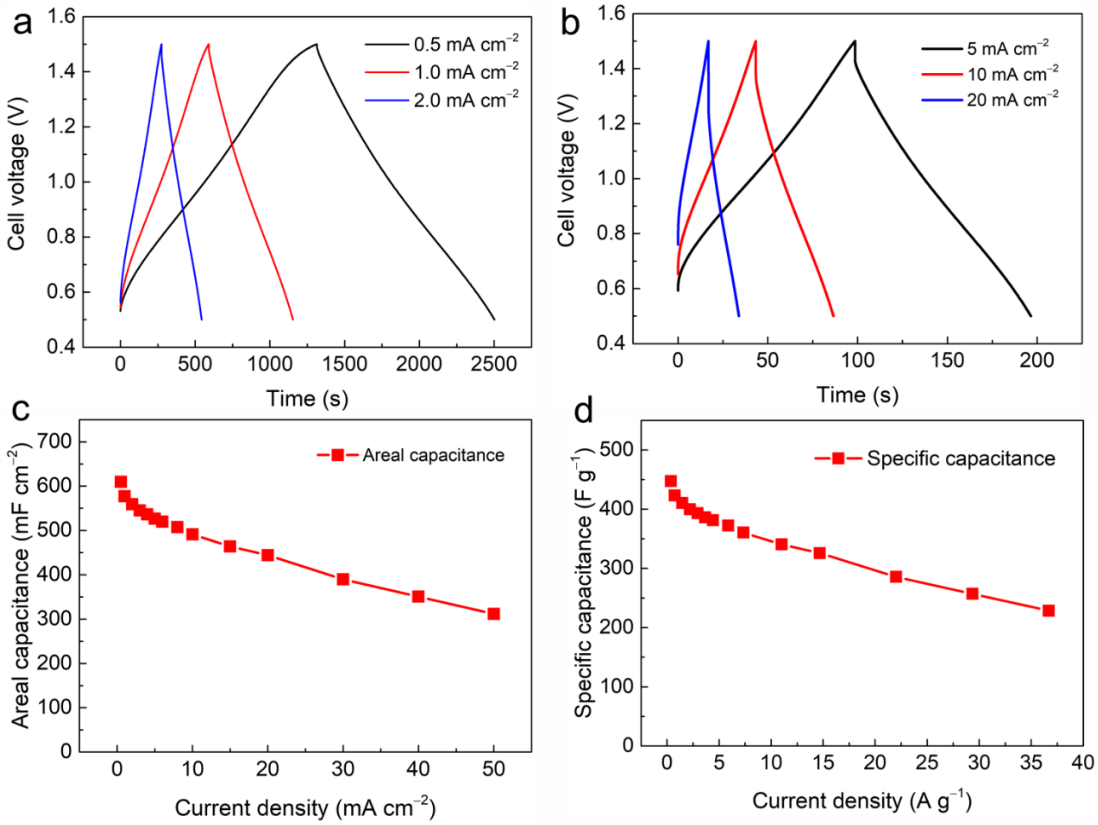


**Figure S5.10.** Zn-PPy/EGO supercapacitor using 1 M $ZnBr_2$: **(a)** and **(b)** galvanostatic charge-discharge profiles at various current densities; **(c)** and **(d)** rate performance.

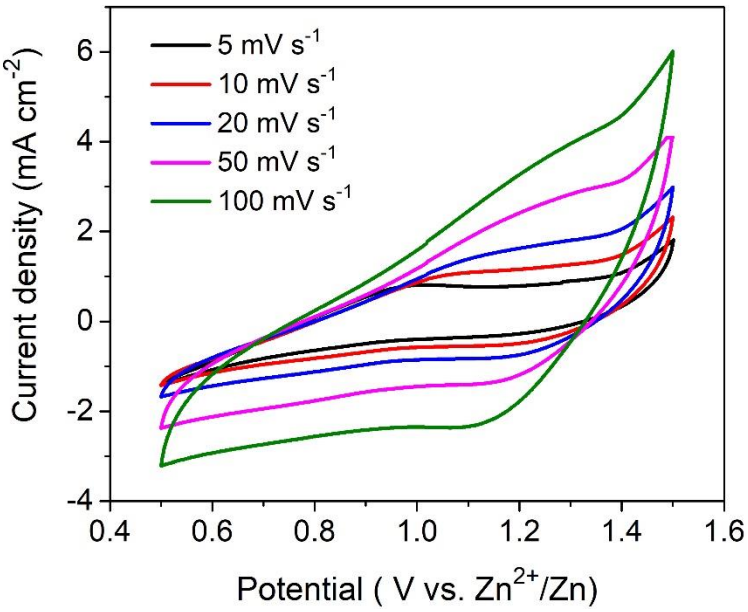


**Figure S5.11.** CVs of Zn-PPy/EGO supercapacitor using 1 M $ZnSO_4$.

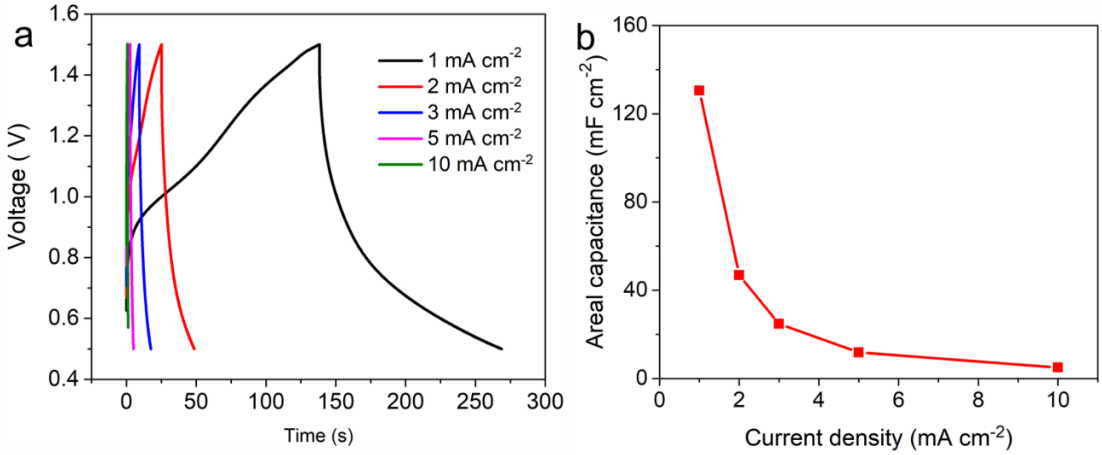


**Figure S5.12. (a)** Galvanostatic charge-discharge profiles and **(b)** rate performance at various current densities in Zn-PPy/EGO supercapacitor using 1 M $ZnSO_4$.

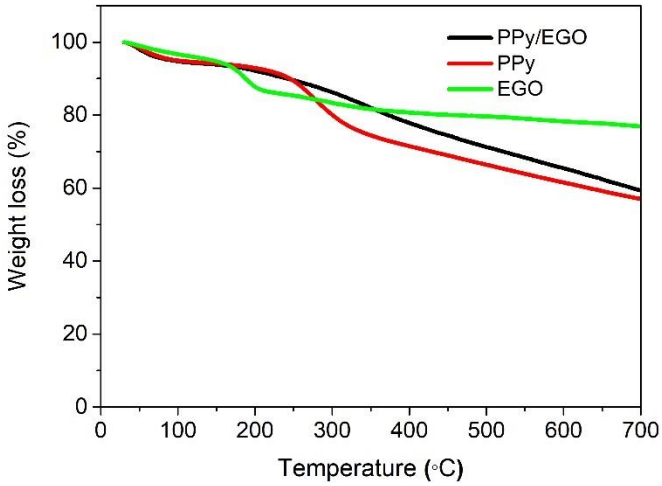


**Figure S5.13.** Thermogravimetric analysis of the PPy/EGO composite, PPy and EGO at nitrogen atmosphere.

The weight losses of the pure PPy and pure EGO are about 43% and 23%, respectively, while for the PPy/EGO composite the weight loss is 41%. According to these values, the percentage of PPy in the composite is estimated to be about 90%.

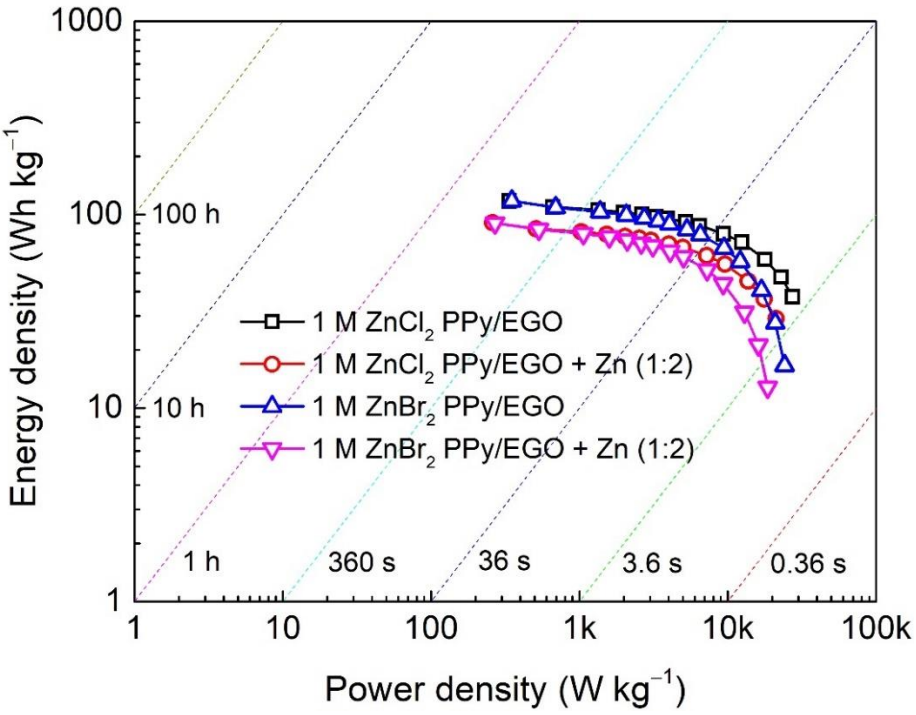


**Figure S5.14.** Ragone plot of Zn-PPy/EGO supercapacitors using 1 M $ZnCl_2$ and 1 M $ZnBr_2$.

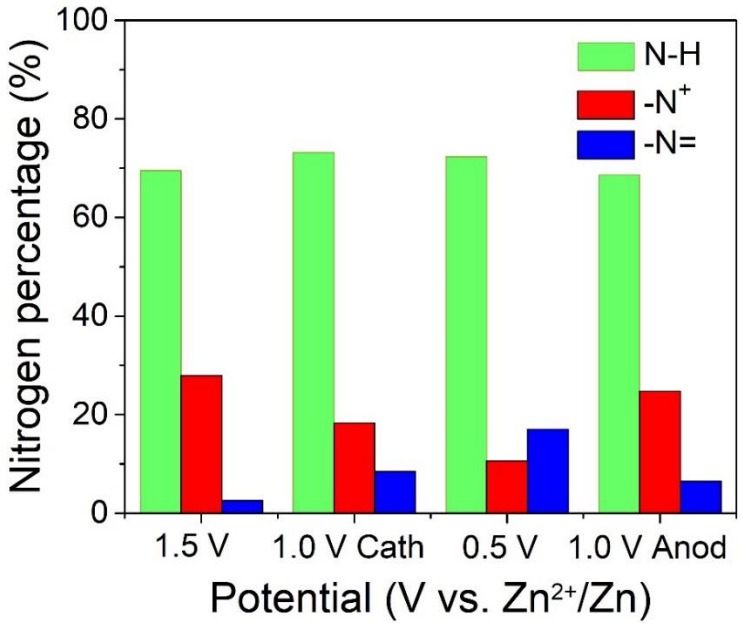


**Figure S5.15.** Contents of various types of nitrogen sites at different stages.

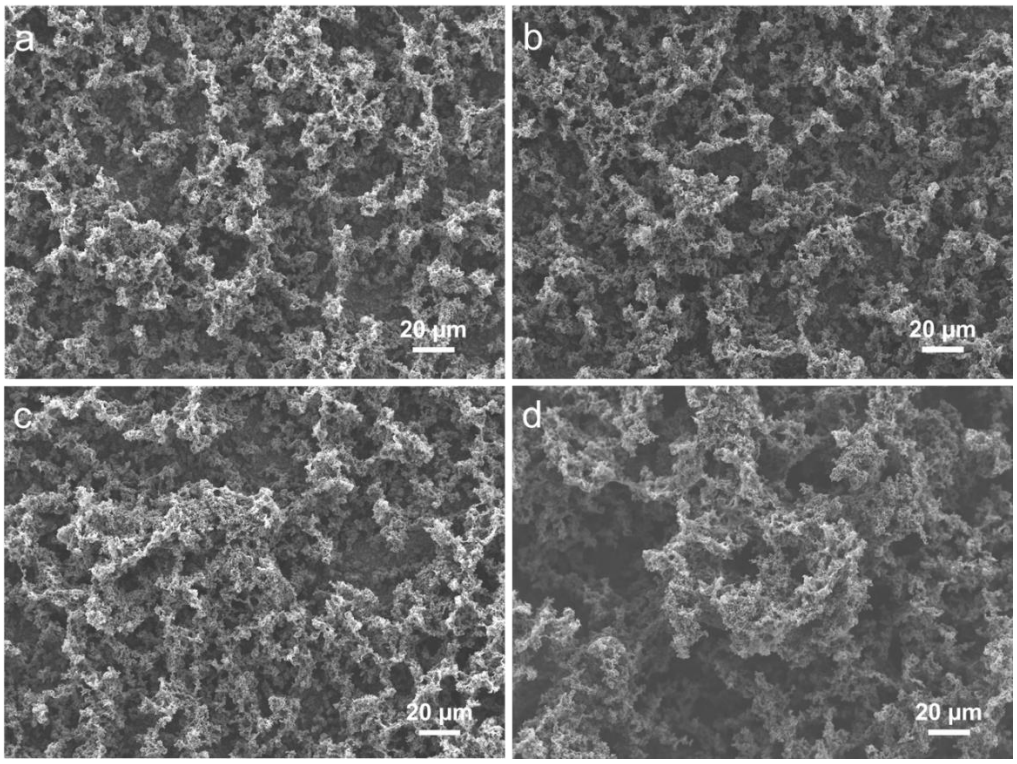


**Figure S5.16.** SEM images of the PPy/EGO samples at different charge-discharge stages in 1 M $ZnCl_2$: **(a)** 1.5 V (i.e., fully charged state), **(b)** 1.0 V Cathodic scan (i.e., half discharged state), **(c)** 0.5 V (i.e., fully discharged state (0.5 V), **(d)** 1.0 V Anodic scan (i.e., half charged state).

## Supplementary Tables

**Table S5.1.** Contents of elements in the investigated samples

| Samples | 1.5 V | 1.0 V Cath | 0.5 V | 1.0 V Anod |
|---|---|---|---|---|
| C (at. %) | 73.19 | 72.60 | 70.82 | 73.91 |
| O (at. %) | 14.18 | 15.51 | 16.82 | 15.01 |
| N (at. %) | 10.31 | 10.55 | 9.36 | 9.72 |
| Cl (at. %) | 2.18 | 1.03 | 2.53 | 1.12 |
| Zn (at. %) | 0.14 | 0.30 | 0.47 | 0.25 |

**Table S5.2.** Contents of various types of nitrogen sites

| Sample | Different stages | | | |
|---|---|---|---|---|
| | 1.5 V | 1.0 V Cath | 0.5 V | 1.0 V Anod |
| -N-H (at. %) | 69.52 | 73.20 | 72.35 | 68.63 |
| $-N^{+}$ (at. %) | 27.91 | 18.32 | 10.64 | 24.72 |
| -N= (at. %) | 2.58 | 8.47 | 17.01 | 6.65 |

**Table S5.3.** Comparison of our Zn-PPy/EGO device with reported PPy-based energy storage devices

| Energy storage system (Cathode//Electrolyte//Anode) | Capacity or capacitance | Operating voltage | Maximum energy density | Cycling retention | References |
|---|---|---|---|---|---|
| PPy// bioionic liquid+water// Zn | 60 mAh $g^{-1}$ (0.5 A $g^{-1}$) | 0-1.4 V | - | 43.75% over 50 cycles | [8] |
| PPy Composite Aerogels// 2 M $ZnCl_2$ and 3 M $NH_4Cl$(aq.) // Zn-coated graphite paper | 151.1 mAh $g^{-1}$ (0.5 A $g^{-1}$) (normalized by the mass of PPy only) | 0-1.6 V | 64 Wh $kg^{-1}$ at 11.7 kW $kg^{-1}$ | 76.7% over 1000 cycles | [9] |
| PPy// PVA-KCl-Zn$(CH_3COO)_2$ (gel.) //Zn | 123 mAh $g^{-1}$ (1.9 A $g^{-1}$) | 0-1.2 V | - | 38% over 200 cycles | [10] |
| PPy nanowire// $Na_2SO_4$ (aq.) // PPy nanowire | 155 F $g^{-1}$ (1.5 A $g^{-1}$) | 0-1.2 V | - | - | [11] |
| PPy/CNTP// PVA-$H_2SO_4$ (gel.) //PPy/CNTP | 2185.1 mF $cm^{-2}$ (1 mA $cm^{-2}$) | 0-0.8 V | 194.23 μWh $cm^{-2}$ | - | [12] |
| GO/PPy // 1 M KCl // GO/PPy | 377.6 mF $cm^{-2}$ (0.2 mA $cm^{-2}$) | 0-0.8 V | 16.4 Wh $kg^{-1}$ | 84.8% over 5000 cycles | [13] |
| α-$MnO_2$@PPy//1 M $ZnSO_4$ + 0.1 M $MnSO_4$ (aq.)//Zn | 148 mAh $g^{-1}$ (0.1 A $g^{-1}$) | 1-1.8 V | - | 57.43% over 100 cycles | [14] |
| CNT-GO-PPy // PVA-$H_3PO_4$ (gel.) // CNT-GO-PPy | 70.0 mF $cm^{-2}$ (10 mV $s^{-1}$) | 0-0.8 V | 6.3 μWh $cm^{-2}$ | 87.7% over 10000 cycles | [15] |
| sulfonated graphene-PPy// 1 M KCl // $ZnSO_4$ (aq.)// sulfonated graphene-PPy | 253 F $g^{-1}$ (0.3 A $g^{-1}$) | -0.2-0.5 V | 4.3 Wh $kg^{-1}$ | 71% over 1500 cycles | [16] |
| holey graphene-PPy//1 M $Na_2SO_4$// holey graphene-PPy | 328 F $cm^{-3}$ (0.5 A $g^{-1}$) | 0-1.4 V | 22.3 Wh $L^{-1}$ | 82.4% over 2000 cycles | [17] |
| PPy-EGO// 1M $ZnCl_2$ (aq.)//Zn | 445 F $g^{-1}$ (122 mAh $g^{-1}$) 663 mF $cm^{-2}$ (0.35 A $g^{-1}$) | 0.5 to 1.5 V | 117.7 Wh $kg^{-1}$ (0.3 kW $kg^{-1}$) 72.1 Wh $kg^{-1}$ (12 kW $kg^{-1}$) | 81% over 5000 cycles | This work |

## References

[1] J. Cao, P. He, M.A. Mohammed, X. Zhao, R.J. Young, B. Derby, I.A. Kinloch, R.A.W. Dryfe, J. Am. Chem. Soc. , 139 (2017) 17446-17456.

[2] W.S.H. Jr., R.E. Offeman, J. Am. Chem. Soc. , 80 (1958) 1339.

[3] P. He, B. Derby, 2D Mater., 4 (2017) 021021.

[4] S. Ji, J. Yang, J. Cao, X. Zhao, M.A. Mohammed, P. He, R.A.W. Dryfe, I.A. Kinloch, ACS Appl. Mater. Interfaces, 12 (2020) 13386-13399.

[5] M.M. Lucchese, F. Stavale, E.H.M. Ferreira, C. Vilani, M.V.O. Moutinho, R.B. Capaz, C.A. Achete, A. Jorio, Carbon, 48 (2010) 1592-1597.

[6] L.G. Cancado, A. Jorio, E.H. Ferreira, F. Stavale, C.A. Achete, R.B. Capaz, M.V. Moutinho, A. Lombardo, T.S. Kulmala, A.C. Ferrari, Nano Lett, 11 (2011) 3190-3196.

[7] Y. Peng, J. Cao, J. Yang, W. Yang, C. Zhang, X. Li, R.A.W. Dryfe, L. Li, I.A. Kinloch, Z. Liu, Adv. Funct. Mater., 30 (2020) 2001756.

[8] A. Lahiri, L. Yang, G. Li, F. Endres, ACS Appl. Mater. Interfaces, 11 (2019) 45098-45107.

[9] X. Li, X. Xie, R. Lv, B. Na, B. Wang, Y. He, Energy Technology, 7 (2019) 1801092.

[10] J. Wang, J. Liu, M. Hu, J. Zeng, Y. Mu, Y. Guo, J. Yu, X. Ma, Y. Qiu, Y. Huang, J. Mater. Chem. A, 6 (2018) 11113-11118.

[11] J. Zhao, J. Wu, B. Li, W. Du, Q. Huang, M. Zheng, H. Xue, H. Pang, Prog. Nat. Sci., 26 (2016) 237-242.

[12] L. Tong, M. Gao, C. Jiang, K. Cai, J. Mater. Chem. A, 7 (2019) 10751-10760.

[13] J. Cao, Y. Wang, J. Chen, X. Li, F.C. Walsh, J.-H. Ouyang, D. Jia, Y. Zhou, J. Mater. Chem. A, 3 (2015) 14445-14457.

[14] C. Guo, S. Tian, B. Chen, H. Liu, J. Li, Mater. Lett., 262 (2020) 127180.

[15] H. Zhou, H.-J. Zhai, Org. Electron., 37 (2016) 197-206.

[16] X. Zuo, Y. Zhang, L. Si, B. Zhou, B. Zhao, L. Zhu, X. Jiang, J. Alloys Compd., 688 (2016) 140-148.

[17] Z. Fan, J. Zhu, X. Sun, Z. Cheng, Y. Liu, Y. Wang, ACS Appl. Mater. Interfaces, 9 (2017) 21763-21772.

# Chapter 6 Hierarchically porous carbon (HPC) derived from starch via $CO_2$ activation for high performance zinc-ion hybrid supercapacitors

Jie Yang,[‡a,b] Han Li,[‡c] Mark Bissett,[b] and Robert A. W. Dryfe[*ab], Vitaliy L. Budarin,[c] James H. Clark,[c] Michael North[*c]

[a] Department of Chemistry, University of Manchester, Oxford Road, Manchester, M13 9PL, UK.

[b] National Graphene Institute, University of Manchester, Oxford Road, M13 9PL, UK.

[c] Green Chemistry Centre of Excellence, Department of Chemistry, University of York, Heslington, YO10 5DD, UK.

Corresponding authors:

E-mail: robert.dryfe@manchester.ac.uk; michael.north@york.ac.uk

‡These authors contributed equally to this work.

**To be submitted to Green Chemistry.**

## Author contributions:

The synthesis, characterization, and electrochemical measurement were carried out by J. Yang and H. Li. The article was written by J. Yang with comments from Prof. R. A. W. Dryfe and Prof. M. North. All authors discussed the results and commented on the manuscript.

**Abstract:** To create a renewable resource-based sustainable society, it is urgent and vital to utilize green chemistry principles to prepare renewable materials for harnessing clean energy to alleviate energy crisis and reduce carbon dioxide emissions. Herein, the greenhouse gas ($CO_2$) has been selected as activating agent to prepare high-value hierarchically porous carbon with high specific surface area of up to 2457 $m^2$ $g^{-1}$ derived from starch. The method can effectively avoid the use of the common corrosive reagents like KOH or $H_3PO_4$ and exploit the potential application of $CO_2$. The activation process can be readily regulated by the reaction time. The as-prepared material was further used in an aqueous zinc-ion hybrid supercapacitor which emerges as a promising energy storage device integrating the merits of battery-type electrode (Zn metal) with capacitor-type electrode (porous carbon). It has demonstrated that the high specific surface area provides sufficient active sites for charge storage and the hierarchical pore structure facilitates rapid ion transport. Such a hybrid supercapacitor exhibits a high specific capacitance of 259 F $g^{-1}$ at 0.5 A $g^{-1}$ (160 F $g^{-1}$ at 30 A $g^{-1}$) and a high energy density of 94.1 Wh $kg^{-1}$ at a power density of 399 W $kg^{-1}$ (58.5 Wh $kg^{-1}$ at 24.5 kW $kg^{-1}$) as well as excellent cycling stability with 97% capacitance retention over 10000 cycles.

## *Introduction*

The excessive consumption of non-renewable resources like oil and coal has given rise to a serious environmental crisis, thus driving the search for renewable energy resources [1, 2]. The utilization of various green sources of energy, such as solar, wind and tidal energy, is highly dependent on advanced energy storage devices like batteries and supercapacitors [3, 4]. The commonly used battery technologies include lead-acid batteries, nickel-cadmium batteries, nickel-metal hydride batteries and lithium-ion batteries. However, to some extent, some intrinsic drawbacks of these batteries hinder their further large-scale applications. For example, lead-acid and nickel-cadmium batteries contain heavy metals, which are harmful to the environment and human health

and suffer from a low energy density of about 50 Wh $kg^{-1}$ [5, 6]. Nickel-metal hydride batteries exhibit inferior performance at low temperatures and suffer from a severe self-discharge [7-9]. Although lithium-ion batteries have dominated the rechargeable battery market because of the higher energy density, longer lifetime and lighter weight since they were first commercialized by Sony Corporation in 1991, safety issues, high cost and environmental unfriendliness hinder their further large-scale applications due to the toxic and flammable organic electrolytes as well as the demanding environment required for manufacturing [10-12]. Unlike batteries, supercapacitors, also known as electrochemical capacitors, are characterized by excellent power densities and ultra-long cyclability. The term supercapacitors include electrical double-layer capacitors (EDLCs), operating through charge storage at the electrode/electrolyte interface, and pseudocapacitors which operate via fast reversible redox reactions near the surface of active materials [13, 14]. However, the low energy densities (5-10 Wh $kg^{-1}$) of supercapacitors retard their further penetration into various applications. These factors are encouraging researchers to develop novel energy storage devices which are safe, cost-effective and eco-friendly whilst retaining high performance.

Constructing hybrid supercapacitors is believed to be an effective approach to improve both energy density and power density. In recent years, aqueous zinc-ion hybrid supercapacitors have been attracting extensive attention as novel energy storage devices: they are composed of a capacitor-type carbon material as the cathode, with a battery-type Zn foil as the anode and aqueous $Zn^{2+}$-containing solution as the electrolyte [15, 16]. A fast reversible electrostatic adsorption/desorption of electrolyte ions on the carbon-based cathode ensures excellent power capability and a Zn metal anode with a high theoretical capacity of 820 mAh $g^{-1}$ endows a high energy density. The combination of respective merits of supercapacitors and batteries in this system attempts to bridge the energy gap between supercapacitors and batteries. Moreover, both the cathode and anode materials along with electrolytes are abundant, cost-effective and eco-friendly. The electrochemical performance of zinc-ion hybrid supercapacitors is highly dependent on the properties of the carbon-based cathode

materials, such as specific surface area and pore size, considering that the charge storage mechanism of carbon-based electrode in this type of device involves ions adsorption/desorption at the interface of electrode/electrolyte.

Carbon-based materials are widely employed as electrode materials for energy storage and conversion owing to their high specific surface area, outstanding electrical conductivity, good thermal stability, superb chemical stability, low cost and environmental benignity [17, 18]. Generally, the presence of micropores (< 2 nm) in carbon materials can significantly increase the specific surface area, but lead to poor rate capability because of slower mass transport within the micropores [1, 19, 20]. Therefore, it is necessary to optimize the pore size and structure of carbon materials to boost their electrochemical performance. Hierarchical porous carbon (HPC) materials integrating micropores (< 2 nm) with mesopores (2-50 nm) as well as macropores (> 50 nm) are considered as promising candidates for electrode materials to improve their specific capacitance and rate capability. Generally, macropores can act as reservoirs to minimize the diffusion distances of electrolyte ions from the bulk to the electrode/electrolyte interface. Mesopores allow more accessible sites and provide pathways for rapid ion migration to enhance the accessibility of micropores [19, 21, 22].

To meet the increasing demand for cost-effective, eco-friendly and easily available sources, there is a growing trend in the development of carbon-based materials from biomass resources, thus achieving the ultimate goal “from waste to wealth” and maintaining the sustainable development of our society [1, 23]. Different biomass sources, such as rice bran [24], bamboo [25] and spores [26], have been widely used as precursors to prepare porous carbon materials by physical or chemical activation for various applications, such as energy storage [27, 28], water treatment [29], hydrogen storage [30], and carbon dioxide capture [31, 32]. Basically, the method of transforming biomass into carbon involves carbonisation (i.e., pyrolysis and hydrothermal carbonisation) and subsequent activation (i.e., physical activation and chemical activation). Chemical activation has been widely adopted by most researchers to

produce porous carbon since it is more likely to obtain a high specific surface area via this method [14, 19, 20, 24]. However, this method always involves large amount of hazardous chemicals, such as KOH, NaOH, or $H_3PO_4$, thus leading to secondary environmental pollution in the disposal process. Additionally, the resultant products need plenty of distilled water to completely remove impurities, which further complicates the synthesis process and increases the manufacturing cost. Compared with chemical activation, research regarding physical activation on biomass-derived carbon remains much less explored, especially for supercapacitor electrodes [4, 33-38]. Physical activation is generally performed under an atmosphere of $CO_2$, steam or air, which thus avoids the post-process to remove by-products [4].

Herein, we make full use of the principal greenhouse gas (i.e., $CO_2$), as an activating agent to prepare high-value hierarchically porous carbon derived from biomass. The porous carbon was prepared by using starch as a precursor undergoing different processes including expansion, drying and carbonization as well as the final $CO_2$ activation. The reaction mechanism was investigated by in-situ thermogravimetric analysis (TGA) and real-time Fourier-transform infrared spectroscopy (FTIR). The as-prepared samples were characterized by $N_2$ physisorption, X-ray diffraction (XRD), Raman spectroscopy, scanning electron microscopy (SEM) and transmission electron microscopy (TEM). The as-prepared materials were further used in aqueous zinc-ion hybrid supercapacitors, exhibiting a high specific capacitance of 259 F $g^{-1}$ at a current density of 0.5 A $g^{-1}$ and high rate capability (160 F $g^{-1}$ at 30 A $g^{-1}$) due to the high specific surface area and optimal pore structure. Additionally, the device showed excellent cycling stability with 97% capacity retention after 10000 cycles. A high energy density of 94.1 Wh $kg^{-1}$ was achieved at a power density of 399 W $kg^{-1}$ (58.5 Wh $kg^{-1}$ at 24.5 kW $kg^{-1}$) based on the mass of active materials. The combination of sustainable electrode materials with a safe and environmentally friendly energy storage device is expected to provide alternative solutions to the growing environmental concerns and increasing energy demand.

## *Results and discussion*

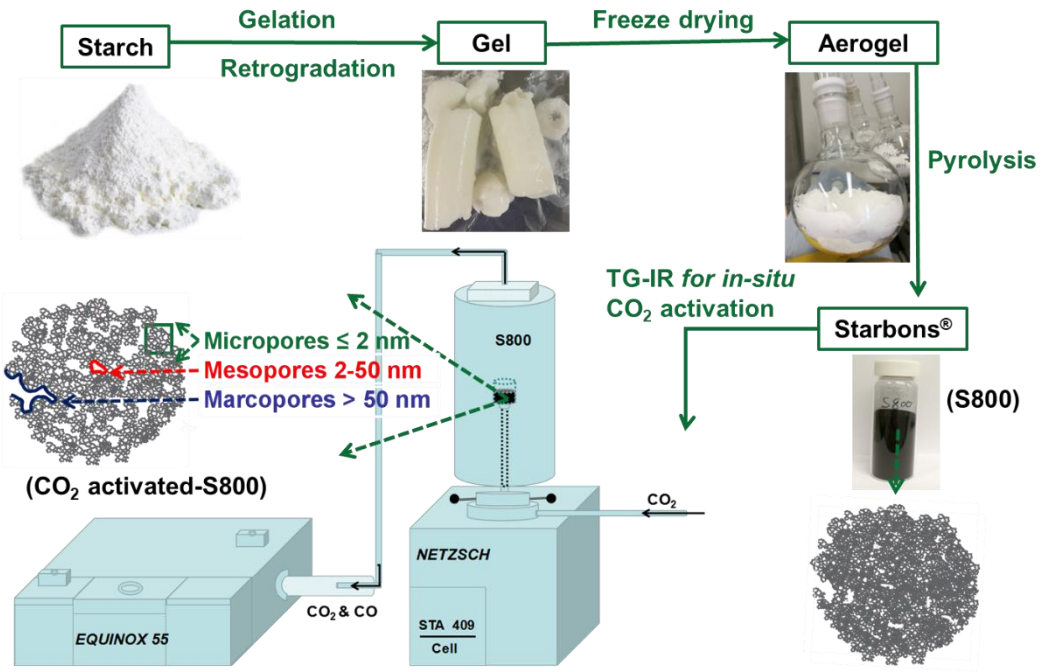


**Figure 6.1.** The overall process for synthesis of hierarchical porous carbon by $CO_2$ activation using starch as precursor.

### 1. $CO_2$ activation mechanism of HPC

High temperature is required for the $CO_2$ activation process to etch carbon atoms due to the endothermic character of the activation reaction. The corresponding reaction can be described as follows:

$$C\,(s) + CO_2\,(g) \rightarrow 2\,CO\,(g) \qquad (6.1)$$

The product CO can be further used as fuel to generate heat and regenerate $CO_2$, thus realizing the repeated utilization of $CO_2$. To better understand the reaction, the burn-off (wt%) of the reactant was monitored by TGA and the real-time compositions of the resultant gases were analysed by for FTIR during the activation process. From the thermogravimetric curve shown in Figure 6.1a, the reduction of mass at the initial stage of heating (temperature below 150 °C) can be ascribed to the loss of water and carbon

dioxide absorbed by the precursor. The sample starts to obviously lose weight with the temperature further increasing to about 600 °C, indicating the initial reaction temperature for $CO_2$ activation. As shown in Figure 6.1b, with the duration time increasing to 90 minutes, the yield of the product would significantly decrease from 100 % to 29.12 % due to the consumption of the precursor. If the reaction time was long enough, the precursor would be totally consumed. Therefore, it is important to balance the yield and specific surface area of the obtained products.

From infrared spectroscopy shown in Figure 6.1c, the peaks located at 2114 $cm^{-1}$ and 2173 $cm^{-1}$ can be ascribed to CO stretching vibrations [39]. As the reaction proceeds, the signal intensity due to CO strengthens since the higher temperature can accelerate the reaction rate. The CO signal is first detected after 3400 s, which is consistent with the time at which the sample starts to react with $CO_2$. From the TGA and FTIR results, we can determine the initial reaction temperature for $CO_2$ activation is about 600 °C.

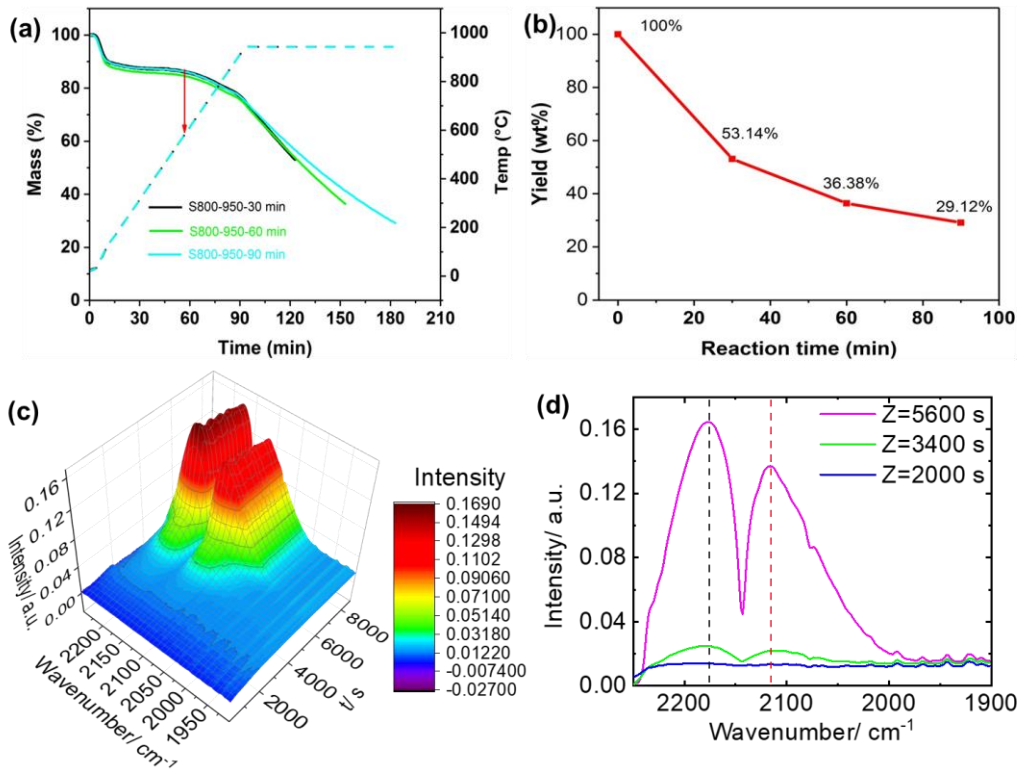


**Figure 6.2. (a)** in-situ TGA of different activation time, **(b)** sample yield as a function of the activation time, **(c)** real-time FTIR, **(d)** IR spectra at different time.

## 2. Characterization of the HPC

The nitrogen adsorption-desorption isotherms of the prepared samples are presented in Figure 6.2a. According to the International Union of Pure and Applied Chemistry (IUPAC) classification, the isotherms of the four samples can be classified as type IV [40]. An initial sharp increase in the adsorption curve is observed at very low relative pressures ($P/P_0 < 0.05$), suggesting the presence of a large amount of micropores (<2 nm) in the samples. As the relative pressure increases, the isotherms display a hysteresis loop in the relative pressure from 0.8 to 1, suggesting that capillary condensation take places in mesopores (2-50 nm). Compared with S800 (detailed information shown in the Experimental), the adsorption volumes of the $CO_2$ activated samples (S800-950-30min, S800-950-60min, S800-950-90min) dramatically increase, indicating a significant increase in specific surface area after activation. It is noted that the adsorption volume shows an increase trend as the activation time increases. The pore size distributions (PSD) using a slit-pore model based on non-local density functional theory (NLDFT) [41] are shown in Figure 6.2b. The PSD of S800 is found to be 0.5 nm to 2 nm. After activation, the pore size distribution has expanded to 6 nm with pronounced increase in mesopores, leading to the formation of hierarchically porous carbon materials. The corresponding BET specific surface areas of the samples are calculated to be 722 $m^2 g^{-1}$, 1618 $m^2 g^{-1}$, 2180 $m^2 g^{-1}$, and 2457 $m^2 g^{-1}$, respectively. Generally, the high specific surface area can provide more active sites for charge storage, thus enhancing the electrochemical performance. The BET specific surface areas and specific pore parameters of the samples are summarized in Table S1. The specific surface areas increase as the activation time increases. This increase may be attributed to the fact that, during the activation process, $CO_2$ initially react with the precursor to produce micropores on the surface. With further reaction, more micropores would be created and the adjacent micropores previously created are connected to produce mesopores, giving rise to the formation of hierarchically porous structure. This can be confirmed by the increased pore volume as the activation time further increases. It is believed that the relatively high specific surface area can provide more accessible sites

for ions adsorption, thus leading to high electrical double layer capacitance. Basically, hierarchical architecture of porous materials is expected to maximize the structural features of different pores. The presence of micropores enables a relatively high surface area for reversible adsorption/desorption of electrolyte ions, while the mesopores facilitate the penetration and transport of electrolyte ions [21, 22]. Therefore, the hierarchical pores of the as-prepared samples should be advantageous in achieving high electrochemical perform for energy storage.

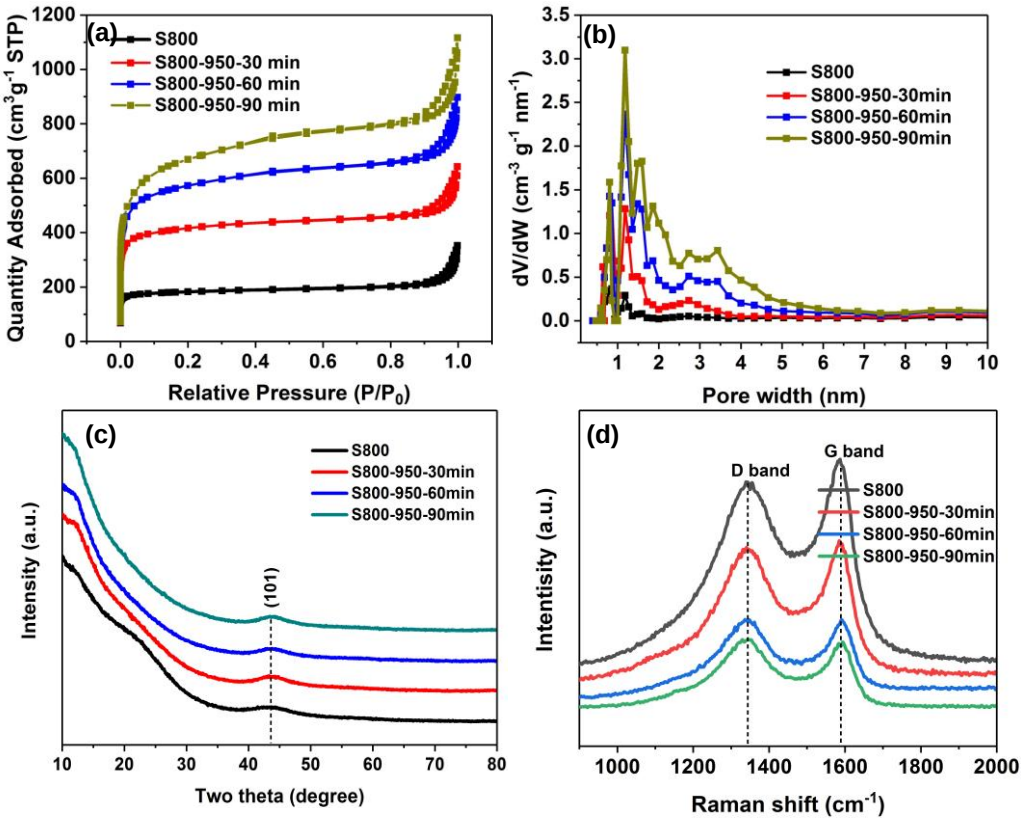


**Figure 6.3.** Characterization of the samples: **(a)** Nitrogen adsorption-desorption isotherms, **(b)** Pore size distributions, **(c)** XRD patterns and **(d)** Raman spectra.

As shown in Figure 6.2c, the structure of the four samples was characterized by using x-ray diffraction (XRD). No distinct peaks can be observed in the samples, suggesting their structure is highly amorphous. A weak and broad peak at about 43.2° can be assigned to the (101) planes of the graphitic carbon, indicating a low degree of graphitization and crystallinity due to the defects in the amorphous samples [42]. The absence of (002) peak further confirms the highly amorphous structure of the as-

prepared samples. The defective nature of the samples was further investigated by Raman spectroscopy in Figure 6.2d. There are two broad bands located at around 1348 $cm^{-1}$ (D-band) and 1589 $cm^{-1}$ (G-band), respectively. The D-band is caused by the breathing mode vibration of carbon 6-fold ring at the free edges and the G-band can be ascribed to the in-plane stretching mode vibration [43, 44]. The intensity ratio of these bands ($I_D/I_G$) is generally employed as an indication of defects in carbon materials. The $I_D/I_G$ values of S800, S800-950-30min, S800-950-60min, S800-950-90min were calculated to be 0.90, 0.96, 1.01, 1.05, respectively. The relatively high ratios of $I_D/I_G$ are consistent with a highly disordered structure in all the samples, which can be attributed to the abundant defects existing in the carbon materials.

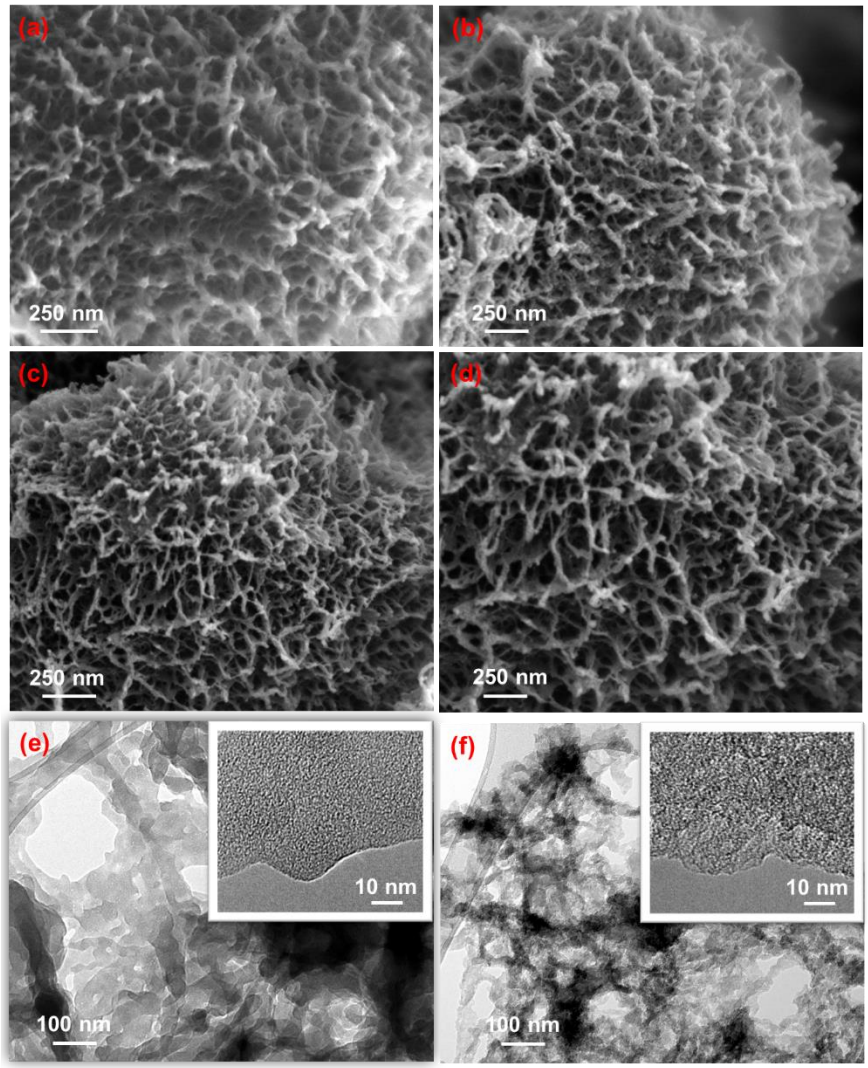


**Figure 6.4.** Morphololology characterization. SEM images of **(a)** S800, **(b)** S800-950-

30min, **(c)** S800-950-60min and **(d)** S800-950-90min; TEM images of **(e)** S800 and **(f)** S800-950-90min.

The morphology and microstructure of the samples were observed by scanning electron microscopy (SEM) and transmission electron microscopy (TEM). The typical SEM images of the four samples are shown in Figure 6.3(a-d). All the investigated samples show a rough surface with abundant macropores and mesopores. Compared with S800, the samples exhibit a highly porous structure after activation. The samples consist of a hollow interconnected network constructed by nanorods, which would facilitate the penetration and transport of electrolyte, thereby improving the accessible active sites and boosting the rate performance. The morphology and structural characteristics were further investigated by TEM images, shown in Figure 6.3(e-f). Sample S800 and S800-950-90min shows a porous structure. The pore size revealed by TEM images seems to be a lot larger than that predicted by BET isotherm, since some larger pores are constructed by the gap among different small particles which cannot be well reflected by the gas probe in gas adsorption/desorption measurement. The high-resolution TEM images further reveal the amorphous structure due to numerous of micropores and mesopores.

### 3. Electrochemical measurement

It is widely accepted that the energy density of a supercapacitor is dependent on the specific capacitance of the active material and the square of the cell voltage [45, 46]. Therefore, expanding the operating voltage is considered as a more effective approach to increase the energy density compared with increasing the specific capacitance. It is generally recognized that the stable potential window is highly dependent on the properties of the chosen electrolytes. The operating voltage of alkaline and acidic aqueous electrolytes is restricted to 1.2 V due to thermodynamics of the hydrogen and oxygen evolution reactions, while the stable potential window of organic electrolytes can be expanded to 2.5-2.7 V [47, 48]. However, organic electrolytes are toxic and flammable as well as sensitive to moisture. Ionic liquids have a much wider electrochemical stability window ranging from 2 to 6 V (typically about 4.5 V), high

thermal stability, low flammability and low vapour pressure [49], but their high viscosity means their conductivity is usually low [47]. Therefore, neutral aqueous electrolytes are regarded as promising electrolytes due to the relatively wide stability window (up to 2 V), high conductivity, low cost, high safety and environmental benignity. The extended operation window in neutral aqueous electrolytes can be attributed to the strong interaction between ions and water molecules, which increase the overpotential for the decomposition of water [50]. The operating voltage is a key parameter of hybrid supercapacitors since it directly determines the electrochemical performance of the device in terms of power density, energy density and lifetime. Therefore, the operating cell voltage was first investigated by cyclic voltammetry (CV) and galvanostatic charge-discharge (GCD) measurement.

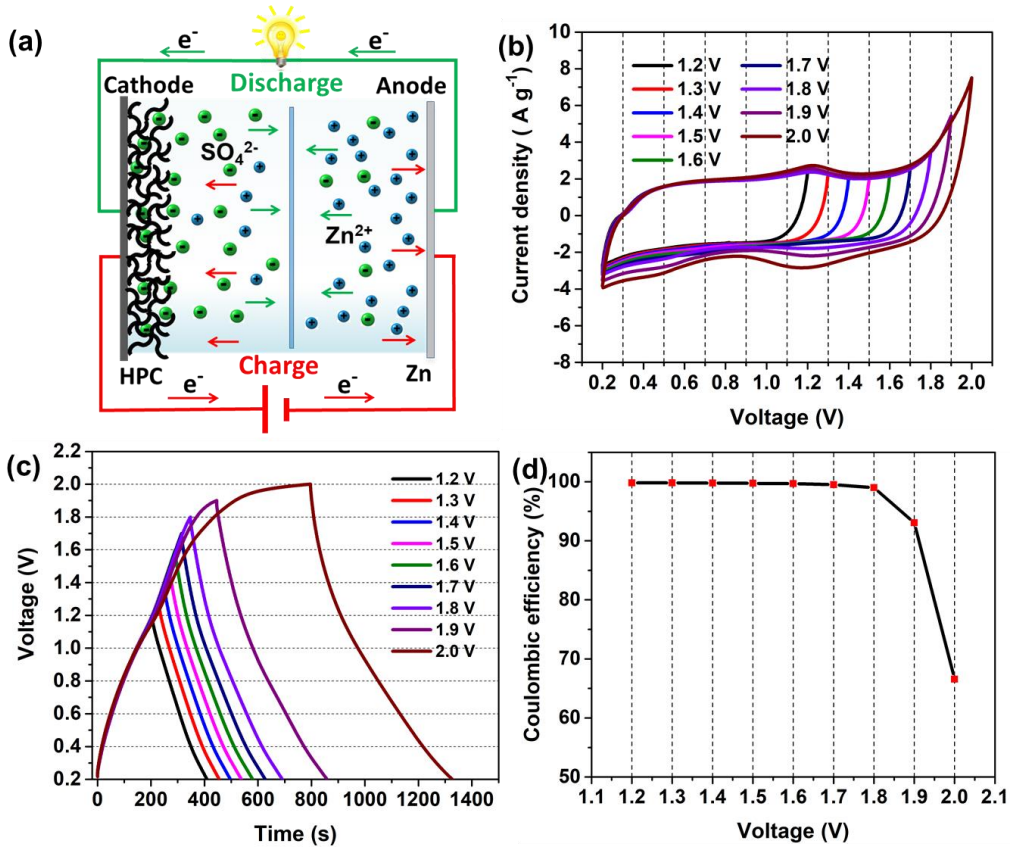


**Figure 6.5. (a)** Schematic diagram of HPC//2 M $ZnSO_4$ (aq)//Zn hybrid supercapacitor, **(b)** Cyclic voltammograms (10 mV $s^{-1}$) with stepwise increasing cell voltage, **(c)** Galvanostatic charge/discharge (GCD) profiles with stepwise increasing cell voltage, and **(d)** Coulombic efficiency based on GCD profiles.

To investigate the electrochemical performance of the samples, zinc ion hybrid supercapacitors were assembled in CR2032 coin cells with the HPC electrode as cathode, zinc foil as anode, 2 M $ZnSO_4$ as electrolyte and a cellulose membrane as separator, as schematically depicted in Figure 6.4a. Considering that both the $Zn^{2+}$ deposition and hydrogen evolution reactions can occur at the relatively low potential versus $Zn^{2+}$/Zn electrode, the starting potential is selected to be 0.2 V (vs. $Zn^{2+}$/Zn) based on our previous work [51]. CV was first performed by stepwise increasing cell voltage to determine the stable electrochemical window at 10 mV $s^{-1}$, shown in Figure 6.4b. The CV still maintain a quasi-rectangular shape without steep increase in the anodic current as the upper voltage is stepwise increased to 1.8 V from 1.2 V. However, when the upper cut-off voltage is further expanded to 2.0 V, a significant increase in anodic current can be observed probably due to the oxidation of the carbon surface functional group or carbon bulk [52, 53]. It is also noted that there are redox humps located at around 1.2 V, which can be attributed to the redox reaction of quinone-hydroquinone on the carbon surface [52, 54]. In view of abundant defects present in the porous carbon materials, they are easily to be electro-oxidized to form surface oxides such as carbonyl and carboxyl and even gaseous products (e.g., CO and $CO_2$) at high potentials [53]. The occurrence of carbon corrosion at high operating potential is detrimental to the long-term performance of the devices. According to the CV results, the stable potential window based on the HPC (S800-950-90min) electrode was preliminarily selected to vary from 0.2 V to 1.8 V in 2 M $ZnSO_4$ aqueous electrolyte. As shown in Figure 6.4c, the electrochemical window was also determined by the GCD technique. When the upper limit voltage is in the range from 1.2 V to 1.8 V, the GCD curves show a nearly triangular shape with good symmetry, suggesting a typical capacitor behaviour and efficient charge storage. However, as the upper cut-off voltage is further expanded to 2.0 V, an approximate plateau can be observed at the top of charging curve due to the oxidation of carbon surface functional group or carbon bulk. The input charge is consumed by the side reaction, thus distorting the linear shape of the charging curve and breaking the symmetry of GCD profile. It is well known that

coulombic efficiency is a key indicator of energy devices for evaluating the stability. Consequently, the corresponding coulombic efficiency was calculated as a quantitative index to determine the stable potential window. As show in Figure 6.4d, when the upper cut-off voltage varies from 1.2 V to 1.8 V, the coulombic efficiency is almost 100%, indicating an ideal reversibility of energy storage. When the cut-off voltage is increased to 1.9 V, the corresponding coulombic efficiency falls to 93%. As it is further increased to 2.0 V, the coulombic efficiency dramatically decreases to 65%, indicating inefficient energy storage. The GCD results are therefore consistent with the CV measurements. The operating voltage window is determined to vary from 0.2 V to 1.8 V in 2 M $ZnSO_4$ aqueous electrolyte. The expanded window in this neutral aqueous electrolyte can be ascribed to the strong hydration between the electrolyte ions (i.e., zinc ions and sulfate ions) with water molecules, which is able to reduce the activity of $H_2O$ and thus expand the operating window of aqueous electrolytes [55-57]. Such an effect can be more pronounced in aqueous electrolytes with super-concentrated ions [57, 58].

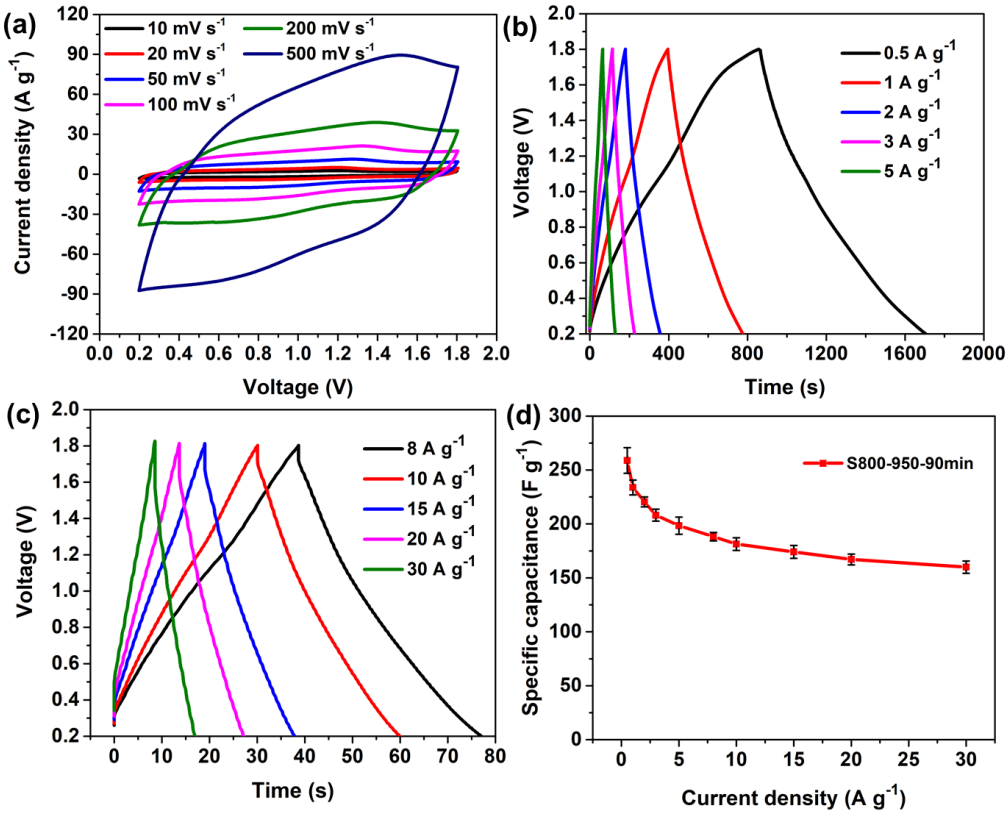


**Figure 6.6.** Electrochemical behaviors of the sample S800-950-90min: **(a)** CV curves

at various scanning rates, **(b-c)** GCD profiles at various current densities, and **(d)** Specific capacitances at different current densities.

The electrochemical performance of the zinc ion hybrid supercapacitors based on HPC electrode was comprehensively studied by CV and GCD methods within the stable voltage range of 0.2 V to 1.8 V, established above. As shown in Figure 6.5a, the CV profiles based on S800-950-90min sample were obtained at various scan rates between 10 mV $s^{-1}$ and 500 mV $s^{-1}$, exhibiting near-rectangular shapes without well-defined redox peaks. The CV obtained at a high scan rate of 500 mV $s^{-1}$ still maintains a quasi-rectangular shape with slight distortion, suggesting good rate performance of zinc ion hybrid supercapacitors using HPC electrode as cathode. The mechanism of the zinc ion hybrid supercapacitor is based on the reversible ion adsorption/desorption on the HPC cathode and plating/stripping of $Zn^{2+}$ ions on the Zn anode [15, 51]. GCD profiles of the zinc ion hybrid supercapacitors at various current densities are shown in Figure 6.5(b-c). The shapes of the GCD curves are nearly symmetric and linear without charge/discharge plateau, indicating a typical supercapacitor behaviour. The corresponding rate performance is shown in Figure 6.5d. It exhibits a high specific capacitance of 259 F $g^{-1}$ at a current density of 0.5 A $g^{-1}$. When the current density is further increased to 30 A $g^{-1}$, a high specific capacitance of 160 F $g^{-1}$ is maintained, indicating excellent rate capability with a high capacitance retention of 62%.

The comparison of specific capacitance of different samples is shown in Figure 6.6a. It is noted that sample S800-950-90min shows the highest specific capacitance of 259 F $g^{-1}$ among the samples (160 F $g^{-1}$ for S800, 197 F $g^{-1}$ for S800-950-30min, 229 F $g^{-1}$ for S800-950-60min) at 0.5 A $g^{-1}$ since the electrical double-layer capacitance is highly dependent on the accessible surface area. All the specific capacitances show a downward trend with increasing the current density owing to the sluggish mass transport. As the current density is further increased to 30 A $g^{-1}$, the capacitance retention is about 23%, 58%, 63% and 62% for S800, S800-950-30min, S800-950-60min and S800-950-90min, respectively. The evolution of the retention can be ascribed to the different pore architectures of the samples. The carbon materials

containing abundant micropores usually suffer from poor rate capability because of slow mass transport within the micropores [14, 19, 20]. After activation, more mesopores were introduced to texture of the carbon materials, which would facilitate the electrolyte transport and improve the rate capability.

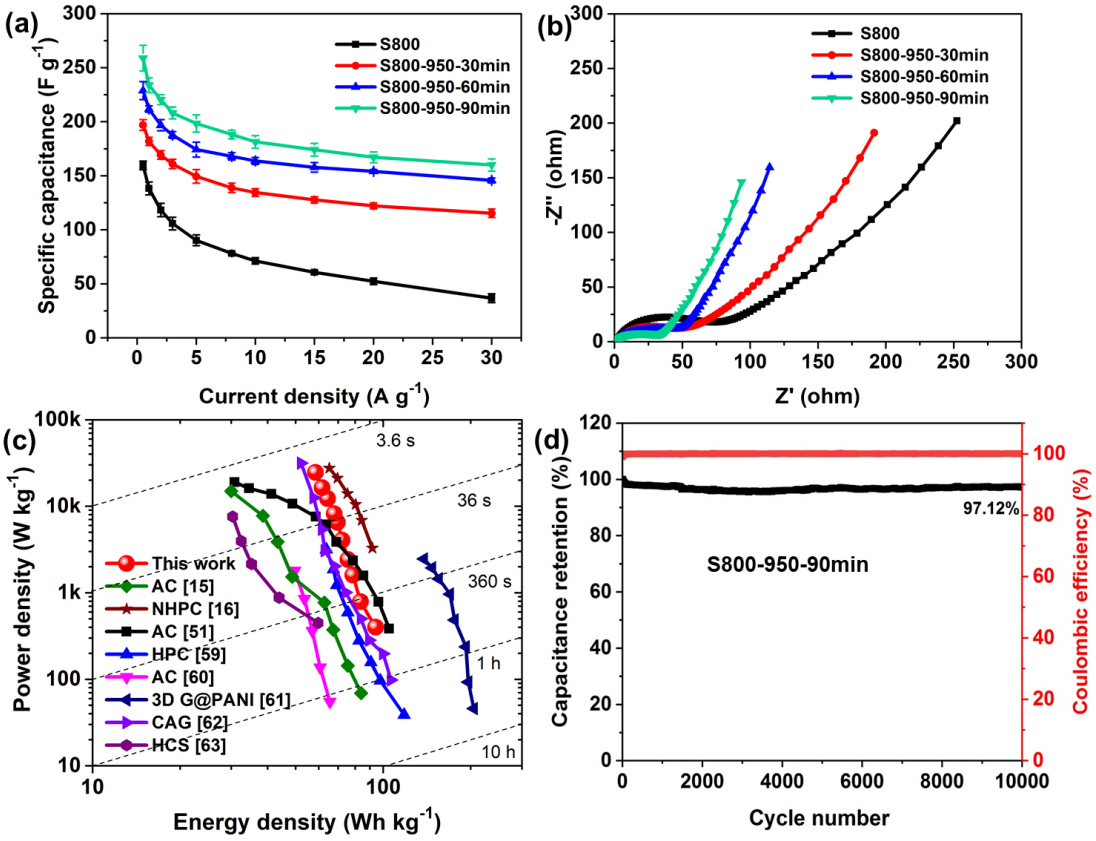


**Figure 6.7. (a)** Specific capacitances of different samples as a function of current density, **(b)** Nyquist plots, **(c)** Ragone plots of zinc-ion hybrid supercapacitors based on mass of active materials (AC represents activated carbon, NHPC represents N-doped hierarchically porous carbon, HPC represents hierarchical porous carbon, 3D G@PANI represents 3D graphene@ polyaniline composite, CAG represents chemical activated graphene, and HCS represents hollow carbon sphere.), and **(d)** Cycling stability of zinc-ion hybrid supercapacitors based on S800-950-90min sample at a current density of 5 A $g^{-1}$.

The kinetics of charge and ion transport were further investigated by electrochemical impedance spectroscopy (EIS). Figure 6.6b shows the Nyquist plots of zinc ion hybrid

supercapacitors based on different samples. All the Nyquist plots show a semicircle at the mid-high frequency region and a slanted line at the low frequency region. The equivalent series resistance (the real axis intercept) is about 1.43 Ω (S800), 1.29 Ω (S800-950-30min), 1.30 Ω (S800-950-60min), and 1.32 Ω (S800-950-90min). The small values of the intercept indicate good electrical conductivity of the samples. The diameters of the semicircles arrange in the order of S800 > S800-950-30min > S800-950-60min> S800-950-90min, which means S800-950-90min possesses the smallest charge transfer resistance of the four samples. The slope of straight lines at low frequency can be ascribed to the diffusion resistance known as Warburg impedance. If the straight line is more inclined to Y axis, it indicates less Warburg impedance and better diffusion. From the slope, the diffusion resistance is sequenced as S800 > S800-950-30min > S800-950-60min > S800-950-90min, which indicates the effectiveness of hierarchically porous structures in boosting mass transport.

The energy and power densities were calculated based on the weight of active material, shown in Figure 6.6c. The maximum energy density up to 94.1 Wh $kg^{-1}$ was obtained at a power density of 0.5 kW $kg^{-1}$ and the maximum power density of 24.5 kW $kg^{-1}$ was achieved at an energy density of 58.5 Wh $kg^{-1}$. The excellent performance surpasses those of most reported Zn-based energy storage devices [15, 16, 51, 59-63], shown in Figure 6.6c. Stability is one of the key parameters for the practical application of supercapacitors. The cycling stability of this hybrid supercapacitor based on sample S800-950-90min was measured at a current density of 5 A $g^{-1}$, shown in Figure 6.6d. The device has demonstrated excellent stability with a high capacitance retention of about 97% along with a high coulombic efficiency close to 100% after 10000 cycles. The as-prepared hierarchically porous carbon has demonstrated great promise in its applications in aqueous zinc-ion hybrid supercapacitors.

## *Conclusions*

In summary, hierarchically porous carbon as cathode for zinc-ion hybrid supercapacitors have been prepared via $CO_2$ activation by using starch as precursor. The specific surface area and pore structure of the as-prepared materials can be tuned by the activation time. The optimized porous carbon possesses hierarchical porous nanostructure with proper porosity, high specific surface area (2457 $m^2\ g^{-1}$) and pore volume (1.64 $cm^3\ g^{-1}$). The resultant zinc ion hybrid supercapacitors operate in a voltage range from 0.2 V to 1.8 V, delivering a high capacitance of 259 F $g^{-1}$ at a current density of 0.5 A $g^{-1}$, a high energy density of 94.1 Wh $kg^{-1}$ at 399 W $kg^{-1}$ as well as a high power density of 24.5 kW $kg^{-1}$ at 58.5 Wh $kg^{-1}$. It also exhibits excellent cycling stability with 97% capacitance retention after 10000 cycles. The excellent electrochemical performance can be attributed to the high specific surface area and well-combined micropores/mesopores within the texture, thus providing effective surface sites and facilitating high rate performance. Since this energy storage device uses nontoxic electrode materials and aqueous electrolyte, it can potentially resolve the safety concerns and environmental issues associated with organic-based energy storage. Moreover, abundant biomass resources can effectively reduce the cost of the electrode materials and further reduce the cost of the final devices, thereby facilitating the wide application of this device to harvest renewable and green energy. Considering the facile, green and cost-effective synthesis, it also provides various potential applications such as adsorbent, catalyst support or gas storage.

## *Experimental*

### Materials preparation

(1) Synthesis of Starbons® by using freeze drying method

The synthesis process is composed of three steps including expansion, drying and then carbonization. Firstly, starch (Hylon VII, National starch & Chemical Ltd, UK) is gelatinized by microwave heating in water (9.1 wt%) at 140 °C and subsequently cooled down to 5 °C for 48 h for retrogradation to yield a porous gel [64]. Secondly, 30 wt% of tert-butanol (99% purity, Fluka Analytical) and 5 wt% of organic acid p-

toluenesulfonic acid (98% purity, Alfa Aesar), relative to the weight of starch, was added to the porous gel following the procedure previously reported [64], followed by overnight stirring at room temperature. Then the obtained gel was frozen with liquid nitrogen and freeze dried for more than 24 h until the dry expanded-starch powder was obtained. The resulting power was finally carbonized by heating at 800 °C under vacuum which is called Starbons® and denoted as S800 for brevity.

(2) $CO_2$ activation of Starbons®

$CO_2$ activation was carried out in a Thermogravimetric Analyzer (TGA, NETZSCH STA 409) coupled with Fourier-transform infrared spectroscopy (FT-IR, Bruker Equinox 55). The burn-off wt% of the reactant was monitored by TGA and the real-time composition of resultant gases from the carbon-$CO_2$ reaction were analyzed using FT-IR during the activation process. S800 was subjected to pure $CO_2$ flow and heated from room temperature up 950 °C at a heating rate of 10 °C $min^{-1}$ and $CO_2$ flow rate of 50 $cm^3$ $min^{-1}$. Then the maximum temperature was maintained for different periods of time (30 minutes, 60 minutes, 90 minutes). At the end of the activation period, the sample was cooled under $CO_2$. The final products are denoted as S800-950-30min, S800-950-60min and S800-950-90min, respectively. The overall synthesis process of hierarchically porous carbon from starch via $CO_2$ activation is depicted in Figure 6.1.

**Materials characterization**

Nitrogen physisorption analysis at 77 K was carried out on Micromeritics TriStar II Plus to characterize the surface area and pore structure of the samples. The surface area was evaluated by using the Brunauer-Emmett-Teller (BET) model and the corresponding pore size distribution was derived by a non-local density functional theory (NLDFT) model [41]. The morphology was observed using scanning electron microscopy (SEM, ZEISS Supra 55) with an acceleration voltage of 5 kV and transmission electron microscopy (TEM, FEI Tecnai G2 F30) operating at 200 kV. SEM samples were placed on conductive carbon tapes to reduce the charging effect during the imaging process while TEM samples were prepared by drop-casting the corresponding diluted suspensions onto copper grids supported by carbon film. Powder

X-ray diffraction (XRD) data was collected on a Bruker D8 Advance powder diffractometer with Cu-Kα radiation (λ= 1.54 Å) operating at 40 kV. Raman spectra were collected using a Horiba modular Raman system with a wavelength of 532 nm.

**Electrochemical measurement**

Briefly, the working electrode consists of the active materials, binder polytetrafluoroethylene (PTFE, 60 wt% dispersion in $H_2O$ purchased from Sigma Aldrich) and conductive carbon (Super-P, purchased from Alfa Aesar) in a weight ratio of 80:10:10, respectively. The components were fully mixed and ground into a paste in a mortar by adding isopropanol (>99%, purchased from Fisher Chemical) as solvent. Afterwards, the paste was rolled into sheets with thickness of about 60-70 μm and cut into 1 cm × 1 cm pieces. The free-standing samples were dried at 100 °C for 12 h under vacuum to remove solvent. The mass loading of the active materials varied from 1 to 2 mg $cm^{-2}$. The electrochemical tests were performed in a CR2032 coin-cell type device with the porous carbon electrode as cathode, zinc metal (15 mm diameter, ~191 mg) as anode, 2 M $ZnSO_4$ aqueous solution as electrolyte and a cellulose membrane as separator. The cyclic voltammetry (CV) measurement and electrochemical impedance spectroscopy (EIS) tests were performed on an Autolab Potentiostat (PGSTAT320N). The EIS data were collected with an AC amplitude of 5 mV in the frequency range of 0.01 Hz–100 kHz under open circuit voltage conditions. The galvanostatic charge–discharge (GCD) measurement was carried out on a Battery Test System (BaSyTec, Germany). All the electrochemical tests were carried out at room temperature.

The specific capacitance (C) was calculated from the discharge curve by using the following equation:

$$C = \frac{I\Delta t}{m\Delta V} \qquad (6.2)$$

where $I$ is the current, $\Delta t$ represents the discharge time, $\Delta V$ is the potential window and $m$ is the mass loading of the active material.

The energy density (*E*) and power density (*P*) were calculated from the following equations:

$$E = \int_0^{\Delta t} V(t) I dt \qquad (6.3)$$

$$P = \frac{E}{\Delta t} \qquad (6.4)$$

where *Δt* is the discharge time, *V(t)* is the voltage and *I* is the current density.

## *Conflicts of interest*

There are no conflicts to declare.

## *Acknowledgements*

Jie Yang acknowledges the University of Manchester for the President's Doctoral Scholarship Award.

## *References*

[1] Z. Bi, Q. Kong, Y. Cao, G. Sun, F. Su, X. Wei, X. Li, A. Ahmad, L. Xie, C.-M. Chen, J. Mater. Chem. A, 7 (2019) 16028-16045.

[2] P.A. Owusu, S. Asumadu-Sarkodie, S. Dubey, Cogent Eng., 3 (2016) 1167990.

[3] T.M. Gür, Energy Environ. Sci., 11 (2018) 2696-2767.

[4] H. Lu, X.S. Zhao, Sustain. Energy Fuels, 1 (2017) 1265-1281.

[5] D.R. Battlebury, J. Power Sources, 80 (1999) 7-11.

[6] A.K. Shukla, S. Venugopalan, B. Hariprakash, J. Power Sources, 100 (2001) 125-148.

[7] J.Y. Luo, Y.Y. Xia, Adv. Funct. Mater., 17 (2007) 3877-3884.

[8] K.-h. Young, S. Yasuoka, Batteries, 2 (2016) 3.

[9] M. Winter, R.J. Brodd, Chem. Rev., 104 (2004) 4245-4270.

[10] J.B. Goodenough, Energy Environ. Sci., 7 (2014) 14-18.

[11] J.-M. Tarascon, M. Armand, Nature, 414 (2001) 359-367.

[12] C.P. Grey, J.M. Tarascon, Nat. Mater., 16 (2016) 45-56.

[13] P. Simon, Y. Gogotsi, Nat. Mater., 7 (2008) 845-854.

[14] J. Yang, H. Wu, M. Zhu, W. Ren, Y. Lin, H. Chen, F. Pan, Nano Energy, 33 (2017) 453-461.

[15] L. Dong, X. Ma, Y. Li, L. Zhao, W. Liu, J. Cheng, C. Xu, B. Li, Q.-H. Yang, F. Kang, Energy Stor. Mater., 13 (2018) 96-102.

[16] H. Zhang, Q. Liu, Y. Fang, C. Teng, X. Liu, P. Fang, Y. Tong, X. Lu, Adv. Mater., 31 (2019) 1904948.

[17] J. Wang, P. Nie, B. Ding, S. Dong, X. Hao, H. Dou, X. Zhang, J. Mater. Chem. A, 5 (2017) 2411-2428.

[18] X. Deng, J. Li, L. Ma, J. Sha, N. Zhao, Mater. Chem. Front., 3 (2019) 2221-2245.

[19] J. Yang, J. Hu, M. Zhu, Y. Zhao, H. Chen, F. Pan, J. Power Sources, 365 (2017) 362-371.

[20] L. Qie, W. Chen, H. Xu, X. Xiong, Y. Jiang, F. Zou, X. Hu, Y. Xin, Z. Zhang, Y. Huang, Energy Environ. Sci., 6 (2013) 2497.

[21] Y. Gong, Z. Wei, J. Wang, P. Zhang, H. Li, Y. Wang, Sci. Rep., 4 (2014) 6349.

[22] Q. Wang, J. Yan, Y. Wang, T. Wei, M. Zhang, X. Jing, Z. Fan, Carbon, 67 (2014) 119-127.

[23] J.H. Clark, Curr. Opin. Green Sustain. Chem., 8 (2017) 10-13.

[24] J. Hou, C. Cao, X. Ma, F. Idrees, B. Xu, X. Hao, W. Lin, Sci Rep, 4 (2014) 7260.

[25] Q.-S. Liu, T. Zheng, P. Wang, L. Guo, Ind Crops Prod., 31 (2010) 233-238.

[26] Y. Jin, K. Tian, L. Wei, X. Zhang, X. Guo, J. Mater. Chem. A, 4 (2016) 15968-15979.

[27] M.M. Titirici, R.J. White, N. Brun, V.L. Budarin, D.S. Su, F. del Monte, J.H. Clark, M.J. MacLachlan, Chem. Soc. Rev., 44 (2015) 250-290.

[28] Z. Gao, Y. Zhang, N. Song, X. Li, Materials Research Letters, 5 (2016) 69-88.

[29] X. Liao, C. Chen, Z. Wang, R. Wan, C.-H. Chang, X. Zhang, S. Xie, Process Biochem., 48 (2013) 312-316.

[30] M. Sevilla, R. Mokaya, Energy Environ. Sci., 7 (2014) 1250-1280.

[31] M. Sevilla, J.A. Maciá-Agulló, A.B. Fuertes, Biomass Bioenergy., 35 (2011) 3152-3159.

[32] N. Balahmar, A.C. Mitchell, R. Mokaya, Adv. Energy Mater., 5 (2015) 1500867.

[33] Y. Yan, J. Wei, F. Zhang, Y. Meng, B. Tu, D. Zhao, Microporous Mesoporous Mater., 113 (2008) 305-314.

[34] J.F. Gonza´lez, S. Roma´n, C.M. Gonza´lez-Garcı´a, J.M.V. Nabais, A.L. Ortiz, Ind. Eng. Chem. Res., 48 (2009) 7474-7481.

[35] T. Zhang, W. Walawender, L. Fan, M. Fan, D. Daugaard, R. Brown, Chem. Eng. J., 105 (2004) 53-59.

[36] J.M. Nabais, J.G. Teixeira, I. Almeida, Bioresour. Technol., 102 (2011) 2781-2787.

[37] A.C. Lua, J. Guo, Carbon, 38 (2000) 1089-1097.

[38] S. Román, J.F. González, C.M. González-García, F. Zamora, Fuel Process. Technol., 89 (2008) 715-720.

[39] JACK W. LONDON, A.T. BELL, J. Catal., 31 (1973) 32-40.

[40] Z. Alothman, Materials, 5 (2012) 2874-2902.

[41] M. Thommes, K. Kaneko, A.V. Neimark, J.P. Olivier, F. Rodriguez-Reinoso, J. Rouquerol, K.S.W. Sing, Pure Appl. Chem., 87 (2015) 1051-1069.

[42] A.C. Lua, T. Yang, J. Colloid Interface Sci., 274 (2004) 594-601.

[43] A.C. Ferrari, J. Robertson, Phys. Rev. B, 61 (2000) 14095-14107.

[44] F. Tuinstra, J.L. Koenig, J. Chem. Phys., 53 (1970) 1126-1130.

[45] V. Khomenko, E. Raymundo-Piñero, F. Béguin, J. Power Sources, 195 (2010) 4234-4241.

[46] B.K. Kim, S. Sy, A. Yu, J. Zhang, Handbook of Clean Energy Systems, (2015) 1-25.

[47] E. Frackowiak, Phys. Chem. Chem. Phys., 9 (2007) 1774-1785.

[48] Q. Gao, L. Demarconnay, E. Raymundo-Piñero, F. Béguin, Energy Environ. Sci., 5 (2012) 9611.

[49] G. Wang, L. Zhang, J. Zhang, Chem. Soc. Rev., 41 (2012) 797-828.

[50] X. Zang, C. Shen, M. Sanghadasa, L. Lin, ChemElectroChem, 6 (2018) 976-988.

[51] J. Yang, M.A. Bissett, R.A.W. Dryfe, ChemSusChem, 14 (2021) 1700-1709.

[52] B. Avasarala, R. Moore, P. Haldar, Electrochim. Acta, 55 (2010) 4765-4771.

[53] M. He, K. Fic, E. Frąckowiak, P. Novák, E.J. Berg, Energy Environ. Sci., 9 (2016) 623-633.

[54] K.H. Kangasniemi, D.A. Condit, T.D. Jarvic, J. Electrochem. Soc., 151 (2004) E125-E132.

[55] K. Fic, G. Lota, M. Meller, E. Frackowiak, Energy Environ. Sci., 5 (2012) 5842-5850.

[56] G. Hasegawa, K. Kanamori, T. Kiyomura, H. Kurata, T. Abe, K. Nakanishi, Chem. Mater., 28 (2016) 3944-3950.

[57] L. Suo, O. Borodin, T. Gao, M. Olguin, J. Ho, X. Fan, C. Luo, C. Wang, K. Xu, Science, 350 (2015) 938-943.

[58] H. Tomiyasu, H. Shikata, K. Takao, N. Asanuma, S. Taruta, Y.Y. Park, Sci. Rep., 7 (2017) 45048.

[59] P. Yu, Y. Zeng, Y. Zeng, H. Dong, H. Hu, Y. Liu, M. Zheng, Y. Xiao, X. Lu, Y. Liang, Electrochim. Acta, 327 (2019) 134999.

[60] H. Wang, M. Wang, Y. Tang, Energy Stor. Mater., 13 (2018) 1-7.

[61] J. Han, K. Wang, W. Liu, C. Li, X. Sun, X. Zhang, Y. An, S. Yi, Y. Ma, Nanoscale, 10 (2018) 13083-13091.

[62] S. Wu, Y. Chen, T. Jiao, J. Zhou, J. Cheng, B. Liu, S. Yang, K. Zhang, W. Zhang, Adv. Energy Mater., 9 (2019) 1902915.

[63] S. Chen, L. Ma, K. Zhang, M. Kamruzzaman, C. Zhi, J.A. Zapien, J. Mater. Chem. A, 7 (2019) 7784-7790.

[64] A. Borisova, M. De Bruyn, V.L. Budarin, P.S. Shuttleworth, J.R. Dodson, M.L. Segatto, J.H. Clark, Macromol. Rapid Commun., 36 (2015) 774-779.

# Supplementary Information

## Hierarchically porous carbon derived from starch via $CO_2$ activation for high performance zinc-ion hybrid supercapacitors

Jie Yang,‡[a,b] Han Li,‡[c] Mark Bissett,[b] and Robert A. W. Dryfe,*[ab] Vitaliy L. Budarin,[c] James H. Clark,[c] Michael North*[c]

[a] Department of Chemistry, University of Manchester, Oxford Road, Manchester, M13 9PL, UK.

[b] National Graphene Institute, University of Manchester, Oxford Road, M13 9PL, UK.

[c] Green Chemistry Centre of Excellence, Department of Chemistry, University of York, Heslington, YO10 5DD, UK.

E-mail: robert.dryfe@manchester.ac.uk

E-mail: michael.north@york.ac.uk

‡These authors contributed equally to this work.

**Table S6.1.** The BET specific surface areas and specific pore parameters of the samples

| | $S_{BET}$ ($m^2g^{-1}$) | $V_{ultramicro}$ ($cm^3g^{-1}$) | $V_{micropore}$ ($cm^3g^{-1}$) | $V_{mesopore}$ ($cm^3g^{-1}$) 2~50nm | $V_{marcopore}$ ($cm^3g^{-1}$) >50nm | $V_{total}$ ($cm^3g^{-1}$) |
|---|---|---|---|---|---|---|
| S800 | 722 | 0.23 | 0.28 | 0.08 | 0.14 | 0.51 |
| S800-950-30 min | 1618 | 0.46 | 0.64 | 0.13 | 0.14 | 0.94 |
| S800-950-60 min | 2180 | 0.55 | 0.89 | 0.26 | 0.17 | 1.32 |
| S800-950-90 min | 2457 | 0.56 | 1.04 | 0.34 | 0.25 | 1.64 |

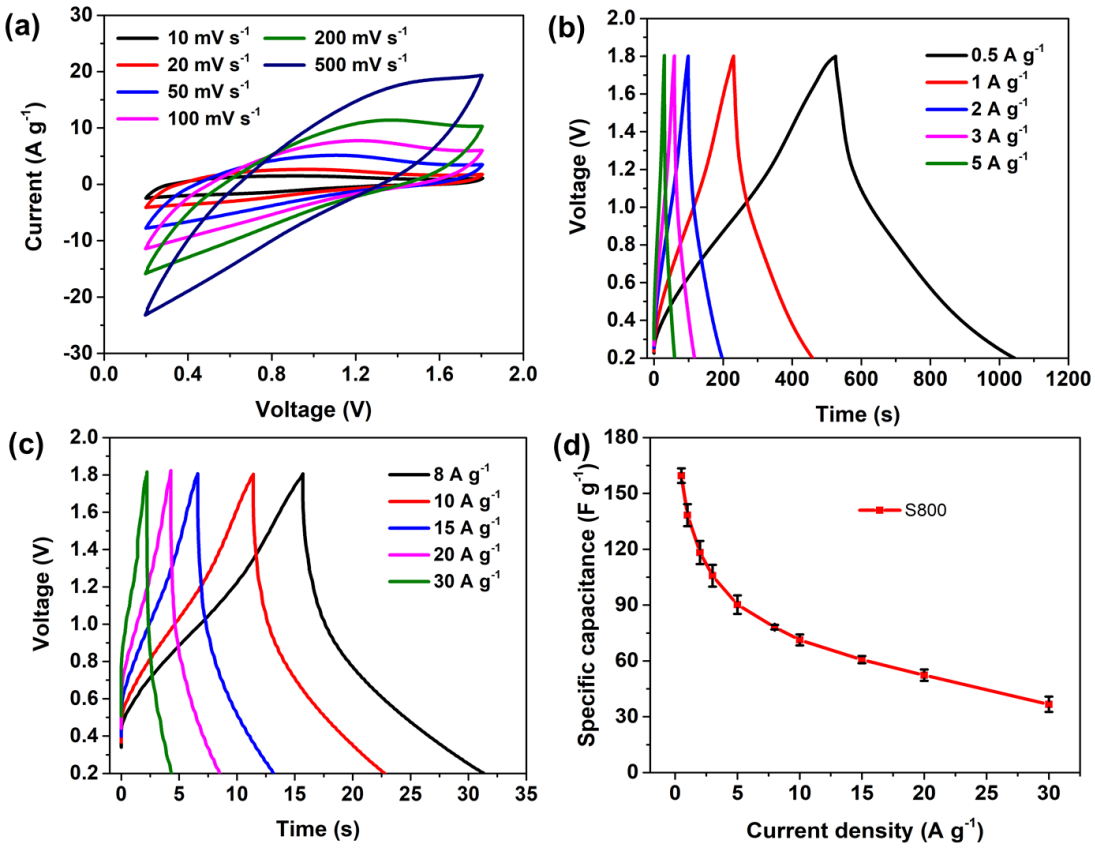


**Figure S6.1.** Electrochemical behaviors of the sample S800: **(a)** CV curves at various scanning rates, **(b-c)** GCD profiles at various current densities, and **(d)** Specific capacitances at different current densities.

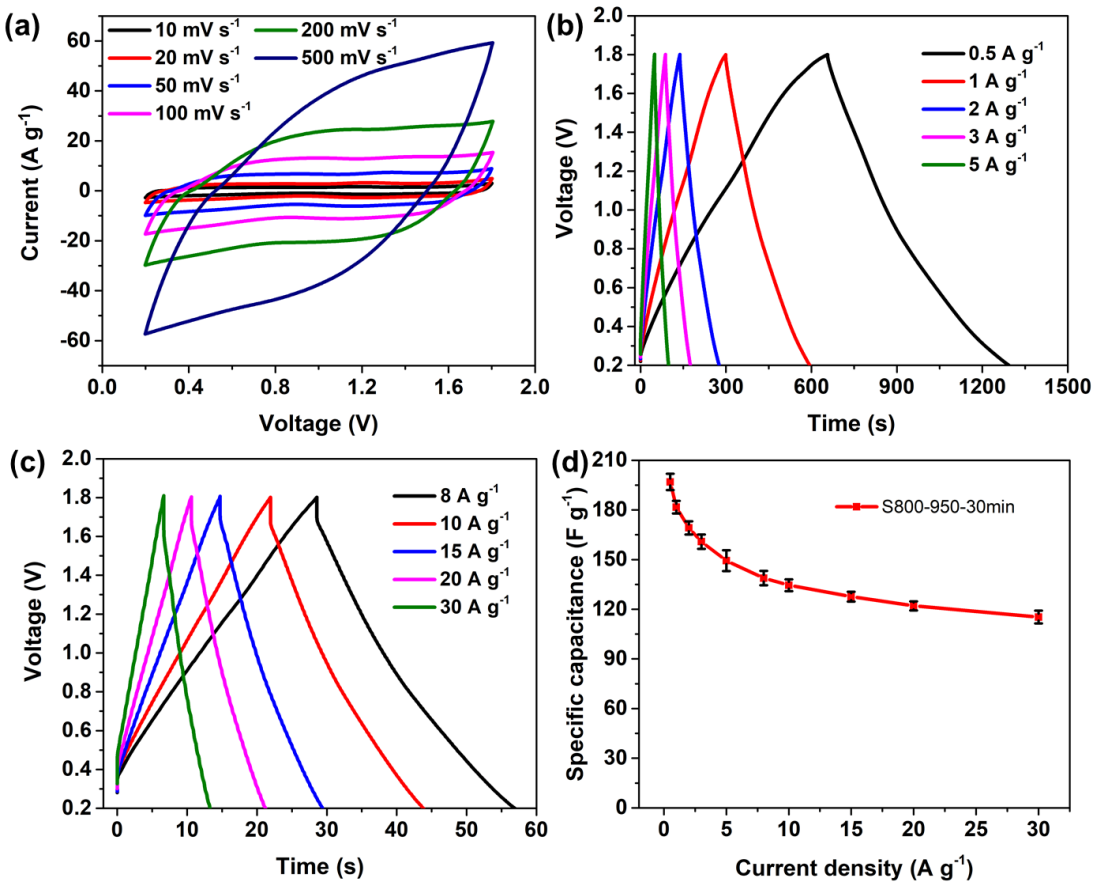


**Figure S6.2.** Electrochemical behaviors of the sample S800-950-30min: **(a)** CV curves at various scanning rates, **(b-c)** GCD profiles at various current densities, and **(d)** Specific capacitances at different current densities.

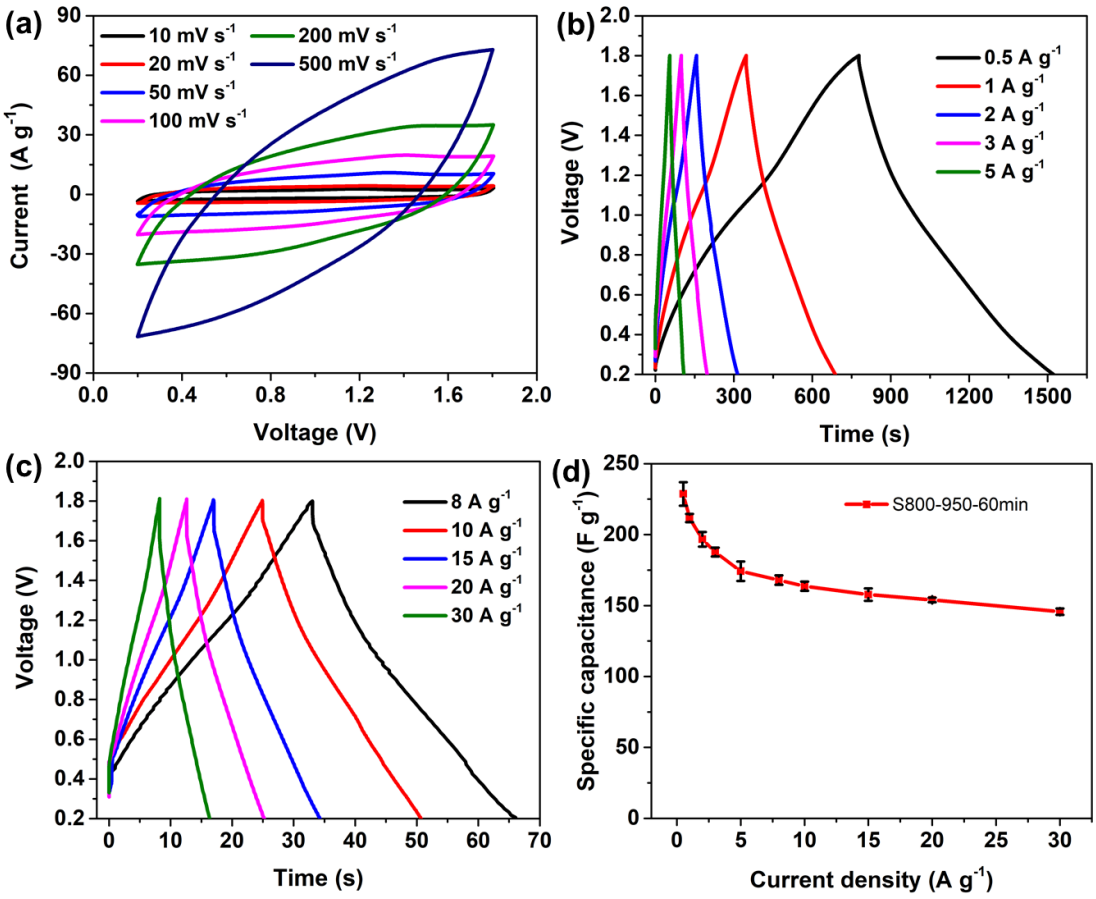


**Figure S6.3.** Electrochemical behaviors of the sample S800-950-60min: **(a)** CV curves at various scanning rates, **(b-c)** GCD profiles at various current densities, and **(d)** Specific capacitances at different current densities.

**Table S6.2.** Comparison with Zn-based energy storage devices

| Carbon Source | Activation Method | Energy storage system (Cathode//Electrolyte//Anode) | Capacity | Operating voltage (V) | Maximum Energy density | Maximum Power density | References |
|---|---|---|---|---|---|---|---|
| Commercial carbon | - | AC// 2 M $ZnSO_4$ (aq.)// Zn | 121 mAh $g^{-1}$ (0.1 A $g^{-1}$) | 0.2-1.8 | 84 Wh $kg^{-1}$ | 14.9 kW $kg^{-1}$ | 1 |
| Coconut shells | KOH | AC//1 M $Zn(CF_3SO_3)_2$ (DME-DOL-AN)//Zn | 170 F $g^{-1}$ (0.1 A $g^{-1}$) | 0-1.8 | 52.7 Wh $kg^{-1}$ | 1725 W $kg^{-1}$ | 2 |
| bagasse and coconut shell | KOH | HPC// 2 M $ZnSO_4$ + 1M $Na_2SO_4$ (aq.) //Zn | 305 mAh $g^{-1}$ (0.1 A $g^{-1}$) | 0.01-1.8 | 118 Wh $kg^{-1}$ | 3158.2 W $kg^{-1}$ | 3 |
| Carbon nanotubes (CNT) | - | CNT// $ZnSO_4$ (aq. or gel.)//Zn | 83.2 mF $cm^{-2}$ (1 mA $cm^{-2}$) | 0.2-1.8 | 29.6 μWh $cm^{-2}$ | 8 mW $cm^{-2}$ | 4 |
| Graphene oxide | KOH | aMEGO//3 M $Zn(CF_3SO_3)_2$ (aq.)//Zn | 210 F $g^{-1}$ (0.1 A $g^{-1}$) | 0-1.9 | 106.3 Wh $kg^{-1}$ | 31.4 kW $kg^{-1}$ | 5 |
| Co-polymer derived hollow carbon spheres | - | carbon// $ZnSO_4$ (gel)//Zn | 86.8 mAh $g^{-1}$ (0.5 A $g^{-1}$) | 0.15-1.95 | 59.7 Wh $kg^{-1}$ | 7573W $kg^{-1}$ | 6 |
| 3D graphene@PANI | - | 3D graphene@PANI//2 M $ZnSO_4$ (aq.)//Zn | 437 F $g^{-1}$ (0.1 A $g^{-1}$) | 0.3-1.6 | 205 Wh $kg^{-1}$ | 2455 W $kg^{-1}$ | 7 |
| $Ti_3C_2$ | - | $Ti_3C_2$//$ZnSO_4$(gel )//Zn | 132 F $g^{-1}$ (0.5 A $g^{-1}$) | 0.1-1.35 | - | - | 8 |
| Chitosan | $KHCO_3$ | N-HPC// $ZnSO_4$ (aq.)//Zn | 136.8 mAh·$g^{-1}$ 0.1 A $g^{-1}$ | 0.2-1.8 | 191 Wh $kg^{-1}$ | 3633.4 W $kg^{-1}$ | 9 |
| N-doped porous carbon | Ammonia | HNPC// $ZnSO_4$ (aq.)//Zn | 177.8 mAh·$g^{-1}$ 4.2 A $g^{-1}$ | 0-1.8 | 107.3 Wh $kg^{-1}$ | 24.9 kW $kg^{-1}$ | 10 |
| Starch | $CO_2$ | HPC// 2 M $ZnSO_4$ (aq.)//Zn | 259 F $g^{-1}$ (0.5 A $g^{-1}$) | 0.2-1.8 | 94.1 Wh $kg^{-1}$ | 24.5 kW $kg^{-1}$ | This work |

## References

[1] L. Dong, X. Ma, Y. Li, L. Zhao, W. Liu, J. Cheng, C. Xu, B. Li, Q.-H. Yang, F. Kang, Energy Stor. Mater., 13 (2018) 96-102.

[2] H. Wang, M. Wang, Y. Tang, Energy Stor. Mater., 13 (2018) 1-7.

[3] P. Yu, Y. Zeng, Y. Zeng, H. Dong, H. Hu, Y. Liu, M. Zheng, Y. Xiao, X. Lu, Y. Liang, Electrochim. Acta, 327 (2019) 134999.

[4] G. Sun, H. Yang, G. Zhang, J. Gao, X. Jin, Y. Zhao, L. Jiang, L. Qu, Energy Environ. Sci., 11 (2018) 3367-3374.

[5] S. Wu, Y. Chen, T. Jiao, J. Zhou, J. Cheng, B. Liu, S. Yang, K. Zhang, W. Zhang, Adv. Energy Mater., 9 (2019) 1902915.

[6] S. Chen, L. Ma, K. Zhang, M. Kamruzzaman, C. Zhi, J.A. Zapien, J. Mater. Chem. A, 7 (2019) 7784-7790.

[7] J. Han, K. Wang, W. Liu, C. Li, X. Sun, X. Zhang, Y. An, S. Yi, Y. Ma, Nanoscale, 10 (2018) 13083-13091.

[8] Q. Yang, Z. Huang, X. Li, Z. Liu, H. Li, G. Liang, D. Wang, Q. Huang, S. Zhang, S. Chen, C. Zhi, ACS Nano, 13 (2019) 8275-8283.

[9] P. Liu, Y. Gao, Y. Tan, W. Liu, Y. Huang, J. Yan, K. Liu, Nano Res., 12 (2019) 2835-2841.

[10] H. Zhang, Q. Liu, Y. Fang, C. Teng, X. Liu, P. Fang, Y. Tong, X. Lu, Adv. Mater., 31 (2019) 1904948.

# Part III

# Conclusions and Future Work

# Chapter 7 Conclusions

This thesis focuses on the investigation of zinc-based electrochemical energy storage devices in terms of reaction mechanism and improvement of their electrochemical performance by exploring advanced cathode materials used in this type of device. It aims to obtain better understanding of the underlying science and accelerate the practical development of zinc-based electrochemical energy devices based on various cathode materials.

In Chapter 3, the direct evidence of the importance of $Mn^{2+}$ in rechargeable aqueous Zn-$MnO_2$ batteries was provided by investigating the discharge-charge behavior. The reaction mechanism was studied with a home-made cell containing a large amount of electrolyte (ca. 12 mL) without separator. Without $Mn^{2+}$ pre-added in the electrolyte, the dissolved $Mn^{2+}$ ions are not easily returned to the electrode, resulting in the instantaneous failure of the cell. This provides a direct way to identify the degradation mechanism of the rechargeable aqueous Zn-$MnO_2$ batteries, thus helping to reveal the underlying reaction mechanism. By increasing the content of $Mn^{2+}$ in the electrolyte, the loss of $MnO_2$ from the electrode can be replenished by electrodeposition of $MnO_2$ from the pre-addition $Mn^{2+}$ in the electrolyte, leading to a normal charging behaviour. This degradation and charging mechanism also apply to other manganese oxides such as β-$MnO_2$. More interestingly, the in-depth investigation of morphology and structure of the discharged cathode reveals that there is a conversion reaction between $MnO_2$ and MnOOH without zinc ion intercalation into the tunnel of α-$MnO_2$ to form the $ZnMn_2O_4$ or $Zn_xMnO_2$ phase. The dissolution of $Mn^{2+}$ is caused by the acidic disproportionation of MnOOH. The precipitation of zinc hydroxide sulfate hydrate is essential to buffer the pH value of the solution. These findings shed light on the degradation and reaction mechanism of rechargeable aqueous Zn-$MnO_2$ batteries and provide useful guidance in designing high-performance rechargeable aqueous Zn-$MnO_2$ batteries.

In Chapter 4, the voltage range and self-discharge phenomena have been systematically investigated in aqueous zinc-ion hybrid supercapacitors, which leads to better understanding of this hybrid device. Three universal approaches based on CV and GCD techniques were employed to thoroughly investigate the voltage window in this aqueous zinc-ion hybrid supercapacitor based on 2 M $ZnSO_4$. The mechanism of the zinc-ion hybrid supercapacitor involves the simultaneous adsorption–desorption of ions on the AC cathode and zinc ion plating/stripping on the Zn anode. Constructed by the high capacity of the Zn metal negative electrode, with its relatively low standard redox potential of 0.76 V (vs. standard hydrogen electrode) and neutral aqueous electrolyte, the hybrid supercapacitors have demonstrated excellent electrochemical performances including high specific capacitance (308 F $g^{-1}$ at 0.5 A $g^{-1}$ and 110 F $g^{-1}$ at 30 A $g^{-1}$), good cycling stability (10000 cycles with 95.1% capacitance retention) and a high energy density 104.8 Wh k $g^{-1}$ at 383.5 W $kg^{-1}$ (30.8 Wh k $g^{-1}$ at 19.0 kW $kg^{-1}$) based on the active materials, which exceed those of most reported zinc-based hybrid supercapacitors and symmetrical supercapacitors. Additionally, self-discharge was substantially suppressed in the hybrid supercapacitors compared with the symmetric supercapacitors because the energy barrier for spontaneous plating and stripping of Zn is much higher than that in electrostatic adsorption and desorption of ions on the electrode surface. Since the zinc foil can be simultaneously used as both current collector and active material, the unnecessary weight and volume of the devices can potentially be reduced to some extent. The performance of this device can be further boosted by developing novel advanced carbon-based materials or other composites. This work is expected to provide more insight into the hybrid supercapacitors and accelerate industrial development of high-voltage aqueous hybrid supercapacitors for next-generation energy storage devices.

In Chapter 5, for the first time, binder free composite electrodes of EGO and PPy have been prepared by a facile one-step electrochemical co-deposition method and used in combination with Zn halides electrolyte for aqueous Zn-PPy hybrid supercapacitors. This electrochemical co-deposition leads to device-ready composite electrodes that

have a porous structure formed by the PPy coated EGO nanosheets. The porous structure and the thin PPy coating allow fast transport of electrolyte ions in electrode pores and short diffuse pathway in the solid phase of PPy, respectively. The electrochemical reduction of the incorporated EGO nanosheets during the initial CV cycling of the PPy/EGO composite electrode ensures good electron conduction in the composites. The enhanced electronic and ionic conduction in the PPy/EGO composite electrodes lead to a high specific capacitance of 444.2 F $g^{-1}$ at 0.35 A $g^{-1}$ (633.0 mF $cm^{-2}$ at 0.5 mA $cm^{-2}$). The Zn-PPy hybrid supercapacitor based on the PPy/EGO cathode and a 1 M $ZnCl_2$ aqueous electrolyte exhibits high energy densities of 117.7 and 72.1 Wh $kg^{-1}$ at 0.34 and 12.4 kW $kg^{-1}$, respectively, together with good cycling stability (81% retention after 5000 cycles). Experimental evidence indicates that the charge-discharge mechanism of the PPy/EGO composite cathode mainly involves fast monovalent anion (e.g., $Cl^-$) insertion/de-insertion into/from the PPy. This high performance, yet safe and low cost, aqueous Zn-PPy hybrid supercapacitor is particularly promising for large scale energy storage that requires a combination of high energy density and power density. Furthermore, the insights into the charge storage mechanism of the Zn-PPy system would potentially guide its future designs of high-performance electrodes and electrolytes.

In Chapter 6, hierarchically porous carbon as cathode for zinc-ion hybrid supercapacitors have been prepared via $CO_2$ activation by using starch as precursor. The specific surface area and pore structure of the as-prepared materials can be tuned by the activation time. The optimized porous carbon possesses hierarchical porous nanostructure with a pore size distribution from 0.5 nm to 6 nm as well as a high specific surface area of 2457 $m^2$ $g^{-1}$. The resultant zinc ion hybrid supercapacitors operate in a voltage range from 0.2 V to 1.8 V, delivering a high capacitance of 259 F $g^{-1}$ at a current density of 0.5 A $g^{-1}$, high rate capability (160 F $g^{-1}$ at 30 A $g^{-1}$), a high energy density of 94.1 Wh $kg^{-1}$ at 399 W $kg^{-1}$ as well as a high power density of 24.5 kW $kg^{-1}$ at 58.5 Wh $kg^{-1}$. It also exhibits excellent cycling stability with 97% capacitance retention after 10000 cycles. The excellent electrochemical performance can be attributed to the high

specific surface area and well-combined micropores/mesopores within the texture, thus providing effective surface sites and facilitating high rate performance. Since this energy storage device uses nontoxic electrode materials and aqueous electrolyte, it can potentially resolve the safety concerns and environmental issues associated with organic-based energy storage. Moreover, abundant biomass resources can effectively reduce the cost of the electrode materials and further reduce the cost of the final devices, thereby facilitating the wide application of this device to harvest renewable and green energy. Considering the facile, green and cost-effective synthesis, it also provides various potential applications such as adsorbent, catalyst support or gas storage.

# Chapter 8 Future work

Although manganese oxides possess lots of merits such as low cost, a high operation voltage and a high capacity used as cathode in aqueous zinc-ion batteries, their cycling stability is not very satisfactory due to the dissolution of $Mn^{2+}$ ions over the repeated cycles. Although the additive of $Mn^{2+}$ ions can improve the cyclability to some degree, appropriate concentration of $Mn^{2+}$ needs to be carefully considered in specific situations to balance the dissolution and the re-oxidation of $Mn^{2+}$ ion. Additionally, how to effectively suppress the Jahn-Teller effect of $Mn^{3+}$ remains a big challenge, thus avoiding the use of additive of $Mn^{2+}$ ions and further enhancing the cycling stability. Pre-insertion ions and doping or coating can be attempted to improve the structural stability of manganese oxides. Moreover, the poor electronic conductivity of manganese oxides limits their rate capability. Constructing composites of manganese oxides and graphene or carbon nanotubes can be adopted to improve the electrochemical performance.

As to the aqueous zinc-ion hybrid supercapacitors, the electrochemical performance is mainly determined by the cathode materials. Therefore, rational design of microstructure of carbon-based materials and development of novel cathode materials such as composites with low cost can still be the future directions to optimize this technology. Also, non-aqueous electrolytes can be attempted to further expand the operational window to enhance the output energy density. The thickness or mass loading of the zinc anode can be optimized to reduce the dead weight, thus enhancing the utilization of zinc metal and reducing the volume of the device.

To scale up Zn-based electrochemical energy devices, the priority is to consider the safety issue and cost. The main issue related to Zn-based electrochemical energy devices is probably the zinc dendrite. In principle, it is possible to mitigate the zinc dendrite growth during the repeated cycles, considering that the Zn dendrite growth is not as severe as the Li dendrite. It should be noted that the Zn dendrite growth is highly influenced by the electrolytes and the charge-discharge current. In the laboratory test,

most electrochemical measurements are usually carried out in a coin cell, which is difficult to reflect the practicability. The mass loading of the active materials is relatively low compared with the commercial cell. Therefore, the absolute current used for cycling test is quite low. As a result, the Zn dendrite growth is not obvious to cause the failure of the cell. The zinc plating and stripping behavior should be further investigated under high charge-discharge current or in the practical operating environment. Furthermore, large-scale cell should be fabricated to test the safety issue although this type of aqueous device is safe in principle.

Although the cathode materials such as $MnO_2$, activated carbon and polypyrrole are widely used in the Zn-based electrochemical energy storage devices, the promising research results obtained are only limited on the laboratory scale. How to transfer the knowledge obtained in the laboratory to practical technology is really a valuable issue. More large-scale experiments in practical situations should be carried out to reflect the feasibility and problems.